# Tight-Binding based Investigation of Semiconductor Quantum Dots and Molybdenum Disulfide Nanobubbles

## From Atomic Structure to Optical Spectra

**Christian Carmesin**

University of Bremen

Universität Bremen

ITP

# Tight-Binding based Investigation of Semiconductor Quantum Dots and Molybdenum Disulfide Nanobubbles

## From Atomic Structure to Optical Spectra

dem Fachbereich Physik/Elektrotechnik
der Universität Bremen

zur Erlangung des akademischen Grades
**Doktor der Naturwissenschaften (Dr. rer. nat)**
genehmigte Dissertation

vorgelegt von

M. Sc. Christian Carmesin
aus New York

| | |
|---|---|
| 1. Gutachter: | Prof. Dr. rer. nat. Frank Jahnke |
| 2. Gutachter: | Prof. Dr. rer. nat. Gerd Czycholl |

| | |
|---|---|
| Eingereicht am: | 13.08.2018 |
| Tag des Promotionskolloquiums: | 14.09.2018 |

# Contents


**1. Introduction** **1**

1.1. Topics . . . 3

1.1.1. III-V Semiconductor Quantum Dots . . . 3

1.1.2. Molybdenum Disulfide Nanobubbles . . . 4

1.2. Outline of the Content . . . 4

**2. Fundamentals of Solid State Physics** **6**

2.1. III-V Bulk Semiconductors . . . 6

2.1.1. Zinc Blende Structure . . . 6

2.1.2. Reciprocal Space and Brillouin Zone . . . 7

2.1.3. Electrons in a Periodic Potential . . . 9

2.1.4. Electronic Bulk Band Structure . . . 10

2.2. Low-Dimensional Semiconductor Systems . . . 12

2.3. Semiconductor Quantum Dots . . . 15

2.3.1. Structure and Electronic Properties . . . 16

2.3.2. Growth Techniques . . . 16

2.4. Optical Properties . . . 18

2.4.1. Excitons in Bulk Crystals . . . 18

2.4.2. Excitonic Configurations in Quantum Dots . . . 19

**3. Electronic Properties of III-V Semiconductors** **21**

3.1. $k \cdot p$ Model . . . 22

3.2. Pseudopotential Model . . . 23

3.3. Tight-Binding Model . . . 24

3.3.1. Two-Center Approximation . . . 27

3.3.2. Empirical Tight-Binding . . . 28

3.3.3. Implementation of the $sp^3s^*$ Model . . . 29

3.3.4. Spin-Orbit Coupling . . . 31

**4. Tight-Binding Description of III-V Semiconductor Quantum Dots** 33
4.1. Spatially-Resolved Model . . . 33
4.1.1. Atom Numbers . . . 35
4.1.2. Tight-Binding Matrix . . . 36
4.1.3. Coupling Matrix Elements . . . 38
4.2. Description of Interfaces . . . 41
4.3. Description of Alloyed Nanostructures . . . 44
4.4. Piezoelectricity . . . 46
4.5. Strain . . . 46
4.5.1. Continuum Mechanics . . . 47
4.5.2. Valence Force Field Method . . . 47
4.5.2.1. Keating Potential . . . 47
4.5.2.2. Tersoff Potential . . . 48
4.6. Implementation of Strain . . . 50
4.6.1. Strain-Induced Coordinates . . . 51
4.6.2. Incorporation of Strain . . . 51
4.7. Matrix Diagonalization . . . 52
4.8. Sample Calculation . . . 53

**5. Optical Properties of III-V Semiconductors** 57
5.1. Coulomb Matrix Elements . . . 58
5.2. Dipole Matrix Elements . . . 60
5.3. Optical Spectra . . . 61
5.3.1. Semiconductor Bloch Equations . . . 62
5.3.2. Semiconductor Luminescence Equations . . . 64
5.3.3. Configuration Interaction and Fermi's Golden Rule . . . 66

**6. Quaternary 1.55 $\mu$m Telecom Quantum Dots** 73
6.1. Experimental Analysis . . . 73
6.1.1. Sample Growth and Optical Characterization . . . 74
6.1.2. Structural Analysis . . . 74
6.2. Theoretical Results . . . 77
6.3. Local Indium Accumulations . . . 81

**7. Ternary 1.55 $\mu$m Telecom Quantum Dots** 84
7.1. Experimental Analysis . . . 85
7.1.1. Sample Growth and Optical Characterization . . . 85
7.1.2. Structural Analysis . . . 86
7.2. Theoretical Results . . . 88

7.3. Multi-Exciton Spectra . . . . . 92
7.4. Temperature-Dependent Analysis . . . . . 97

**8. Atomically Thin Semiconductors** **100**
8.1. Transition Metal Dichalcogenides . . . . . 100
8.1.1. Molybdenum Disulfide . . . . . 101
8.1.2. Production Techniques . . . . . 102
8.2. Nanostructured TMDCs . . . . . 102
8.3. Monolayer Tight-Binding Model . . . . . 105
8.3.1. Hamiltonian at Points of High Symmetry . . . . . 108
8.3.2. Implementation of Strain . . . . . 109
8.3.3. Implementation of Dielectric Effect . . . . . 110
8.4. Modeling $MoS_2$ Nanobubbles . . . . . 111

**9. Summary and Outlook** **122**
9.1. III-V Semiconductors . . . . . 122
9.2. Molybdenum Disulfide Nanobubbles . . . . . 124

**A. Appendix** **127**
A.1. Tight-Binding Parameters for III-V Semiconductors . . . . . 128
A.2. Neighbor Numbers . . . . . 128
A.3. Force Field Parameters . . . . . 130
A.3.1. Keating Potential . . . . . 130
A.3.2. Tersoff Potential . . . . . 130
A.3.3. Energy Minimization . . . . . 131
A.4. Strain-Induced Coordinates . . . . . 135
A.5. Tight-Binding Diagonalization . . . . . 135
A.6. Calculation of Tight-Binding Coulomb Matrix Elements . . . . . 137
A.7. Coulomb Matrix Elements in Envelope-Function Approximation . . . . . 138

**Bibliography** **141**

**Publications and Conference Contributions** **159**

**Acknowledgements** **163**

# Abstract

The present work achieves an understanding of the interplay between morphology, electronic, and optical properties of semiconductor nanostructures for single-photon emission. The latter is important for various quantum information applications, including future quantum communication devices.

In the first part of this thesis, III-V semiconductor quantum dots are investigated. These systems have emerged as promising candidates for deterministic single-photon sources due to high repetition rates, integrability into electrical devices, and tunable emission energy. In particular, we analyze two different quantum dot systems, which are capable of single-photon emission in the technologically important telecom C-band. The electronic single-particle energies and wave functions are calculated using a nearest neighbour $sp^3s^*$ empirical tight-binding (TB) model. Strain arising from lattice mismatch of the constituent materials is calculated atomistically by employing a valence-force field method. The theoretical model is based on realistic quantum dot geometries and concentration profiles, which are obtained from transmission electron microscopy. When using the measured results for a representative quantum dot geometry as well as experimentally reconstructed alloy concentrations, a combination of strain-field and TB calculations is able to reproduce the quantum dot emission wavelength in agreement with the experimentally determined photoluminescence spectrum. The inhomogeneous broadening of the latter can be related to calculated variations of the emission wavelength for the experimentally deduced In-concentration fluctuations and size variations. The results provide a deeper understanding of the interplay between morphology, electronic, and optical properties of semiconductor quantum dots.

In the second part of this thesis, we investigate atomically thin layers of transition metal dichalcogenides (TMDCs), which have recently emerged as a new class of optically active materials for opto-electronic applications. These systems offer a relative ease of fabrication and the potential for large-scale applications. Engineering of the local confinement situation can lead to discretized states, which opens the possibility for deterministic single-photon generation. One possible platform are molybdenum disulfide nanobubbles that develop when air is enclosed during the stacking of layers. An analysis of strain and dielectric effects in nanostructures reveals that an interplay of these physical effects leads to the formation of confined quantum-dot-like single-particle states that give rise to single-photon emission. The confinement of these states is caused by a wrinkling of the material, that supports the formation of strain-induced pockets. The results provide a deeper understanding of the interplay between strain, dielectric effects, electronic, and optical properties of TMDC nanostructures.

# 1. Introduction

The present work achieves an understanding of the interplay between morphology, electronic, and optical properties of semiconductor nanostructures for single-photon emission. The latter is important for quantum information applications [1] and in particular quantum key distribution (as schematically depicted in Fig. 1.1). Prerequisite for this procedure are light sources, which emit a single-photon at a time. Such single-photon sources or, more generally, sources of quantum light, can be characterized by a Hanbury-Brown and Twiss (HBT) measurement [2], as illustrated in Fig. 1.2. Essential techniqual requirements and corresponding physical problems for single-photon sources include an ease of fabrication as well as an on-demand generation of single-photons with high repetition rate and tunable emission energy. In particular, emission in the telecom C-band at 1.55 $\mu$m [3] is desirable as the latter provides a global absorption minimum in optical fibers [4], an atmospheric transmission window [5], and sets the frequency standard in mature silicon integrated photonics [6]. Possible candidates for single-photon emission currently include nitrogen-vacancy (NV) centers in diamond [7, 8, 9], trapped atoms and ions systems [10, 11], semiconductor quantum dots [12, 13], or even more recently atomically thin two-dimensional transition metal dichalcogenides (TMDCs) [14, 15, 16, 17, 18, 19]. In this work, we focus on semiconductor quantum dots and TMDC nanostructures. The former have emerged as promising candidates for deterministic single-photon sources [20] due to high repetition rates, tunable emission energy [21], and integrability into electrical devices [22, 23]. On the other hand, TMDCs offer a relative ease of fabrication and the potential for large-scale applications.

In the first part of this work, we investigate semiconductor quantum dots and analyze the interplay between morphology and emission in the technologically important telecom C-band. To provide an insight between the connection of atomic structure and electronic properties, we employ an empirical tight-binding (TB) model. The latter proves to be a suitable choice for electronic state calculations in combination with experimentally available transmission electron microscopy results, which provide access to realistic quantum dot geometries and concentration profiles. In order to achieve an agreement between the calculated emission energies and the experimentally determined photoluminescence (PL) spectrum, we utilize a combination of strain-field and TB calculations for a representative

quantum dot geometry and alloy concentration. The inhomogeneous broadening of the PL spectrum can be related to calculated variations of the emission wavelength for the experimentally deduced In-concentration fluctuations and size variations.

In the second part, we investigate TMDC nanostructures. We focus on $MoS_2$ nanobubbles [24, 19] that develop when air is enclosed during the stacking of layers. In our analysis, the methods of atomistic modeling that have been successfully applied to III-V semiconductor quantum dots are transferred and extended to model $MoS_2$ nanobubbles. Within this novel approach of modeling 2D nanostructures, the valence force field method is combined an atomistic tight-binding model. Our results show the formation of strain pockets, which originate from the high bending-rigidity of $MoS_2$. In these strain pockets, we find highly localized charge carriers, which are responsible for strong emission.

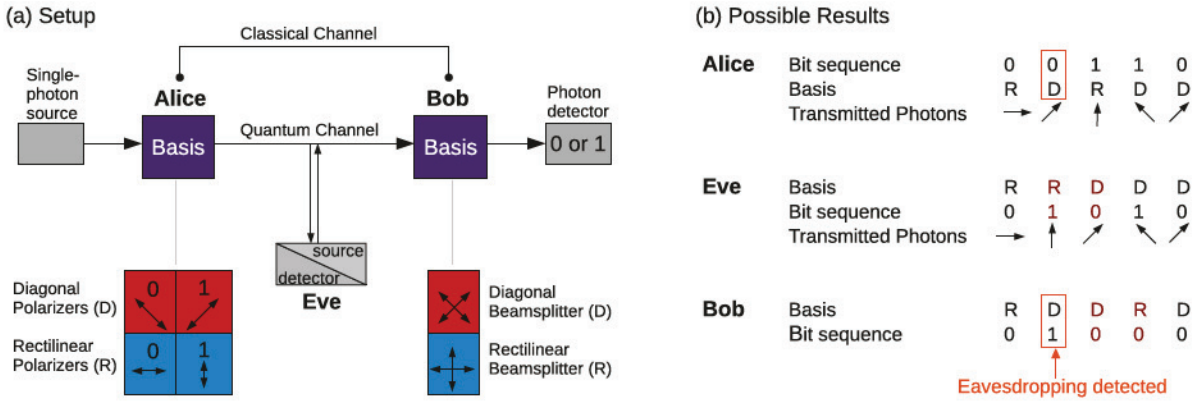


**Figure 1.1. | Quantum key distribution**. Procedure of the BB84 protocol [25] under eavesdropping, example from Ref. [26]. In a first step, Alice prepares a binary sequence (00110) and chooses a random basis sequence (RDRDD). Eve intercepts each photon and measures it in her randomly chosen basis (RRDDD), producing her sequence of bits (01010). Subsequently, Eve substitutes the photons she has intercepted, by encoding her bits in her randomly chosen basis. These photons from Eve are measured by Bob in his randomly chosen bases (RDDRD), obtaining his sequence of bits (01000). In the last step, Alice and Bob compare their basis choices and detect eavesdropping via the second bit, for which they used identical bases but obtained different values.

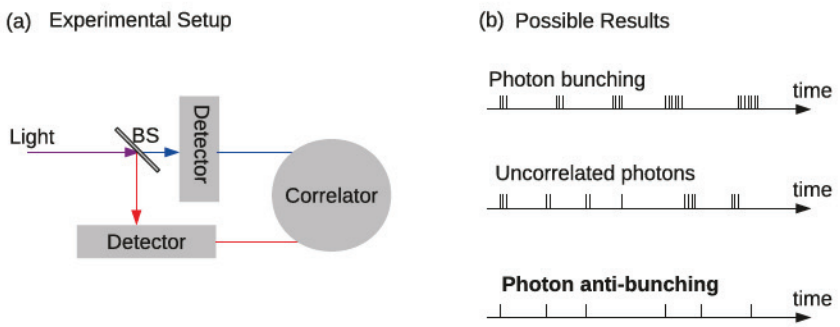


**Figure 1.2. | Characterization of light**. (a) Setup as initially proposed by HBT [2]: The incident beam (violet) is split by a beam splitter (BS). Each of the two beams (red, blue) is focused onto a different detector. A correlation between detections as a function of time is measured. (b) Possible results include more than one photon at a time (photon bunching), just a single-photon (anti-bunching), or a random intermediate behavior (uncorrelated photons).

## 1.1. Topics

As indicated above, this work consists of two parts, each containing a theoretical description of a material system as a platform for single-photon emission. On the one hand, we present results on the relatively established system of III-V semiconductor quantum dots and explain the mechanism behind emission in the technologically important telecom C-band. On the other hand, we investigate single-photon emission in rather new TMDC-based nanostructures.

### 1.1.1. III-V Semiconductor Quantum Dots

Advances in the production of nano-scale semiconductors have made it possible to faciliate the growth of quantum dots. Such systems can be obtained by embedding a semiconductor material with a lower band gap into one with a larger band gap. As a result, one obtains electronic confinement and localized wave functions. A central property of quantum dots is the dependence of the confinement potential on size, geometry, material composition, and strain, which makes it possible to modify their properties by controlling the growth parameters [27, 28, 29]. For instance, the emission wavelength can be varied from arsenic-based quantum dots in the infra-red [30] to nitride-based quantum dots in the blue spectral range [31]. Due to these possibilities as well as years of industrial experience in the growth and fabrication of semiconductors, quantum dots have emerged as a promising platform for optoelectronic components [32, 33, 34, 35]. Moreover, quantum dots have recently even been used to produce particularly bright and colorful displays for televisions [36, 37]. For the emission in the C-band at 1.55 $\mu$m, different approaches have been successfully applied to grow InAs quantum dots on InP substrates, such as the double-cap method [38], the insertion of ultrathin GaAs layers [39], or droplet epitaxy [40]. Recently, this goal has been achieved by using InAs/InGaAs/GaAs quantum dots [41].

In particular, two different quantum dot systems, which are capable of single-photon emission in the technologically important telecom C-band, are investigated. In order to achieve the goal of analyzing the connection between morphology, composition, electronic and optical properties, a collaboration has taken place. Within this collaboration state of the art growth of quantum dot samples as well as their optical characterization was performed in the groups of Prof. Reithmaier in Kassel and Prof. Michler in Stuttgart. Additionally, structural information about the shape, geometry, and alloy concentration of individual quantum dots was obtained from transmission electron microscopy in the group of Prof. Rosenauer in Bremen. A combination of the above experimental results with our atomistic TB calculations provides a deeper understanding of the interplay between morphology, electronic, and optical properties of the investigated systems.

### 1.1.2. Molybdenum Disulfide Nanobubbles

An alternative system for single-photon emission are 2D materials, which consist of only a single layer of atoms. Since the exfoliation of graphene [42], for which the Nobel Prize in Physics was awarded in 2010, 2D materials have been a growing field of research as new physical properties emerge in a single atomic layer compared to a bulk crystal. An interesting class of 2D materials for optoelectronic applications are transition metal dichalcogenides (TMDCs) due to the change from an indirect band gap in $MoS_2$, $WS_2$, $MoSe_2$, and $WSe_2$ bulk crystals to a direct band gap in the visible frequency range in monolayers [43, 44, 45, 46, 47].

In the rapidly developing field of TMDCs, attention has increasingly shifted towards manufacturing nanostructures since local confinements can be generated comparatively easily within these materials. Due to the two-dimensional nature of TMDCs, they are strain-sensitive with respect to bending, which can be used to generate a local confinement, as demonstrated for instance in Refs. [15, 16]. Additionally, the Coulomb interaction within the material can be changed via the dielectric environment. Depending on the material surrounding the two-dimensional TMDC, a confinement/repulsion potential is generated. Exploiting these properties to produce single-photon sources, TMDC nanostructures have been manufactured by change of the dielectric environment [48, 49], placing single TMDC layers on gold substrates [15, 16], substrates with etched holes [14], or even on top of an array of nanowires [17, 18].

The interplay between strain and dielectric effects on the confinement situation in TMDC-based nanostructures is investigated by means of an atomistic model. As indicated above, we focus on $MoS_2$ nanobubbles [24, 19] that develop when air is enclosed during the stacking of layers. Single-photon emission has been demonstrated in such nanobubbles [19], which renders them interesting from both a fundamental and technological point of view. Our results for $MoS_2$ nanobubbles are prototypical for TMDC-based nanostructures. They open the door for further research on similar structures that can be optimized for large-scale single-photon emission by deterministically engineering the confinement potential on an atomistic level.

## 1.2. Outline of the Content

After this introduction, Chapter 2 summarizes fundamentals of solid state physics, which lay the foundation for our results of electronic and optical properties of III-V semiconductors and their respective nanostructures within this work. In Chapter 3, different methods are presented for modeling the electronic properties of III-V semiconductor bulk materials.

Hereby, an emphasis is placed on the atomistic tight-binding model, which is employed throughout this work, and its implementation. Chapter 4 builds on Chapter 3 and discusses the extension of the tight-binding method to model the electronic properties of semiconductor quantum dots. To this end, the treatment of alloyed nanostructures within the tight-binding approach is presented in detail, including the treatment of relevant influences, such as band alignment, averaging of parameters, and strain. Due to the atomistic character of the tight-binding model, we combine it with the valence force field method to account for strain effects. For each of the above points, details on the numerical implementation are provided. To give a complete picture, subsequently an example calculation is presented and shortly discussed. Based on the tight-binding calculation, as presented in Chapter 4, we demonstrate how to determine the dipole and Coulomb matrix elements from the tight-binding coefficients in order to subsequently calculate optical spectra. To this end, different methods are presented in Chapter 5. We combine the configuration interaction method with Fermi's golden rule, which provides access to optical spectra for the full Coulomb-correlated many-body eigenstates within first order perturbation theory. In Chapter 6 and 7, results for semiconductor quantum dots for the emission in the telecom C-band are presented, which include an analysis of the structural, electronic, and optical properties. After these results regarding III-V semiconductors, in Chapter 8, atomically thin transition metal dichalcogenides are introduced as an alternative class of materials for single-photon emission. We study the interplay of strain and dielectric effects on the confinement situation of $MoS_2$ nanobubbles, for which we provide an atomistic model. In Chapter 9, the results of this work are summarized and an outlook is given.

# 2. Fundamentals of Solid State Physics

In this chapter, basic concepts of the theory of crystalline solids are summarized in order to lay the foundation for the subsequently presented results in this work. In section 2.1, the essential properties of the zinc blende structure as well as the reciprocal space and the electronic structure are presented. This overview is followed by a focus on systems of lower spatial dimension in sections 2.2 and 2.3. For further reading, we refer to textbooks, e.g. see [50, 51, 52, 53] and dissertations, see [54, 55, 56].

## 2.1. III-V Bulk Semiconductors

The materials InAs, GaAs and AlAs are III-V semiconductors, which consist of elements of the third and the fifth main group of the periodic table. The corresponding zinc blende crystal structure is a face-centered cubic (fcc) Bravais lattice (see Fig. 2.1) with a diatomic base, consisting of one anion and one cation.

### 2.1.1. Zinc Blende Structure

In Cartesian coordinates, the two circled atoms in Fig. 2.1 can be described by

$$\{(0,0,0),\ \ \frac{a}{4}(1,1,1)\}. \tag{2.1}$$

These two atoms form the diatomic basis. For this basis, a possible set of primitive lattice vectors is given by

$$\{\mathbf{a}_1 = \frac{a}{2}(1,1,0),\ \ \mathbf{a}_2 = \frac{a}{2}(1,0,1),\ \ \mathbf{a}_3 = \frac{a}{2}(0,1,1)\}, \tag{2.2}$$

where $a$ is the edge length of the conventional unit cell (see Fig. 2.1). Using the primitive lattice vectors in Eq. (2.2), all positions of the Bravais lattice can be represented by

$$\mathbf{R}_n = n_1\mathbf{a}_1 + n_2\mathbf{a}_2 + n_3\mathbf{a}_3 \ \ \text{with} \ \ n_i \in \mathbb{Z}. \tag{2.3}$$

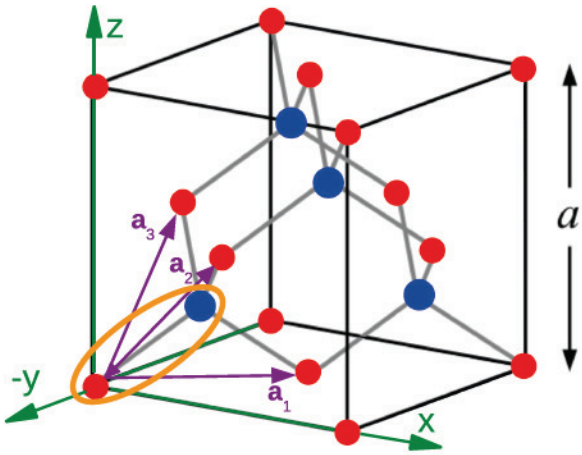


**Figure 2.1. | Conventional zinc blende unit cell**. The structure consists of a diatomic base (circled atoms) as well as three primitive lattice vectors $\mathbf{a}_1, \mathbf{a}_2$ and $\mathbf{a}_3$.

A periodic arrangement of the unit cells (see Fig. 2.1) defines the bulk crystal, which is translationally invariant. As a result of this property, any physical quantity of the bulk crystal can be written as a periodic function

$$f(\mathbf{r}) = f(\mathbf{r} + \mathbf{R}_n). \tag{2.4}$$

### 2.1.2. Reciprocal Space and Brillouin Zone

Due to the spatial periodicity of the quantity $f$, it can be expanded in terms of a Fourier series

$$\begin{aligned} f(\mathbf{r}) &= \sum_m f_m e^{i\mathbf{G}_m \cdot \mathbf{r}} \\ f(\mathbf{r} + \mathbf{R}_n) &= \sum_m f_m e^{i\mathbf{G}_m \cdot (\mathbf{r} + \mathbf{R}_n)} = \sum_m f_m e^{i\mathbf{G}_m \cdot \mathbf{r}} e^{i\mathbf{G}_m \cdot \mathbf{R}_n}. \end{aligned} \tag{2.5}$$

Since $f(\mathbf{r})$ and $f(\mathbf{r} + \mathbf{R}_n)$ must be equal (see Eq. (2.4)), it follows

$$\mathbf{G}_m \cdot \mathbf{R}_n = 2\pi N \quad \text{with} \quad N \in \mathbb{Z}. \tag{2.6}$$

Consequently, the set of all wave vectors $\mathbf{G}_m$ that satisfy Eq. (2.6) for all lattice point position vectors $\mathbf{R}_n$, define the reciprocal lattice. It can be expressed as [57]

$$\mathbf{G}_m = m_1\mathbf{k}_1 + m_2\mathbf{k}_2 + m_3\mathbf{k}_3 \quad \text{with} \quad m_i \in \mathbb{Z}, \tag{2.7}$$

where the primitive reciprocal vectors $\{\mathbf{k}_1, \mathbf{k}_2, \mathbf{k}_3\}$ satisfy

$$\mathbf{a}_i \cdot \mathbf{k}_j = 2\pi\delta_{ij} \quad \text{with} \quad i, j \in \{1, 2, 3\}. \tag{2.8}$$

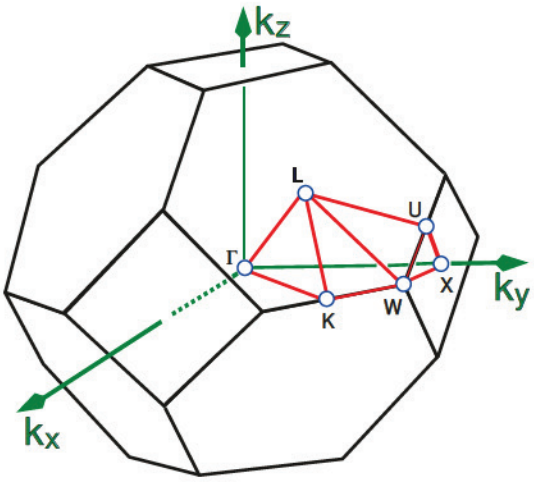


**Figure 2.2. | First Brillouin zone of the fcc lattice.** The irreducible part is characterized by points of high symmetry (blue circles) and connecting lines (red).

For the fcc lattice (see Fig. 2.1), the corresponding reciprocal lattice is body-centered cubic (bcc) and vice versa [50]. The primitive Wigner-Seitz cell of the reciprocal lattice defines the first Brillouin zone[1] and can be described by a polyhedron that encloses the region around a reciprocal lattice point, which is closer to this point than to any other lattice point [50]. The first Brillouin zone of the fcc lattice is depicted in Fig. 2.2. It includes points of high symmetry, such as the center of the Brillouin zone $\mathbf{\Gamma}$, the center of a face $\mathbf{X}$, the middle of an edge joining a hexagonal and a square face $\mathbf{U}$, the middle of an edge joining two hexagonal faces $\mathbf{K}$, the center of a hexagonal face $\mathbf{L}$ and a corner point $\mathbf{W}$. In Cartesian coordinates, these points are given by

$$\begin{aligned}
\mathbf{\Gamma} &= (0,\ 0,\ 0)\,, \\
\mathbf{X} &= \frac{2\pi}{a}\,(0,\ 1,\ 0)\,, \\
\mathbf{U} &= \frac{2\pi}{a}\,(1/4,\ 1,\ 1/4)\,, \\
\mathbf{K} &= \frac{2\pi}{a}\,(3/4,\ 3/4,\ 0)\,, \\
\mathbf{L} &= \frac{2\pi}{a}\,(1/2,\ 1/2,\ 1/2)\,, \\
\mathbf{W} &= \frac{2\pi}{a}\,(1/2,\ 1,\ 0)\,.
\end{aligned} \tag{2.9}$$

The connecting lines between these points of high symmetry $\mathbf{\Gamma}, \mathbf{X}, \mathbf{U}, \mathbf{K}, \mathbf{L}$, and $\mathbf{W}$ enclose a region called irreducible Brillouin zone. Due to the symmetry and periodicity of the crystal, it is possible to restrict the analysis of physical properties to this region. An example are band structures, as presented in Fig. 2.3.

[1] It is sufficient to describe all processes in the first Brillouin zone. Therefore, the term Brillouin zone always refers to the first Brillouin zone.

### 2.1.3. Electrons in a Periodic Potential

Since the lattice point positions of the bulk crystal are translationally invariant (see Eq. (2.3)), this must also hold for the crystal potential

$$V(\mathbf{r}) = V(\mathbf{r} + \mathbf{R}_n) \tag{2.10}$$

and thus the electronic probability density

$$\psi^\star(\mathbf{r})\psi(\mathbf{r}) = \psi^\star(\mathbf{r} + \mathbf{R}_n)\psi(\mathbf{r} + \mathbf{R}_n). \tag{2.11}$$

The invariance of the probability density implies that the single-particle wave functions

$$\psi(\mathbf{r} + \mathbf{R}_n) = e^{i\mathbf{k}\mathbf{R}_n}\psi(\mathbf{r}) \tag{2.12}$$

can only deviate by a phase factor, which is known as Bloch's theorem [58]. Let us formulate this theorem in a more prominent way by introducing the Bloch functions

$$u_\mathbf{k}(\mathbf{r}) = e^{-i\mathbf{k}\mathbf{r}}\psi(\mathbf{r}), \tag{2.13}$$

which carry the periodicity of the Bravais lattice:

$$\begin{aligned} u_\mathbf{k}(\mathbf{r} + \mathbf{R}_n) &= e^{-i\mathbf{k}(\mathbf{r}+\mathbf{R}_n)}\psi(\mathbf{r} + \mathbf{R}_n) \\ &= e^{-i\mathbf{k}\mathbf{r}}e^{-i\mathbf{k}\mathbf{R}_n}\psi(\mathbf{r} + \mathbf{R}_n) \\ &= e^{-i\mathbf{k}\mathbf{r}}e^{-i\mathbf{k}\mathbf{R}_n}e^{i\mathbf{k}\mathbf{R}_n}\psi(\mathbf{r}) \\ &= e^{-i\mathbf{k}\mathbf{r}}\psi(\mathbf{r}) = u_\mathbf{k}(\mathbf{r}). \end{aligned} \tag{2.14}$$

By rewriting Eq. (2.13), we obtain

$$\psi_{n\mathbf{k}}(\mathbf{r}) = e^{i\mathbf{k}\cdot\mathbf{r}}u_{n\mathbf{k}}(\mathbf{r}) \tag{2.15}$$

for the single-particle wave function of an electron in the translationally invariant bulk crystal. The wave function is a product of plain waves and Bloch functions with the same periodicity as the crystal. The index $\mathbf{k}$ denotes the crystal wave vector and $n$ is the band index, which distinguishes between different electronic states with the same wave vector $\mathbf{k}$ (see Fig. 2.3).

### 2.1.4. Electronic Bulk Band Structure

The band structures for GaAs, AlAs, and InAs, which are obtained from diagonalizing the tight-binding Hamiltonian in Eq. (3.23), are depicted in Fig. 2.3. Here, the position of the Fermi level corresponds to zero on the energy scale as marked by the dashed horizontal line. Consequently, the four bands below zero are fully occupied by valence electrons. Therefore, the occupied bands are referred to as valence bands (VBs), while the bands of higher energy are called conduction bands (CBs). The energy difference between the maximum of the VB and the minimum of the CB defines the band gap, which can be direct or indirect. The CB minimum and the VB maximum are each characterized by a wave vector **k** in the Brillouin zone. If the **k**-vectors are the same, the band gap is called direct. Accordingly, for different **k**-vectors, it is referred to as indirect. An electronic vacancy in VB, which results from excitation of an electron from a VB into a CB, is called a hole. In the case of a direct band gap, a photon can be directly emitted by the annihilation of an electron-hole pair, whereas in the case of an indirect gap, a photon cannot be directly emitted since the electron first needs to exchange momentum with the crystal lattice. This process is possible, but at a much slower rate, as it requires the electron to interact not only with the photon, but also with a lattice vibration, called a phonon, in order to either gain or lose momentum. The band structure of GaAs is displayed in Fig. 2.3(a). It can be

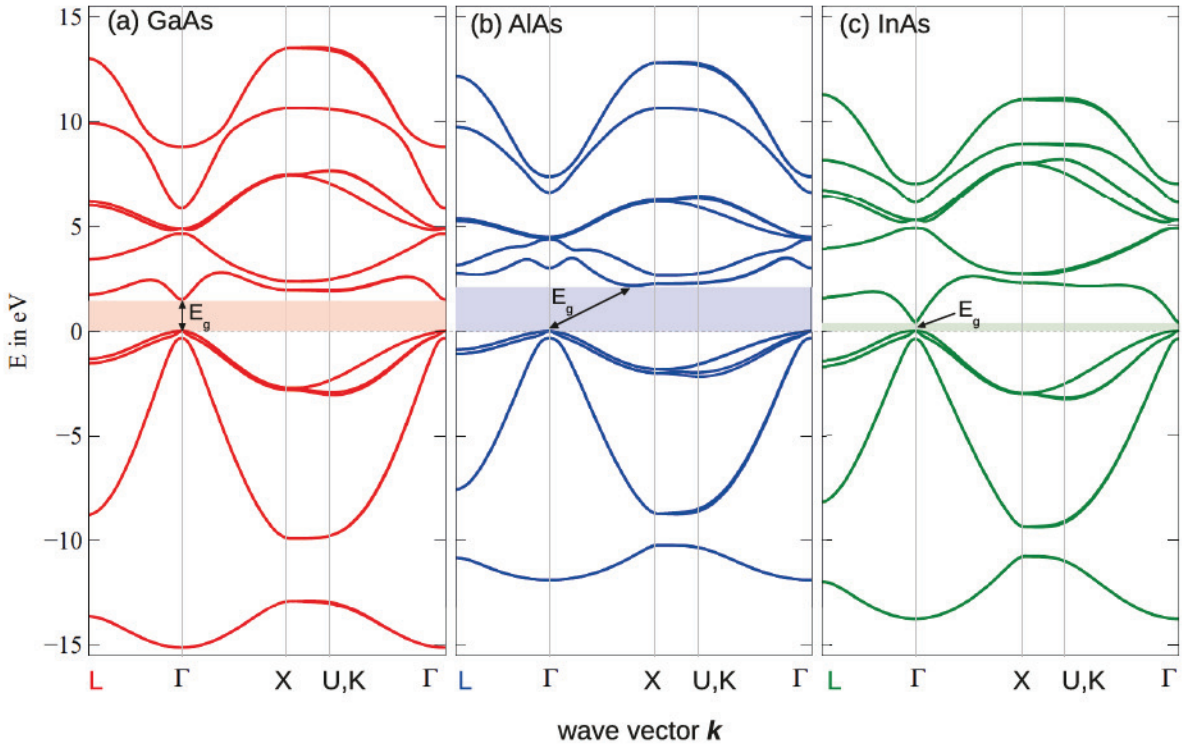


**Figure 2.3. | Electronic band structures**. The III-V semiconductors under investigation include (a) GaAs, (b) AlAs, and (c) InAs. The Fermi level is marked by the the dashed horizontal line and the band gaps by $E_g$. The corresponding energy interval is marked in color.

seen that both the CB minimum as well as the VB maximum are located at the $\mathbf{\Gamma}$-point, which gives rise to a direct band gap of energy difference $E_g$ at $\mathbf{\Gamma}$. As a consequence, the optical properties are substantially determined by the band structure around the $\mathbf{\Gamma}$-point. Since the CB/VB are almost parabolic around their min./max. at $\mathbf{\Gamma}$, it is reasonable to approximate them in that way. To this end, a Taylor expansion of the energy around $\mathbf{k} = 0$ up to the second order is performed, which gives

$$E(\mathbf{k}) \approx \frac{\hbar^2 \mathbf{k}^2}{2m^*}. \tag{2.16}$$

The term is reminiscent of the dispersion of free particles with the difference that here an effective mass $m^*$ occurs. It is determined by the second derivative of the energy with respect to the wave number

$$\frac{1}{m^*_{ij}} = \frac{1}{\hbar^2} \frac{\partial^2 E(\mathbf{k})}{\partial k_i \partial k_j} \tag{2.17}$$

and therefore describes the curvature of the bands. A schematic representation of the GaAs band structure around the $\mathbf{\Gamma}$-point, including the lowest CB and the three highest VBs is displayed in Fig. 2.4. The upper two VBs can be considered degenerate[2] at $\mathbf{k} = 0$.

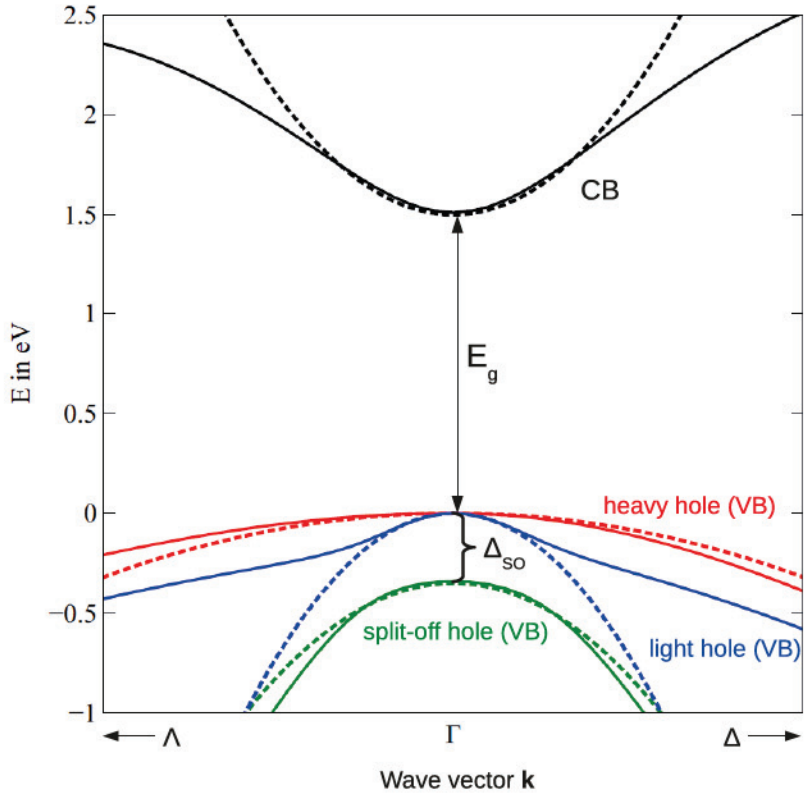


**Figure 2.4. | Parabolic approximation**. The band structure of GaAs with direct band gap $E_g$ in the vicinity of the $\mathbf{\Gamma}$-point, including the lowest CB (black) and three VBs: the heavy hole (red), light hole (blue) and split-off hole (green), which is energetically lowered by the amount of spin-orbit coupling $\Delta_{SO}$. The dashed lines illustrate the parabolic approximation of the bands.

The highest VB with the smallest curvature and thus largest effective mass (see Fig. 2.4) is called heavy hole. Analogously, the second highest VB with larger curvature and smaller effective mass is referred to as light-hole. The third valence band is energetically lowered by the amount of the spin-orbit coupling $\Delta_{SO}$ at the $\mathbf{\Gamma}$-point and therefore called split-off hole.

The band structure of AlAs with an indirect band gap of about 3.0 eV between the $\mathbf{\Gamma}$-point at the VB and a minimum near the $\mathbf{X}$-point at the CB is depicted in Fig. 2.3(b). Furthermore, there is a slightly larger direct band gap at the $\mathbf{\Gamma}$-point. This makes it particularly interesting to alloy this material with GaAs, which shows the opposite behavior and a relatively flat band around the $\mathbf{X}$-point.

The band structure of InAs with a direct band gap at the $\mathbf{\Gamma}$-point of 0.4 eV is displayed in Fig. 2.3(c). Due to the larger band gaps of GaAs of about 1.5 eV and AlAs of about 3.0 eV the small band gap of InAs is important for generating semiconductor alloys with a band gap in the energy range of the technologically important telecom C- and O-band at 0.8 eV and 1 eV, respectively.

## 2.2. Low-Dimensional Semiconductor Systems

So far, we have discussed bulk semiconductors. Their electronic properties can be characterized by band structures, as introduced in the previous section. In addition to bulk systems, it is possible to manufacture nanostructures with a lower spatial dimension. To illustrate their different electronic properties, we introduce the electronic density of states (DOS). It describes the number of different states at a particular energy level that electrons are allowed to occupy. A high DOS means that many states are available for occupation, whereas a DOS of zero means that no states can be occupied at that energy level. In the following, we use the isotropic quasi-free electronic DOS in the parabolic approximation (see Eq.(2.16)) to analyze systems of different spatial dimension (see Fig. 2.5). For a 3d-system, the electronic density of states for two spin configurations is given by

$$D^{3d}(E) = 2 \cdot \sum_k \delta\left(E - \frac{\hbar^2 k^2}{2m^*}\right), \tag{2.18}$$

which can be converted into the integral

$$D^{3d}(E) = 2 \cdot \frac{\Omega}{(2\pi)^3} \int \delta\left(E - \frac{\hbar^2 k^2}{2m^*}\right) d^3k, \tag{2.19}$$

[2]Around 1950, Dresselhaus [59] estimated that the degeneracy is lifted by a maximum of $10^{-4}$ eV by using perturbation theory and symmetry considerations. However, this number is negligible compared to the band gap $E_g$, which is on the order of magnitude of eV.

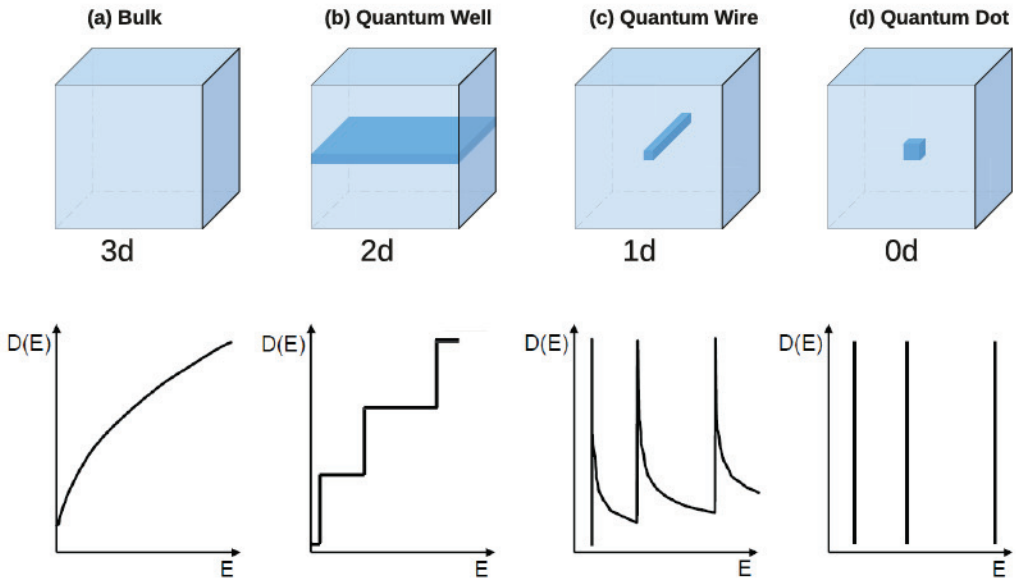


**Figure 2.5. | Electronic properties**. Systems of different spatial dimension and their corresponding quasi-free electronic density of states. (a) 3d: Square-root. (b) 2d: Stepwise. (c) 1d: Reciprocal of the square-root. (d) 0d: Discrete levels.

where $(2\pi)^d/\Omega$ is the normalization[3]. By introducing spherical coordinates, one obtains

$$D^{3d}(E) = 2 \cdot \frac{4\pi\Omega}{(2\pi)^3} \int_0^\infty \delta\left(E - \frac{\hbar^2 k^2}{2m^*}\right) k^2 dk \tag{2.20}$$

for the 3d density of states. Using the parabolic approximation in Eq. (2.16) with $k = \sqrt{2m^* E/\hbar}$ and $\frac{dE}{dk} = \frac{\hbar^2 k}{m^*}$, results in

$$D^{3d}(E) = 2 \cdot \frac{\Omega}{2\pi^2} \int_0^\infty dE' \, \frac{m^*}{\hbar^2} \sqrt{\frac{2m^* E'}{\hbar^2}} \delta(E - E') = \frac{\Omega (2m)^{*3/2}}{2\pi^2 \hbar^3} \sqrt{E}, \tag{2.21}$$

which shows the typical square-root behavior for the electronic density of states in a 3d-system (see Fig. 2.5 (a)).

In case of the 2d- and 1d-systems the motion of the charge carriers is spatially restricted to the $x$-$y$ and $x$-direction, respectively. Along these directions, continous energy states are available, whereas discrete states occur along the spatially restricted dimensions. Consequently, the total energy contains energies of both discrete and continous modes. When assuming an infinitely high confinement potential in the $y$-$z$ or $z$-direction, we

[3]It originates from the generalization of the 1d case, where the discretized momentum is given by $k_x = 2\pi n_x/L_x$. For the dimension $d = 3$, every $\mathbf{k}$-value occupies the volume $(\Delta k)^3 = (2\pi)^3/\Omega$.

obtain the following eigenenergies:

$$\begin{aligned} E^{2d}_{k_x,k_y,n_z} &= E_{n_z} + \frac{\hbar^2}{2m^*}\left(k_x^2 + k_y^2\right), \\ E^{1d}_{k_x,n_y,n_z} &= E_{n_y,n_z} + \frac{\hbar^2}{2m^*}k_x^2. \end{aligned} \tag{2.22}$$

Here,

$$\begin{aligned} E_{n_z} &= \frac{\hbar^2\pi^2}{2m^*}\frac{n_z^2}{L_z^2}, \quad \text{with } n_z \in \mathbb{N}^*, \\ E_{n_y,n_z} &= \frac{\hbar^2\pi^2}{2m^*}\left(\frac{n_y^2}{L_y^2} + \frac{n_z^2}{L_z^2}\right), \quad \text{with } n_y, n_z \in \mathbb{N}^* \end{aligned} \tag{2.23}$$

denote the energy modes $n_i$ of the particle in a box of length $L_i$ for $i \in \{x, y\}$. By utilizing the energy $E^{2d}_{k_x,k_y,n_z}$ in Eq. (2.22) and polar coordinates, we can determine the electronic density of states

$$\begin{aligned} D^{2d}(E) &= 2 \cdot \frac{2\pi\Omega}{(2\pi)^2}\int_0^\infty \sum_{n_z=1}^{\infty} \delta\left(E - E^{2d}_{k_x,k_y,n_z}\right) k\, dk \\ &= \frac{\Omega}{\pi}\int_0^\infty \sum_{n_z=1}^{\infty} \delta\left(E - E_{n_z} - \frac{\hbar^2 k^2}{2m^*}\right) k\, dk \\ &= \frac{\Omega}{\pi}\frac{m^*}{\hbar^2}\int_0^\infty dE' \sum_{n_z=1}^{\infty} \delta\left(E - E_{n_z} - E'\right) \\ &= -\frac{\Omega}{\pi}\frac{m^*}{\hbar^2} \sum_{n_z=1}^{\infty} \Theta\left(E - E_{n_z} - E'\right)\Big|_0^\infty \\ &= -\frac{\Omega}{\pi\hbar^2}m^* \sum_{n_z=1}^{\infty} \left[\Theta\left(E - E_{n_z} - \infty\right) - \Theta\left(E - E_{n_z}\right)\right] \\ &= \frac{\Omega}{\pi\hbar^2}m^* \sum_{n_z=1}^{\infty} \Theta\left(E - E_{n_z}\right). \end{aligned} \tag{2.24}$$

Note that $\Theta(E - \infty) = 0$, as the energy of the physical system does not reach infinity. According to Eq. (2.24), we obtain a constant density of states for each single discrete energy mode for the 2d-system. The sum of three step functions is used to generate the

graph in Fig. 2.5 (b). Analogous to the 2D-case, we can use $E^{1d}_{k_x,n_y,n_z}$ to calculate

$$\begin{aligned} D^{1d}(E) &= 2 \cdot \frac{\Omega}{2\pi} \int_0^\infty \sum_{\{n_y,n_z\}=1}^{\infty} \delta\left(E - E_{n_y,n_z} - \frac{\hbar^2 k^2}{2m^*}\right) dk \\ &= \frac{\Omega}{\pi} \int_0^\infty dE' \frac{m^*}{\hbar^2 k} \sum_{\{n_y,n_z\}=1}^{\infty} \delta\left(E - E_{n_y,n_z} - E'\right) \\ &= \frac{\Omega}{\pi\hbar} \int_0^\infty dE' \frac{2m^*}{\sqrt{2m^*(E - E_{n_y,n_z} - E')}} \sum_{\{n_y,n_z\}=1}^{\infty} \delta\left(E - E_{n_y,n_z} - E'\right) \\ &= \frac{\Omega}{\pi\hbar} \sum_{n_y,n_z} \sqrt{\frac{2m^*}{E - E_{n_y,n_z}}}\, \Theta(E - E_{n_y,n_z}). \end{aligned} \tag{2.25}$$

Note that the substitution of $k$ introduces $2\hbar^{-1}\sqrt{2m^* E'}$. As in the case of the 2d-system, jumps occur in the electronic density of states due to the discrete modes. Between these jumps, the DOS follows a reciprocal square root behavior, as depicted in Fig. 2.5 (c). For a 0d-system, the motion of the charge carriers is restricted in all three spatial directions by a confinement potential and consequently a discrete spectrum

$$D^{0d}(E) = 2 \sum_n \delta(E - E_n) \tag{2.26}$$

with a $\delta$-like electronic density of states is obtained (see Fig. 2.5 (d)). Such a spectrum is characteristic for quantum dots. The number of bound states and their electronic levels is determined by the shape of the confinement potential. Therefore, quantum dots are regarded as an interesting optoelectronic system since they in principle offer the possibility to engineer such a $\delta$-like density of states as desired for various applications. Details on quantum dots are given in the next section.

## 2.3. Semiconductor Quantum Dots

Within this work, we are interested in semiconductor nanostructures, especially quantum dots. They can be generated by embedding a material with a lower band gap in a host material with a larger band gap. The corresponding structure and electronic properties as well as a short description of experimental production techniques are given in the following.

### 2.3.1. Structure and Electronic Properties

An outline of spatial representations of semiconductor quantum dots is displayed in Fig. 2.6(a-b). A material with a smaller band gap (dark blue) is deposited on top of a barrier material with a larger band gap (light blue). During the growth process, a wetting-layer (WL) and quantum dots (QDs) are formed [60]. The energy level scheme for a QD structure is depicted in Fig. 2.6(c). The energies of the 2D WL are confined with

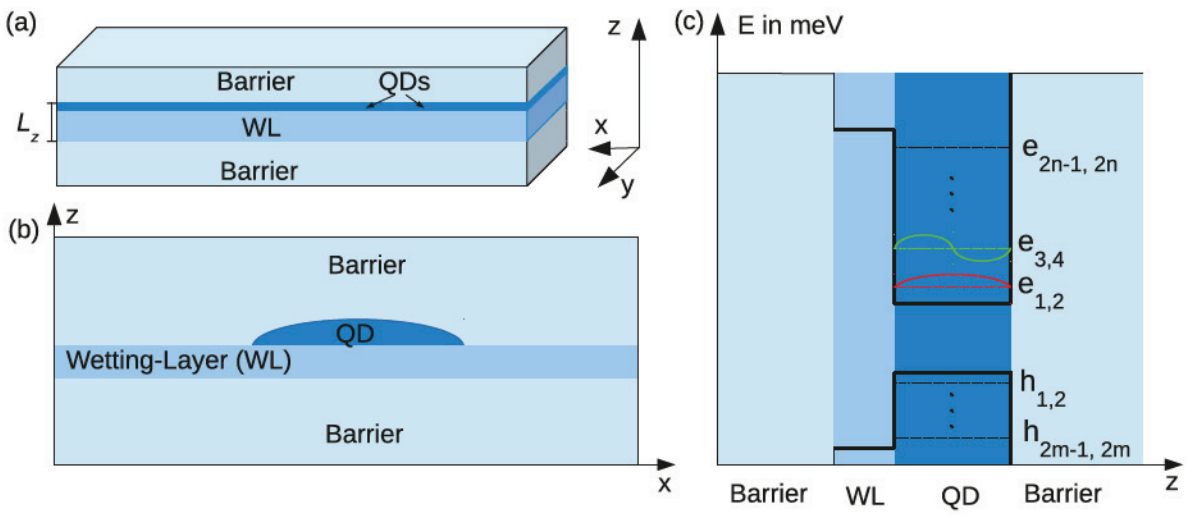


**Figure 2.6. | Structural and energetic outline of quantum dots**. (a) Spatial representation of quantum dots (QDs, dark blue) and a wetting-layer (WL, lighter blue) of thickness $L_z$ that are embedded in a barrier material (light blue). (b) Cross-section of the structure for a single QD. (c) Energy level scheme for a QD structure corresponding to (b) along the growth direction $z$.

respect to the energy of the 3D barrier material. An additional confinement is obtained for $2(n+m)$ QD states[4]. These states are classified as electrons (e) and holes (h), depending on whether they originate from the VB or CB. In a simplified picture, $e_{1,2}$ (red) and $e_{3,4}$ (green) can be considered as particle-in-a-box-like wave functions (infinite potential well) with an increasing number of maxima.

### 2.3.2. Growth Techniques

Since the lateral dimensions of self-assembled semiconductor quantum dots are within the range of a few nanometers, the manufacturing process is relatively demanding. One way to grow self-organized quantum dots is by using molecular beam epitaxy (MBE), which is described below following Ref. [61].

MBE is an established standard process for the production of thin semiconductor layers on a substrate. It offers the possibility of a relatively precise control of the growth process,

[4]Due to the two possible spin configurations, each state is two times Kramer's degenerate.

so that the numbers of defects may be minimized. For more details, see Ref. [61]. In epitaxial layer growth, the arrangement of the deposited atoms is mainly determined by the crystal structure of the substrate material [61, 62]. The way in which atoms are deposited on a substrate is determined by several factors. When the same materials are grown on one another, the temperature is decisive since it determines the mobility of the adsorbed atoms on the surface. Under optimal thermal conditions, complete sets of monolayers can be grown [63]. However, when growing different materials on one another such a quality can only be achieved in specific situations, e.g. similar crystal structures and lattice constants. Consequently, for most materials a lattice-matched growth is not possible and the arising tension can lead to dislocations, cracks and defects. When several InAs layers are deposited on GaAs under suitable conditions, the tension in the material can be reduced in a way that leads to the formation of self-organized quantum dots [64], as schematically depicted in Fig. 2.7. In this case the first monolayer of InAs, called

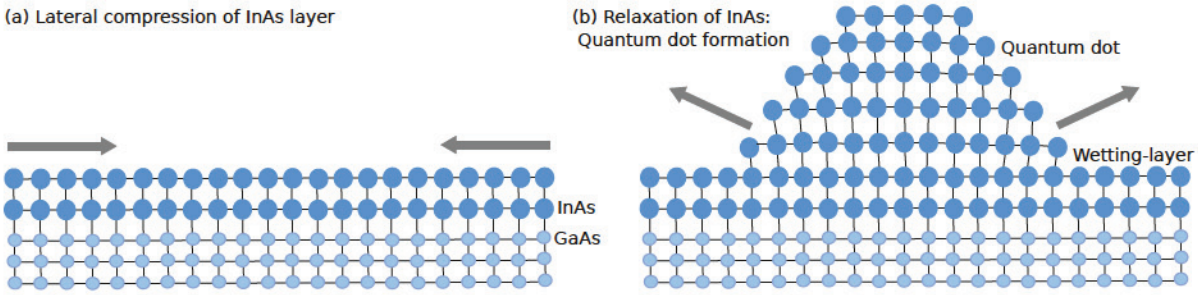


**Figure 2.7. | Lattice distortions.** Schematic representation of Stranski-Krastanov growth of quantum dots. (a) Lattice mismatch leads to lateral compression. (b) The strain is reduced by the self-organized formation of a quantum dot on top of a wetting-layer.

wetting-layer, grows on GaAs without any displacements despite the strongly different lattice constants of the two materials. The InAs-based wetting-layer is strongly compressed in the lateral direction due to its approximately 7 % larger lattice constant compared to the GaAs substrate. The lateral compression is compensated for by a relaxation along the growth-direction. Above a critical layer thickness of about two GaAs lattice-matched monolayers of InAs, the material system can no longer compensate for the compression, and begins to form three-dimensional islands. Due to such energy minimization, the resulting quantum dots are called self-organized. The entire process is referred to as Stranski-Krastanov growth [64].

## 2.4. Optical Properties

In this section, excitons in semiconductor bulk materials and excitonic configurations in semiconductor quantum dots are discussed. We start with excitons in bulk crystals before we describe various excitonic configurations in quantum dots, which form the basis for the analysis of corresponding optical spectra.

### 2.4.1. Excitons in Bulk Crystals

As discussed at the electronic band structure, the excitation of an electron from the VB into the CB can be described by an electron-hole pair. Holes ($h$) are quasi-particles of opposite charge and spin with respect to electrons ($e$). A single electron-hole pair, which is coupled by Coulomb interaction, is called an exciton ($X$). Its energy is described by

$$H_X = H_e + H_h + H_{\text{Coul}}. \tag{2.27}$$

One distinguishes between strongly and weakly bound excitons. The former are characterized by the fact that their interaction is essentially based on the overlap of charge clouds, which are localized at different lattice sites. Consequently, these excitons tend to occur in ionic materials and compounds with high binding energy. Such strongly bound excitons are referred to as Frenkel excitons [51] and are not important in the III-V semiconductor materials studied in this work.

On the other hand, in most semiconductors Wannier excitons with weaker binding energy and greater spatial separation are present [51]. In bulk crystals, they can be described analogous to the hydrogen atom by using a center of mass and relative coordinate. The attractive electron-hole interaction leads to a reduction of the total energy. In a parabolic approximation with effective mass (see Eq. (2.16)), one obtains [51]

$$E_X = E_g - R_y \frac{\mu_{eh}^*}{\mu_H} \frac{1}{\varepsilon_r^2 n^2} + \frac{\hbar^2 k^2}{2M} \tag{2.28}$$

for the exciton energy $E_X$. Here, $E_g$ is the band gap, $R_y = 13.6\,\text{eV}$ the Rydberg constant, $n$ the principal quantum number, $k$ the wave number, $\varepsilon_r$ the static dielectric constant of the material, $\hbar = h/(2\pi)$ the reduced Planck constant and $M = m_e^* + m_h^*$ the excitonic mass. Additionally, $1/\mu_{eh}^* = 1/m_e^* + 1/m_h^*$ and $1/\mu_H = 1/m_e + 1/m_p$ denote the reduced effective masses of the electron-hole pair and the reduced mass of the hydrogen atom, respectively.

The energy difference between excitons in bulk materials is proportional to $1/n^2$, similar

to the Rydberg series [65] of the hydrogen atom. In both cases, the attractive electron-hole interaction reduces the total energy compared to the respective unbound states. On the other hand, the binding energy of the Wannier exciton is usually smaller and spatially more separated than the electron-hole pair in the hydrogen atom. This is caused by the influence of the surrounding material, which screens the Coulomb interaction between electron and hole. The screening is considered in the description of the Wannier exciton by an effective dielectric constant. To illustrate the analogy of these excitons to the hydrogen atom, an exciton Bohr-radius

$$a_B^X = a_B^H \frac{\varepsilon_r \mu_H}{\mu_{eh}^*} \tag{2.29}$$

is introduced for the spatial extension.

### 2.4.2. Excitonic Configurations in Quantum Dots

In order to obtain light emission from a QD, the respective localized states inside the QD must be occupied by at least one electron and hole. Different configurations can be formed by occupying the various single-particle states with charge carriers (see Fig. 2.8). The Coulomb interaction between the charge carriers that changes the configuration energies and thus the transition energies with respect to the single-particle states, will be detailed later in the theoretical section. For a qualitative discussion, a quantum dot with two spin-degenerate states for electrons and holes is displayed in Fig. 2.8. The ground state corresponds to the situation, in which no charge carriers are present inside the QD, and

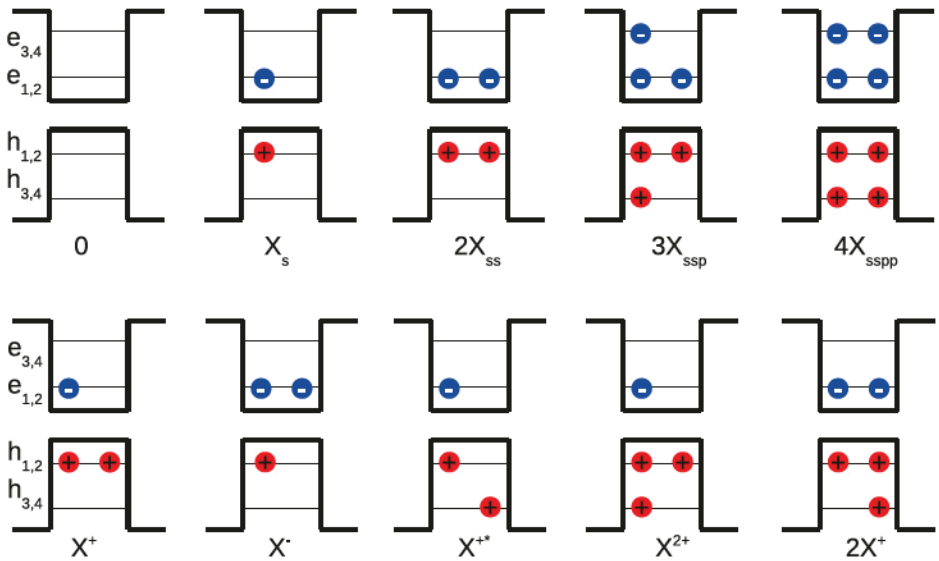


**Figure 2.8. | Quantum dot configurations**. Ten examples for a system with one s- and p-shell for electrons and holes. Neutral configurations (top) consist of an equal number of electrons and holes, whereas charged complexes (bottom) are composed of an unequal number. Charged states are denoted by the corresponding charge in the exponent and excited states are marked with $*$.

is denoted by 0. On the other hand, the configuration $X_s$, corresponds to the situation, in which one electron-hole pair with the lowest possible energy is formed. The index originates from the analogy to the hydrogen atom, where the eigenstates are classified with respect to the angular momentum. A commonly used shorthand notation for $1X_s$ is $X$. Analogously, configurations with a higher number of electron-hole pairs are possible (see Fig. 2.8 top). An example is the biexciton $2X_{ss}$, which consists of two electron-hole pairs. Corresponding abbreviations include $XX$ and $2X$.

Apart from excitons, which are composed of electron-hole pairs, charged complexes can occur. They consist of an unequal number of electrons and holes (see Fig. 2.8 bottom). An example are the charged excitons $X^+$ and $X^-$ that are composed of an electron-hole pair and an additional charge carrier. Since they consist of three particles, they are also referred to as trions. By recombination of an electron-hole pair and the emission of a photon, the configurations inside the quantum dot can decay into complexes with fewer charge carriers. We will come back to such decay cascades when discussing the individual lines in a quantum dot emission spectrum.

# 3. Electronic Properties of III-V Semiconductors

The aim of this chapter is to give an overview of different methods for modeling the electronic properties of III-V semiconductors. Further reading on this topic can be found in the textbooks [50, 51, 52, 53]. In section 3.1, we start with a short outline of the theoretical background, including Bloch's theorem. Subsequently, in sections 3.2 and 3.3 we briefly describe the pseudopotential and $\mathbf{k} \cdot \mathbf{p}$ methods before we go over the tight-binding (TB) model and its implementation in section 3.4 in more detail. Thereby, we follow the notations used in the dissertations [54, 55, 56].

In order to determine the electronic properties of III-V semiconductors one needs to solve the time-independent stationary non-relativistic Schrödinger equation [66] for the many-electron wave function $\Psi_{el}$ given by [67]

$$\begin{aligned} H\Psi_{el} &= \left[\sum_j T_j + \sum_{j,l} V_{K-el}(\mathbf{r}_j, \mathbf{R}_l) + \frac{1}{2}\sum_{j\neq j'} V_{el-el}(\mathbf{r}_j, \mathbf{r}'_j)\right]\Psi_{el} \\ &= \left[-\frac{\hbar^2}{2m_e}\sum_j \nabla_j^2 - \sum_{j,l}\frac{Z_l e^2}{|\mathbf{r}_j - \mathbf{R}_l|} + \frac{1}{2}\sum_{j\neq j'}\frac{e^2}{|\mathbf{r}_j - \mathbf{r}'_j|}\right]\Psi_{el} \\ &= E\Psi_{el}, \end{aligned} \tag{3.1}$$

where $\mathbf{r}_j$ are the positions of the electrons and $\mathbf{R}_l$, $Z_l$ the positions and atomic numbers of the nuclei. This equation includes the Born-Oppenheimer [68] approximation, in which the significantly heavier nuclei are considered as fixed in space with respect to the electron dynamics. Solving Eq. (3.1) is a challenging task in general. To this end, different numerical methods exist in the literature. Density functional theory (DFT) [67] is an approach, where the number of approximations is reduced to a minimum, as it aims at solving the many-electron Schrödinger equation without restricting the consideration to a single representative electron. Within this method, the calculation of electronic properties of bulk materials is numerically feasible, whereas the calculation of electronic properties of nanostructures with a broken translational-symmetry and extensions of a few nanometers is practically impossible. Since we are interested in the properties of nanostructures, an

alternative method needs to be employed. In what follows, different approaches are shortly summarized. The common property of these methods is that the many-body problem in Eq. (3.1) is simplified by considering the single-particle Schrödinger equation

$$H\psi(\mathbf{r}) = \left[-\frac{\hbar^2}{2m_e}\Delta + V(\mathbf{r})\right]\psi(\mathbf{r}) = E\psi(\mathbf{r}) \tag{3.2}$$

for a representative electron (one-electron approximation) in an effective lattice-periodic potential $V(\mathbf{r})$. Since we choose to employ the TB model throughout this work, this method will be described in more detail.

## 3.1. $k \cdot p$ Model

The idea behind the $\mathbf{k}\cdot\mathbf{p}$ method is a perturbative treatment of the band structure in the vicinity of a wave vector $\mathbf{k}_0$ [69]. By inserting Bloch wave functions $\psi_{n\mathbf{k}}(\mathbf{r}) = e^{i\mathbf{k}\cdot\mathbf{r}}u_{n\mathbf{k}}(\mathbf{r})$ from Eq. (2.15) into the single-particle Schrödiger equation (see Eq. (3.2)), one obtains the so-called $\mathbf{k}\cdot\mathbf{p}$-equation

$$H^{\mathbf{k}\cdot\mathbf{p}}u_{n\mathbf{k}}(\mathbf{r}) = \left[\frac{p^2}{2m} + \frac{\hbar}{m}\mathbf{k}\cdot\mathbf{p} + \frac{\hbar^2k^2}{2m} + U(\mathbf{r})\right]u_{n\mathbf{k}}(\mathbf{r}) = E_n(\mathbf{k})u_{n\mathbf{k}}(\mathbf{r}). \tag{3.3}$$

For every $\mathbf{k} = \mathbf{k}_0$, the $\{u_{n\mathbf{k}_0}(\mathbf{r})\}$ form a set of orthonormal eigenfunctions of the Hilbert space. Consequently, we can formulate Eq. (3.3) as

$$H^{\mathbf{k}\cdot\mathbf{p}}u_{n\mathbf{k}}(\mathbf{r}) = \left[H^{\mathbf{k}_0\cdot\mathbf{p}} + \frac{\hbar}{m}(\mathbf{k}-\mathbf{k}_0)\cdot\mathbf{p} + \frac{\hbar^2}{2m}(k^2-k_0^2)\right]u_{n\mathbf{k}}(\mathbf{r}) = E_n(\mathbf{k})u_{n\mathbf{k}}(\mathbf{r}) \tag{3.4}$$

by introducing the Hamiltonian

$$H^{\mathbf{k}_0\cdot\mathbf{p}} = \left[\frac{p^2}{2m} + \frac{\hbar}{m}\mathbf{k}_0\cdot\mathbf{p} + \frac{\hbar^2k_0^2}{2m} + U(\mathbf{r})\right] \tag{3.5}$$

for $\mathbf{k} = \mathbf{k}_0$. The eigenvalues $E_n(\mathbf{k})$ and eigenfunctions $u_{n\mathbf{k}}$ of Eq. (3.4) are obtained as an expansion in terms of the energies $E_{n\mathbf{0}}$ and basis functions $u_{n\mathbf{k}_0}(\mathbf{r})$ by solving the corresponding eigenvalue problem in the basis of a finite set of $\{u_{n\mathbf{k}_0}(\mathbf{r})\}$. The respective matrix elements are given by

$$\langle u_{n\mathbf{k}_0}|H^{\mathbf{k}\cdot\mathbf{p}}|u_{n'\mathbf{k}_0}\rangle = \left[E_n(\mathbf{k}_0) + \frac{\hbar^2}{2m}(k^2-k_0^2)\right]\delta_{nn'} + \frac{\hbar}{m}(\mathbf{k}-\mathbf{k}_0)\cdot\mathbf{p}_{nn'}, \tag{3.6}$$

where the off-diagonal terms

$$\mathbf{p}_{nn'} = \langle u_{n\mathbf{k}_0}|\mathbf{p}|u_{n'\mathbf{k}_0}\rangle \tag{3.7}$$

define the coupling strength between the electronic bands $n$ and $n'$. For $\mathbf{k} = \mathbf{k}_0$, the perturbation $\frac{\hbar}{m}(\mathbf{k} - \mathbf{k}_0) \cdot \mathbf{p}_{nn'}$ vanishes and the matrix $H^{\mathbf{k}\cdot\mathbf{p}}$ is diagonal, since the $u_{n\mathbf{k}_0}(\mathbf{r})$ are eigenstates of $H^{\mathbf{k}_0\cdot\mathbf{p}}$. In this case, $H^{\mathbf{k}\cdot\mathbf{p}}$ equals the exact Hamiltonian at $\mathbf{k} = \mathbf{k}_0$. Consequently, $\mathbf{k} \cdot \mathbf{p}$ perturbation theory is most accurate for small values of $\mathbf{k} - \mathbf{k}_0$. However, the model can also provide accurate results for arbitrary wave vectors within the Brillouin zone and has therefore been successfully applied, as shown for instance in Refs. [70, 71].

## 3.2. Pseudopotential Model

The idea behind the pseudopotential method [72] is to combine the many-body Schrödinger equation with the one-electron approximation. Following this approach, the nucleus-electron potential $V_{K-el}$ and the electron-electron potential $V_{el-el}$ in Eq. (3.1) are merged into an effective all-electron potential. Numerical solutions render difficult as the electronic wave functions exhibit short wavelength oscillations close to the cores. To get around this problem, within the pseudopotential method, the electronic wave functions are divided into two parts following Ref. [73]:

$$\psi = \psi_{pp} + \sum_c a_c \psi_c. \tag{3.8}$$

The first summand contains the smooth part, the so-called pseudo wave function $\psi_{pp}$, whereas the oscillations close to the core are included in the sum over occupied core states $\psi_c$. A central assumption of the pseudopotential method is that a pseudopotential $V_{pp}$ can be constructed in a way that the wave function $\psi$ is orthogonal to the core states $\psi_c$. Correspondingly, the overlap $\langle\psi_c|\psi\rangle = 0$ vanishes, whereby the valence electrons are kept out of the core. In the following the pseudopotential is derived, containing these physics. According to Ref. [73], the wave function in Eq. (3.8) can be written as

$$\psi = \psi_{pp} - \sum_c \langle\psi_c|\psi_{pp}\rangle \, \psi_c. \tag{3.9}$$

Operating on the wave function $\psi$ with the Hamiltonian $H$ yields

$$H\psi_{pp} + \sum_c (E - E_c)\psi_c \, \langle\psi_c|\psi_{pp}\rangle = E\psi_{pp}, \tag{3.10}$$

which can be rewritten as

$$H_{pp}\psi_{pp} = E\psi_{pp} \tag{3.11}$$

by introducing the pseudopotential Hamiltonian

$$H_{pp} = -\frac{\hbar^2}{2m_e}\Delta + \sum_i V_{pp}^i(\mathbf{r} - \mathbf{R}_i), \tag{3.12}$$

which includes the pseudopotentials $V_{pp}(\mathbf{r} - \mathbf{R}_i)$ at the lattice sites $\mathbf{R}_i$. At large distances, the pseudopotentials act like Coulomb potentials of ions with effective charges at the positions $\mathbf{R}_i$. For practical calculations, the atomistic pseudopotentials $V_{pp}(\mathbf{r} - \mathbf{R}_i)$ are determined by fitting the desired band structure to experimentally known properties or DFT calculations, as discussed for instance in Ref. [73]. In order to solve the eigenvalue problem in Eq. (3.11), the pseudopotential wave functions

$$\psi_{pp} = \sum_{\mathbf{k}} c_{\mathbf{k}} e^{i\mathbf{kr}} \tag{3.13}$$

are typically expanded in the basis of plain waves, which are the eigenstates of the the single-particle Schrödinger equation for a vanishing potential $V(\mathbf{r}) = 0$. Since the Hamiltonian $H_{pp}$ consists of atomistic pseudopotentials $V_{pp}^i(\mathbf{r} - \mathbf{R}_i)$, it contains not only the potential at individual atomic sites, but also microscopic information in between. As a result, pseudopotential calculations are computationally demanding. Nevertheless, this method has been successfully applied, as shown for instance in Refs. [74, 75, 76].

## 3.3. Tight-Binding Model

In the TB model, the crystal is described as an arrangement of weakly interacting, neutral atoms [50]. The name of the method originates from the assumption that the electrons are tightly bound to their respective nuclei. Despite this strong localization, there is an overlap of the electronic wave functions, so that this model provides corrections to the case of isolated atoms. In the TB model, these corrections lead to the bonding between individual atoms and the subsequent formation of electronic bands. The two basic assumptions of the TB model are that the bulk band structure is well approximated by a small number of orbital basis states per atom and that the overlap of these orbitals decreases rapidly with an increasing distance of the atoms [50]. These basis states $|\mathbf{R}, \alpha, \nu, \sigma\rangle$ are characterized by their position $\mathbf{R}$, the atom type $\alpha$ at which they are localized, their orbital type $\nu$ and their spin $\sigma$ with the notation following former works [54, 55, 56].

The TB method provides particularly good results for the calculation of electronic structures of semiconductors as well as transition metals with partially occupied $d$-shells [50]. Additionally, the TB method holds two major advantages compared to the $\mathbf{k} \cdot \mathbf{p}$ and the pseudopotential method. In contrast to the $\mathbf{k} \cdot \mathbf{p}$ model, it includes the

underlying crystal symmetry and thus provides access to quantities, such as the fine-structure splitting. Compared to the pseudopotential approach, in the TB method the electronic wave functions are not explicitly taken into account, but only individual matrix elements between them. This leads to a significantly lower computational effort. Moreover, unlike the artificial pseudopotentials the matrix elements in the TB approach have a simple physical interpretation as they represent couplings between electrons localized at neighboring atoms. In the light of these aspects, we employ the TB model throughout this work.

As mentioned above, the TB model provides corrections to the picture of isolated atoms. Consequently, for its description, we start from the Schrödinger equation for an isolated atom $\alpha$ at the position $\mathbf{R}_l$. Following the notation of [54, 56], we obtain

$$H^{at} \left|\mathbf{R}_l, \alpha, \nu, \sigma\right\rangle = \frac{\mathbf{p}^2}{2m} + V^0(\mathbf{R_l}, \alpha) = E^{at} \left|\mathbf{R}_l, \alpha, \nu, \sigma\right\rangle . \tag{3.14}$$

Here, $V^0(\mathbf{R_l}, \alpha)$ denotes the atomic potential of the atom at the position $\mathbf{R}_l$. The situation of a single atom in Eq. (3.14) is modified by the presence of all other atoms in the crystal. Considering these additional potentials, the respective Hamiltonian is given by

$$H^{bulk} = H^{at}(\mathbf{R}_l, \alpha) + \sum_{\substack{n \neq l \\ \alpha'}} V^{crystal}(\mathbf{R}_n, \alpha'), \tag{3.15}$$

where an additional potential at the positions $\mathbf{R}_n$, occupied by atoms of type $\alpha'$; has been added. For practical calculations of bulk band structures, one takes advantage of the periodicity and formulates Eq. (3.15) in $\mathbf{k}$-space

$$H^{bulk} \left|\mathbf{k}\right\rangle = E(\mathbf{k}) \left|\mathbf{k}\right\rangle , \tag{3.16}$$

where $\mathbf{k}$ denotes the crystal wave vector and $|\mathbf{k}\rangle$ the corresponding wave function. To solve Eq. (3.16), the electronic wave functions $|\mathbf{k}\rangle$ are expanded in terms of linear combinations of atomic orbitals (LCAO). Due to the translational symmetry of the crystal, Bloch functions

$$\left|\mathbf{k}\right\rangle = \sqrt{\frac{V_0}{V}} \sum_{n,\alpha,\nu,\sigma} e^{i\mathbf{k}\cdot\mathbf{R}_n} u_{\alpha,\nu,\sigma}(\mathbf{k}) \left|\mathbf{R}_n, \alpha, \nu, \sigma\right\rangle \tag{3.17}$$

are used, where $u_{\alpha,\nu,\sigma}(\mathbf{k})$ are the Bloch factors and $V_0/V$ is the ratio of the volume of one unit cell to the whole crystal. As introduced above and following the notation in [54, 56], $\alpha$ denotes the atom type, $\nu$ the atomic orbital and $\sigma$ the spin. Due to the periodicity of the crystal, it is sufficient to restrict $\mathbf{k}$ to the first Brillouin zone, as explained in chapter 2. Inserting the Hamiltonian of Eq. (3.15) and the wave function $|\mathbf{k}\rangle$ of Eq. (3.17) into

Eq. (3.16) yields

$$\begin{aligned} H^{bulk}\left|\mathbf{k}\right\rangle &= H^{bulk}\sqrt{\frac{V_0}{V}}\sum_{n,\alpha,\nu,\sigma} e^{i\mathbf{k}\cdot\mathbf{R}_n} u_{\alpha,\nu,\sigma}(\mathbf{k})\left|\mathbf{R}_n,\alpha,\nu,\sigma\right\rangle \\ &= E(\mathbf{k})\sqrt{\frac{V_0}{V}}\sum_{n,\alpha,\nu,\sigma} e^{i\mathbf{k}\cdot\mathbf{R}_n} u_{\alpha,\nu,\sigma}(\mathbf{k})\left|\mathbf{R}_n,\alpha,\nu,\sigma\right\rangle \\ &= E(\mathbf{k})\left|\mathbf{k}\right\rangle . \end{aligned} \tag{3.18}$$

By applying a given

$$\left\langle\mathbf{k},\alpha',\nu',\sigma'\right| = \sqrt{\frac{V_0}{V}}\sum_m e^{-i\mathbf{k}\cdot\mathbf{R}_m} u^{\star}_{\alpha',\nu',\sigma'}(\mathbf{k})\left\langle\mathbf{R}_m,\alpha',\nu',\sigma'\right| \tag{3.19}$$

to Eq. (3.18), one obtains a generalized eigenvalue problem for each $\mathbf{k}$-value, which reads

$$\begin{aligned} &\sum_{\alpha,\nu,\sigma}\frac{V_0}{V}\sum_{n,m} e^{i\mathbf{k}\cdot(\mathbf{R}_n-\mathbf{R}_m)}\left\langle\mathbf{R}_m,\alpha',\nu',\sigma'\right|H^{bulk}\left|\mathbf{R}_n,\alpha,\nu,\sigma\right\rangle u_{\alpha,\nu,\sigma}(\mathbf{k})u^{\star}_{\alpha',\nu',\sigma'}(\mathbf{k}) \\ =&\sum_{\alpha,\nu,\sigma}\frac{V_0}{V}\sum_{n,m} e^{i\mathbf{k}\cdot(\mathbf{R}_n-\mathbf{R}_m)}\left\langle\mathbf{R}_m,\alpha',\nu',\sigma'\right|\left.\mathbf{R}_n,\alpha,\nu,\sigma\right\rangle E(\mathbf{k})u_{\alpha,\nu,\sigma}(\mathbf{k})u^{\star}_{\alpha',\nu',\sigma'}(\mathbf{k}) \end{aligned} \tag{3.20}$$

and can be reduced to

$$\begin{aligned} &\sum_{\alpha,\nu,\sigma}\underbrace{\frac{V_0}{V}\sum_{n,m} e^{i\mathbf{k}\cdot(\mathbf{R}_n-\mathbf{R}_m)}\left\langle\mathbf{R}_m,\alpha',\nu',\sigma'\right|H^{bulk}\left|\mathbf{R}_n,\alpha,\nu,\sigma\right\rangle}_{H^{bulk}_{\alpha',\nu',\sigma';\alpha,\nu,\sigma}(\mathbf{k})} u_{\alpha,\nu,\sigma}(\mathbf{k}) \\ =&\sum_{\alpha,\nu,\sigma}\underbrace{\frac{V_0}{V}\sum_{n,m} e^{i\mathbf{k}\cdot(\mathbf{R}_n-\mathbf{R}_m)}\left\langle\mathbf{R}_m,\alpha',\nu',\sigma'\right|\left.\mathbf{R}_n,\alpha,\nu,\sigma\right\rangle}_{S_{\alpha',\nu',\sigma';\alpha,\nu,\sigma}(\mathbf{k})} E(\mathbf{k})u_{\alpha,\nu,\sigma}(\mathbf{k}), \end{aligned} \tag{3.21}$$

by cancelling out $u^{\star}_{\alpha',\nu',\sigma'}(\mathbf{k})$. In Eq. (3.21), $H^{bulk}_{\alpha'\nu'\sigma';\alpha\nu\sigma}(\mathbf{k})$ and $S_{\alpha',\nu',\sigma';\alpha,\nu,\sigma}(\mathbf{k})$ denote the Hamilton matrix elements and the overlap-matrix elements, respectively. Following the Löwdin-transformation [77], an orthogonal TB basis can be generated. In this case, the overlap-matrix elements are given by

$$S_{\alpha',\nu',\sigma';\alpha,\nu,\sigma}(\mathbf{R}_n,\mathbf{R}_m) = \left\langle\mathbf{R}_m,\alpha',\nu',\sigma'\right|\left.\mathbf{R}_n,\alpha,\nu,\sigma\right\rangle = \delta_{\mathbf{R}_n,\mathbf{R}_m}\delta_{\alpha,\alpha'}\delta_{\nu,\nu'}\delta_{\sigma,\sigma'} \tag{3.22}$$

and Eq. (3.21) reduces to a standard eigenvalue problem

$$\sum_{\alpha,\nu,\sigma} H^{bulk}_{\alpha',\nu',\sigma';\alpha,\nu,\sigma}(\mathbf{k})u_{\alpha,\nu,\sigma}(\mathbf{k}) = E(\mathbf{k})u_{\alpha',\nu',\sigma'}(\mathbf{k}). \tag{3.23}$$

The eigenvalues, obtained from diagonalizing Eq. (3.23) with the matrix elements

$$H^{bulk}_{\alpha\nu\sigma;\alpha'\nu'\sigma'}(\mathbf{k}) = \frac{V_0}{V}\sum_{n,m} e^{i\mathbf{k}\cdot(\mathbf{R}_n-\mathbf{R}_m)} \langle \mathbf{R}_m, \alpha', \nu', \sigma' | H^{bulk} | \mathbf{R}_n, \alpha, \nu, \sigma \rangle \,, \tag{3.24}$$

provide access to the TB band structure for each reciprocal vector $\mathbf{k}$. In the case of equal atomic positions $\mathbf{R}_m$ and $\mathbf{R}_n$ in Eq. (3.24), the TB matrix elements

$$H^{on-site}_{\alpha\nu\sigma;\alpha'\nu'\sigma'}(\mathbf{R}) = \langle \mathbf{R}_m, \alpha', \nu', \sigma' | H^{bulk} | \mathbf{R}_n, \alpha, \nu, \sigma \rangle \, \delta_{\mathbf{R}_n,\mathbf{R}_m} \delta_{\alpha,\alpha'} \delta_{\nu,\nu'} \delta_{\sigma,\sigma'} = E_{\alpha,\nu,\sigma} \tag{3.25}$$

correspond to the expectation value of two identical atomic orbitals $\nu$ being located at the same atom type $\alpha$. These matrix elements are referred to as on-site terms and represent the orbital energies $E_{\alpha,\nu,\sigma}$. In the case of unequal positions $\mathbf{R}_m$ and $\mathbf{R}_n$, the TB matrix elements

$$H^{hopping}_{\alpha\nu\sigma;\alpha'\nu'\sigma'}(\mathbf{R}) = \langle \mathbf{R}_m, \alpha', \nu', \sigma' | H^{bulk} | \mathbf{R}_n, \alpha, \nu, \sigma \rangle \, \delta_{\sigma,\sigma'} = V(\mathbf{R}_m - \mathbf{R}_n)_{\alpha\alpha',\nu\nu'} \tag{3.26}$$

describe the coupling between orbitals $\nu$ and $\nu'$ at different atomic sites of atom types $\alpha$ and $\alpha'$. They are called hopping matrix elements, as they represent the probability amplitude of an electron hopping from one atomic site to another. From a theoretical point of view, a hopping can be described between two lattice sites $\mathbf{R}_m$ and $\mathbf{R}_n$, which are arbitrarily far away. On the other hand, the corresponding probability amplitude would be very small due to the rapid decay of the overlap of the atomic orbitals with increasing distance $\mathbf{R}_m - \mathbf{R}_n$ of the atomic sites. Consequently, in practical calculations only hopping matrix elements between neighbors up to a given order are considered. In the case of III-V semiconductors, good approximations of the band structure can already be obtained when considering nearest-neighbor hopping elements only (see Fig. 2.3). Therefore, we employ a TB model using such a nearest-neighbor approximation.

### 3.3.1. Two-Center Approximation

A prominent and commonly applied simplification of the hopping matrix elements in Eq. (3.26) is the so-called two-center approximation, which has been suggested by Slater and Koster [78]. For the discussion of this approach, we consider the TB matrix elements $H_{\alpha\nu\sigma;\alpha'\nu'\sigma'}(\mathbf{R})$ in Eq. (3.24) and use the definition of $H^{bulk}$ from Eq. (3.15). As a result, we obtain

$$\begin{aligned} &\langle \mathbf{R}_m, \alpha', \nu', \sigma' | H^{bulk} | \mathbf{R}_n, \alpha, \nu, \sigma \rangle \\ &= \langle \mathbf{R}_m, \alpha', \nu', \sigma' | \frac{\mathbf{p}^2}{2m} + \sum_l \sum_{\alpha''=\{\alpha,\alpha'\}} V^{crystal}(\mathbf{R}_l, \alpha'') | \mathbf{R}_n, \alpha, \nu, \sigma \rangle \,, \end{aligned} \tag{3.27}$$

which describes the interaction between two orbitals $\nu'$ and $\nu$ located at the positions $\mathbf{R}_m$ and $\mathbf{R}_n$ that correspond to atom types $\alpha$ and $\alpha'$. Additionally, Eq. (3.27) contains a potential $V^{crystal}$, which can be located at an arbitrary lattice site $\mathbf{R}_l$. Consequently, the general case of an interaction includes three different positions $\mathbf{R}_l$, $\mathbf{R}_m$, and $\mathbf{R}_n$. These positions are referred to as centers. In the line of the basic assumption that the overlap of the atomic orbitals decays rapidly with increasing distance of the atomic sites, approximations can be made.

In the framework of the two-center approximation, three-center contributions ($\mathbf{R}_l \neq \mathbf{R}_m \neq \mathbf{R}_n$), which are considerably smaller than two-center contributions, are neglected. Within this approach, the potential $V^{crystal}$ can either be located at the orbital position $\mathbf{R}_l = \mathbf{R}_m$ or $\mathbf{R}_l = \mathbf{R}_n$. This simplification leads to

$$\begin{aligned}
&\langle \mathbf{R}_m, \alpha', \nu', \sigma' | \frac{\mathbf{p}^2}{2m} + \sum_l \sum_{\alpha''=\{\alpha,\alpha'\}} V^{crystal}(\mathbf{R}_l, \alpha'') | \mathbf{R}_n, \alpha, \nu, \sigma \rangle \\
\overset{\text{two-center}}{\approx} &\langle \mathbf{R}_m, \alpha', \nu', \sigma' | \frac{\mathbf{p}^2}{2m} + \sum_{l=\{n,m\}} \sum_{\alpha''=\{\alpha,\alpha'\}} V^{crystal}(\mathbf{R}_l, \alpha'') | \mathbf{R}_n, \alpha, \nu, \sigma \rangle \\
= &\langle \mathbf{R}_m, \alpha', \nu', \sigma' | \frac{\mathbf{p}^2}{2m} + V^{crystal}(\mathbf{R}_m, \alpha') + V^{crystal}(\mathbf{R}_n, \alpha) | \mathbf{R}_n, \alpha, \nu, \sigma \rangle \,,
\end{aligned} \tag{3.28}$$

which significantly reduces the effort and is therefore a popular approximation. Additionally, the two-center approximation allows for a straightforward treatment of the interaction matrix elements and strain effects that we will discuss later in this work.

### 3.3.2. Empirical Tight-Binding

For the calculation of the TB matrix elements (see Eqs. (3.25), (3.26)), two different approaches are possible. One can either calculate the matrix elements directly, as in the DFTB approach [79] for instance, or treat them as empirical parameters. With both methods a microscopic description is obtained. The latter approach is referred to as empirical TB, in which numerical parameters are chosen in a way that characteristic properties of the bulk band structure, such as band gaps and effective masses are reproduced. The idea behind this method is to simplify the calculation by explicitly considering only points of high symmetry and interpolating over the remainder of the Brillouin zone between these points. Consequently, the computational effort of this method is relatively low. Therefore, empirical TB models are employed throughout this work. Before we discuss a detailed implementation of our TB model, the underlying approximations are summarized.

We consider

(1) the TB matrix elements as empirical parameters;

(2) the two-center approximation;

(3) a finite number of orbital basis states;

(4) nearest-neighbor couplings only.

In the following, a detailed implementation of the nearest-neighbor Slater-Koster empirical TB approach is given for the zinc blende structure in the framework of the two-center approximation.

### 3.3.3. Implementation of the $sp^3s^*$ Model

In the framework of the empirical model, the orbital basis set is chosen as a balance of accuracy and computational effort. On the one hand, it needs to include all orbitals, which are relevant for the chemical bonding and the formation of the electronic bands of interest. On the other hand, often a minimal basis set is chosen to keep the computational effort as low as possible. This aspect becomes increasingly important when large supercells with millions of atoms are considered as discussed in the following chapter. The III-V semiconductors of interest, such as GaAs, are dominantly $sp^3$-bonded. Therefore, it appears reasonable to choose a minimal $sp^3$ nearest-neighbor basis set. Following this approach, it turned out however that the lowest energy conduction bands are not accurately described. An alternative approach is the nearest-neighbor $sp^3s^*$ model of Vogl [80], in which a virtual orbital $s^*$ is introduced to compensate for the minimal orbital basis set. A further improvement of this approach could be the additional consideration of next-nearest neighbor couplings. We choose to employ the nearest-neighbor $sp^3s^*$ model of Vogl [80], as it already provides satisfactory bulk band structures (see Fig. 2.3).

In the framework of this model, the orbital energies at atom type $\alpha$ are given by $E_{s\alpha}, E_{s^*\alpha}$ and $E_{p_i\alpha}$ with $i \in \{x, y, z\}$. The corresponding coupling matrix elements between anions and cations of atom types $\alpha$ and $\alpha'$ are $V_{ss}, V^{\alpha\alpha'}_{sp_i}, V^{\alpha\alpha'}_{s^*p_i}, V^{\alpha\alpha'}_{p_ip_i}$ and $V^{\alpha\alpha'}_{p_ip_j}$ with $i, j \in \{x, y, z\}$. Due to the empirical approach these matrix elements have to be determined only once in advance. Using the $sp^3s^*$ basis set, one can calculate the electronic bulk band structure following Eq. (3.23). To this end, one considers the diatomic unit cell (see Fig. 2.1) with one anion $A$ and one cation $C$. At each of these two atoms, five basis orbitals $\{s, p_x, p_y, p_z, s^*\}$ are localized, resulting in a TB matrix of rank 10 (number of

atoms × number of orbitals). The corresponding hermitian TB matrix

$$H = \begin{bmatrix} H_{AA} & H_{AC} \\ H_{CA} & H_{CC} \end{bmatrix} \tag{3.29}$$

is composed of the four $5 \times 5$ submatrices $H_{AA}$, $H_{AC}$, $H_{CA}$, and $H_{CC}$. For the sake of clarity, we assign red to the anions and blue to the cations. We will maintain this assignment later in the description of quantum dots. The diagonal submatrices for atom type $\alpha$ are

$$H_{\alpha\alpha} = \begin{bmatrix} E_{s\alpha} & 0 & 0 & 0 & 0 \\ 0 & E_{p\alpha} & 0 & 0 & 0 \\ 0 & 0 & E_{p\alpha} & 0 & 0 \\ 0 & 0 & 0 & E_{p\alpha} & 0 \\ 0 & 0 & 0 & 0 & E_{s^*\alpha} \end{bmatrix}, \quad \text{with } \alpha \in \{A, C\}. \tag{3.30}$$

Keeping in mind Eq. (3.25) for the on-site matrix elements, there is no coupling between different orbitals at the same atom. Consequently, the matrices $H_{\alpha\alpha}$ only contain diagonal elements. The submatrices coupling an anion $A$ with a cation $C$ are given by

$$H_{AC} = \begin{bmatrix} V_{ss} \cdot g_0 & V_{sp}^{ac} \cdot g_1 & V_{sp}^{ac} \cdot g_2 & V_{sp}^{ac} \cdot g_3 & 0 \\ -V_{ps}^{ac} \cdot g_1 & V_{xx} \cdot g_0 & V_{xy} \cdot g_3 & V_{xy} \cdot g_2 & -V_{ps^*}^{ac} \cdot g_1 \\ -V_{ps}^{ac} \cdot g_2 & V_{xy} \cdot g_3 & V_{xx} \cdot g_0 & V_{xy} \cdot g_1 & -V_{ps^*}^{ac} \cdot g_2 \\ -V_{ps}^{ac} \cdot g_3 & V_{xy} \cdot g_2 & V_{xy} \cdot g_1 & V_{xx} \cdot g_0 & -V_{ps^*}^{ac} \cdot g_3 \\ 0 & V_{s^*p}^{ac} \cdot g_1 & V_{s^*p}^{ac} \cdot g_2 & V_{s^*p}^{ac} \cdot g_3 & 0 \end{bmatrix} \tag{3.31}$$

and

$$H_{CA} = \begin{bmatrix} V_{ss} \cdot g_0^* & -V_{ps}^{ac} \cdot g_1^* & -V_{ps}^{ac} \cdot g_2^* & -V_{ps}^{ac} \cdot g_3^* & 0 \\ V_{sp}^{ac} \cdot g_1^* & V_{xx} \cdot g_0^* & V_{xy} \cdot g_3^* & V_{xy} \cdot g_2^* & V_{s^*p}^{ac} \cdot g_1^* \\ V_{sp}^{ac} \cdot g_2^* & V_{xy} \cdot g_3^* & V_{xx} \cdot g_0^* & V_{xy} \cdot g_1^* & V_{s^*p}^{ac} \cdot g_2^* \\ V_{sp}^{ac} \cdot g_3^* & V_{xy} \cdot g_2^* & V_{xy} \cdot g_1^* & V_{xx} \cdot g_0^* & V_{s^*p}^{ac} \cdot g_3^* \\ 0 & -V_{ps^*}^{ac} \cdot g_1^* & -V_{ps^*}^{ac} \cdot g_2^* & -V_{ps^*}^{ac} \cdot g_3^* & 0 \end{bmatrix}. \tag{3.32}$$

Note, that corresponding *sp*-coupling matrix elements are marked in green for better readability and the notation $V_{xx}$ for the coupling between two p-orbitals $V_{p_i p_i}$ of the same type has been introduced. Accordingly, $V_{xy}$ denotes the coupling between two p-orbitals $V_{p_i p_j}$ of different types. The factors $g_l$ with $l \in \{0, 1, 2, 3\}$ originate from the Bloch-sums

(see Eq. (3.24)). In our model [80], they are given by

$$\begin{aligned}
g_0 &= \cos\left(k_x\frac{a}{4}\right)\cos\left(k_y\frac{a}{4}\right)\cos\left(k_z\frac{a}{4}\right) - i\sin\left(k_x\frac{a}{4}\right)\sin\left(k_y\frac{a}{4}\right)\sin\left(k_z\frac{a}{4}\right)\\
g_1 &= -\cos\left(k_x\frac{a}{4}\right)\sin\left(k_y\frac{a}{4}\right)\sin\left(k_z\frac{a}{4}\right) + i\sin\left(k_x\frac{a}{4}\right)\cos\left(k_y\frac{a}{4}\right)\cos\left(k_z\frac{a}{4}\right)\\
g_2 &= -\sin\left(k_x\frac{a}{4}\right)\cos\left(k_y\frac{a}{4}\right)\sin\left(k_z\frac{a}{4}\right) + i\cos\left(k_x\frac{a}{4}\right)\sin\left(k_y\frac{a}{4}\right)\cos\left(k_z\frac{a}{4}\right)\\
g_3 &= -\sin\left(k_x\frac{a}{4}\right)\sin\left(k_y\frac{a}{4}\right)\cos\left(k_z\frac{a}{4}\right) + i\cos\left(k_x\frac{a}{4}\right)\cos\left(k_y\frac{a}{4}\right)\sin\left(k_z\frac{a}{4}\right),
\end{aligned} \tag{3.33}$$

where $a$ is the lattice constant and $\mathbf{k} = (k_x, k_y, k_z) \in 1.\mathrm{BZ}$ a reciprocal vector from the first Brillouin zone.

### 3.3.4. Spin-Orbit Coupling

So far, our TB model does not include spin-orbit coupling. Following the approach of Chadi [81], the spin-orbit interaction $H_{SO}$ can be added to the TB Hamiltonian $H_0^{\mathrm{bulk}}$ via

$$H^{\mathrm{bulk}} = H_0^{\mathrm{bulk}} + H_{SO}. \tag{3.34}$$

It is assumed that $H_{SO}$ acts on the TB basis states in the same way as the atomic spin-orbit operator

$$H_{SO}^{\mathrm{atom}} = \frac{1}{2m^2c^2r}\frac{\partial V_{\mathrm{atom}}}{\partial r}\mathbf{Ls} \tag{3.35}$$

does on atomic orbitals [82]. Here, $V_{\mathrm{atom}}$ is the atomic potential, $\mathbf{s}$ the spin operator and $\mathbf{L}$ the operator of the angular momentum. In the following, we consider the implications for our $sp^3s^*$ model. The $s$-orbitals have zero angular momentum and are therefore not split. Accordingly, the virtual excited state $s^*$ of the same symmetry is not split. As a result, only the $p$-orbitals in our model are coupled by spin-orbit interaction, allowing for a description with a single parameter $\lambda$. A detailed discussion of the spin-orbit coupling is presented in Ref. [54], from which we obtain the following non-zero matrix elements

$$\begin{aligned}
\langle p_x \pm |H_{SO}|p_z\mp\rangle &= \pm\lambda\\
\langle p_x \pm |H_{SO}|p_y\pm\rangle &= \mp i\lambda\\
\langle p_y \pm |H_{SO}|p_z\mp\rangle &= -i\lambda
\end{aligned} \tag{3.36}$$

and their complex conjugates. In Eq. (3.36), the spin states $|\uparrow\rangle$ and $|\downarrow\rangle$ are denoted with $|+\rangle$ and $|-\rangle$, respectively. The parameter $\lambda$ is used to reproduce the splitting of the heavy-hole, light-hole and split-off hole VBs around the $\mathbf{\Gamma}$-point (see Fig. 2.4).

In the following, we demonstrate how the spin-orbit coupling can be incorporated into the TB Hamiltonian in Eq. (3.29). Due to the two possible spin directions, each orbital energy in Eq. (3.30) is included twice. Additionally, we consider the spin-orbit coupling matrix elements from Eq. (3.36). As a result, we obtain

$$H_{\alpha\alpha}^{SO} = \begin{bmatrix} H_{\alpha\alpha} & 0_{5\times5} \\ 0_{5\times5} & H_{\alpha\alpha} \end{bmatrix} + H_{SO,\alpha}, \quad \text{with } \alpha \in \{A, C\}, \tag{3.37}$$

where

$$H_{SO,\alpha} = \lambda_\alpha \left[\begin{array}{ccccc|ccccc} 0 & 0 & 0 & 0 & 0 & 0 & 0 & 0 & 0 & 0 \\ 0 & 0 & -i & 0 & 0 & 0 & 0 & 0 & 1 & 0 \\ 0 & i & 0 & 0 & 0 & 0 & 0 & 0 & -i & 0 \\ 0 & 0 & 0 & 0 & 0 & 0 & -1 & i & 0 & 0 \\ 0 & 0 & 0 & 0 & 0 & 0 & 0 & 0 & 0 & 0 \\ \hline 0 & 0 & 0 & 0 & 0 & 0 & 0 & 0 & 0 & 0 \\ 0 & 0 & 0 & -1 & 0 & 0 & 0 & i & 0 & 0 \\ 0 & 0 & 0 & -i & 0 & 0 & -i & 0 & 0 & 0 \\ 0 & 1 & i & 0 & 0 & 0 & 0 & 0 & 0 & 0 \\ 0 & 0 & 0 & 0 & 0 & 0 & 0 & 0 & 0 & 0 \end{array}\right]. \tag{3.38}$$

For better readability, the non-zero matrix elements are marked in green. Since the number of orbital energies has doubled when taking into account two spin directions (see Eq. (3.37)), twice as many couplings

$$H_{AC}^{SO} = \begin{bmatrix} H_{AC} & 0_{5\times5} \\ 0_{5\times5} & H_{AC} \end{bmatrix} \tag{3.39}$$

need to be considered in the TB model. Summarizing the above steps, the final TB Hamiltonian including spin-orbit coupling is given by

$$H^{SO} = \left[\begin{array}{cc|cc} H_{AA} & 0_{5\times5} & H_{AC} & 0_{5\times5} \\ 0_{5\times5} & H_{AA} & 0_{5\times5} & H_{AC} \\ \hline H_{CA} & 0_{5\times5} & H_{CC} & 0_{5\times5} \\ 0_{5\times5} & H_{CA} & 0_{5\times5} & H_{CC} \end{array}\right] + \left[\begin{array}{c|c} H_{SO,A} & 0_{10\times10} \\ \hline 0_{10\times10} & H_{SO,C} \end{array}\right]. \tag{3.40}$$

The individual parameters for III-V semiconductor bulk materials, which are used in this work, are listed in Table A.1 in the appendix.

# 4. Tight-Binding Description of III-V Semiconductor Quantum Dots

In this chapter, we explain how to adopt the TB model to the calculation of electronic properties of semiconductor quantum dots. To provide an accurate modeling of nanostructures, the following points are addressed:

(1) Supercell Calculations;

(2) Interfaces;

(3) Alloyed Systems;

(4) Piezoelectricity;

(5) Calculation of Strain Effects;

(6) Incorporation of Strain Effects;

(7) Matrix Diagonalization.

For each of the above points details of the employed methods and implementation are presented as well as a description of the overall workflow and numerics.

## 4.1. Spatially-Resolved Model

As previously discussed in the subsection 'Growth Techniques', quantum dots can be generated by the systematic embedding of one semiconductor material inside another semiconductor host material. Modeling such a system is challenging since the system is no longer translation invariant compared to the bulk material. As a consequence, the **k**-space TB model, where only one unit cell needs to be considered, cannot be applied. Instead, a real space TB model is employed, which is composed of many zinc blende unit cells as depicted in Fig. 4.1. In such supercell calculations, the entire nanostructure is repeated periodically (as illustrated in Fig. 4.2) instead of a single unit cell. Employing a supercell calculation for semiconductor quantum dots allows for an atom by atom modeling of the system, but requires a rather large computational effort due to the spatial extension of the

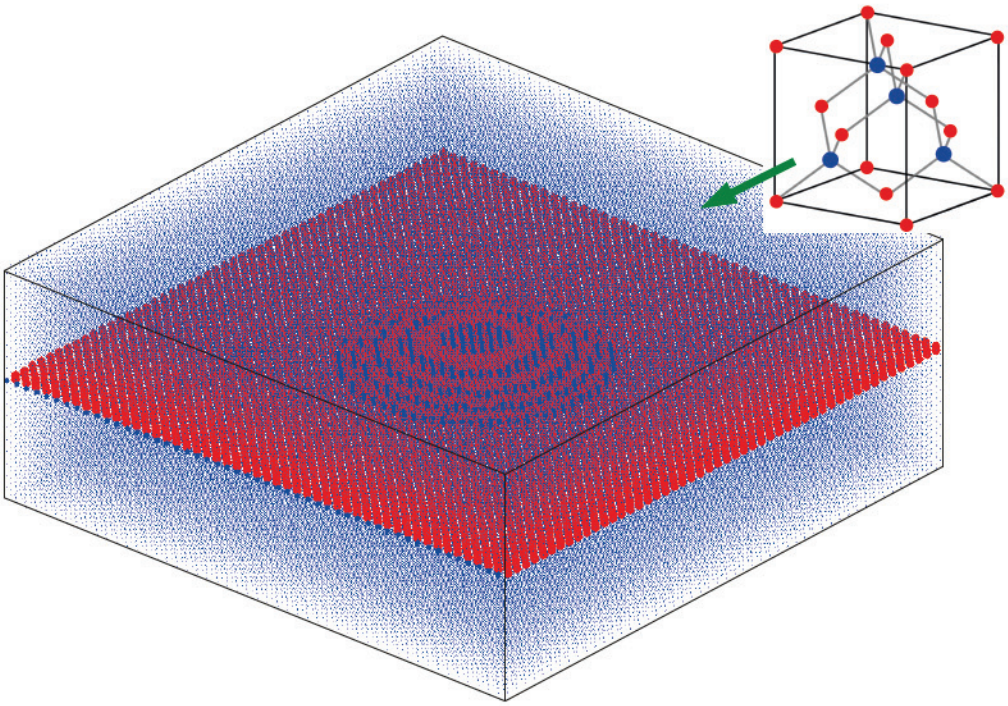

**Figure 4.1. | Supercell**. It is composed of many zinc blende unit cells with anions (red) and cations (blue). For better visibility only the anions forming the wetting-layer and lens-shaped quantum dot are displayed.

supercell. To keep the computational effort as low as possible we employ an $sp^3s^*$ basis set with nearest neighbor couplings as presented for bulk systems in the previous chapter. For practical TB calculations, the atoms inside the supercell need to be numbered and nearest neighbor atoms need to be determined.

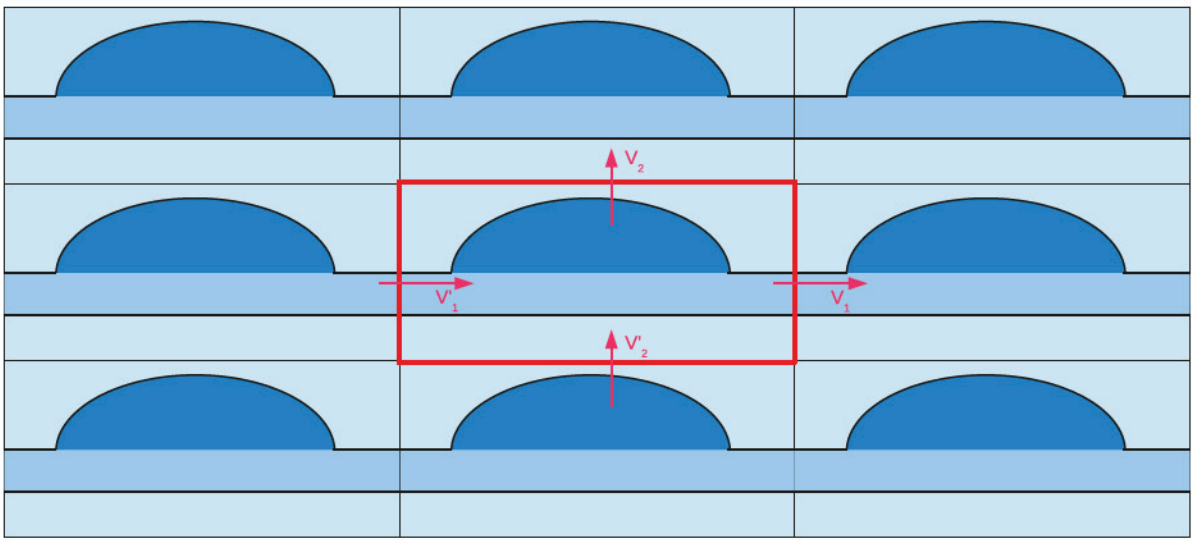


**Figure 4.2. | Supercell boundary conditions**. Crossing the original supercell (red) by $\mathbf{v}_1(\mathbf{v}_2)$, corresponds to re-entering by $\mathbf{v}_1'(\mathbf{v}_2')$.

### 4.1.1. Atom Numbers

To demonstrate the implementation of the TB model for QDs, we choose a specific way of numbering the atoms. In our case, we number the atoms inside the supercell in reverse lexicographical order as shown for the example in Fig. 4.3. A possible way to determine the nearest neighbor numbers for the selected numbering is presented in the appendix.

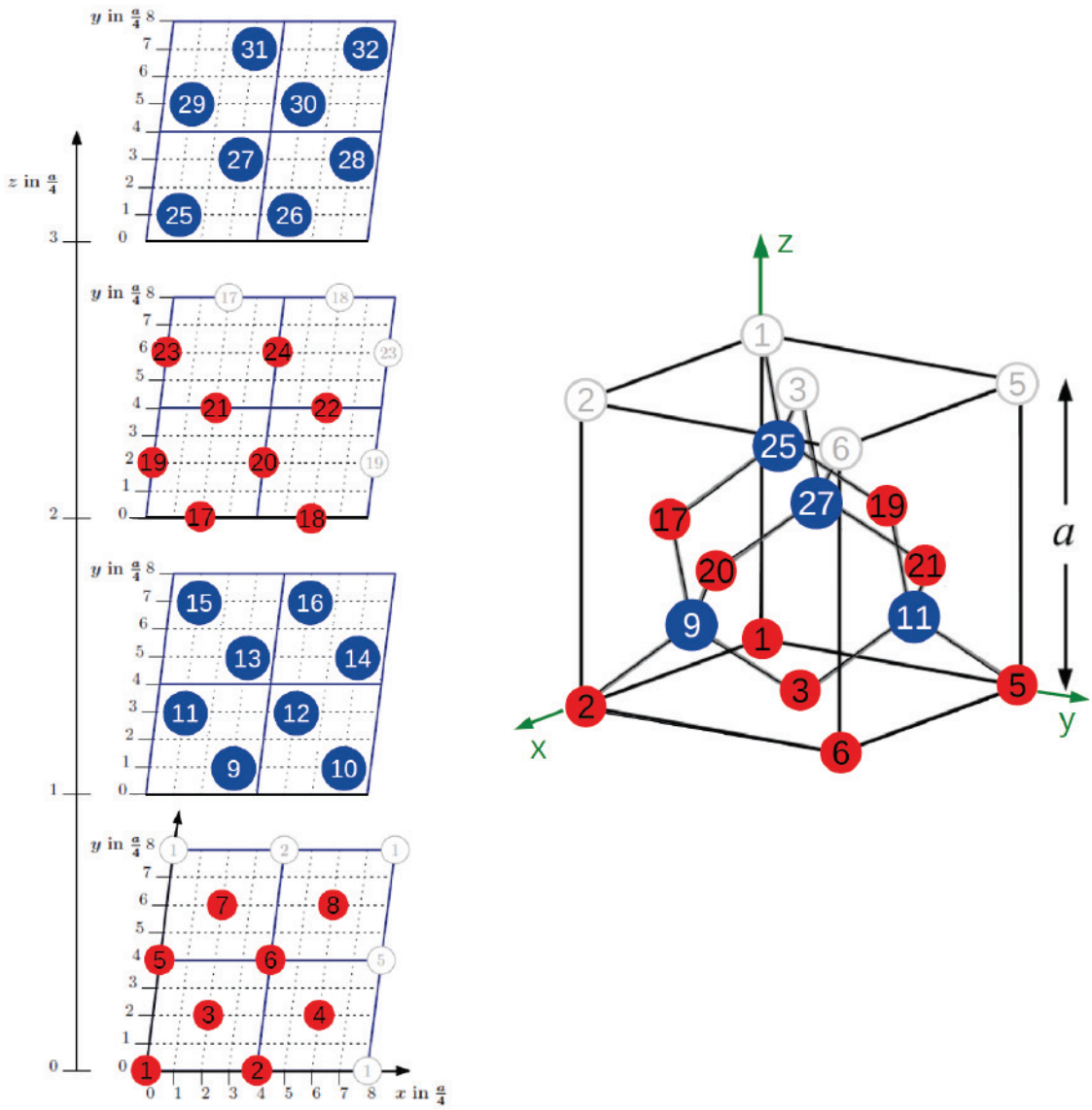


**Figure 4.3.** | **Atom numbering**. Left: Supercell consisting of 2/2/1 unit cells in $x$-/$y$-/$z$-direction with atoms numbered in reverse lexicographical order. Atom numbers that follow from periodic boundary conditions are marked in gray. Right: Conventional zinc blende unit cell with atom numbers according to the situation on the left.

### 4.1.2. Tight-Binding Matrix

According to the selected numbering and colors in Fig. 4.3, the TB matrix is composed of submatrices $H_{AiAi}$ and $H_{CjCj}$, accounting for the orbital energies at the lattice sites $i$ and $j$. Since we employ a nearest-neighbor TB model, we consider couplings between nearest neighbors only. For each of two neighboring atoms, one is an anion $A$ and the other one a cation $C$. To account for this situation, we introduce a function $\Theta_{AiCj}$ with $i, j \in \{1...N\}$. This function equals one if the anion $A$ with atom number $i$ and the cation $C$ with atom number $j$ are nearest neighbors and is zero otherwise. Looking at the underlying zinc blende structure and atom numbering (see Fig. 4.3), each anion has four nearest neighbor cations and vice versa. Each of the couplings with one of the four neighbors is described by a submatrix $\frac{1}{4}H_{AC}$ or $\frac{1}{4}H_{CA}$. Summarizing the structure of the TB matrix, for each of the $N/2$ anions, there is a diagonal submatrix $H_{AiAi}$ and four coupling matrices $\frac{1}{4}H_{AC}$. Accordingly, the remaining $N/2$ cations are described by $H_{CjCj}$ and for each $H_{AC}$, there is a corresponding coupling matrix $H_{CA}$. Following the procedure above, the TB matrix looks like

$$H_{TB} = \begin{bmatrix} H_{A1A1} & \frac{1}{4}H_{AC}\Theta_{A1C2} & \frac{1}{4}H_{AC}\Theta_{A1C3} & 0 & \frac{1}{4}H_{AC}\Theta_{A1C5} & \dots \\ \frac{1}{4}H_{CA}\Theta_{C2A1} & H_{C2C2} & 0 & \frac{1}{4}H_{CA}\Theta_{C2A4} & 0 & \dots \\ \frac{1}{4}H_{CA}\Theta_{C3A1} & 0 & H_{C3C3} & \frac{1}{4}H_{CA}\Theta_{C3A4} & 0 & \dots \\ 0 & \frac{1}{4}H_{AC}\Theta_{A4C2} & \frac{1}{4}H_{AC}\Theta_{A4C3} & H_{A4A4} & \frac{1}{4}H_{AC}\Theta_{A4C5} & \dots \\ \frac{1}{4}H_{CA}\Theta_{C5A1} & 0 & 0 & \frac{1}{4}H_{CA}\Theta_{C5A4} & H_{C5C5} & \dots \\ \vdots & \vdots & \vdots & \vdots & \vdots & \ddots \end{bmatrix}. \tag{4.1}$$

Introducing a shorthand notation for the submatrices $H_{\alpha i,\alpha j}$ and following the atom numbering of the example in Fig. 4.3, the TB Hamiltonian for these 32 atoms is given by

$$H_{TB} = \begin{bmatrix}
H_{1,1} & 0_{\xi\times 8\xi} & H_{1,10} & 0_{\xi\times 4\xi} & H_{1,15} & 0_{\xi\times 9\xi} & H_{1,25} & 0_{\xi\times 6\xi} & H_{1,32} & \\
0_{\xi\times\xi} & H_{2,2} & 0_{\xi\times 6\xi} & H_{2,9} & 0_{\xi\times 6\xi} & H_{2,16} & 0_{\xi\times 9\xi} & H_{2,26} & 0_{\xi\times 4\xi} & H_{2,31} & 0_{\xi\times\xi} \\
0_{\xi\times 2\xi} & H_{3,3} & 0_{\xi\times 5\xi} & H_{3,9} & 0_{\xi\times\xi} & H_{3,11} & 0_{\xi\times 13\xi} & H_{3,25} & 0_{\xi\times\xi} & H_{3,27} & 0_{\xi\times 5\xi} \\
0_{\xi\times 3\xi} & H_{4,4} & 0_{\xi\times 5\xi} & H_{4,10} & 0_{\xi\times\xi} & H_{4,12} & 0_{\xi\times 13\xi} & H_{4,26} & 0_{\xi\times\xi} & H_{4,28} & 0_{\xi\times 4\xi} \\
0_{\xi\times 4\xi} & H_{5,5} & 0_{\xi\times 5\xi} & H_{5,11} & 0_{\xi\times 2\xi} & H_{5,14} & 0_{\xi\times 13\xi} & H_{5,28} & & H_{5,29} & 0_{\xi\times 3\xi} \\
0_{\xi\times 5\xi} & H_{6,6} & 0_{\xi\times 5\xi} & H_{6,12} & & H_{6,13} & 0_{\xi\times 13\xi} & H_{6,27} & 0_{\xi\times 2\xi} & H_{6,30} & 0_{\xi\times 2\xi} \\
0_{\xi\times 6\xi} & H_{7,7} & 0_{\xi\times 5\xi} & H_{7,13} & 0_{\xi\times\xi} & H_{7,15} & 0_{\xi\times 13\xi} & H_{7,29} & 0_{\xi\times\xi} & H_{7,31} & 0_{\xi\times\xi} \\
0_{\xi\times 7\xi} & H_{8,8} & 0_{\xi\times 5\xi} & H_{8,14} & 0_{\xi\times\xi} & H_{8,16} & 0_{\xi\times 13\xi} & H_{4,30} & 0_{\xi\times\xi} & H_{8,32} & \\
0_{\xi\times\xi} & H_{9,2} & & H_{9,3} & 0_{\xi\times 5\xi} & H_{9,9} & 0_{\xi\times 7\xi} & H_{9,17} & 0_{\xi\times 2\xi} & H_{9,20} & 0_{\xi\times 12\xi} \\
H_{10,1} & & 0_{\xi\times 2\xi} & H_{10,4} & 0_{\xi\times 5\xi} & H_{10,10} & 0_{\xi\times 7\xi} & H_{10,18} & & H_{10,19} & 0_{\xi\times 13\xi} \\
0_{\xi\times 2\xi} & H_{11,3} & 0_{\xi\times\xi} & H_{11,5} & 0_{\xi\times 5\xi} & H_{11,11} & 0_{\xi\times 7\xi} & H_{11,19} & 0_{\xi\times\xi} & H_{11,21} & 0_{\xi\times 11\xi} \\
0_{\xi\times 3\xi} & H_{12,4} & 0_{\xi\times\xi} & H_{12,6} & 0_{\xi\times 5\xi} & H_{12,12} & 0_{\xi\times 7\xi} & H_{12,20} & 0_{\xi\times\xi} & H_{12,22} & 0_{\xi\times 10\xi} \\
0_{\xi\times 5\xi} & H_{13,6} & & H_{13,7} & 0_{\xi\times 5\xi} & H_{13,13} & 0_{\xi\times 7\xi} & H_{13,21} & 0_{\xi\times 2\xi} & H_{13,24} & 0_{\xi\times 8\xi} \\
0_{\xi\times 4\xi} & H_{14,5} & 0_{\xi\times 2\xi} & H_{14,8} & 0_{\xi\times 5\xi} & H_{14,14} & 0_{\xi\times 7\xi} & H_{14,22} & & H_{14,23} & 0_{\xi\times 9\xi} \\
H_{15,1} & & 0_{\xi\times 5\xi} & H_{15,7} & 0_{\xi\times 7\xi} & H_{15,15} & 0_{\xi\times\xi} & H_{15,17} & 0_{\xi\times 5\xi} & H_{15,23} & 0_{\xi\times 9\xi} \\
0_{\xi\times\xi} & H_{16,2} & 0_{\xi\times 5\xi} & H_{16,8} & 0_{\xi\times 7\xi} & H_{16,16} & 0_{\xi\times\xi} & H_{16,18} & 0_{\xi\times 5\xi} & H_{16,24} & 0_{\xi\times 8\xi} \\
0_{\xi\times 8\xi} & H_{17,9} & 0_{\xi\times 5\xi} & H_{17,15} & 0_{\xi\times\xi} & H_{17,17} & 0_{\xi\times 7\xi} & H_{17,25} & 0_{\xi\times 5\xi} & H_{17,31} & 0_{\xi\times\xi} \\
0_{\xi\times 9\xi} & H_{18,10} & 0_{\xi\times 5\xi} & H_{18,16} & 0_{\xi\times\xi} & H_{18,18} & 0_{\xi\times 7\xi} & H_{18,26} & 0_{\xi\times 5\xi} & H_{18,32} & \\
0_{\xi\times 9\xi} & H_{19,10} & & H_{19,11} & 0_{\xi\times 7\xi} & H_{19,19} & 0_{\xi\times 5\xi} & H_{19,25} & 0_{\xi\times 2\xi} & H_{19,28} & 0_{\xi\times 4\xi} \\
0_{\xi\times 8\xi} & H_{20,9} & 0_{\xi\times 2\xi} & H_{20,12} & 0_{\xi\times 7\xi} & H_{20,20} & 0_{\xi\times 5\xi} & H_{20,26} & & H_{20,27} & 0_{\xi\times 5\xi} \\
0_{\xi\times 10\xi} & H_{21,11} & 0_{\xi\times\xi} & H_{21,13} & 0_{\xi\times 7\xi} & H_{21,21} & 0_{\xi\times 5\xi} & H_{21,27} & 0_{\xi\times\xi} & H_{21,29} & 0_{\xi\times 3\xi} \\
0_{\xi\times 11\xi} & H_{22,12} & 0_{\xi\times\xi} & H_{22,14} & 0_{\xi\times 7\xi} & H_{22,22} & 0_{\xi\times 5\xi} & H_{22,28} & 0_{\xi\times\xi} & H_{22,30} & 0_{\xi\times 2\xi} \\
0_{\xi\times 13\xi} & H_{23,14} & & H_{23,15} & 0_{\xi\times 7\xi} & H_{23,23} & 0_{\xi\times 5\xi} & H_{23,29} & 0_{\xi\times 2\xi} & H_{23,32} & \\
0_{\xi\times 12\xi} & H_{24,13} & 0_{\xi\times 2\xi} & H_{24,16} & 0_{\xi\times 7\xi} & H_{24,24} & 0_{\xi\times 5\xi} & H_{24,30} & & H_{24,31} & 0_{\xi\times\xi} \\
H_{25,1} & & 0_{\xi\times\xi} & H_{25,3} & 0_{\xi\times 13\xi} & H_{25,17} & 0_{\xi\times\xi} & H_{25,19} & 0_{\xi\times 5\xi} & H_{25,25} & 0_{\xi\times 7\xi} \\
0_{\xi\times\xi} & H_{26,2} & 0_{\xi\times\xi} & H_{26,4} & 0_{\xi\times 13\xi} & H_{26,18} & 0_{\xi\times\xi} & H_{26,20} & 0_{\xi\times 5\xi} & H_{26,26} & 0_{\xi\times 6\xi} \\
0_{\xi\times 2\xi} & H_{27,3} & 0_{\xi\times 2\xi} & H_{27,6} & 0_{\xi\times 13\xi} & H_{27,20} & & H_{27,21} & 0_{\xi\times 5\xi} & H_{27,27} & 0_{\xi\times 5\xi} \\
0_{\xi\times 3\xi} & H_{28,4} & & H_{28,5} & 0_{\xi\times 13\xi} & H_{28,19} & 0_{\xi\times 2\xi} & H_{28,22} & 0_{\xi\times 5\xi} & H_{28,28} & 0_{\xi\times 4\xi} \\
0_{\xi\times 4\xi} & H_{29,5} & 0_{\xi\times\xi} & H_{29,7} & 0_{\xi\times 13\xi} & H_{29,21} & 0_{\xi\times\xi} & H_{29,23} & 0_{\xi\times 5\xi} & H_{29,29} & 0_{\xi\times 3\xi} \\
0_{\xi\times 5\xi} & H_{30,6} & 0_{\xi\times\xi} & H_{30,8} & 0_{\xi\times 13\xi} & H_{30,22} & 0_{\xi\times\xi} & H_{30,24} & 0_{\xi\times 5\xi} & H_{30,30} & 0_{\xi\times 2\xi} \\
0_{\xi\times\xi} & H_{31,2} & 0_{\xi\times 4\xi} & H_{31,7} & 0_{\xi\times 9\xi} & H_{31,17} & 0_{\xi\times 6\xi} & H_{31,24} & 0_{\xi\times 6\xi} & H_{31,31} & 0_{\xi\times\xi} \\
H_{32,1} & & 0_{\xi\times 6\xi} & H_{32,8} & 0_{\xi\times 9\xi} & H_{32,18} & 0_{\xi\times 4\xi} & H_{32,23} & 0_{\xi\times 8\xi} & H_{32,32} &
\end{bmatrix}. \tag{4.2}$$

Here, $\xi$ is the number of basis orbitals and $\mathbf{0}_{r\xi \times c\xi}$ denotes a matrix with $r\xi$ rows and $c\xi$ columns that contains $r\xi \times c\xi$ zeros. In case of our $sp^3s^*$ model with five basis orbitals per atom per spin direction, we obtain an orbital basis of $\xi = 10$ and a Hamiltonian of size $320 \times 320$ for 32 atoms. Each row of the TB matrix in Eq. (4.2) consists of a submatrix with orbital energies $H_{i,i}$, which is marked in red or blue, depending on the atomic type. In addition, each row contains four coupling matrices $H_{i,j}$, whose indices are displayed in red and blue according to the respective atomic type. Due to structure of the TB matrix, each row in Eq. (4.2) contains one block of orbital energies of size $(\xi \times \xi)$ and four coupling matrices of a combined size of $(\xi \times 4\xi)$. The remaining $\mathbf{0}_{\xi \times 27\xi}$ entries are zeros in each row.

### 4.1.3. Coupling Matrix Elements

In Eqs. (4.1) and (4.2) in the previous subsection, we have discussed the structure of the TB matrix without going into detail about the individual matrix elements. The orbital energies $H_{\alpha\alpha}$ with $\alpha \in \{A, C\}$ do not change in comparison to the bulk situation (see Eqs. (3.30), (3.37)). In contrast, the hopping matrix elements, which can generally be represented by

$$H_{AC} = \begin{bmatrix} H_{ss} & H_{sp}^{ac} & H_{sp}^{ac} & H_{sp}^{ac} & 0 \\ H_{ps}^{ac} & H_{xx} & H_{xy} & H_{xy} & H_{ps^*}^{ac} \\ H_{ps}^{ac} & H_{xy} & H_{xx} & H_{xy} & H_{ps^*}^{ac} \\ H_{ps}^{ac} & H_{xy} & H_{xy} & H_{xx} & H_{ps^*}^{ac} \\ 0 & H_{s^*p}^{ac} & H_{s^*p}^{ac} & H_{s^*p}^{ac} & 0 \end{bmatrix} \tag{4.3}$$

within the $sp^3s^*$ basis, need to be modified. In the following, we determine the coupling matrix elements and take advantage of the above introduced two-center approximation.

The bonding situation between an $s$-orbital located at $\mathbf{R}_m$ and one $p_i$ orbital ($i \in \{x, y, z\}$) located at $\mathbf{R}_n$ is illustrated in Fig. (4.4)(a). In the framework of the two-center approximation, such a situation with a difference vector $\mathbf{d} = \mathbf{R}_m - \mathbf{R}_n$ between two atoms is analogous to the situation of diatomic molecules with a molecular axis, where the effective potential is rotationally symmetric with respect to this axis. As a consequence, the angular momentum with respect to $\mathbf{d}$ is a good quantum number[5]. In order to take advantage of this symmetry, the $p_i$-orbitals are decomposed analogously to the molecular orbital theory by

[5]Good quantum number are associated with operators that commute with the Hamiltonian. They correspond to conserved quantities.

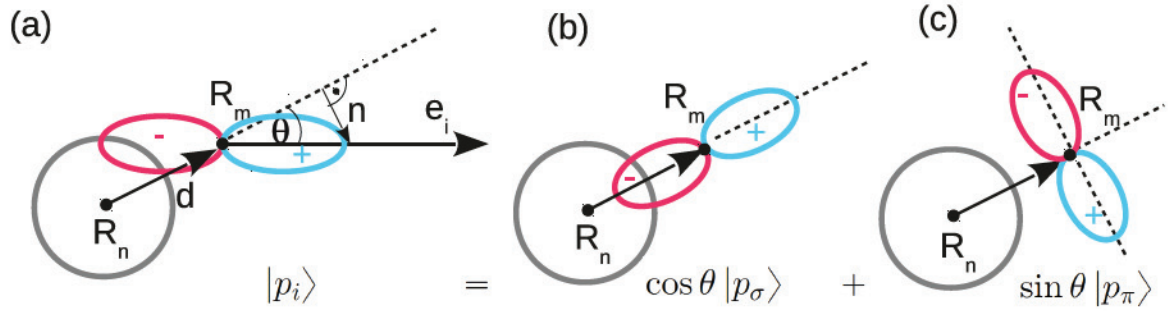


**Figure 4.4. | Two-center bond model**. The situation for an $s$-orbital located at $\mathbf{R}_m$ and one $p_i$ orbital located at $\mathbf{R}_n$ is illustrated. (a) $p_i$ orbital along is decomposed into a bond-parallel part (b) and a bond-normal part (c).

$$|p_i\rangle = \cos\theta\,|p_\sigma\rangle + \sin\theta\,|p_\pi\rangle = \mathbf{d}\cdot\mathbf{e}_i\,|p_\sigma\rangle + \mathbf{n}\cdot\mathbf{e}_i\,|p_\pi\rangle \tag{4.4}$$

into a bond-parallel and a bond-normal part (see Fig. (4.4) (b-c)). In the case of an $s$- and one $p$-orbital, we obtain

$$\langle s|H|p_i\rangle = \underbrace{\mathbf{e}_i\cdot\mathbf{d}}_{d_i}\underbrace{\langle s|H|p_\sigma\rangle}_{V_{sp\sigma}} + \mathbf{e}_i\cdot\mathbf{n}\underbrace{\langle s|H|p_\pi\rangle}_{=0}, \tag{4.5}$$

where the bond-normal part equals zero, as illustrated in Fig. 4.4(c). For two p-orbitals, Eq. (4.4) is applied twice and leads to

$$\langle p_i|H|p_i\rangle = \underbrace{(\mathbf{e}_i\cdot\mathbf{d})^2}_{d_i^2}\underbrace{\langle p_\sigma|H|p_\sigma\rangle}_{V_{pp\sigma}} + \underbrace{(\mathbf{e}_i\cdot\mathbf{n})^2}_{1-d_i^2}\underbrace{\langle p_\pi|H|p_\pi\rangle}_{V_{pp\pi}}. \tag{4.6}$$

Analogously, one obtains

$$\langle p_i|H|p_j\rangle = d_i d_j V_{pp\sigma} - d_i d_j V_{pp\pi}. \tag{4.7}$$

Since the $s^*$-orbital holds the same symmetry as the $s$-orbital, it can be treated in the same manner. As it is a virtual orbital, there is no coupling between two $s^*$-orbitals. Summarizing the procedure above, one obtains the following $sp^3s^*$ nearest neighbor TB matrix elements as linear combinations of the orbital basis states in the framework of the two-center approximation:

$$\begin{aligned}
\langle s|H|s\rangle &= V_{ss\sigma}\\
\langle s_\alpha|H|p_{i,\alpha'}\rangle &= d_i V_{sp\sigma}^{\alpha\alpha'}\\
\langle s^*_\alpha|H|p_{i,\alpha'}\rangle &= d_i V_{s^*p\sigma}^{\alpha\alpha'}\\
\langle p_{i,\alpha}|H|p_{i,\alpha'}\rangle &= d_i^2 V_{pp\sigma}^{\alpha\alpha'} + (1-d_i^2)V_{pp\pi}^{\alpha\alpha'}\\
\langle p_{i,\alpha}|H|p_{j,\alpha'}\rangle &= d_i d_j V_{pp\sigma}^{\alpha\alpha'} - d_i d_j V_{pp\pi}^{\alpha\alpha'}.
\end{aligned} \tag{4.8}$$

Due to the parity of the $p$ orbitals one finds the relations

$$\begin{aligned} \langle s_\alpha | H | p_{x,\alpha'} \rangle &= - \langle p_{x,\alpha'} | H | s_\alpha \rangle \\ \langle p_{x,\alpha} | H | p_{y,\alpha'} \rangle &= \langle p_{y,\alpha'} | H | p_{x,\alpha} \rangle \,. \end{aligned} \tag{4.9}$$

Summarizing the procedure above, the TB coupling matrices are given by

$$H_{AC} = \begin{bmatrix} V_{ss\sigma} & d_x V_{sp}^{ac} & d_y V_{sp}^{ac} & d_z V_{sp}^{ac} & 0 \\ -d_x V_{ps}^{ac} & d_x^2 V_{pp\sigma} + \tilde{d_x}^2 V_{pp\pi} & d_x d_y \tilde{V} & d_x d_z \tilde{V} & -d_x V_{ps^*}^{ac} \\ -d_y V_{ps}^{ac} & d_x d_y \tilde{V} & d_y^2 V_{pp\sigma} + \tilde{d_y}^2 V_{pp\pi} & d_y d_z \tilde{V} & -d_y V_{ps^*}^{ac} \\ -d_z V_{ps}^{ac} & d_x d_z \tilde{V} & d_y d_z \tilde{V} & d_z^2 V_{pp\sigma} + \tilde{d_z}^2 V_{pp\pi} & -d_z V_{ps^*}^{ac} \\ 0 & d_x V_{s^*p}^{ac} & d_y V_{s^*p}^{ac} & d_z V_{s^*p}^{ac} & 0 \end{bmatrix} \tag{4.10}$$

and

$$H_{CA} = \begin{bmatrix} V_{ss\sigma} & d_x V_{ps}^{ac} & d_y V_{ps}^{ac} & d_z V_{ps}^{ac} & 0 \\ -d_x V_{sp}^{ac} & d_x^2 V_{pp\sigma} + \tilde{d_x}^2 V_{pp\pi} & d_x d_y \tilde{V} & d_x d_z \tilde{V} & -d_x V_{s^*p}^{ac} \\ -d_y V_{sp}^{ac} & d_x d_y \tilde{V} & d_y^2 V_{pp\sigma} + \tilde{d_y}^2 V_{pp\pi} & d_y d_z \tilde{V} & -d_y V_{s^*p}^{ac} \\ -d_z V_{sp}^{ac} & d_x d_z \tilde{V} & d_y d_z \tilde{V} & d_z^2 V_{pp\sigma} + \tilde{d_z}^2 V_{pp\pi} & -d_z V_{s^*p}^{ac} \\ 0 & d_x V_{ps^*}^{ac} & d_y V_{ps^*}^{ac} & d_z V_{ps^*}^{ac} & 0 \end{bmatrix} \tag{4.11}$$

with

$$\begin{aligned} \tilde{V} &= (V_{pp\sigma} - V_{pp\pi}) \\ \tilde{d_x}^2 &= (1 - d_x^2) \\ \tilde{d_y}^2 &= (1 - d_y^2) \\ \tilde{d_z}^2 &= (1 - d_z^2) \end{aligned} \tag{4.12}$$

and

$$\begin{aligned} V_{sp}^{ac} &= V_{sp\sigma}^{ac}, \\ V_{s^*p}^{ac} &= V_{s^*p\sigma}^{ac}, \\ V_{ps}^{ac} &= V_{ps\sigma}^{ac}, \\ V_{ps^*}^{ac} &= V_{ps^*\sigma}^{ac}. \end{aligned} \tag{4.13}$$

As in the case of the bulk model, corresponding $sp$-couplings are marked in green for better readability. In an unstrained zinc blende structure with lattice constant $a$, the connecting vectors of an atom to its four neighbors are given by

$$
\begin{aligned}
\mathbf{d}_1 &= \frac{a}{4}(1,1,1) \\
\mathbf{d}_2 &= \frac{a}{4}(-1,1,-1) \\
\mathbf{d}_3 &= \frac{a}{4}(-1,-1,1) \\
\mathbf{d}_4 &= \frac{a}{4}(1,-1,-1).
\end{aligned}
\tag{4.14}
$$

As a result, for a coefficient $d_i$ we obtain

$$
d_i = \mathbf{e}_i \cdot \mathbf{d}_j = \frac{\mathbf{d}_j(i)}{|\mathbf{d}_j|} = \frac{\pm 1}{\sqrt{3}}, \tag{4.15}
$$

with $i \in \{x, y, z\}$ and $j \in \{1, 2, 3, 4\}$.

## 4.2. Description of Interfaces

The interface between two semiconductor materials $A$ and $B$ (or $C$) with unequal band gaps $E_g^A$, $E_g^B$, and $E_g^C$ as displayed in Fig. 4.5 forms a heterojunction. The total difference

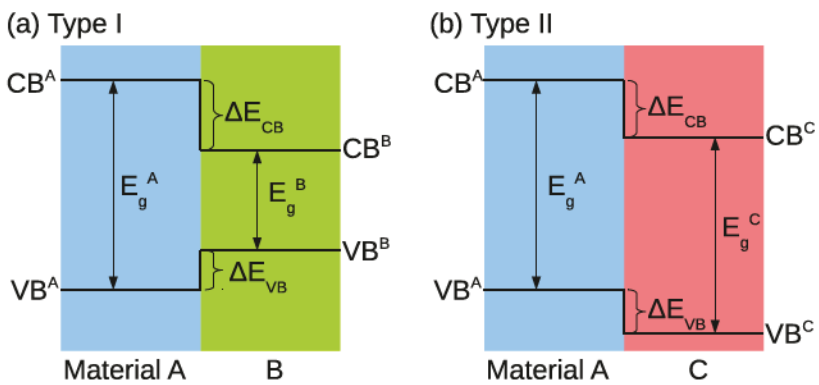


**Figure 4.5.** | **Heterojunctions**. (a) 'Type I' heterojunction, where both electrons and holes are spatially localized in material B. (b) 'Type II' heterojunction, where electrons are localized in material C, whereas holes are energetically more favorable in material A.

in band gap between materials $A$ and $B$ is given by

$$
\Delta E_g^{A/B} = E_g^A - E_g^B = \Delta E_{\mathrm{CB}}^{A/B} + \Delta E_{\mathrm{VB}}^{A/B}, \tag{4.16}
$$

which is distributed among the VB and CB offsets $\Delta E_{\mathrm{VB}}^{A/B}$ and $\Delta E_{\mathrm{CB}}^{A/B}$. Depending on the sign of these energy offsets, one distinguishes between two types of heterojunctions as depicted in Fig. 4.5 (a) and (b). In a 'type I' structure, electrons and holes are located in the same region, whereas in a 'type II' they are spatially separated. Consequently, the

electronic properties of semiconductor heterojunctions strongly depend on the energetic alignment at the interface. In our work, only 'type I' structures are considered. As a result, in the following we discuss the situation with materials $A$ and $B$ as displayed in Fig. 4.5 (a).

For the design and theoretical simulation of semiconductor devices, two of the three quantities $\Delta E_{\mathrm{CB}}, \Delta E_{\mathrm{VB}}$, and $\Delta E_g$ need to be known. In the framework of the TB model, the energy difference $\Delta E_g$ is available for given parametrizations of materials $A$ and $B$ with band gaps $E_g^A$ and $E_g^B$. Consequently, one of the band offsets needs to be determined, which is typically the valence band offset (VBO). The natural VBO is the asymptotic value for the energy difference

$$\Delta E_{\mathrm{VB}}^{A/B} = E_{\mathrm{VB}}^{A} - E_{\mathrm{VB}}^{B} \tag{4.17}$$

between the highest valence bands far from the $A/B$ interface without additional strain-induced corrections. For its determination an energetic alignment with respect to a common reference level is necessary. To this end, an intuitive approach could be to utilize the vacuum level, which can be achieved by comparing the electron affinities of the constituent materials, as described in Ref. [83]. However, the presence of interfaces and surfaces influences the electronic properties, so that using such bulk values does not give satisfactory results [84, 85]. Another well established approach that renders good results is the determination of a common charge neutrality level by means of the so-called branch point (BP) method, as presented in Ref. [85] for instance. For the calculation of the BP energies $E_{\mathrm{BP}}$, the approach of Schleife et al. [86] yields an orientation-independent value of

$$E_{\mathrm{BP}} \approx \frac{1}{2} \int dE\ E \left[ \frac{1}{N_{\mathrm{CB}}} \sum_{i}^{N_{\mathrm{CB}}} D_{\mathrm{CB}}^{i}(E) + \frac{1}{N_{\mathrm{VB}}} \sum_{j}^{N_{\mathrm{VB}}} D_{\mathrm{VB}}^{j}(E) \right], \tag{4.18}$$

where $D_{\mathrm{CB}}^{i}(D_{\mathrm{VB}}^{i})$ are the band-resolved densities of states for a number of $N_{\mathrm{CB}}(N_{\mathrm{VB}})$ CBs (VBs). Since donor(acceptor) states predominantly take their spectral weight from the VB(CB), the branch point energies $E_{\mathrm{BP}}$ in Eq. (4.18) describe the crossover level between a donor-like and acceptor-like character. Determination of the BP energies $E_{\mathrm{BP}}$ of each material ($A$ and $B$) with respect to its VB edge, gives rise to the VBO [85]

$$\Delta E_{\mathrm{VB}}^{A/B} = E_{\mathrm{BP}}^{A} - E_{\mathrm{BP}}^{B} + E_{\mathrm{dip}}. \tag{4.19}$$

Since the BPs define a charge neutrality level, from a theoretical point of view, all dipole contributions $E_{\mathrm{dip}}$ cancel each other out in case of an exact alignment. However, in real heterojunctions, the local charge neutrality condition is always violated to some extent and a net dipole arises due the difference in the electron affinities [85]. These dipole

corrections $E_{\text{dip}}$ are small for III-V semiconductors and can be calculated following the approach of Mönch [87] via

$$E_{\text{dip}} = D_x \left( X_B - X_A \right), \tag{4.20}$$

where $X_A$ and $X_B$ are electronegativity values from the Miedema scale [88] and

$$D_x = \frac{A_X}{1 + 0.1 \left( \varepsilon_\infty - 1 \right)^2} \tag{4.21}$$

is a phenomenological slope parameter with the high-frequency dielectric constant $\varepsilon_\infty$ of the semiconductor. The factor $A_x = 0.86\,\text{eV}/\text{Miedema-unit}$ scales Eq. (4.20) back to the practical and widely used units electron volt.

Following the procedure above, the VBOs for the materials in this work have been determined by Daniel Mourad. For the TB calculations in the following chapters, a value of

$$\Delta E_{\text{VB}}^{\text{AlAs/GaAs}} = 0.59\,\text{eV} \tag{4.22}$$

for the GaAs/AlAs interface is employed, which is in very good agreement with recent findings from density-functional and many-body perturbation theory. [89]. In systems like InAs/GaAs, the small absolute value of the VBO and the large lattice mismatch render similar approaches difficult and may even lead to a sign ambiguity, for instance see Ref. [89]. Furthermore, the widely spanning experimentally available values (see Ref. [90]) are often subject to erroneous double counting corrections of the strain contribution that can be traced back to the use of different substrates or inconsistent sets of deformation potentials. Consistent with Ref. [90], we assume a small positive value of

$$\Delta E_{\text{VB}}^{\text{InAs/GaAs}} = 0.06\,\text{eV}. \tag{4.23}$$

For practical TB calculations, we use the VB alignment as displayed in Fig. 4.6 and choose the zero point of energy at the top edge of the InAs VB. Note that depending on the

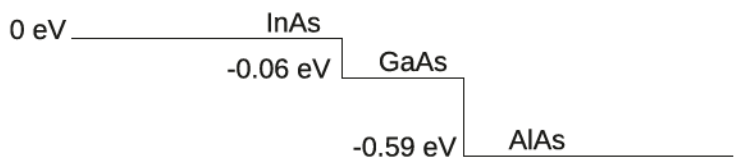


**Figure 4.6. | Valence band alignment**. Energy level scheme for the valence band top edges of InAs, GaAs, and AlAs. The valence band offset (VBO) is determined with respect to InAs.

choice of the zero point in the TB model the absolute value of the VBO is added to the

onsite matrix elements of the binary compounds with smaller band gap, whereas it is subtracted for materials with larger band gap.

## 4.3. Description of Alloyed Nanostructures

As introduced in the previous chapter, the TB parametrizations of bulk crystals are only available for binary compounds like GaAs, InAs, and AlAs (see Table A.1). This poses the question, how bulk crystals of alloyed $\mathrm{In}_x\mathrm{Ga}_y\mathrm{Al}_{1-x-y}\mathrm{As}$ should be treated in such a model.

One simple option is the so-called virtual-crystal approximation (VCA). Following this approach for a ternary material $A_xB_{1-x}C$, it is assumed that the atomic potential $V(ABC)$ of the alloy can be described by a linear dependency

$$V(ABC) = x \cdot V(AC) + (1-x) \cdot V(BC) \tag{4.24}$$

on the concentrations $V(AC)$ and $V(BC)$ of the constituents. Within this approach, the TB parameters are averaged according to the mean alloy concentration in the respective region, such as bulk, wetting-layer or quantum dot. This averaging procedure is a non-local approach. Since we employ an atomistic tight-binding model it appears reasonable to choose a more microscopic approach.

In the following, a novel treatment of alloyed nanostructures in the framework of the $sp^3s^*$ nearest neighbor TB model is proposed. Its applicability is verified by means of experimentally available bowing curves [90, 91, 92]. These curves describe the concentration-dependent change of band gap in alloyed bulk crystals. When alloying two materials, such as InAs and GaAs, the band gap of the alloy generally does not change linearly with the concentration of its constituents. The deviation from the linear behavior is described by a quadratic bowing curve

$$E_g^{\mathrm{InAs/GaAs}}(x) = x \cdot E_g^{\mathrm{InAs}} + (1-x) \cdot E_g^{\mathrm{GaAs}} - bx \cdot (1-x), \tag{4.25}$$

which provides corrections to the linear behavior. The coefficient $b$ of the quadratic term is referred to as the bowing coefficient.

In this paragraph, two novel averaging procedures are derived as illustrated in Figs. 4.7 and 4.8. An intuitive and more atomistic option compared to the VCA would be to choose the TB parameters when possible and reduce the averaging to a minimum. Within this approach, the cation on-site matrix elements and the coupling matrix elements can be chosen according to the elements on the respective lattice sites, which are displayed in

light and dark blue in Fig. 4.7. However, the anion onsite matrix elements of As (red) vary for the different binary compounds, which necessitates an averaging procedure. One could average the anion on-site matrix elements according to the four nearest neighbor cations inside the tetrahedron of the zinc blende unit cell. Within this procedure, we obtain the averaged on-site matrix element (GaAs + 3·InAs)/4 for the left anion in Fig. 4.7. While this procedure gives satisfactory results for the bowing curves [90, 91, 92] of a bulk

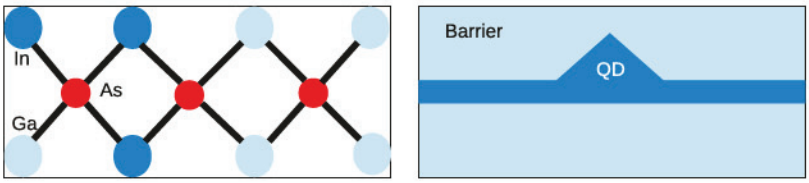


**Figure 4.7. | Outline of the structure**. Left: Lattice with In-atoms (dark blue), As-atoms (red) and Ga-atoms (light blue). Right: The cross-section of the supercell is divided into the barrier (light blue) and the quantum dot (QD, dark blue).

material calculation, it leads to band gaps that strongly depart from the experimentally observed ones for nanostructures (see Fig. 4.8). We interpret this as a shortcoming of the

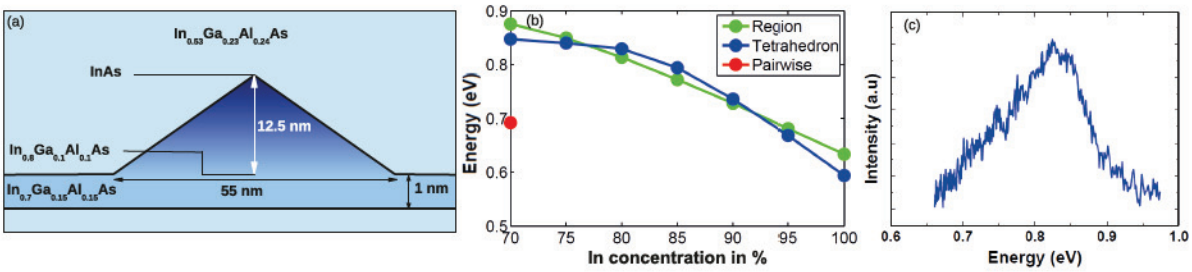


**Figure 4.8. | Averaging procedures**. (a) QD model as obtained from a TEM analysis of the low density sample. (b) Variation of the single-particle band gap $E_G$ for different In-concentrations at the base of the pyramidal QD for pairwise couplings (red) averaged couplings within a tetrahedron (blue), and averaged couplings within the regions QD and barrier (green). (c) Comparison of the calculated emission energies with the macro PL spectrum of the QD ensemble (Fig. by M. Benyoucef from Ref. [93], copyright by the American Physical Society).

nearest neighbor approximation within this scheme for nanostructures. Instead, we opt to distinguish between the QD and the barrier as shown in Fig. 4.7 and determine the coupling matrix elements $V^{QD}$ und $V^{Barr}$ according to the overall concentration in the respective region. At the interface, we average $V = (V^{QD} + V^{Barr})/2$. In a more atomistic approach, we alternatively propose to average the coupling matrix elements within a tetrahedron, as employed for on-site elements. A comparison of the results obtained from both methods is shown Fig. 4.8. Both approaches do not only reproduce in a satisfactory way the bulk material bowing curves but also enhance the agreement with experiments for nanostructures considerably. In our calculations, we chose the averaging procedure within the tetrahedron.

## 4.4. Piezoelectricity

Piezoelectricity arises when the electric charge in a solid is spatially accumulated. As an example for III-V semiconductors, we discuss the situation in GaAs. The electron configurations of Ga and As are $[\mathrm{Ar}]3d^{10}4s^2 4p^1$ and $[\mathrm{Ar}]3d^{10}4s^2 4p^3$, respectively. Consequently, in GaAs the $4s$ and $4p$ sub-shells contribute eight valence electrons, three from Ga and five from As. The extreme case of a totally ionic bond yields $\mathrm{Ga}^{+3}\mathrm{As}^{-3}$. In unstrained GaAs, the atoms are at their bulk lattice positions and there is no net charge distribution in the system. If strain arises, the atoms are displaced into new equilibrium positions, which minimize the strain energy. As a result, the local charge distribution can be non-vanishing and a polarization might emerge. This is referred to as the piezoelectric effect and was first discovered by the Curie brothers [94] in 1880. In pseudomorphically grown[6] zinc blende semiconductors it is caused by shear strain. For semiconductor quantum wells and superlattices grown along the [001] direction, the shear strain can be neglected and therefore no piezoelectric polarization is expected [95]. In general, piezoelectricity is much stronger in GaAs than in InAs. Consequently, in InAs/GaAs QDs the piezoelectric potential is considerably smaller inside the quantum dot than in the barrier [96] and thus only small corrections to the energy levels are expected due to the piezoelectric effect. The literature of the past two decades contains an ongoing discussion [97, 70, 98, 99, 100, 71] regarding the treatment of piezoelectricity in InGaAs systems. While initially only linear terms were taken into account [97, 70, 101, 102, 103, 104, 105], Bester [99] pointed out that the second order term is of the same order of magnitude as the linear term but of opposite sign. In addition, he concluded that one should rather neglect the piezoelectric effect altogether than include only linear terms. Moreover, the piezoelectric effect of a few milli-electron volts is considerably small compared to confinement energies of several hundred meV [100]. In the light of these aspects, piezoelectric effects are neglected in our model.

## 4.5. Strain

As described in the experimental growth techniques section, self-organized quantum dots grow due to the strain, which arises from lattice-mismatch between the host and the quantum dot material. In the case of InAs/GaAs, the lattice constants of GaAs ($a_{\mathrm{GaAs}} \approx 5.6\,\text{Å}$) and InAs ($a_{\mathrm{InAs}} \approx 6.0\,\text{Å}$) deviate by approximately 7 %. Consequently, relatively large tensions occur and the atoms are displaced from the positions of the host

[6] This describes the epitaxial growth of atomically thin layers on top of each other. In the case of materials with different lattice constants, the deposited layer will grow with the substrate lattice parameter and thus will be strained, as in the case of InAs/GaAs for instance.

material into new equilibrium positions, which minimize the global strain energy. In order to calculate these strain-induced displacements, different approaches exist in the literature. In the following, the continuum mechanical model is briefly described, and the valence force field approach, which will be the method of choice in combination with our atomistic TB model, is presented in more detail.

### 4.5.1. Continuum Mechanics

The energy in continuum elasticity theory can be considered as a generalization of the harmonic oscillator model, where it yields $E = \frac{1}{2}k(\mathbf{x} - \mathbf{x}_0)^2$ for a displacement $\mathbf{x} - \mathbf{x}_0$ and a constant $k$. Within the continuum mechanical model [106], the total strain energy is given by

$$E_{CM} = \frac{1}{2} \sum_{i,j,k,l}^{3} C_{ijkl}(\mathbf{r})\varepsilon_{ij}(\mathbf{r})\varepsilon_{kl}(\mathbf{r}). \tag{4.26}$$

Here, the elastic moduli are $C_{ijkl}(\mathbf{r})$ and the components of the strain tensor are given by $\varepsilon_{ij}(\mathbf{r})$ and $\varepsilon_{kl}(\mathbf{r})$. The components $\varepsilon_{ij}$ are obtained from $\varepsilon_{ij} \propto \partial u_i/\partial x_j$, where $\mathbf{u}(\mathbf{r}) = \mathbf{r} - \mathbf{r}_0$ is the displacement vector field that results from the change of an atomic position from $\mathbf{r}_0$ to $\mathbf{r}$. In the framework of the continuum elasticity theory, the displacement field is determined in a way that the energy $E_{CM}$ is minimized. A detailed discussion of this method is presented in [107].

### 4.5.2. Valence Force Field Method

An alternative to the continuum mechanical model is the valence force field (VFF) method of Keating [108]. Since the atoms are treated individually within this approach, it appears to be the natural choice in combination with our atomistic TB model. Consequently, this method is used throughout this work. As in the case of the continuum model the global strain energy is minimized with the difference that an empirical potential is considered in the VFF approach. Hence, the choice of an appropriate potential is of importance to accurately describe individual material systems. In the following, we discuss two commonly applied potentials that we will use throughout this thesis to describe III-V semiconductor materials.

#### 4.5.2.1. Keating Potential

The Keating potential [108] describes the elastic energy $E$ as a function of the atomic positions $\mathbf{R}_i$ by

$$
\begin{aligned}
E_{Keat} = \sum_i \sum_{j>i} V_{ij} = \sum_i \sum_{j>i} \frac{3\alpha_{ij}}{16\left(d_{ij}^0\right)^2} \left[(\mathbf{R}_j - \mathbf{R}_i)^2 - \left(d_{ij}^0\right)^2\right]^2 \\
+ \sum_j \sum_{k>j} \sum_{i\neq j,k} \frac{3\beta_{ijk}}{8\left(d_{ij}^0\right)\left(d_{ik}^0\right)} \left[(\mathbf{R}_j - \mathbf{R}_i)(\mathbf{R}_k - \mathbf{R}_i) - \cos\theta_0 \left(d_{ij}^0\right)\left(d_{ik}^0\right)\right]^2,
\end{aligned}
\tag{4.27}
$$

where $d_{ij}^0$ and $d_{ik}^0$ are the bulk equilibrium distances between an atom $i$ and its nearest neighbor $j$ and $k$, respectively. Moreover, $\cos\theta_0 = -1/3$ is the equilibrium bulk bond angle in the zinc blende lattice. Additionally, $\alpha_{ij}$ and $\beta_{ijk}$ are material-dependent parameters. The first term is zero for $|\mathbf{R}_j - \mathbf{R}_i| = d_{ij}^0$ and therefore describes a change of bond length with respect to the equilibrium positions. The second term includes the angle between the bonds $ij$ and $ik$ of the three atoms $i, j$ and $k$. It is zero for $\angle(\mathbf{R}_{ij}, \mathbf{R}_{ik}) = \theta_0$ and consequently describes the influence of bond-bending with respect to the equilibrium bulk bond angle. One advantage of the Keating potential is that the material parameters $\alpha_{ij}$ and $\beta_{ijk}$ can be expressed as functions of only the stiffness parameters $c_{11}, c_{12}$ and the lattice constant $a$ by

$$
\begin{aligned}
\alpha_{ij} &= (c_{11} + 3c_{12})\frac{a}{4} \\
\beta_{ijk} &= (c_{11} - c_{12})\frac{a}{4},
\end{aligned}
\tag{4.28}
$$

which makes it particularly easy to parameterize this potential. An additional advantage is a rather low computational effort. The parameters used in this thesis can be directly obtained from experiments and are given in Table 4.1. Based on these values, the parameters

| Material | $c_{11}$ | $c_{12}$ | $a$ |
|---|---|---|---|
| GaAs (Ref. [109]) | 11.88 | 5.38 | 5.6533 |
| InAs (Ref. [110]) | 8.34 | 4.54 | 6.0583 |
| AlAs (Ref. [109]) | 12.02 | 5.70 | 5.6611 |

Table 4.1.: Stiffness parameters $c_{ij}$ in units of $10^{11}$ dyn/(cm$^2$) and lattice constants $a$ in Å.

in Table A.2 are obtained.

#### 4.5.2.2. Tersoff Potential

In some cases a three-body potential does not provide a sufficiently accurate description of material properties, such as the cohesive energy. Following a straightforward approach, a step towards improving the accuracy would be a consideration of higher orders in the many-body potential. However, the general form of a four- or five-body potential would

be computationally demanding and contain too many free parameters. A more practical alternative is the Tersoff potential as described in Ref. [111]. The idea behind this potential is the identification of relevant bonding aspects and their incorporation into the potential, while abandoning the general $N$-body form. One aspect of such a bond-order[7] potential is that the bond $ij$ between atoms $i$ and $j$ is weakened by the presence of another bond $ik$ at atom $i$. Consequently, the strength of the chemical bonds of atom $i$ is determined by its coordination number. Following the Tersoff approach, the elastic energy is given by

$$\begin{aligned} E_{Ters} &= \sum_i \sum_{j>i} V_{ij} \\ V_{ij} &= f_C(r_{ij}) \left[ f_R(r_{ij}) + b_{ij} f_A(r_{ij}) \right], \end{aligned} \tag{4.29}$$

where $r_{ij}$ is the distance between atoms $i$ and $j$. The functions $f_R$ and $f_A$ represent a repulsive and an attractive pair potential, respectively. The term $f_R$ is a two-body term, whereas $f_A$ additionally includes three-body interactions. Both terms are given by

$$\begin{aligned} f_R(r_{ij}) &= A \cdot e^{-\lambda_1 r_{ij}} \\ f_A(r_{ij}) &= -B \cdot e^{-\lambda_2 r_{ij}}. \end{aligned} \tag{4.30}$$

The characteristic term of the potential is the function $b_{ij}$ in Eq. (4.29). It represents a measure of the bond-order, and is assumed to be a monotonically decreasing function of the coordination of atoms $i$ and $j$. It is given by

$$\begin{aligned} b_{ij} &= (1 + \beta^n \zeta_{ij}^n)^{-\frac{1}{2n}} \\ \zeta_{ij} &= \sum_{k \neq i,j} f_C(r_{ij}) g(\theta_{ijk}) exp\left[\lambda_3^m (r_{ij} - r_{ik})^m\right] \\ g(\theta_{ijk}) &= \gamma_{ijk} \left( 1 + \frac{c^2}{d^2} - \frac{c^2}{d^2 + (\cos\theta_{ijk} - \cos\theta_0)^2} \right), \end{aligned} \tag{4.31}$$

where $\theta_{ijk}$ is the angle between the bonds $ij$ and $ik$ between the three atoms $i, j$ and $k$ and $\theta_0$ is the respective equilibrium angle. In Eqs. (4.30) and (4.31), the parameters $n, \beta, \lambda_2, B, \lambda_1$, and $A$ are used to describe two-body interactions, whereas $m, \gamma, \lambda_3, c, d$, and $\cos\theta_0$ are only used for three-body interactions. The corresponding parameters are listed in Table A.3 in the appendix. The additional term $f_C$ in Eq. (4.29) is a smooth

[7] Bond order is the number of chemical bonds between a pair of atoms.

cut-off function

$$f_C(r_{ij}) = \begin{cases} 1, & \text{for } r_{ij} < R - D \\ \frac{1}{2} - \frac{1}{2}\sin\left(\frac{\pi}{2}\frac{r_{ij}-R}{D}\right), & \text{for } R - D < r_{ij} < R + D \\ 0, & \text{for } r_{ij} > R + D, \end{cases} \tag{4.32}$$

which has a continuous value and derivative for all $r_{ij}$ and reaches values between 1 and 0 in a small range around $R$. The cut-off is defined by the distance $R + D$ that is defined by the parameters $R$ and $D$. The main advantage of the Tersoff potential over the Keating potential is a higher accuracy as more features are included in the potential. These advantages come in hand with a more difficult parametrization (see [112]) and a rising computational effort[8]. The parameters used within this thesis are listed in Table A.3.

## 4.6. Implementation of Strain

Throughout this thesis, the strain-induced equilibrium atomic positions are obtained by employing the VFF method implemented in the LAMMPS code (Large-scale Atomic/ Molecular Massively Parallel Simulator [113]). LAMMPS is a highly-parallelized molecular dynamics program from Sandia National Laboratories. It includes potentials for solid-state materials, such as metals and semiconductors, as well as soft matter, such as biomolecules and polymers [114]. In order to determine the strain-induced new equilibrium positions, an energy minimization is performed, which consists of three steps that are explained in the following.

In a first step, all atoms are placed at the bulk positions of the host material as in the experimental situation. The LAMMPS input file corresponding to the example in Fig. 4.3 is presented in Table A.4 in the appendix.

In a second step, the valence force field calculation is performed, which provides access to the strain energy and forces acting on the atoms. Based on these quantities, the atoms are moved along their individual force vectors to obtain a new configuration. This procedure is iterated until a convergence with respect to a given tolerance is reached. In that case, the strain-induced equilibrium positions are obtained. The commands, which are used to set up an energy minimization calculation with LAMMPS are listed in Table A.5 in the appendix.

[8] On the supercomputer 'HLRN' in Berlin, the computational time compared to the Keating potential increased by a factor of about 4 for a system of 100 million atoms on 2400 processors on the 'mpp2' platform.

### 4.6.1. Strain-Induced Coordinates

In our calculations, we use different box sizes for the strain-field calculation and the tight-binding diagonalization. For the former, a larger box size is required to ensure that the strain field has sufficiently fallen off towards the edges. For the subsequent TB diagonalization, it is possible to reduce the size of the box since we are interested only in confined states inside the quantum dot. Consequently, we cut a smaller box out of the larger one so that the quantum dot is centered in both boxes as shown in Fig. 4.9. Within

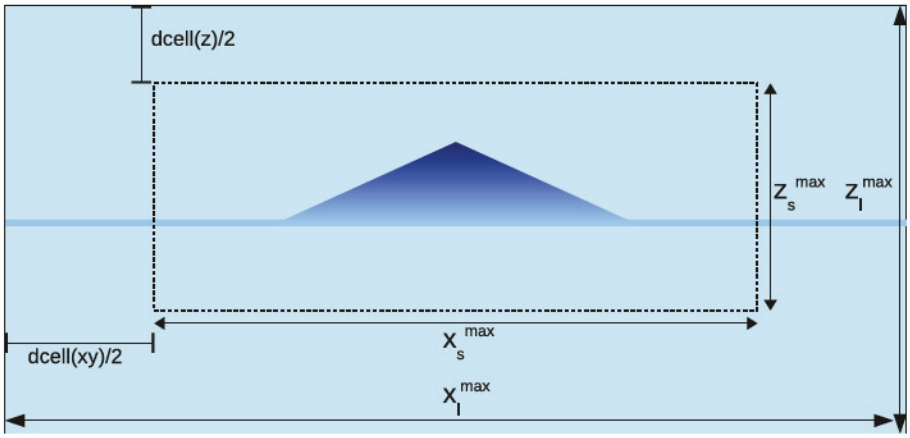


**Figure 4.9.** | **Supercell sizes**. Outer box: Large supercell of size $x_l^{\max} \times z_l^{\max}$ as used for the strain-field calculation. Inner box: Small supercell of length $x_s^{\max} = x_l^{\max} - \mathrm{dcell}(xy)$ and $z_s^{\max} = z_l^{\max} - \mathrm{dcell}(z)$ as used for the tight-binding diagonalization.

this procedure, one faces the problem that the strain-induced atomic positions can no longer be addressed in terms of $n \cdot a/4$, with $n \in \mathbb{N}$. Instead, the atom numbers in both boxes are used to identify individual atoms. Subsequently, for given atom numbers in both boxes, the strain-induced equilibrium positions that are known within the large box are assigned to the corresponding coordinates in the small box. This procedure is detailed in the appendix.

### 4.6.2. Incorporation of Strain

In the third and last step, these strain-induced equilibrium positions are incorporated into the TB Hamiltonian. To this end, different approaches are available in the literature. As discussed above, we have formulated the unstrained TB Hamiltonian in the two-center approximation (see Eq. (3.28)). Within this approach, strain leads to a modification of the coupling terms $V_{ss\sigma}, V_{sp\sigma}, V_{pp\sigma}$ and $V_{pp\pi}$. The physical idea is that the coupling strength between two atoms $i$ and $j$ changes with the inter-atomic distance $d_{ij}$. If $d_{ij}$ equals the atomic distance in the unstrained lattice $d_{ij}^0$, the coupling matrix elements are not changed. If the distance is smaller/larger than in the unstrained lattice, the matrix elements increase/decrease. To quantify such behavior, the power-law scaling

$$
\begin{aligned}
V_{ss}(d_{ij}) &= V_{ss\sigma}\left(\frac{d_{ij}^0}{d_{ij}}\right)^{\eta}, \\
V_{sp_\mu}(d_{ij}) &= d_\mu V_{sp\sigma}\left(\frac{d_{ij}^0}{d_{ij}}\right)^{\eta}, \\
V_{p_\mu p_\nu}(d_{ij}) &= d_\mu d_\nu V_{pp\sigma}\left(\frac{d_{ij}^0}{d_{ij}}\right)^{\eta} - d_\mu d_\nu V_{pp\pi}\left(\frac{d_{ij}^0}{d_{ij}}\right)^{\eta}
\end{aligned}
\tag{4.33}
$$

with $\mu, \nu \in \{x, y, z\}$ and $\eta = 2$ has been suggested by Harrison [115]. Based on this approach, different proposals have been developed in the literature. These ideas include the determination of an individual parameter $\eta$ for each type of bonding [116] $V_{ss\sigma}$, $V_{sp\sigma}$, $V_{pp\sigma}$, and $V_{pp\pi}$ or even an additional modification of the on-site matrix elements [117, 118, 119]. In our model, we use a generalized Harrison rule, in which the parameter $\eta$ of the power law scaling in Eq. (4.33) is numerically adjusted to our system. For our $sp^3s^*$ model, values of $\eta_{\mathrm{InGaAs}} = 2.9$ and $\eta_{\mathrm{AlGaAs}} = 3.4$ are chosen, following Refs. [120] and [121], respectively. These values were obtained from experiments in which pressure on the bulk material was exerted and the results were reproduced with the $sp^3s^*$ TB basis set. Additionally, these values were verified, using TB supercell calculations and bowing curves for the two ternary and the quaternary [90, 91, 92] materials. As a result, these values were used for modeling the nanostructures within this work.

## 4.7. Matrix Diagonalization

Once the TB matrix has been established it needs to be diagonalized in order to obtain the corresponding eigenvectors and eigenvalues. Due to the large number of atoms and thus large rank of the matrix, the diagonalization is performed numerically. In order to choose the method, which is best suited, we classify the properties of the TB matrix. Obviously, it is Hermitian since it describes the eigenenergies of a physical system. Furthermore, the TB matrix can be considered 'sparse', which means that only a few of the total number of matrix elements are non-zero. This is demonstrated in the following.

Within the framework of our $sp^3s^*$ TB model, we consider five orbital energies per atom per spin. The inclusion of spin-orbit coupling requires the consideration of an additional six entries per spin direction. Due to the nearest neighbor interaction with four neighbors, there are $4 \cdot (5 \cdot 5 - 3)$ coupling matrix elements per spin direction, since the elements $V_{ss^*}$,

$V_{s^*s}$, and $V_{s^*s^*}$ are zero. Summarizing the considerations above, the TB matrix contains

$$nnz = \underbrace{2}_{\text{Spin direction}} \cdot \left[ \underbrace{5}_{\text{on-site}} + \underbrace{6}_{\text{SO-coupling}} + \underbrace{4 \cdot (5 \cdot 5 - 3)}_{\text{coupling}} \right] = 198 \tag{4.34}$$

non-zero entries per atom, whereas the total number of matrix elements is given by $(10 \cdot N)^2$ entries. In the case of $N = 10^8$ atoms, only about $\frac{2 \cdot 10^{10}}{10^{18}} \approx 10^{-8}$ of the matrix elements are non-zero. Consequently, the matrices in this work can be considered 'sparse'. Of course, a full matrix diagonalization for such large matrices is numerically demanding. Usually, we are only interested in a few eigenvalues, which correspond to the lowest electron and hole states. To this end, efficient numerical methods for sparse matrices exist, which are based on subspaces. In this work, we use the 'Krylov Schur' subspace solver implemented in the SLEPC (Scalable Library for Eigenvalue Problem Computations) code [122], for which suitable parameters are given in Table A.6 in the appendix.

## 4.8. Sample Calculation

Having so far addressed the individual steps of an electronic TB calculation for semiconductor quantum dots, in this section we provide an example calculation. The latter consists of eight steps, which are given in Fig. 4.10. For the following discussion, we define

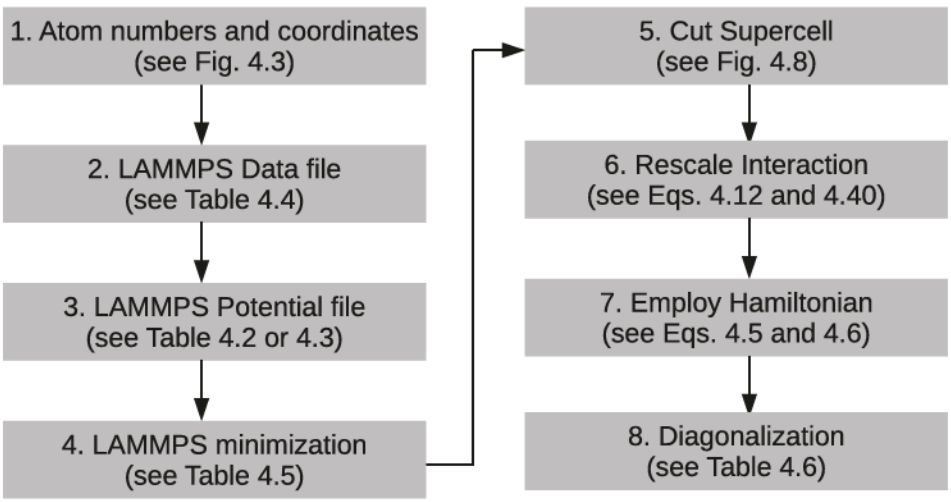


**Figure 4.10. | Flow chart of our TB calculation**. The individual steps are subsequently applied.

a specific InAs/GaAs QD as displayed in Fig. 4.11. We model this structure by placing In, Ga and As atoms on a zinc blende lattice in a way that the geometry and concentration in Fig. 4.11 is obtained.

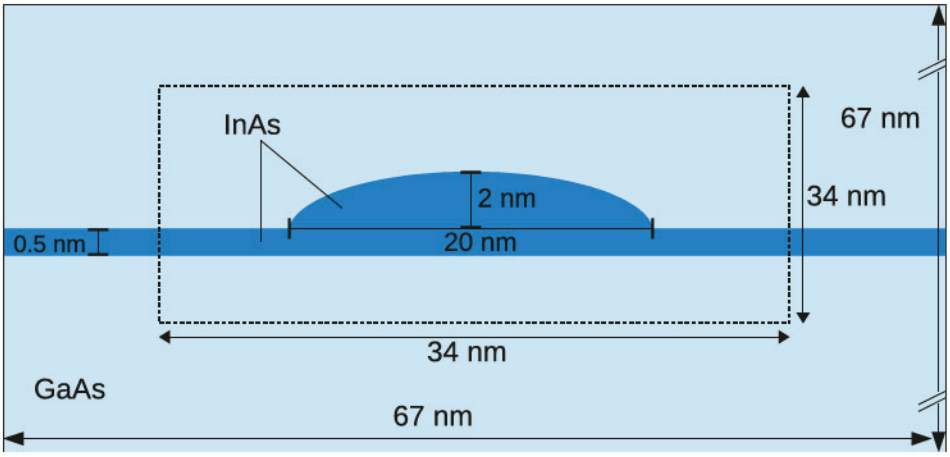


**Figure 4.11.** | **Sample quantum dot**. A pure InAs QD and WL (dark blue) are embedded in a GaAs barrier (light blue). Two different sizes of supercells are used in our calculations. Larger box: for valence-force field calculation. Smaller box: for the TB diagonalization.

In an initial analysis, we investigate the strain-field. To determine the local displacements of the individual atoms due to strain effects, we employ a valence force field calculation using the Keating potential [108] implemented in the LAMMPS code [113] as described above. Before we take a look at specific components of the strain tensor, let us recall

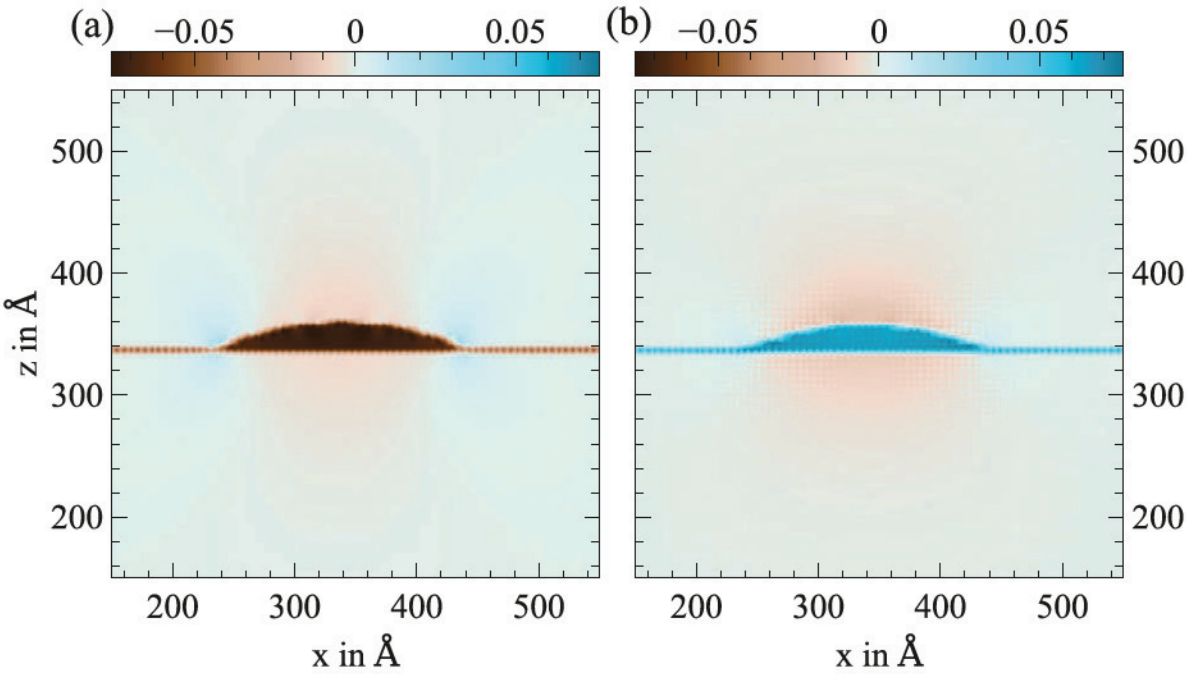


**Figure 4.12.** | **Strain filed**. (a) and (b) Calculated strain components $\varepsilon_{xx}$ (left) and $\varepsilon_{zz}$ (right) along a cross section through the center of QD of Fig. 4.11. For better visibility only the area close the QD is displayed.

the experimental situation. When growing InAs with lattice constant $a_{\mathrm{InAs}} \approx 6.0\,\text{Å}$ on GaAs ($a_{\mathrm{GaAs}} \approx 5.6\,\text{Å}$), lateral compression arises due to the smaller lattice constant of the substrate. On the other hand, a relaxation in growth direction is possible. We reproduce

this behavior in our calculations of the strain components $\varepsilon_{xx}$ and $\varepsilon_{zz}$. By utilizing the atomic displacements and following Ref. [123], the strain components can be determined by $\varepsilon_{ij} = \frac{a_{\text{sub}}}{a_{\text{ref}}} \cdot \frac{a_{ij}^{\text{final}} - a_{\text{sub}}}{a_{\text{sub}}} - \delta_{ij} \frac{a_{\text{ref}} - a_{\text{sub}}}{a_{\text{ref}}}$, where a lattice constant of $a_{\text{ref}} = a_{\text{sub}}$ in the barrier and $a_{\text{ref}} = a_{\text{QD}}$ inside QD and WL is assumed. In our example (see Fig. 4.11), the reference lattice constants are given by $a_{\text{sub}} = a_{\text{GaAs}}$ and $a_{\text{QD}} = a_{\text{InAs}}$ for the region inside the barrier and quantum dot, respectively. The lattice constant after the relaxation $a_{ij}^{\text{final}}$ is obtained by taking the component $i$ of the difference vector between neighboring atoms along direction $j$. The calculated strain field is displayed in Fig. 4.12. For $\varepsilon_{xx}$ (left), compressive strain arises inside the QD and tensile strain propagates into the barrier, whereas for $\varepsilon_{zz}$ (right), the opposite situation is observed. The amplitude of strain corresponds to the lattice mismatch $\frac{a_{\text{InAs}} - a_{\text{GaAs}}}{a_{\text{InAs}}}$. From a technical point of view, it can be seen that the strain-field propagates by several hundred angstrom into the barrier and thus a large simulation box around the QD becomes necessary to converge the strain-field calculation. Convergence is achieved when the strain-field has fallen off towards zero at the edges.

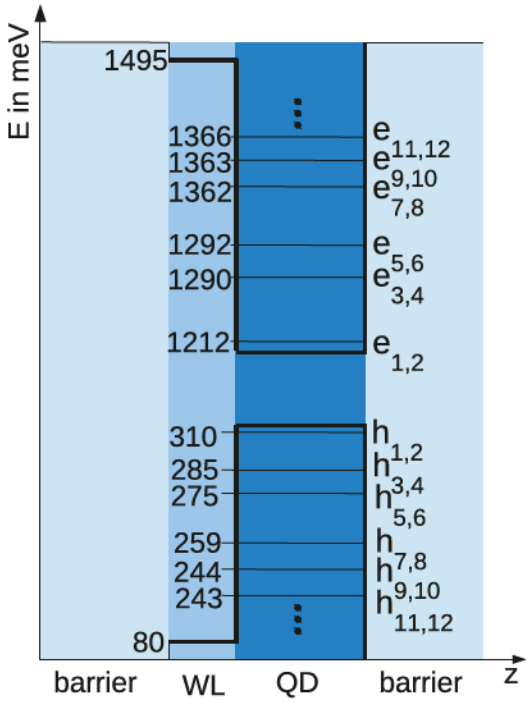


**Figure 4.13.** | **Energy level scheme**. Electron states with energies lower than 1495 meV and hole states with energies above 80 meV are confined inside the QD displayed in Fig. 4.11.

For electronic state calculations, the strained atomic positions are incorporated into the TB Hamiltonian. To this end, we employ a generalized Harrison rule [115] to rescale the coupling matrix elements as discussed above. Diagonalizing the TB Hamiltonian provides access to the single-particle energies and wave functions. The 12 lowest bound electron and hole states are depicted in Fig. 4.13. Generally, all electrons and holes that exhibit a lower energy than the lowest bound WL state are confined within the QD. That energy

can be obtained by performing a supercell calculation, in which the WL but no QD is included. For the structure in Fig. 4.11, we obtain energies of 1495 meV and 80 meV for the electrons and holes, respectively (see Fig. 4.13). To provide information about the

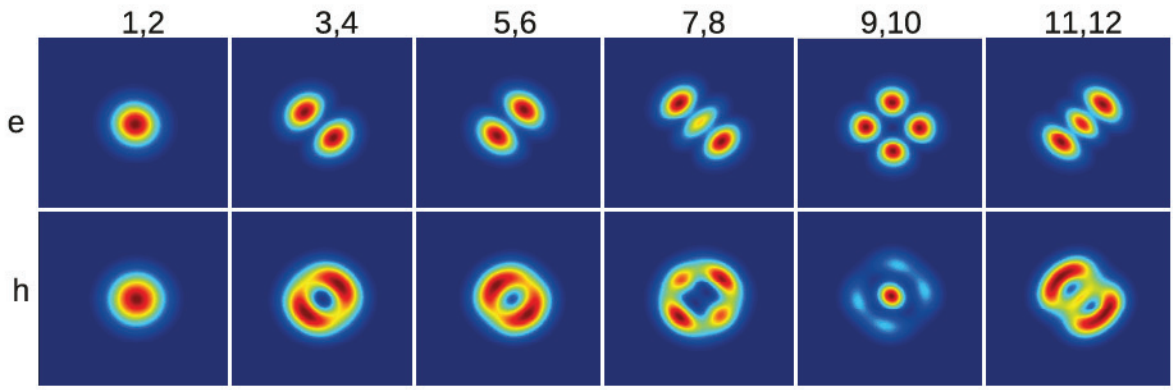


**Figure 4.14.** | **Probability densities**. The 12 lowest electron (e) and hole (h) states are visualized, whose energy levels are displayed in Fig. 4.13. Dark blue equals to zero, whereas red corresponds to a high density.

shape of the electronic wave functions, the probability densities of the 12 lowest bound electron and hole states are displayed in Fig. 4.14.

# 5. Optical Properties of III-V Semiconductors

Once the TB Hamiltonian is diagonalized, the single-particle eigenenergies of confined electron and hole states are obtained. Due the to Coulomb interaction between these states, new eigenvalues and eigenfunctions of the interacting problem arise. For the calculation of these many-body states the Coulomb matrix elements between the single-particle states are required. Additionally, the dipole matrix elements are required for the light-matter interaction and the subsequent calculation of optical spectra.

In the first two sections, we explain how to calculate the Coulomb and dipole matrix elements from the eigenvectors of the TB Hamiltonian. Depending on the physical system, these matrix elements can be used within different methods for calculating optical spectra. Therefore, in the third section we give a brief overview of three methods, each of which is best suited in different situations. First, we shortly discuss the Semiconductor Bloch Equations (SBEs), which come into play when describing the response of a semiconductor to optical excitation by a classical light source. Within this approach, the material is treated quantum-mechanically. Secondly, we briefly discuss the Semiconductor Luminescence Equations (SLEs), where a quantized electromagnetic field is considered instead of a classical light source. The SLEs include a full quantum-mechanical treatment of light-matter interaction and hence provide access to the photoluminescence spectrum.

In the last part of this chapter, we discuss the configuration interaction (CI) approach, which can be used to calculate the Coulomb-correlated states in systems with a discrete density of states. An advantage of this method is that trions and biexcitons are directly accessible within the configuration basis that is obtained from matrix diagonalization. Since we are only interested in the Coulomb-correlated many-body states and energies and not in the time dynamics, we choose to employ the CI method. We combine this approach with Fermi's golden rule, from which we obtain optical spectra within first order perturbation theory.

## 5.1. Coulomb Matrix Elements

By diagonalizing our TB Hamiltonian, we obtain the eigenvectors in a way that the $i^{th}$ eigenvector contains the coefficients $\tilde{c}^i_{\alpha\nu\sigma}$. These coefficients are related to the respective single-particle wave functions by

$$\psi_i(\mathbf{r}) = \sum_{\mathbf{R}\alpha\nu\sigma} \tilde{c}^i_{\alpha\nu\sigma}(\mathbf{R})\tilde{\Phi}_{\mathbf{R}\alpha\nu\sigma}(\mathbf{r}) = \sum_{\mathbf{R}} c^i(\mathbf{R})\Phi_{\mathbf{R}}(\mathbf{r}), \tag{5.1}$$

where $\tilde{\Phi}_{\mathbf{R}\alpha\nu\sigma}(\mathbf{r})$ are the Löwdin orbitals of atom of type $\alpha$ and spin $\sigma$. The sum over the spins $\sigma$ and the orbitals $\nu$ is performed to obtain just one contribution per lattice site. Additionally, the atom type index $\alpha$ can be dropped because it is implicitly determined by the atom at the position $\mathbf{R}$. In the simple picture of a monopole approximation, the Coulomb interaction is induced by point charges, where the expansion coefficients are the probability amplitude for a localization at the positions $\mathbf{R}$ [54, 55]. Within this approximation, the Coulomb matrix elements

$$V_{ijkl} = \int\int \psi_i^*(\mathbf{r})\psi_j^*(\mathbf{r}')\psi_k(\mathbf{r}')\psi_l(\mathbf{r})\tilde{v}(\mathbf{r}-\mathbf{r}')d\mathbf{r}d\mathbf{r}' \tag{5.2}$$

can be calculated by utilizing the TB coefficients $c^i(\mathbf{R})$ from Eq. (5.1). This results in the sum

$$V_{ijkl} \approx \sum_{\mathbf{R}}\sum_{\mathbf{R}'} c_i^*(\mathbf{R})c_j^*(\mathbf{R}')c_k(\mathbf{R}')c_l(\mathbf{R})v(\mathbf{R}-\mathbf{R}') \tag{5.3}$$

over all atomic positions $\mathbf{R}$ and $\mathbf{R}'$ in the supercell. Note that Coulomb potential

$$v(\mathbf{R}-\mathbf{R}') = \frac{e^2}{\varepsilon(\mathbf{R},\mathbf{R}')|\mathbf{R}-\mathbf{R}'|} \tag{5.4}$$

includes the dielectric term $\varepsilon = \varepsilon_0\varepsilon_r(\mathbf{R},\mathbf{R}')$. Its evaluation is generally challenging since $\varepsilon_r$ is spatially dependent. In the case of self-organized semiconductor quantum dots, we consider an effective and isotropic $\varepsilon_r$. This is justified for the III-V semiconductor materials in this work, as it holds $\varepsilon_{\text{InAs}} \approx \varepsilon_{\text{AlAs}} \approx \varepsilon_{\text{GaAs}} \approx 10$, where no strong spatial dependence is expected. Since the effective $\varepsilon_r$ enters the Coulomb matrix elements in the form of $1/\varepsilon_r$, any type of averaging $\varepsilon_{\text{InAs}}, \varepsilon_{\text{AlAs}}$, and $\varepsilon_{\text{GaAs}}$ is reasonable. For an InAs/$\text{In}_x\text{Al}_y\text{Ga}_{1-y}\text{As}$ QD, we choose to approximate

$$\varepsilon_r \approx \left[(1+x)\cdot\varepsilon_{\text{InAs}} + y\cdot\varepsilon_{\text{AlAs}} + (1-y)\cdot\varepsilon_{\text{GaAs}}\right]/2. \tag{5.5}$$

Having discussed the dielectric term, we go back to Eq. (5.3). Its evaluation is challenging for two reasons. First, it includes a singularity for $\mathbf{R} = \mathbf{R}'$. Additionally, for large supercells, e.g. containing $\sim 10^8$ atoms, it is numerically demanding to perform two sums $\mathbf{R}$ and $\mathbf{R}'$

over all lattice sites. An alternative approach is to evaluate the Coulomb matrix elements in $\mathbf{k}$-space, which is presented in the following. By Fourier transform of $v(\mathbf{R}-\mathbf{R}')$, we obtain

$$v(\mathbf{R}-\mathbf{R}') = \frac{e^2}{\varepsilon|\mathbf{R}-\mathbf{R}'|} = \frac{1}{V}\sum_{\mathbf{k}} \underbrace{\frac{e^2}{\varepsilon \mathbf{k}^2}}_{v_{\mathbf{k}}} e^{i\mathbf{k}\cdot(\mathbf{R}-\mathbf{R}')}. \tag{5.6}$$

Combining Eq. (5.6) with Eq. (5.3) gives

$$\begin{aligned} V_{ijkl} &= \sum_{\mathbf{R}}\sum_{\mathbf{R}'} c_i^*(\mathbf{R})c_j^*(\mathbf{R}')c_k(\mathbf{R}')c_l(\mathbf{R}) \sum_{\mathbf{k}} v_{\mathbf{k}} e^{i\mathbf{k}\cdot(\mathbf{R}-\mathbf{R}')} \\ &= \sum_{\mathbf{k}} \left[ \left( \sum_{\mathbf{R}} v_{\mathbf{k}}\, c_i^*(\mathbf{R}) e^{i\mathbf{k}\cdot\mathbf{R}} c_l(\mathbf{R}) \right) \left( \sum_{\mathbf{R}'} c_j^*(\mathbf{R}') e^{-i\mathbf{k}\cdot\mathbf{R}'} c_k(\mathbf{R}') \right) \right]. \end{aligned} \tag{5.7}$$

An advantage is that $\mathbf{R}$ and $\mathbf{R}'$ are now decoupled. Changing the sum over $\mathbf{k}$ into an integral and subsequently using spherical coordinates gives

$$\begin{aligned} &V_{ijkl} \\ &= \frac{1}{V}\int_0^{\tilde{k}} v_{\mathbf{k}} k^2 dk \int_0^{2\pi} d\varphi \int_0^{\pi} d\vartheta \sin\vartheta \left( \sum_{\mathbf{R}} v_{\mathbf{k}}\, c_i^*(\mathbf{R}) e^{i\mathbf{k}\cdot\mathbf{R}} c_l(\mathbf{R}) \right) \left( \sum_{\mathbf{R}'} c_j^*(\mathbf{R}') e^{-i\mathbf{k}\cdot\mathbf{R}'} c_k(\mathbf{R}') \right) \\ &= \frac{e^2}{V\varepsilon}\int_0^{\tilde{k}} dk \int_0^{2\pi} d\varphi \int_{-1}^{+1} dz \left( \sum_{\mathbf{R}} v_{\mathbf{k}}\, c_i^*(\mathbf{R}) e^{ikRz} c_l(\mathbf{R}) \right) \left( \sum_{\mathbf{R}'} c_j^*(\mathbf{R}') e^{-ikR'\cos\Omega} c_k(\mathbf{R}') \right), \end{aligned} \tag{5.8}$$

where $\tilde{k}$ is the maximum value of $|\mathbf{k}|$ and $\mathbf{k}\cdot\mathbf{R} = kR\cos\vartheta$ . In the last step, the substitution $\cos\vartheta = z$ was made. The product $R'\cos\Omega$ can be determined via

$$R'\cos\Omega = \mathbf{R}'(1)\sqrt{1-z^2}\cos\varphi + \mathbf{R}'(2)\sqrt{1-z^2}\sin\varphi + \mathbf{R}'(3)z \tag{5.9}$$

by using the definition

$$\mathbf{k} = \begin{pmatrix} \sin\vartheta\cos\varphi \\ \sin\vartheta\sin\varphi \\ \cos\vartheta \end{pmatrix} k \tag{5.10}$$

of spherical coordinates. To numerically evaluate the integral in Eq. (5.8) an adaptive multidimensional integration routine [124] is used to ensure a proper $\mathbf{k}$-point sampling. The corresponding flowchart, according to which an adaptive accuracy of the integration and parallel evaluation of the integrand can be achieved, is depicted in Fig. A.1 in the appendix.

Evaluating the Coulomb matrix elements for systems with a large number of states can be numerically demanding. Therefore, it is advantageous to use symmetries to reduce the number of elements, which need to be calculated. Once $V(i,j,k,l)$ has been determined,

it can be utilized to obtain

$$\begin{aligned} V(i,j,k,l) &= V(l,k,j,i)^\star \\ V(i,j,k,l) &= V(k,l,i,j)^\star \\ V(i,j,k,l) &= V(j,i,l,k). \end{aligned} \tag{5.11}$$

Furthermore, since the Coulomb interaction is spin-diagonal, it follows

$$V(\{i,l\}_\sigma, \{j,k\}_{\sigma'}) = V(\{i,l\}_{\sigma'}, \{j,k\}_\sigma). \tag{5.12}$$

## 5.2. Dipole Matrix Elements

In this section, we describe the interaction of the charge carriers with a classical light field. The light-matter coupling of a dipole $\mathbf{d} = e_0\mathbf{r}$ to an electric field $\mathbf{E}(\mathbf{r},t)$ is given by the dipole Hamiltonian

$$H_D = \sum_{ij} \left( \langle \psi_i^e | e_0 \mathbf{r} \cdot \mathbf{E}(\mathbf{r},t) | \psi_j^h \rangle \, e_i h_j + \langle \psi_j^h | e_0 \mathbf{r} \cdot \mathbf{E}(\mathbf{r},t) | \psi_i^e \rangle \, e_i^\dagger h_j^\dagger \right), \tag{5.13}$$

where $e_0$ is the elementary charge and $\mathbf{r}$ the position operator. The electron and hole wave functions $\psi_i^e$ and $\psi_j^h$ cause a spatial separation of charge distribution, thereby giving rise to a dipole moment. Since the first summand in Eq. (5.13) annihilates an electron-hole pair, it describes emission. Correspondingly, the second summand is associated with absorption. To obtain the selection rules for optical transitions and the oscillator strengths the matrix elements

$$D_{ij} = e_0 \langle \psi_i^e | \mathbf{r} \cdot \mathbf{E} | \psi_j^h \rangle \tag{5.14}$$

need to be determined. To this end, we employ the widely used dipole approximation, which is discussed in Refs. [125, 126] for instance. This approach is justified since the wavelength $\lambda_{\text{C-band}} = 1550\,\text{nm}$ is large compared to 10 nm, which corresponds to the typical spatial extension of InGaAs quantum dot exciton wave functions [127]. Consequently, it yields

$$\mathbf{k} \cdot \mathbf{r} \approx \frac{2\pi}{\lambda_{\text{C-band}}} \cdot 10\,\text{nm} \approx 0.04 \ll 1. \tag{5.15}$$

Furthermore, the dipole matrix elements as material-specific quantities depend on the polarization vector $\mathbf{E}^{[klm]}$ of the external electric field. For quantum dots grown along the $z$-direction, a reasonable choice is a linear polarization in the $x-y$-plane along the [110] and $[1\bar{1}0]$ crystal directions, perpendicular to the growth direction. Therefore, we use the

normalized polarization vectors

$$\begin{aligned} \mathbf{E}^{[110]} &= \frac{1}{\sqrt{2}}(1,1,0) \\ \mathbf{E}^{[1\bar{1}0]} &= \frac{1}{\sqrt{2}}(1,-1,0) \end{aligned} \tag{5.16}$$

to describe the **E**-field. For the evaluation of the dipole matrix elements in Eq. (5.14), we use the approximation

$$\mathbf{r} \approx \sum_{\mathbf{R}} |\mathbf{R}\rangle \, \mathbf{R} \, \langle \mathbf{R}| \,, \tag{5.17}$$

where **R** are all atomic positions in the supercell. Within this approximation, only the envelope contributions at individual lattice sites are considered and the spatial variation in between is neglected. This approximation is emphasized by the fact that an analysis of the interstitial contributions by using Slater-type orbitals as presented in Ref. [128] for the InGaN material system showed that the orbital contribution is negligible compared to the envelope part [54, 129]. We assume that this approximation is also valid for the III-V semiconductors under consideration. Since this level of approximation for the dipole matrix elements is consistent with the approximation for the Coulomb matrix elements in Eq. (5.3), we maintain it throughout this work. Following the approximation in Eq. (5.17), the dipole matrix elements are given by

$$D_{ij} \approx D_{ij}^{env} = e_0 \sum_{\mathbf{R},\nu} \tilde{c}_{i\nu}^{e*}(\mathbf{R}) \tilde{c}_{j\nu}^{h}(\mathbf{R}) \cdot (\mathbf{E}^{[klm]} \cdot \mathbf{R}), \tag{5.18}$$

where $(\mathbf{E}^{[klm]} \cdot \mathbf{R})$ is the scalar product of the atomic position vector $\mathbf{R} = (x, y, z)$ and the polarization vector $\mathbf{E}^{[klm]}$. Numerically, the expression in Eg. (5.18) can be evaluated by pointwise multiplication of $c_{j\nu}^{h}(\mathbf{R})$ with $(\mathbf{E}^{[klm]} \cdot \mathbf{R})$ for every $\nu$ and subsequently evaluating the scalar product of the result with $c_{i\nu}^{e*}(\mathbf{R})$. This is advantageous since the eigenvectors $c_{i,j,\nu}^{e,h}(\mathbf{R})$ are directly obtained from the TB diagonalization and do not need to be assembled and re-parallelized.

## 5.3. Optical Spectra

As mentioned above, three different methods for the calculation of optical spectra are presented in the following. The SBEs provide access to absorption, reflection, and transmission, whereas the SLEs give rise to emission spectra. While the resonance energies are equal in absorption and emission spectra, the weighting of the respective peaks is different. Both the SBEs and the SLEs are formulated in a single-particle basis. As a result, excitons can be obtained comparatively easily, whereas trions and biexcitons can

only be described with substantial additional computational cost. On the other hand time-resolved dynamics are accessible within both methods. Since we are only interested in the Coulomb-correlated many-body states and energies and neither the peak height nor the time dynamics, we choose to employ the CI method. Within this method, we consider the full Coulomb interaction and obtain the Coulomb-correlated eigenstates of the system by diagonalizing the respective Hamiltonian. For the calculation of the optical spectra we combine the CI approach with Fermi's golden rule, which provides access to optical spectra within first order perturbation theory.

### 5.3.1. Semiconductor Bloch Equations

The semiconductor Bloch equations (SBEs) describe the response of semiconductors to optical excitation by a classical light source. Since this method contains a quantum mechanical treatment of the microscopic polarization and charge carrier distribution, it is classified as a semi-classical approach [130, 57]. The SBEs are named after the structural analogy to the optical Bloch equations, which describe the excitation dynamics in a two-level atom. However, the SBEs contain more physics, such as the Coulomb interaction. For a study of optical properties of semiconductors, one is typically interested in the electronic occupation

$$n_\alpha^\lambda = \langle a_\alpha^{\lambda\dagger} a_\alpha^\lambda \rangle \tag{5.19}$$

and the microscopic polarization

$$P_{\alpha\alpha'}^{\lambda\lambda'} = \langle a_\alpha^{\lambda\dagger} a_{\alpha'}^{\lambda'} \rangle, \tag{5.20}$$

where $\lambda, \lambda'$ denote the band index and $\alpha, \alpha'$ distinguish between particles within the same band. For the following discussion, we consider a translation-invariant bulk-semiconductor, where $\alpha, \alpha'$ denote the momentum state $\mathbf{k}$ and $\lambda, \lambda'$ the conduction and valence band. In this case, the microscopic polarization is defined by the expectation value of an electronic interband transition

$$P_{\mathbf{k}}^{cv} = \langle a_{\mathbf{k}}^{c\dagger} a_{\mathbf{k}}^{v} \rangle = \langle c_{\mathbf{k}}^\dagger v_{\mathbf{k}} \rangle \tag{5.21}$$

that describes the transition amplitude for moving an electron from VB to CB. At the same time, the respective occupations are obtained via

$$\begin{aligned} f_{\mathbf{k}}^c &= \langle c_{\mathbf{k}}^\dagger c_{\mathbf{k}} \rangle \,, \\ f_{\mathbf{k}}^v &= \langle v_{\mathbf{k}}^\dagger v_{\mathbf{k}} \rangle . \end{aligned} \tag{5.22}$$

In order to obtain the SBEs, the Heisenberg equations of motion

$$i\hbar\frac{\mathrm{d}}{\mathrm{d}t}\langle\mathcal{O}\rangle = \langle[\mathcal{O}, H]\rangle\,. \tag{5.23}$$

for a Hamiltonian $H$ that consists of a single-particle electronic part, the corresponding Coulomb-interaction, as well as the dipole interaction between classical light and electronic states [57] are formulated for the microscopic polarization and the electronic occupation. Due to the many-body interactions within $H$, the observable $\mathcal{O}$ couples to higher order correlations, such as

$$\begin{aligned} \frac{\mathrm{d}}{\mathrm{d}t}\langle a_1^\dagger a_2\rangle &\propto \langle a_A^\dagger a_B^\dagger a_C a_D\rangle \\ \frac{\mathrm{d}}{\mathrm{d}t}\langle a_A^\dagger a_B^\dagger a_C a_D\rangle &\propto \langle a_1^\dagger a_2^\dagger a_3^\dagger a_4 a_5 a_6\rangle \\ &\vdots \end{aligned} \tag{5.24}$$

so that the equation cannot be closed. One obtains an infinite number of coupled integro-differential equations, which can be systematically truncated with different methods, for instance see Ref. [131]. Within the following discussion, we use the Hartree-Fock factorization

$$\langle a_A^\dagger a_B^\dagger a_C a_D\rangle = \langle a_A^\dagger a_D\rangle\,\langle a_B^\dagger a_C\rangle - \langle a_A^\dagger a_C\rangle\,\langle a_B^\dagger a_D\rangle \tag{5.25}$$

to close the equations in Eq. (5.24) and neglect higher order correlations. Within this approximation the SBEs [130, 57] read in $\mathbf{k}$-basis

$$\begin{aligned} i\hbar\frac{\partial}{\partial t}P_{\mathbf{k}}^{cv} &= (\tilde{\varepsilon}_{\mathbf{k}}^{c} - \tilde{\varepsilon}_{\mathbf{k}}^{v} - \hbar\omega_0 - i\Gamma)\,P_{\mathbf{k}}^{cv} - [1 - f_{\mathbf{k}}^{c}(t) - f_{\mathbf{k}}^{v}(t)]\,\tilde{\Omega}_{\mathbf{k}}\,, \\ i\hbar\frac{\partial}{\partial t}f_{\mathbf{k}}^{\{c,v\}} &= \tilde{\Omega}_{\mathbf{k}}^{\star}P_{\mathbf{k}}^{cv} - \tilde{\Omega}_{\mathbf{k}}P_{\mathbf{k}}^{cv\star}, \end{aligned} \tag{5.26}$$

where a phenomenological line broadening $\Gamma$ has been introduced to account for higher correlations, e.g. from Coulomb interaction. Additionally, the SBEs contain a generalized Rabi energy

$$\tilde{\Omega}_{\mathbf{k}} = \mathbf{d}\cdot\tilde{\mathbf{E}}(t) + \sum_{\mathbf{k}'\neq\mathbf{k}} v_{\mathbf{k}-\mathbf{k}'}P_{\mathbf{k}'}^{cv} \tag{5.27}$$

for a monochromatic field $\mathbf{E}(t) = \tilde{\mathbf{E}}(t)e^{-i\omega_0 t}$ and renormalized single-particle energies

$$\tilde{\varepsilon}_{\mathbf{k}}^{\{c,v\}} = \varepsilon_{\mathbf{k}}^{\{c,v\}} - \sum_{\mathbf{k}'\neq\mathbf{k}} v_{\mathbf{k}-\mathbf{k}'}f_{\mathbf{k}'}^{\{c,v\}}\,, \tag{5.28}$$

where $\varepsilon_{\mathbf{k}}$ are the $\mathbf{k}$-dependent single-particle energies and $v_{\mathbf{k}}$ are the respective Coulomb matrix elements. At first glance, the SBEs in Eq. (5.26) seem to be diagonal in the momentum index $\mathbf{k}$, but the Coulomb terms in the generalized Rabi energy (see Eq. (5.27))

and the renormalized single-particle energies (see Eq. (5.28)) lead to a coupling of all momentum states.

The SBEs reproduce two limiting cases. On the one hand, the optical Bloch equations for free-carrier transitions are obtained when the Coulomb interaction $v_{\mathbf{k}}$ is neglected. On the other hand, the generalized Wannier equation (see Ref. [57]) for electron-hole pairs can be reproduced in the stationary ($\frac{\partial}{\partial t}P = \frac{\partial}{\partial t}f = 0$) and homogeneous ($\mathbf{E} = 0$) case.

### 5.3.2. Semiconductor Luminescence Equations

The semiconductor luminescence equations (SLEs) describe the coupling of electronic transitions in a semiconductor to resonance modes of the quantized electromagnetic field [131]. As the main difference compared to the SBEs, the SLEs include a photon index $\xi$ and are directly coupled to three-particle correlations. Technically, the SLEs are more difficult to solve numerically than the SBEs due to the additional photon degree of freedom. The SLEs are a possible foundation of modern laser theories that are able to access statistical properties of the light emission [132, 133]. For details on this method, see Refs. [134, 135].

We define the photoluminsecence (PL) spectrum $I(\omega)$ by the rate $I(\omega)\mathrm{d}\omega$ of photon emission into the frequency range $[\omega, \omega + \mathrm{d}\omega]$ according to [136, 137, 138]. In the limit of high frequency resolution of a detector, the emission rate is given by the time derivative of the total population of all free-space photon modes $\xi$ of the quantized field that have frequencies within

$$I(\omega)\mathrm{d}\omega = \sum_{\xi, \omega_{xi} \in [\omega, \omega + \mathrm{d}\omega]} \frac{\mathrm{d}}{\mathrm{d}t} n_\xi(t), \tag{5.29}$$

where the mode index $\xi$ contains both the wave vector and the polarization of the photons. As in the case of the SBEs, the derivation of the SLEs starts from a Hamiltonian $H$ that now includes quantized light-matter interaction and additionally free electromagnetic-field contributions [138]. Based on the Hamiltonian $H$, the Heisenberg equations of motion are used to derive a hierarchy of dynamical equations for quantum-mechanical expectation values. The SLEs include the photon population dynamics

$$i\hbar \frac{\mathrm{d}}{\mathrm{d}t} n_\xi(t) = i\hbar \frac{\mathrm{d}}{\mathrm{d}t} \langle b_\xi^\dagger b_\xi \rangle(t) = 2\mathrm{Re} \sum_j \left( g_{j,\xi}^{cv} \right) \langle b_\xi^\dagger v_j^\dagger c_j \rangle(t), \tag{5.30}$$

which is driven by the photon-assisted transition amplitudes

$$\begin{aligned} i\hbar\frac{\mathrm{d}}{\mathrm{d}t}\langle b_\xi^\dagger v_j^\dagger c_j\rangle(t) &= (\tilde{\varepsilon}_j^c - \tilde{\varepsilon}_j^v - \hbar\omega_\xi - i\Gamma)\langle b_\xi^\dagger v_j^\dagger c_j\rangle(t) \\ &+ V_{j,\xi}^{cv}(t)\left[1 - f_j^c(t) - f_j^v(t)\right] + i g_{j,\xi}^{cv}(t) f_j^c(t) f_j^v(t) \end{aligned} \tag{5.31}$$

that describe a carrier transition from CB to VB via the emission of a photon. As in the case of the SBEs, a phenomenological line broadening $\Gamma$ has been introduced. Additionally, $b_\xi^\dagger$ is the creation operator of a photon in mode $\xi$ with frequency $\omega_\xi$, $v_j^\dagger/c_j^\dagger$ are field operators that create an electron with state index $j$ in the VB/CB, $\tilde{\varepsilon}_j^c/\tilde{\varepsilon}_j^v$ are the renormalized energies, $g_{j,\xi}^{cv}$ is the light-matter coupling coefficient, and

$$\begin{aligned} f_j^c &= \langle c_j^\dagger c_j\rangle, \\ f_j^v &= \langle v_j^\dagger v_j\rangle \end{aligned} \tag{5.32}$$

are the single-particle state occupancies. Inserting Eq. (5.32) into Eq. (5.31) gives

$$\begin{aligned} i\hbar\frac{\mathrm{d}}{\mathrm{d}t}\langle b_\xi^\dagger v_j^\dagger c_j\rangle(t) &= (\tilde{\varepsilon}_j^c - \tilde{\varepsilon}_j^v - \hbar\omega_\xi - i\Gamma)\langle b_\xi^\dagger v_j^\dagger c_j\rangle(t) \\ &+ V_{j,\xi}^{cv}(t)\left[1 - \langle c_j^\dagger c_j\rangle(t) - \langle v_j^\dagger v_j\rangle(t)\right] \\ &+ i g_{j,\xi}^{cv}(t)\,\langle c_j^\dagger c_j\rangle(t)\,\langle v_j^\dagger v_j\rangle(t), \end{aligned} \tag{5.33}$$

which couples the electron and photon dynamics. For the discussion of the SLEs, we consider a simplified case, where Coulomb interaction is neglected. Furthermore, since population changes in III-V semiconductors typically occur on a nanosecond timescale, the carrier populations can be assumed to be stationary for the evaluation of the spectrum. In this case, we obtain

$$\langle b_\xi^\dagger v_j^\dagger c_j\rangle_{\mathrm{stat}} = -\frac{i g_{j\xi} f_j^c(1 - f_j^v)}{\varepsilon_j^c - \varepsilon_j^v - \hbar\omega_\xi - i\Gamma} \tag{5.34}$$

for the transition amplitudes and

$$\begin{aligned} I(\omega) &= \frac{2}{\hbar}\mathrm{Re}\sum_j |\tilde{g}_{j\omega}|^2 \langle b_\xi^\dagger v_j^\dagger c_j\rangle_{\mathrm{stat}} \\ &= \frac{2}{\hbar}\mathrm{Re}\sum_j -\frac{i|\tilde{g}_{j\omega}|^2 f_j^c(1 - f_j^v)}{\varepsilon_j^c - \varepsilon_j^v - \hbar\omega - i\Gamma} \\ &= \frac{2\pi}{\hbar}\mathrm{Re}\sum_j |\tilde{g}_{j\omega}|^2 f_j^c(1 - f_j^v)\delta_\Gamma(\varepsilon_j^c - \varepsilon_j^v - \hbar\omega) \end{aligned} \tag{5.35}$$

for the intensity, where $\delta_\Gamma(E) = \frac{1}{\pi}\frac{\Gamma}{E^2+\Gamma^2}$ is a broadened $\delta$-function and $|\tilde{g}_{j\omega}|^2 = \frac{\hbar|\mathbf{d}_{cv}|^2\omega^3}{6\pi^2\varepsilon_0\varepsilon_r c^3}$ a modified light-matter interaction matrix element, which is obtained by performing the

integration over the photon wave vector. This simplified case resembles Fermi's golden rule (see Eq. (5.51), next subsection) with the main difference that in Eq. (5.35) the transition energies $\varepsilon_j^c - \varepsilon_j^v$ correspond to the single-particle energies, whereas in Eq. (5.51) renormalized many-body energies are considered. Additionally, in Eq. (5.35) the transition amplitudes are modified by electronic populations. When additionally taking into account Coulomb correlations, Eq. (5.35) can be systematically extended so that the emission occurs at many-body energies.

### 5.3.3. Configuration Interaction and Fermi's Golden Rule

In the following, we discuss to combination of the configuration interaction (CI) method that gives rise to Coulomb-correlated many-body eigenstates with Fermi's golden rule, which provides access to optical spectra within first order perturbation theory. Within this approach, electronic occupations and time dynamics are neglected compared to the SLE method. On the other hand, the CI method allows for the consideration of full Coulomb interaction and hence provides access to the Coulomb-correlated eigenstates. Similar results within the SLE method would require the establishment of the full many-body hierarchy. As we are interested in the Coulomb-correlated many-body states and energies and neither the peak height nor the time dynamics, we choose to combine the CI method with Fermi's golden rule. Before the latter can be applied, the many-body states need to be determined. To this end, we employ the CI method, which we discuss in the following. For details on this method, see e.g. Refs. [135, 139, 140]. The CI approach systematically includes the Coulomb correlations between the confined single-particle electron and hole states. These correlations are obtained from diagonalization of the Hamiltonian

$$H = H_0 + H_{\text{Coul}}, \tag{5.36}$$

which is composed of the diagonal single-particle part $H_0$ (see Eq. (5.37)) and the interaction part $H_{\text{Coul}}$ (see Eq. (5.38)).

#### Single-Particle Hamiltonian

We start from the single-particle Hamiltonian

$$H_0 = \sum_{i\sigma} \varepsilon_i^c c_{i\sigma}^\dagger c_{i\sigma} + \sum_{i\sigma} \varepsilon_i^v v_{i\sigma}^\dagger v_{i\sigma} \tag{5.37}$$

that contains the TB eigenvalues $\varepsilon_i^v$ and $\varepsilon_i^c$ originating from the VB and CB, respectively. The operators $c_{i\sigma}^\dagger / v_{i\sigma}^\dagger$ create an electron in the CB/VB with spin $\sigma$ and correspondingly

the $c_{i\sigma}/v_{i\sigma}$ annihilate a particle in the respective state.

### Many-body Hamiltonian

The Hamiltonian $H_0$ (see Eq. (5.37)) contains no interaction between the single-particle states. If at least two charge carriers are present, Coulomb interaction arises between these two particles. The corresponding Hamiltonian $H_{\text{Coul}}$ for electrons in the CB and VB is given by

$$\begin{aligned} H_{\text{Coul}} = &\frac{1}{2}\sum_{ijkl\sigma\sigma'} V^{cccc}_{ij,kl} c^\dagger_{i\sigma} c^\dagger_{j\sigma'} c_{k\sigma'} c_{l\sigma} + \frac{1}{2}\sum_{ijkl\sigma\sigma'} V^{vvvv}_{ij,kl} v^\dagger_{i\sigma} v^\dagger_{j\sigma'} v_{k\sigma'} v_{l\sigma} \\ &+ \frac{1}{2}\sum_{ijkl\sigma\sigma'} V^{vccv}_{ij,kl} v^\dagger_{i\sigma} c^\dagger_{j\sigma'} c_{k\sigma'} v_{l\sigma} + \frac{1}{2}\sum_{ijkl\sigma\sigma'} V^{cvvc}_{ij,kl} c^\dagger_{i\sigma} v^\dagger_{j\sigma'} v_{k\sigma'} c_{l\sigma} \\ &+ \frac{1}{2}\sum_{ijkl\sigma\sigma'} V^{cvcv}_{ij,kl} c^\dagger_{i\sigma} v^\dagger_{j\sigma'} c_{k\sigma'} v_{l\sigma} + \frac{1}{2}\sum_{ijkl\sigma\sigma'} V^{vcvc}_{ij,kl} v^\dagger_{i\sigma} c^\dagger_{j\sigma'} v_{k\sigma'} c_{l\sigma}. \end{aligned} \tag{5.38}$$

Due to the description with respect to the VB and CB, the above representation is shortly referred to as $cv$-picture.

### Electron-Hole Picture

The excitation of an electron from the VB into the CB, which can be described by $c^\dagger_{i\sigma} v_{i\sigma}$, creates an electronic vacancy in the VB. This vacancy can be described as a hole $h^\dagger_{i-\sigma}$ with opposite spin. Similarly, the excitation of an electron into the CB can be written as $e^\dagger_{i\sigma}$. Consequently, the entire excitation process $c^\dagger_{i\sigma} v_{i\sigma}$ can be described by $e^\dagger_{i\sigma} h^\dagger_{i-\sigma}$. As a result, we obtain the transformation rule

$$\begin{pmatrix} c^\dagger_{i\sigma} \\ c_{i\sigma} \\ v^\dagger_{i\sigma} \\ v_{i\sigma} \end{pmatrix} \mapsto \begin{pmatrix} e^\dagger_{i\sigma} \\ e_{i\sigma} \\ h_{i-\sigma} \\ h^\dagger_{i-\sigma} \end{pmatrix}. \tag{5.39}$$

By using the commutator relation for fermions $[a_i, a^\dagger_j]_+ = a_i a^\dagger_j + a^\dagger_j a_i = \delta_{ij}$, we can determine the transformed single-particle Hamiltonian $H_0$ in normal order. This is a representation, in which all creation operators are moved to the left of the annihilator operators. Hereby, all single-particle contributions, which originate from permutation of creation and annihilation operators, are neglected. The reason for this is that these terms describe the interaction of electrons and holes with the full VB, and this interaction is already included in the band structure. As a result, the transformed single-particle

Hamiltonian is given by

$$H_0 = \sum_{i\sigma} \varepsilon_i^e e_{i\sigma}^\dagger e_{i\sigma} + \sum_{i\sigma} \varepsilon_i^h h_{i\sigma}^\dagger h_{i\sigma}. \tag{5.40}$$

It contains information about the single-particle spectrum. In the electron-hole picture, $H_{\text{Coul}}$ reads

$$\begin{aligned} H_{\text{Coul}} = &\frac{1}{2} \sum_{ijkl\sigma\sigma'} V_{ij,kl}^{eeee} e_{i\sigma}^\dagger e_{j\sigma'}^\dagger e_{k\sigma'} e_{l\sigma} + \frac{1}{2} \sum_{ijkl\sigma\sigma'} V_{ij,kl}^{hhhh} h_{i\sigma}^\dagger h_{j\sigma'}^\dagger h_{k\sigma'} h_{l\sigma} \\ &- \frac{1}{2} \sum_{ijkl\sigma\sigma'} V_{ij,kl}^{heeh} h_{i\sigma}^\dagger e_{j\sigma'}^\dagger e_{k\sigma'} h_{l\sigma} - \frac{1}{2} \sum_{ijkl\sigma\sigma'} V_{ij,kl}^{ehhe} e_{i\sigma}^\dagger h_{j\sigma'}^\dagger h_{k\sigma'} e_{l\sigma} \\ &- \frac{1}{2} \sum_{ijkl\sigma\sigma'} V_{ij,kl}^{eheh} e_{i\sigma}^\dagger h_{j\sigma'}^\dagger e_{k\sigma'} h_{l\sigma} - \frac{1}{2} \sum_{ijkl\sigma\sigma'} V_{ij,kl}^{hehe} h_{i\sigma}^\dagger e_{j\sigma'}^\dagger h_{k\sigma'} e_{l\sigma}, \end{aligned} \tag{5.41}$$

where the first two summands describe repulsive electron-electron and hole-hole interactions between charge carriers of the same type. The sign is obtained from applying the transformation (see Eq. (5.39)) to Eq. (5.38) and subsequently establishing the normal ordering with the help of the corresponding commutator relations for fermions. The second row represents the direct electron-hole interaction, which is the dominant contribution of the exciton binding energy. The last row describes the electron-hole exchange interaction, which is responsible for the fine-structure splitting. If one is not interested in this property, these terms are usually neglected since the corresponding matrix elements $V^{eheh}$ and $V^{eheh}$ are smaller by several orders of magnitudes compared to the other types of Coulomb interaction. Within the configuration interaction approach, the Hamiltonian $H = H_0 + H_{\text{Coul}}$ in Eq. (5.36) can be diagonalized without any further approximations for a finite number of bound electrons and holes. Before the actual diagonalization the structure of $H$ can be optimized by taking advantage of good quantum numbers[9].

### Good Quantum Numbers

Sorting the single-particle states by good quantum numbers with respect to the Hamiltonian $H = H_0 + H_{\text{Coul}}$ simplifies the system in a way that the so obtained matrix is block diagonal in these quantum numbers. This is numerically advantageous since the different smaller submatrices can be diagonalized[10] individually. Consequently, it is beneficial to identify as many good quantum numbers as possible. It turns out that the number of particles $n$, number of electrons $n_e$, and number of holes $n_h$ prove to be good quantum numbers.

In the following, it is derived that the corresponding operators commute with the

[9] Good quantum numbers are associated with operators that commute with the Hamiltonian. They correspond to conserved quantities.

[10] A full matrix diagonalization of a dense quadratic matrix scales with $n^3$ if $n$ is the rank of the matrix.

Hamiltonian $H = H_0 + H_{\text{Coul}}$. We start with the occupation number operator of electrons $n_e$. This operator commutes with $H_0 = \sum_i \varepsilon_i^e e_i^\dagger e_i + \sum_i \varepsilon_i^h h_i^\dagger h_i$, since it commutes both with itself and with the operator $n_h$ that acts on a different type of particle. It remains to be shown that $n_e$ commutes with $H_{\text{Coul}}$. In other words, it needs to be shown that $n_e$ commutes with all six summands. The operator $n_e$ commutes with the hole operators $h^\dagger h$, because they act on different particles. Consequently, it is sufficient to show that $n_e$ commutes with $e_i^\dagger e_j$, which is derived in the following calculation:

$$\begin{aligned}
\sum_\alpha \sum_{ij} n_\alpha e_i^\dagger e_j &= \sum_\alpha \sum_{ij} e_\alpha^\dagger e_\alpha e_i^\dagger e_j \\
&= \sum_\alpha \sum_{ij} e_\alpha^\dagger \left(\delta_{i\alpha} - e_i^\dagger e_\alpha\right) e_j \\
&= \sum_{ij} e_i^\dagger e_j - \sum_\alpha \sum_{ij} e_\alpha^\dagger e_i^\dagger e_\alpha e_j \\
&= \sum_{ij} e_i^\dagger e_j - \sum_\alpha \sum_{ij} e_i^\dagger e_\alpha^\dagger e_j e_\alpha \\
&= \sum_{ij} e_i^\dagger e_j - \sum_\alpha \sum_{ij} e_i^\dagger \left(\delta_{j\alpha} - e_j e_\alpha^\dagger\right) e_\alpha \\
&= \sum_\alpha \sum_{ij} e_i^\dagger e_j e_\alpha^\dagger e_\alpha = \sum_\alpha \sum_{ij} e_i^\dagger e_j n_\alpha .
\end{aligned} \tag{5.42}$$

As a result, $n_e$ commutes with $H = H_0 + H_{\text{Coul}}$. Analogously, $n_h$ commutes with $H$. Consequently, $n = n_e + n_h$ commutes with $H$, which confirms the fact that the total number of particles is preserved under Coulomb interaction.

### Setting Up the Hamilton Matrix

Within the CI method, each of the $n$ single-particle basis states may be occupied or unoccupied, which yields $2^n$ possible configurations. Consequently, a binary representation of the configuration basis is reasonable. The choice ordering the individual configurations is initially arbitrary, but should not be changed after a block diagonal Hamilton matrix has been achieved by sorting with respect to good quantum numbers. Due to this structure, the individual blocks of the matrix can be constructed separately as demonstrated in the following by means of an example. We can formulate the Coulomb interaction between two electrons

$$\frac{1}{2} \sum_{ijkl} V_{ijkl} e_i^\dagger e_k^\dagger e_j e_l = -\frac{1}{2} \sum_{ijkl} V_{ijkl} e_i^\dagger e_j e_k^\dagger e_l + \frac{1}{2} \sum_{ijl} V_{ijjl} e_i^\dagger e_l \tag{5.43}$$

as pairs of products of creation and annihilation operators $e_A^\dagger e_B$ with $A, B \in \{i, j, k, l\}$. When establishing a matrix representation for each possible $e_A^\dagger e_B$, we can deploy the

Hamilton matrix by matrix multiplication of different $e_A^\dagger e_B$. As an example to demonstrate this procedure, we consider the subspace of $n_e = 2$ electrons that can occupy three single-particle states $A, B \in \{1, 2, 3\}$. The respective basis states are

$$\begin{aligned} |b_1\rangle &= |1,1,0\rangle \\ |b_2\rangle &= |1,0,1\rangle \\ |b_3\rangle &= |0,1,1\rangle\,. \end{aligned} \tag{5.44}$$

By considering pairs of one creation and one annihilation operator $e_A^\dagger e_B$, we ensure that we remain within the subspace of $n_e = 2$ electrons. As an example, we demonstrate this for the case $e_2^\dagger e_3$. By applying the annihilation operator $e_3$ to Eq. (5.44), one obtains

$$\begin{aligned} e_3\,|1,1,0\rangle &= (-1)^{\sum_{i=1}^{3-1} n_i}\; n_3\,|0,0,0\rangle = |0,0,0\rangle \\ e_3\,|1,0,1\rangle &= (-1)^{\sum_{i=1}^{3-1} n_i}\; n_3\,|1,0,0\rangle = -\,|1,0,0\rangle \\ e_3\,|0,1,1\rangle &= (-1)^{\sum_{i=1}^{3-1} n_i}\; n_3\,|0,1,0\rangle = -\,|0,1,0\rangle\,. \end{aligned} \tag{5.45}$$

From a physical point of view, no electron can be annihilated in an unoccupied state. Consequently, we neglect the first row and subsequently apply $e_2^\dagger$ only to the last two rows in Eq. (5.45), which gives

$$\begin{aligned} e_2^\dagger\,(-\,|1,0,0\rangle) &= -(-1)^{\sum_{i=1}^{2-1} n_i}\;(1-n_2)\,|1,1,0\rangle = |1,1,0\rangle = |b_1\rangle \\ e_2^\dagger\,(-\,|0,1,0\rangle) &= -(-1)^{\sum_{i=1}^{2-1} n_i}\;(1-n_2)\,|0,1,0\rangle = |0,0,0\rangle\,. \end{aligned} \tag{5.46}$$

Since no electron can be created in an already occupied state due to the Pauli principle, we are left with the first row in Eq. (5.46). Summarizing the application of the operator $e_2^\dagger e_3$ to Eq. (5.44), one obtains

$$e_2^\dagger e_3\,|b_2\rangle = e_2^\dagger e_3\,|1,0,1\rangle = |1,1,0\rangle = |b_1\rangle\,. \tag{5.47}$$

The corresponding matrix representation that transforms basis state $|b_2\rangle$ into basis state $|b_1\rangle$ is given by

$$e_2^\dagger e_3 = \begin{bmatrix} 0 & 1 & 0 \\ 0 & 0 & 0 \\ 0 & 0 & 0 \end{bmatrix}. \tag{5.48}$$

Following the example above, matrix representations for any block of one creation and annihilation operator $e_A^\dagger e_B$ with $A, B \in \{1, 2, 3\}$ can be deployed for the subspace $n_e = 2$. Moreover, in the same manner matrix representations can be obtained for arbitrary

subspaces. Analogous to Eq. (5.43), we can formulate the Coulomb interaction between two holes by

$$\frac{1}{2}\sum_{ijkl} V_{ijkl} h_i^\dagger h_k^\dagger h_j h_l = -\frac{1}{2}\sum_{ijkl} V_{ijkl} h_i^\dagger h_j h_k^\dagger h_l + \frac{1}{2}\sum_{ijl} V_{ijjl} h_i^\dagger h_l \tag{5.49}$$

and determine the matrix representations of $h_A^\dagger h_B$ with $A, B \in \{i, j, k, l\}$ of the hole states. Following the method above, the Hamiltonian $H_{\text{Coul}}$ can be obtained simply from matrix multiplication of pairs of creation and annihilation operators in an intuitive and robust way. However, for systems with large numbers of configurations, matrix multiplications become numerically increasingly demanding and the Hamiltonian should be established in a different manner, such as presented in Ref. [139]. Once the CI matrix has been deployed and diagonalized, the eigenvalues and eigenfunctions of the interacting problem are obtained. These $N$-exciton states $\{|\phi_i^{N_x}\rangle\}$ can be expressed as an expansion in terms of the uncorrelated single-particle basis states $\{|\varphi_j^n\rangle\}$ by

$$|\phi_i^{N_x}\rangle = \left(\sum_j |\varphi_j^n\rangle \langle\varphi_j^n|\right) |\phi_i^{N_x}\rangle = \sum_j |\varphi_j^n\rangle \underbrace{\langle\varphi_j^n|\phi_i^{N_x}\rangle}_{c_{ij}} = \sum_j c_{ij} |\varphi_j^n\rangle , \tag{5.50}$$

where the coefficients $c_{ij}$ are obtained from diagonalization of the CI matrix.

### Fermi's Golden Rule

The optical spectra can be obtained by calculating the intensity of photoluminescence from the recombination of one electron-hole pair in an $N$-exciton state using Fermi's golden rule [141]

$$I(\omega) = \frac{2\pi}{\hbar}\sum_f |\langle\phi_f^{N-1}|P^-|\phi_i^N\rangle|^2 \delta(E_i - E_f - \hbar\omega), \tag{5.51}$$

where $|\phi_i^N\rangle$ is the initial state of the $N$-exciton system. Correspondingly, $|\phi_f^{N-1}\rangle$ denotes the final state with $N-1$ excitons after emitting a photon. The matrix elements

$$\langle\phi_f^{N-1}|P^-|\phi_i^N\rangle = \sum_{\alpha,\beta} \langle\phi_f^{N-1}|\varphi_\alpha^{n-1}\rangle \langle\varphi_\alpha^{n-1}|P^-|\varphi_\beta^n\rangle \langle\varphi_\beta^n|\phi_i^n\rangle , \tag{5.52}$$

from Eq. (5.51) can be expressed in terms of the single-particle wave functions, where

$$\langle\varphi_\alpha^{n-1}|P^-|\varphi_\beta^n\rangle = \sum_{kl} D_{kl} \langle\varphi_\alpha^{n-1}|e_k h_l|\varphi_\beta^n\rangle , \tag{5.53}$$

describes all possible electron-hole recombination channels. The oscillator strength of the optical transition is determined by the square of the dipole matrix elements $D_{kl}$.

# 6. Quaternary 1.55 $\mu$m Telecom Quantum Dots

This chapter is based on the results of a collaboration with the groups of Prof. Reithmaier in Kassel and Prof. Rosenauer in Bremen. Parts of the presented results have been published in Ref. [93]. One of the current challenges in the realization of quantum light sources is the systematic extension of the emission energies into the low-loss telecom bands [142]. For the O-band at 1.3 $\mu$m, this has been accomplished with InAs/InGaAs quantum dots by including a strain-reducing layer [143, 144, 145] or by dot-in-a-well structures [146, 147]. For the emission at the C-band at 1.55 $\mu$m, different approaches have been successfully applied to grow InAs quantum dots on InP substrates, such as the double-cap method [38], the insertion of ultrathin GaAs layers [39] or droplet epitaxy [40]. On top of that, a new material system consisting of low density InAs/InAlGaAs/InP quantum dots (QDs) [148, 149] has been suggested. Our goal is to characterize this material system and to identify dominant contributions to the connection between morphology, composition, electronic and optical properties. In the following analysis, we employ a combination of theoretical and experimental methods, starting with a structural characterization of individual QDs using quantitative high-resolution scanning transmission electron microscopy (qHRSTEM) [150, 151]. The results are used as input for our atomistic tight-binding (TB) model in order to investigate the influences of size and alloy concentration on the emission wavelength.

## 6.1. Experimental Analysis

The following section regarding the experimental analysis summarizes results [93] of the groups of Prof. Reithmaier in Kassel and Prof. Rosenauer in Bremen. To clarify the experimental contribution, the persons in charge are mentioned in the respective parts.

### 6.1.1. Sample Growth and Optical Characterization

The growth and optical characterization of the QDs has been performed by M. Yacob and in in a leading role by M. Benyoucef from the group of Prof. Reithmaier in Kassel. The sample was grown on a (100) InP substrate using molecular beam epitaxy (MBE). A 228 nm thick $Al_{0.24}Ga_{0.23}In_{0.53}As$ layer, which is lattice-matched to InP, was deposited at 514 °C on top of a 246 nm InP substrate. For the QDs nominally 2 monolayers of InAs were deposited at the same temperature. Afterwards, the substrate temperature was reduced to 413 °C using arsenic overpressure, which leads to the formation of large and sparse InAs QDs as shown in the inset of Fig. 6.1. The sample was capped by 228 nm InAlGaAs. For additional details, see Refs. [148, 149]. Low-temperature (10 $K$) macro-PL measurements (see Fig. 6.1) were performed and show that the emission of the QDs is centered around the telecom C-band wavelength of 1.55 $\mu$m ($\hat{=}$ 0.8 eV).

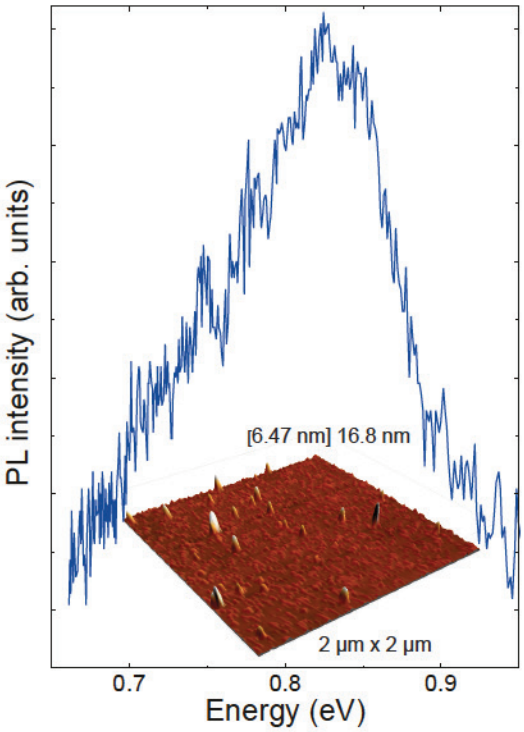


**Figure 6.1. | Low temperature macro-PL spectrum.** Inset: 3D atomic force microscopy image (2 x 2 $\mu m^2$) of an uncapped QD structure showing a minimum (6.47 nm) and a maximum (16.8 nm) height of the QDs (Fig. from M. Benyoucef [93], copyright by the American Physical Society).

### 6.1.2. Structural Analysis

The structural characterization of the QDs has been performed by T. Grieb, K. Müller-Caspary, and in a leading role by M. Schowalter from the group of Prof. Rosenauer in

Bremen. TEM specimens were prepared by using FEI Nova focused ion beam (FIB) and investigated by utilizing a FEI Titan 80/300 ST equipped with a high angle annular dark field (HAADF) detector at 300 kV. In and Al concentrations were measured by utilizing qHRSTEM involving normalization to the incident beam intensity and comparison with simulations as described in Refs. [150, 151, 152]. Here, a Debye-Waller factor[11] from Ref. [153] was used and the static atomic displacements were taken into account according to [154]. From the so obtained HRSTEM images, the In and Al concentrations were quantified following Ref. [151] and using a reference data set for a known local specimen thickness as described in Refs. [155, 156]. Using energy dispersive x-ray spectroscopy (EDX), concentrations of 0.22 Al, 0.25 Ga, and 0.53 In with an error of about $\pm$ 0.02 were found confirming the nominal values of 0.24, 0.23 and 0.53 within the error margins of the measurement.

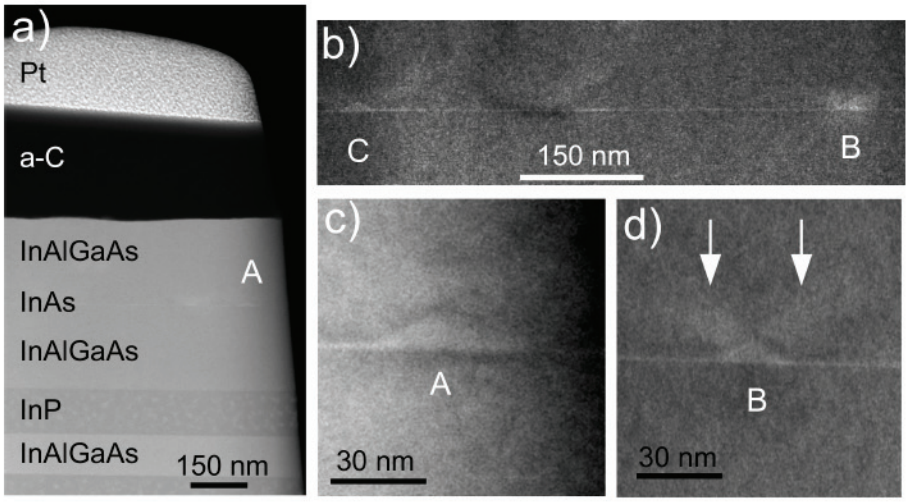


**Figure 6.2. | TEM image**. a) Overview image of the TEM specimen. b) Image of the active region including QDs B and C. The wetting layer between the QDs exhibits fluctuations of the In concentration. c) and d) Images of QDs A and B, showing a pyramidal contrast of the QDs. For QD B stripes (indicated by the arrows) with slightly increased intensity can be observed (Fig. from M. Schowalter [93], copyright by the American Physical Society).

Figure 6.2a) displays a HAADF-STEM image by M. Schowalter from Ref. [93]. Here, the InAs layer, which is embedded in an InAlGaAs matrix, can be identified. Slight fluctuations of the HAADF-intensity indicate the presence of QDs (A and B). An overview image of the area in the vicinity of QDs B and C is depicted in Fig. 6.2b). The wetting-layer in between the two QDs exhibits fluctuations in both intensity and thickness. Figs. 6.2c) and d) display QDs A and B. All identified QDs (A,B and C) exhibit a sharp triangular shape, when viewed in [110] zone axis orientation, indicating a pyramidal shape. A side facet angle around 25° towards the basal plane of the QD was measured, indicating the side facets of the pyramid to be $(1\bar{1}3)$ planes. The type of surface of the QD is in accordance with the measured heights and widths of the QDs at their base. For QD A, a width of

[11] It is used to describe the attenuation of scattering caused by thermal motion.

55 nm and a height of 12.5 nm was determined. Especially for QD B in Fig. 6.2d), regions with an increased intensity (indicated by arrows) evolve into the direction of the side facet normal, hinting on a diffusion of In out of the QD towards the InAlGaAs cap layer. The height of the QD was slightly smaller than the mean height from AFM measurements. However, as the bright stripes above the QDs suggest diffusion from the QDs into the cap layer, a shrinkage of QDs during cap layer overgrowth can be expected. The two other identified QDs appeared to be smaller, so that a focus was placed on the largest QD, for which the height was closest to the mean height from AFM results.

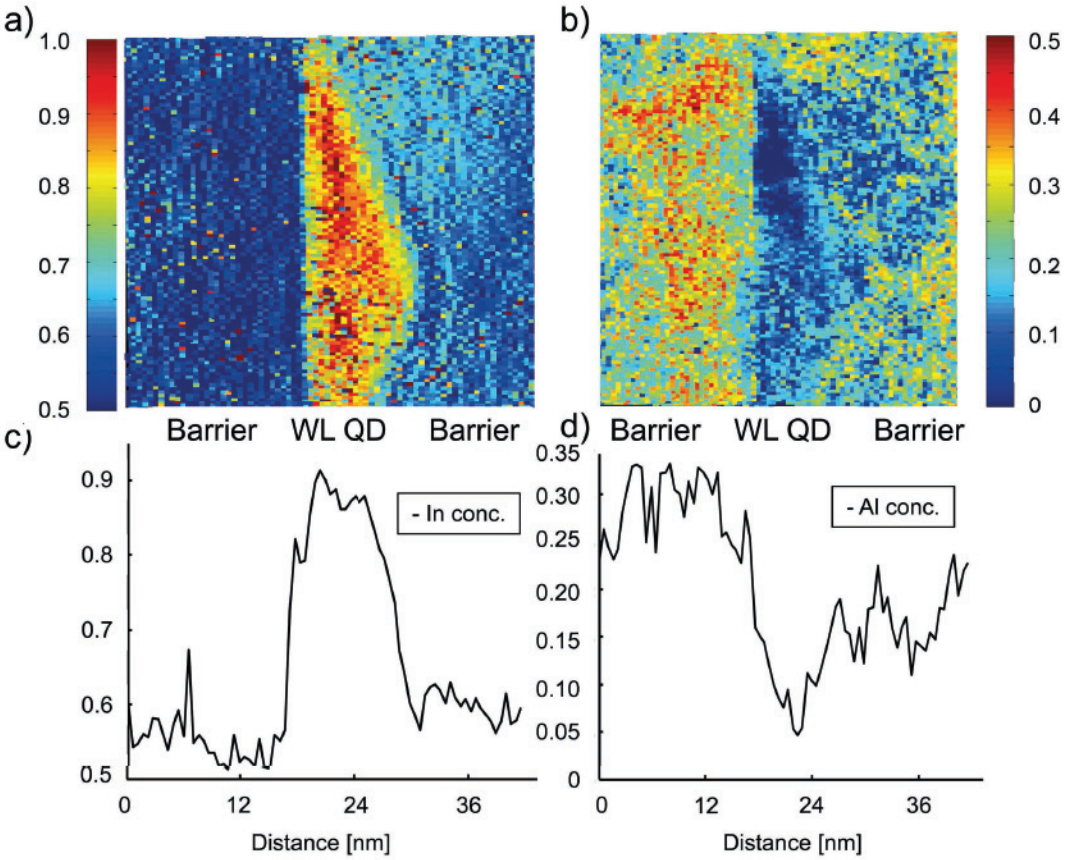


**Figure 6.3. | Concentration profiles**. a) In and b) Al concentration maps from a scan across the TEM lamella in the vicinity of QD A. The given In and Al concentrations represent averages in transmission direction through the TEM specimen. Results of horizontal line scans through the center of the QD in panels a) and b) are displayed as c) and d) (Fig. from M. Schowalter [93], copyright by the American Physical Society).

Figs. 6.3a) and b) represent the In and Al concentration maps, which were obtained in the vicinity of QD A. As an overall trend, the In concentration within the QD and wetting-layer region increases, while the Al concentration is reduced significantly. For the wetting-layer, In and Al concentrations of 0.70 $\pm$ 0.05 and 0.15 $\pm$ 0.05 were determined, respectively. Horizontal line scans from the data in Figs. 6.3a) and b) through the largest extension of the QD are provided in Figs. 6.3c) and d). An approximately constant In concentration within the QD area and an increasing Al concentration from the wetting-

layer towards the top of the QD are obtained. The results in Fig. 6.3 are averaged in transmission direction through the TEM lamella, which contains the wetting layer perpendicular to the specimen surface as well as the side view of the QD surrounded by matrix material. Hence, in the transmission averages, the full wetting-layer contribution is obtained, while the QD contribution decreases from the base to the top at the expense of matrix material contributions. In order to obtain the true In and Al concentrations within the QD, projections through a three-dimensional model QD need to be compared with the observed transmission scans. The results of the correspondingly deduced QD model are summarized in Fig. 6.4.

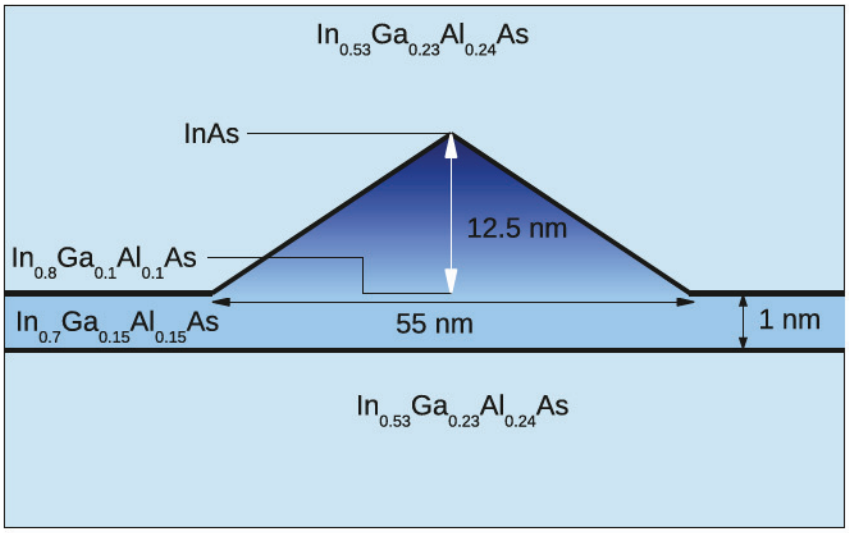


**Figure 6.4. | Quantum dot model**. Geometry as obtained from HRSTEM analysis. The pyramidal QD is situated on top of the wetting layer and shows a linearly increasing In-concentration from bottom (lighter blue) to top (darker blue), whereas the Ga and Al content decreases accordingly. The wetting layer has a height of 1 nm and a slightly smaller In-content than the bottom of the QD. The QD-wetting layer system is embedded in a quaternary barrier material with an even smaller In-concentration (light blue, Fig. from Ref. [93], copyright by the American Physical Society).

## 6.2. Theoretical Results

For electronic state calculations of semiconductor QDs, both continuum models [157, 70, 71] and atomistic TB [117, 158, 159, 160] have been successfully used. Since our experimental investigations involve a HRSTEM characterization of geometry and alloy concentration of individual QDs with atomic resolution, we use an atomistic TB approach. The geometry and spatial distribution of alloy concentrations obtained from TEM results is summarized in Fig. 6.4. We model the QD by placing individual In, Ga, Al and As atoms on a zinc blende lattice in a way that the geometry displayed in Figs. 6.2 c and d as well as the experimentally determined concentration maps in Fig. 6.3 are reproduced. As mentioned before, in our calculations, we use different box sizes (see Fig. 6.5) for the strain-field

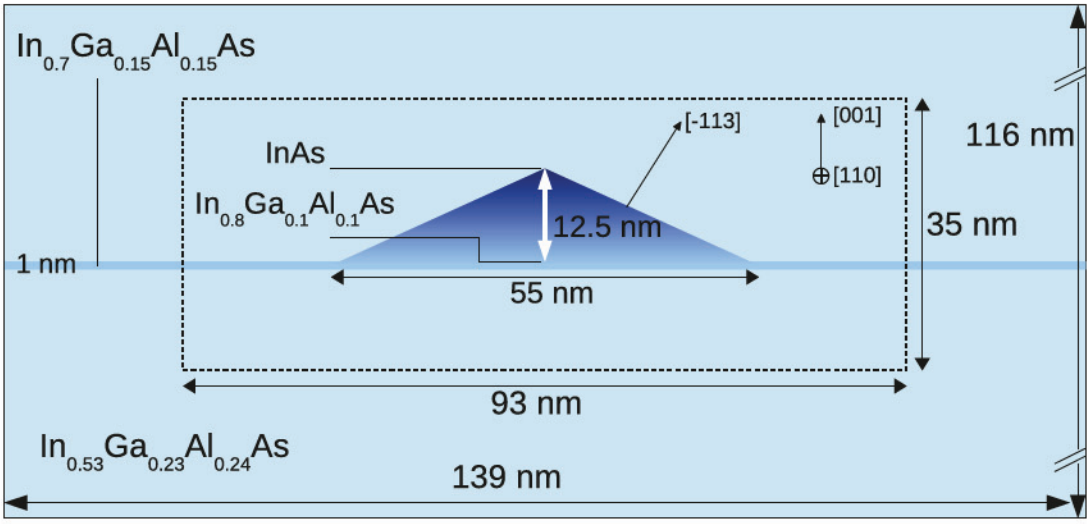


**Figure 6.5.** | **Supercell sizes**. Larger box: for valence-force field calculation. Smaller box: for the TB diagonalization (Fig. from Ref. [93], copyright by the American Physical Society).

calculation and the tight-binding diagonalization. For the former, a larger box size is required to ensure that the strain field has sufficiently fallen off towards the edges. In our case, we use a box of size 139 nm × 139 nm × 116 nm, resulting in a total number of 92 million atoms. For the subsequent TB diagonalization, it is possible to reduce the size of the box since we are interested only in confined states inside the quantum dot. The size of the supercell for the TB diagonalization is determined in a way, that the lowest eigenvalue does not change more than 1 meV when increasing the size by 10 nm along all directions or by 20 nm along one direction. In the present calculations, we utilize a box of size 93 nm × 93 nm × 35 nm, resulting in a total number of 12 million atoms.

To determine the local displacements of the individual atoms due to strain effects, we employ a valence force field calculation using the LAMMPS code [113]. The calculation is performed until a force tolerance of $10^{-3}$ eV/Å or a relative energy tolerance of $10^{-16}$ is reached. Utilizing the atomic displacements and following Ref. [123], the strain components can be determined (see Fig. 6.6). For $\varepsilon_{xx}$ (left column), compressive strain arises inside the QD and tensile strain propagates into the barrier, whereas for $\varepsilon_{zz}$ (right column), the opposite situation is observed. The fluctuations in Fig. 6.6 a) and b) stem from the different lattice constants of the individual atoms in the quaternary barrier. This causes a finite strain with respect to the average lattice constant $a_{\mathrm{InP}}$ for any distance between two neighboring atoms in the barrier. The absolute magnitude of strain in the quaternary barrier is about half as large as in the binary material system. This is caused by the differences of the lattice constants in the quaternary barrier compared to the binary situation: $|a_{\mathrm{InAs}} - a_{\mathrm{InP}}| \approx 1/2 |a_{\mathrm{InAs}} - a_{\mathrm{GaAs}}|$.

The strain-induced equilibrium positions are incorporated into the TB Hamiltonian, following a generalized Harrison rule as discussed above. Diagonalization of the corre-

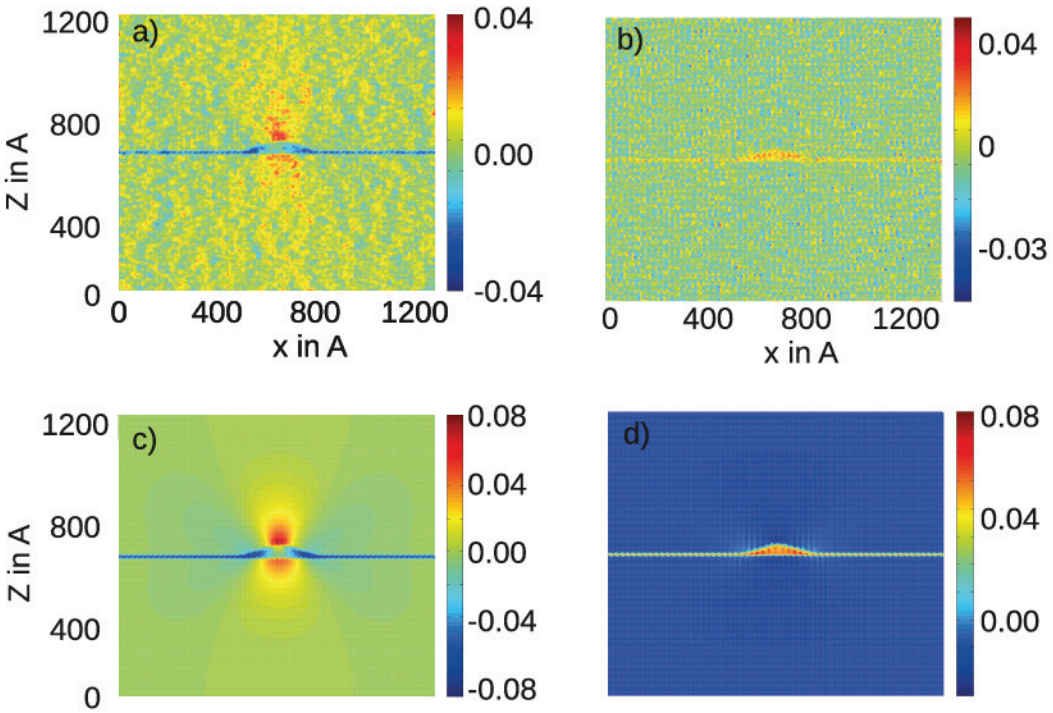


**Figure 6.6.** | **Strain field**. a) and b) Calculated strain components $\varepsilon_{xx}$ and $\varepsilon_{zz}$ along a cross section through the center of the investigated quaternary QD of Fig. 6.4. c) and d) Strain components $\varepsilon_{xx}$ and $\varepsilon_{zz}$ for a binary InAs/GaAs QD of the same size and shape shown for comparison (Fig. from Ref. [93], copyright by the American Physical Society).

sponding matrix provides the confined eigenenergies and eigenstates of electrons and holes inside the QD. The energy level scheme of the QD is displayed in Fig. 6.7, in which 6 states for both electrons and holes are marked. Due to the two possible spin-configurations, each state is two times Kramer's degenerate. In the following discussion, we only consider one of the degenerate states. It can be seen that the probability densities of the lowest bound electron ($e_1$) and hole ($h_1$) state exhibit an s-like shape with one maximum in the center that falls off radially-symmetric. The name originates from the analogy to the hydrogen atom, where the eigenstates are classified with respect to the angular momentum. Additionally, there are two p-like states of bound electrons ($e_3, e_5$) and holes ($h_3, h_5$). In an idealized situation of spherical symmetry, the two states are each degenerate. However, the degeneracy is slightly lifted by the underlying crystal lattice. As a result, we obtain two probability densities, which are rotated by 90° with respect to each other and exhibit two maxima. Due to the large size of the QDs, there are of course more than 12 bound states, however these higher states are not discussed here. The difference between the lowest electron ($e_1$) and highest hole state ($h_1$) defines the single-particle (or quasiparticle) band gap (see Fig. 6.7, GS). This energy is lowered by the exciton binding energy originating from electron-hole Coulomb interaction. For the representative QD structure (see Fig. 6.4) we have performed a configuration interaction calculation [160] with 50 states for both electrons and holes and obtained exciton binding energies of about 30 meV. This number is

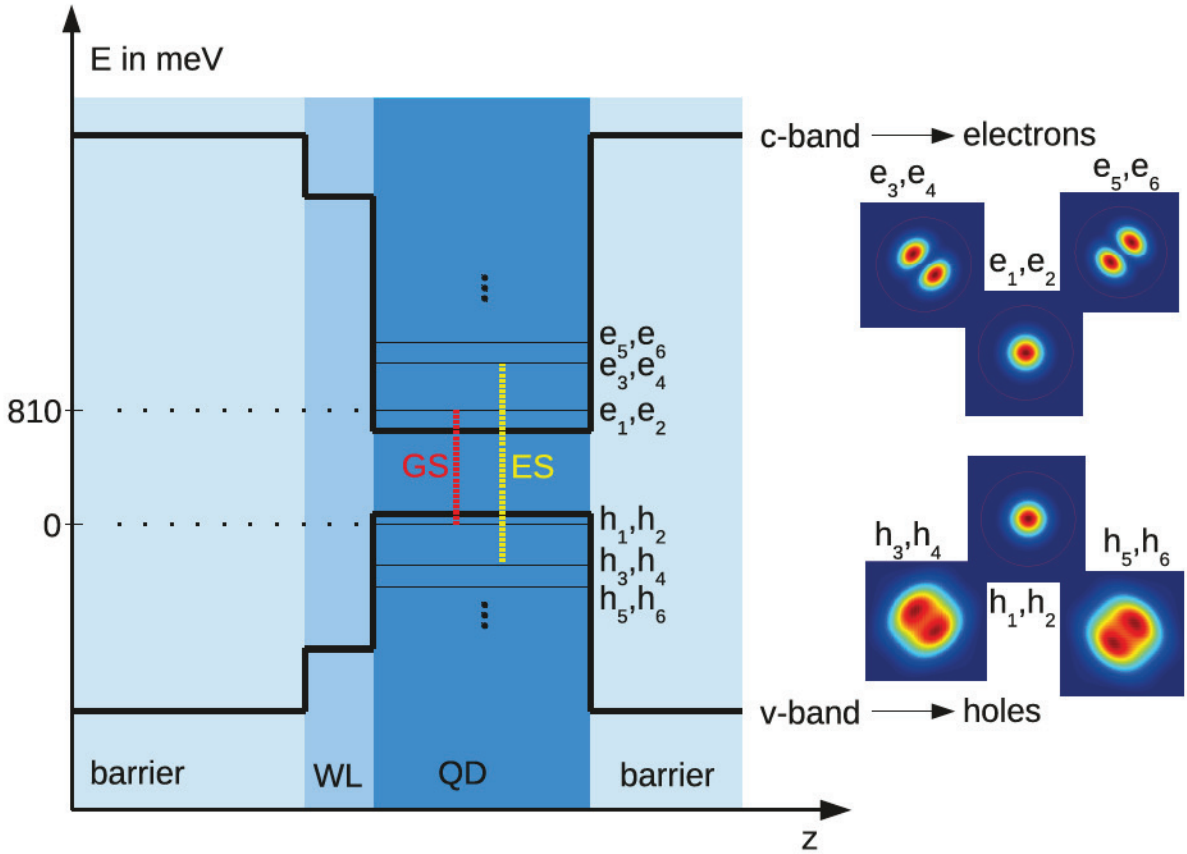


**Figure 6.7.** | **Electronic properties**. Left: Energy level scheme along the z-direction. The ground state (GS) transition (dashed red line), here 810 meV, as well as one excited state transition (dashed yellow line) are marked. Right: Probability densities of electrons (top) and holes (bottom).

small compared to the overall energy scale (see Fig. 6.1) and almost constant for different QDs. Consequently, the subsequent discussion will be performed with respect to the single-particle/quasiparticle band gap $E_G$.

For the structure in Fig. 6.4, we obtain $E_G = 810$ meV (see Fig. 6.8). This energy is near the maximum of the PL spectrum (see Fig. 6.1), which supports that the corresponding morphology and compostion is typical for the QD ensemble. This geometry is used as a starting point for the subsequent investigations of the influences of size and concentration fluctuations on the single-particle/quasiparticle band gaps of the QDs within the ensemble. For the analysis of size fluctuations, we consider a constant diameter to height ratio for all QDs. According to Fig. 6.8, fluctuations of the QD size within a range of 25 % result in a shift of 30 meV. Size fluctuations corresponding to the difference between QDs A and B result in energy fluctuations of about 60 meV. Even the assumption of yet larger size fluctuations alone cannot explain the observed inhomogeneous broadening in Fig. 6.1. For the analysis of concentration fluctuations, the QD structure of Fig. 6.4 with fixed size is used. In different calculations for individual QDs, we vary the In-concentration at the base of the pyramidal QD. In all cases, the In-concentration increases linearly to

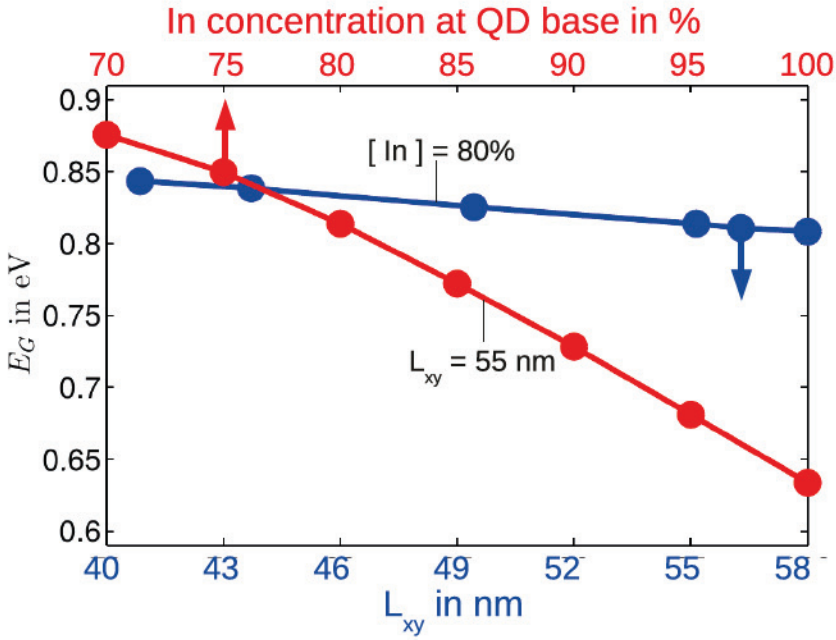


**Figure 6.8. | Change of band gap**. Variation of single-particle/quasiparticle band gap $E_G$ for different QD side lengths of the rectangular basis with a constant diameter-to-height ratio (bottom axis) and for different In-concentrations (top axis) at the base of the pyramid (Fig. from Ref. [93], copyright by the American Physical Society).

100 % at the top, whereas the remaining cation lattice sites are uniformly distributed among Ga and Al. Fig. 6.8 shows that possible fluctuations cover an energy range of over 200 meV. These fluctuations can explain the main contribution to the inhomogeneous broadening of the spectrum in Fig. 6.1. In the limit of a pure InAs quantum dot, we obtain a single-particle/quasiparticle band gap of about $E_G = 630\,\text{meV}$ (see Fig. 6.8). This value corresponds to the low-energy edge of the experimental PL spectrum. The strong influence of concentration fluctuations is a consequence of the fact that the relative conduction band edge positions $E_c = E_g + E_v$ of AlAs ($E_c \sim 2.4\,\text{eV}$), GaAs ($E_c \sim 1.5\,\text{eV}$) and InAs ($E_c \sim 0.4\,\text{eV}$) differ substantially for given valence band alignment in the quaternary material.

## 6.3. Local Indium Accumulations

From the experimentally measured concentration profiles (see Fig. 6.3), it can be inferred that local accumulations of indium atoms occur. Therefore, we additionally present a model to describe such clustering effects. Experimentally, indium accumulations are formed during the growth process and can be caused by temperature-dependent transport phenomena. Since the probability of configurations can be described by a Boltzmann factor $e^{-E/k_BT}$, we develop an analogous approach for our system. Within our model, the

positions of two cation atoms are interchanged by an energy-dependent probability

$$W_{\text{change}} = e^{-\beta E_{\text{change}}}/Z \tag{6.1}$$

with the partition function

$$Z = e^{-\beta E_{\text{change}}} + e^{-\beta E_{\text{stay}}} \tag{6.2}$$

and $\beta = 1/k_B T$. The term

$$E_{\text{stay}}/E_0 = \sum_{j\in\{\text{NN}(A)\}} E_{xj} + \sum_{k\in\{\text{NN}(B)\}} E_{yk} \tag{6.3}$$

describes the interaction energy of the cations $x$ and $y$ at lattice sites $A$ and $B$ with their nearest neighbors NN($A$) and NN($B$) with respect to a reference energy $E_0$. Note that for a given cation, the nearest neighbor cation corresponds to a next-nearest neighbor atom within the tetrahedron of the zinc blende structure. Analogous to Eq. (6.3), we define the energy

$$E_{\text{change}}/E_0 = \sum_{j\in\{\text{NN}(A)\}} E_{yj} + \sum_{k\in\{\text{NN}(B)\}} E_{xk} \tag{6.4}$$

for interchanged cations $x$ and $y$ with respect to $E_0$. In particular, we define the interaction energy as

$$E_{xj} = 12 - \sum_{j=1}^{12} \Theta_{xj}, \tag{6.5}$$

where $\Theta_{xj}$ equals one if the cations $x$ and $j$ are of the same type and zero otherwise. For the investigation of clustering, we determine the probability for interchanging lattice-sites $W_{\text{change}}$ according to Eq. (6.1) and compare the value to a random number *rand* in the intervall [0,1]. If $W_{\text{change}} > rand$, we interchange the cation lattice-sites, while keeping all anions fixed. In our analysis, we have assumed a linear weight of neighboring cations of the same type with respect to the total number of neighboring cations (see Eq. (6.5)) as well as $\beta = E_0$. The parameter $\beta$ can be varied to increase/decrease clustering. We opted to additionally include a gradient in $x$- and $y$-direction, so that an increased number of Ga-atoms is located in the middle and Al-atoms at the edges. Following the procedure above, we obtain the structure as shown in Fig. 6.9. We visualize only Ga- and Al-atoms and no In-atoms, since the QD consists of almost pure InAs. The In-gradient towards the top of the QD is reflected in the fact that fewer Ga- and Al-atoms occur at the top, so that the top of the pyramid appears to be almost flat (see Fig. 6.9(b-c)). Due to the gradient in $x$- and $y$-direction, we obtain an increased number of Ga-atoms in the middle and Al-atoms at the edges (see Fig. 6.9(a)). Compared to the structure in Fig. 6.4, we obtain a change in the the single-particle band gap of 50 meV. Since this change in the band gap was smaller than expected, we did not follow this analysis of clustering any

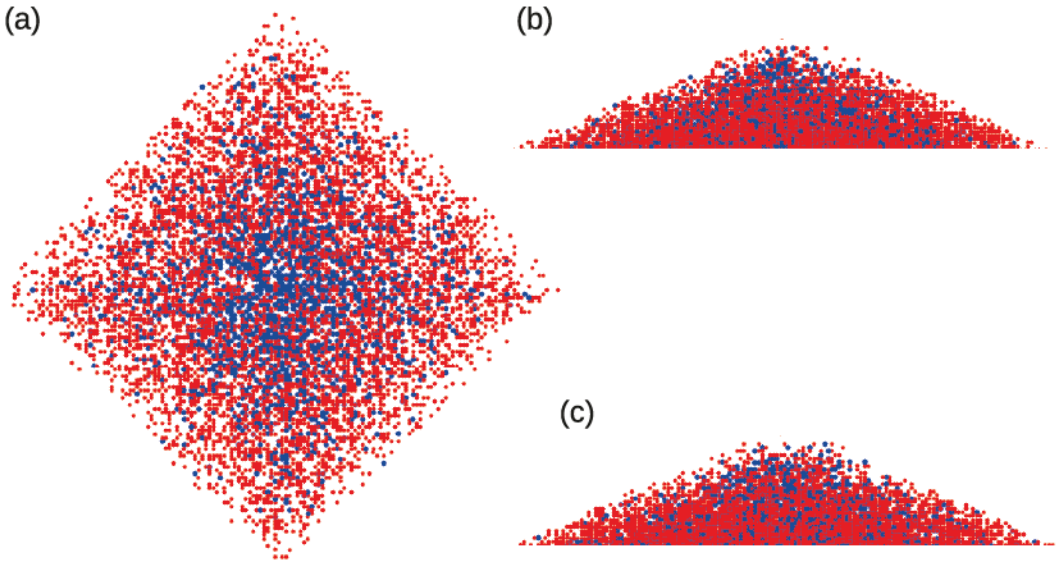


**Figure 6.9.** | **Atom distribution**. (a) Top view, (b) $y-z$ side view, (c) $x-z$ side view of the supercell with Ga-atoms (blue) and Al-atoms (red). In-atoms are not shown since they are dominantly present inside the quantum dot (see Fig. 6.4).

further. However, this could be subject of further systematic investigations.

# 7. Ternary 1.55 $\mu$m Telecom Quantum Dots

This chapter describes the results of a collaboration with the group of Prof. Michler in Stuttgart and Prof. Rosenauer in Bremen. Parts of the presented results have been submitted for publication at [161]. As discussed in the previous chapter, emission in the spectral range of the telecom C-band is desirable for data communication applications on the single photon level [162]. Such light sources were often generated utilizing InP substrates [163, 148]. Alternatively, many requirements for quantum technologies have been met with QDs based on the GaAs material system [164, 165, 166, 167]. The potential of this material system is further underscored by the integration of distributed bragg reflectors (DBRs, see Ref. [168]), which are useful for the fabrication of high-quality photonic cavities.

Within this chapter, we analyze the structural and optical properties of InAs/(In)GaAs/GaAs QDs, which are emitting in the telecom C-band by using a combination of photoluminescence (PL) spectroscopy, atomic force microscopy (AFM), transmission electron microscopy (TEM), atomistic tight-binding (TB), and configuration interaction (CI). In an initial analysis, we explain the mechanism behind the telecom C-band emission. In order to generate a single-photon from a QD, electrons and holes are excited in the barrier material and subsequently captured into the QD states. During this process, not only the exciton but also further charge carrier complexes are formed. We provide a detailed analysis of these multi-exciton states and the corresponding emission lines, which can be used in various quantum-information schemes. In addition to the emission in the C-band, one of the most sought-after goals is the operation of single-photon sources at elevated temperatures. The temperature-dependent behaviour of the QD ensemble and individual QDs is studied and explained with the help of an Arrhenius-type analysis and CI calculations.

# 7.1. Experimental Analysis

The following section regarding the experimental analysis summarizes results [161] of the groups of Prof. Michler in Stuttgart and Prof. Rosenauer in Bremen. To clarify the experimental contribution, the persons in charge are mentioned in the respective parts.

## 7.1.1. Sample Growth and Optical Characterization

The growth and optical characterization of the QDs has been performed by F. Olbrich , S. Schreier, C. Nawrath, M. Paul, J. Höschele, J. Kettler, S.L. Portalupi, M. Jetter from the group of Prof. Michler in Stuttgart. Within this collaboration, F. Olbrich was the person in charge and is therefore named as a reference for the following experimental measurements and results. An outline of the sample can be seen in Fig. 7.1a). It was

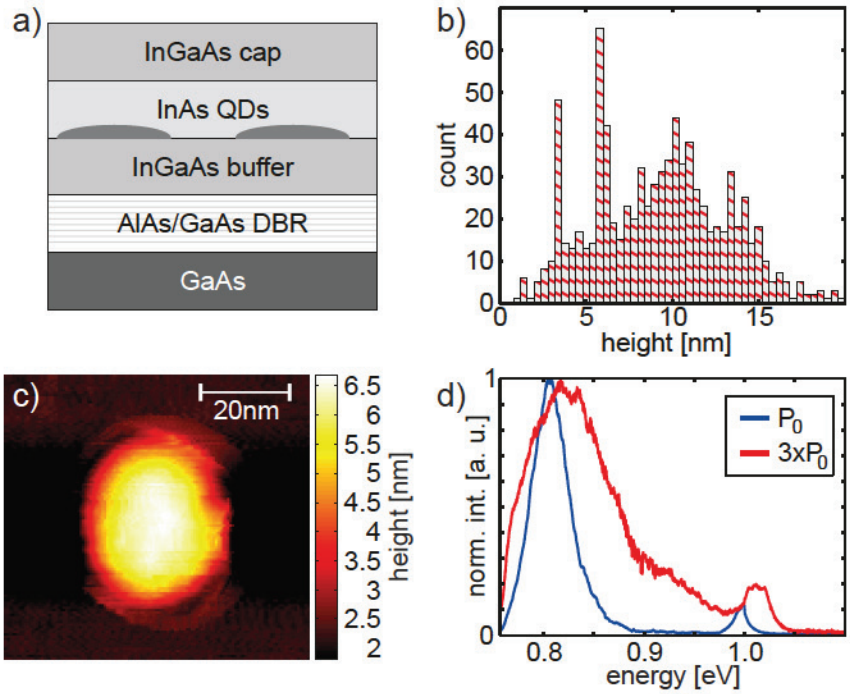


**Figure 7.1. | Sample properties.** a) Schematic drawing of the sample buildup. b) Quantum dot height distribution of a nominally equal, uncapped sample determined by AFM measurements. c) AFM image of a single quantum dot. d) Normalized Ensemble-PL spectra for two different excitation powers $P_0$(red) and $3P_0$(blue) (Fig. from F. Olbrich [161], copyright by the American Physical Society).

fabricated by using metal organic chemical vapor phase epitaxy (MOVPE) in a horizontal flow reactor. An InGaAs metamorphic buffer layer (MMB) of 1000 nm, composed of a linearly increasing indium flux from the substrate to the top of the layer, was deposited on an AlAs/GaAs DBR, which was grown on an (100) oriented GaAs substrate at 710°C. Subsequently, InAs quantum dots were grown on top of the MMB and capped by a

100 nm thick InGaAs layer. Both the cap layer and the quantum dots were deposited at 530 °C. More details on the sample can be found in Ref. [41]. Fig. 7.1b) by F. Olbrich from Ref. [161] shows the QD heights, which were measured before dot overgrowth. A corresponding exemplary measurement is displayed in Fig. 7.1c). Diverse QD sizes are found, whereas most QDs appear at heights of about 10 nm. The overgrowth with a capping layer, which is necessary to complete the dot confinement and suppress surface recombinations or defects, leads to a further material accumulation of the dots fed mainly by the wetting layer, i.e. causing an effective QD size enlargement for the capped sample. The PL emission resulting from this QD ensemble is depicted in Fig. 7.1d). For low excitation powers, high yield telecom C-band emission is observed from the QDs, which motivates our study to further understand these new structures. For higher excitation powers, an intensity increase of the high energy tail of the QD emission can be witnessed. This is caused by the increasing saturation of the ground states of large QDs with deep confinement potential. The remaining, excess charge carriers are subsequently distributed to both smaller QDs with lower confinement potential and higher QD shells. This results in an increased emission proportion at higher energies. The occurrence of both effects is supported by the findings reported in the following.

### 7.1.2. Structural Analysis

The structural characterization of the QDs has been performed by B. Gerken and in a leading role by T. Mehrtens from the group of Prof. Rosenauer in Bremen. A high-resolution TEM analysis of the samples was used to obtain the width, height and shape as well as the chemical composition of the quantum dots after overgrowth. A thin TEM-lamella was prepared by focused ion beam processing using a FEI Nova dual beam system. Subsequently, the sample was treated by low energy ion milling to minimize the impact of amorphous surface layers [169]. Scanning transmission electron microscopy (STEM) images were obtained, using a FEI Titan 80/300 microscope at an acceleration voltage of 300 kV. The electron beam was aligned parallel to the [110]-direction of the sample. Two types of quantum dots (QD1 and QD2) were found in the electron transparent region of the lamella. The corresponding images are shown in Fig. 7.3, in which a lens-shaped cross-section of the QDs can be identified. For QD1, a lateral width of 70 nm and a height of 14 nm was measured, while for QD2 a width of 58 nm and a height of 6.5 nm was found. To determine the In distribution within the QDs, energy dispersive X-ray spectroscopy (EDX) linescans were performed, as illustrated in Fig. 7.2. Here, the electron beam was scanned along the center of the quantum dot parallel to the growth direction. For each scan point, an EDX spectrum has been acquired with an integration time of 60 seconds. The deduced concentration profile of QD1 is shown in Fig. 7.3c). In the InGaAs buffer

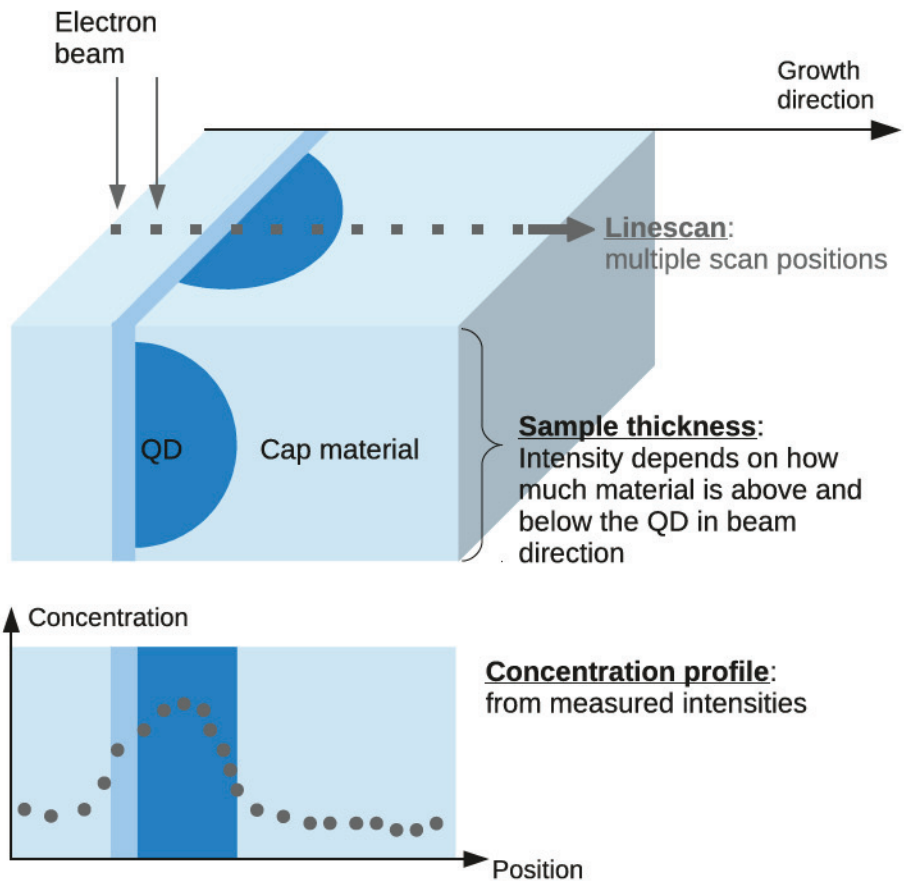


**Figure 7.2. | Illustration of a linescan**. The electron beam is scanned at different points along a line through the QD. A concentration profile can be deduced from the measured intensities.

layer, a maximal In content of $x = 0.25$ was found. Within the QD, the In concentration increases to a maximum of $x = 0.7$ in the center of the QD and then decreases to $x = 0.2$ in the InGaAs cap layer. For QD2, the concentration is shown in Fig. 7.3d). The In composition in the buffer and cap layer is the same as for QD1, while the In concentration in the QD is significantly smaller. Here, a maximum value of $x = 0.45$ was measured. The gradual decrease of the indium content towards the top of the quantum dots in both profiles is most likely due to the decreasing projected thickness of the quantum dots in electron beam direction. When a linescan is acquired along the center of the quantum dot parallel to the growth direction, the projected thickness of the QD decreases to its top, while it is averaged over an increasing amount of cap layer material. This means the projected concentration decreases towards the top of the QD. Consequently, even in case of a constant In composition within the QD, in the EDX profile the In composition decreases towards the top of the QD. Taking into account the projection effect and sample thickness, we assume a constant indium concentration and consider the maximum indium content inside the quantum dot in our subsequent theoretical modeling (see Fig. 7.4). Furthermore, we assume the presence of a wetting layer with a thickness of 0.5 nm. Although it was not

possible to resolve the wetting layer in EDX, there is evidence that such a layer exists. In HAADF-STEM images of regions without quantum dots, a thin layer of approximately 0.5 nm is visible at the interface between the InGaAs buffer and the InGaAs cap layer. As this layer appears brighter than the latter two this indicates a higher indium concentration.

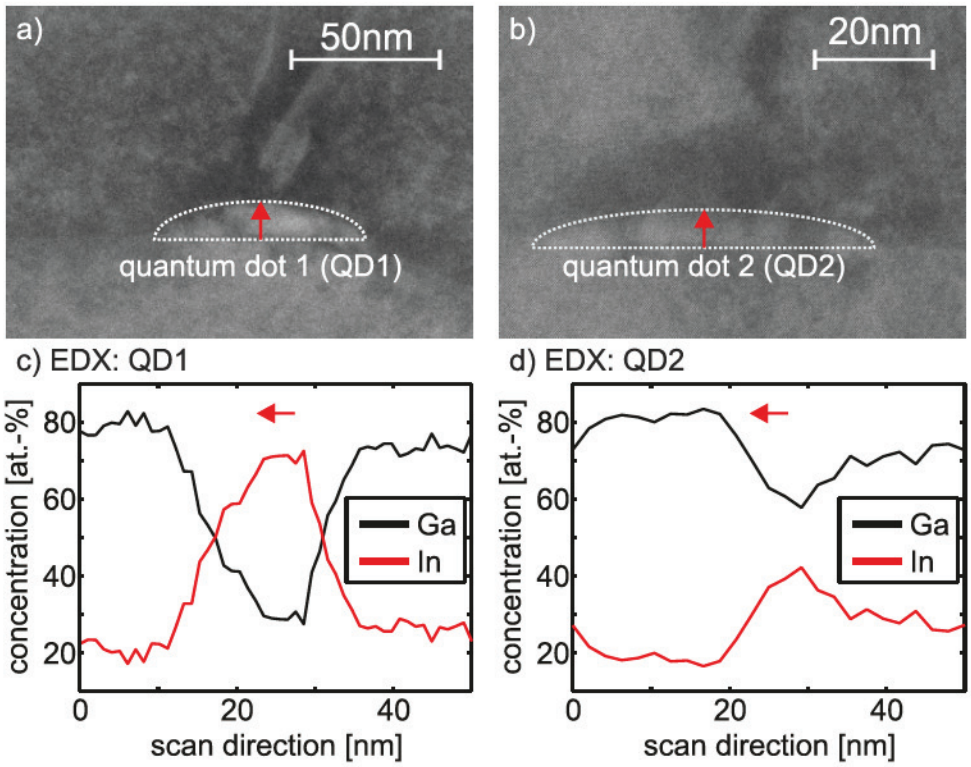


**Figure 7.3. | HAADF-STEM images**. (a) and (b) QD1 and QD2. (c) and (d) Concentration profiles deduced by EDX for QD1 and QD2. The scan direction is indicated by the red arrows (Fig. from T. Mehrtens [161], copyright by the American Physical Society).

## 7.2. Theoretical Results

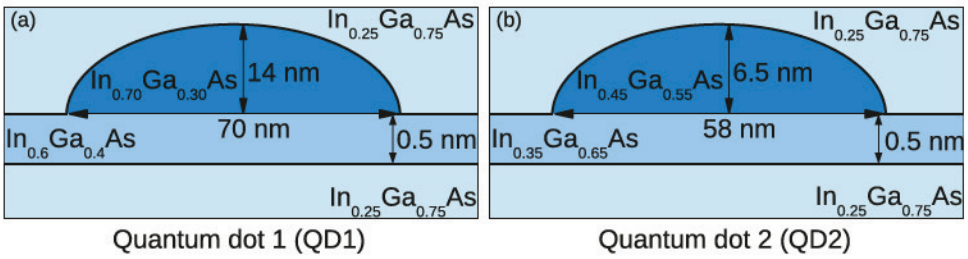


**Figure 7.4. | Quantum dot models**. Lens-shaped QD geometries as obtained from HRSTEM and EDX analysis. (a) QD1 has a diameter of 70 nm, a height of 14 nm and an In-concentration of 70 %. (b) QD2 has a diameter of 58 nm, a height of 6.5 nm and an In-concentration of 45 %. Both QDs are situated on top of a wetting-layer and embedded in $In_{0.25}Ga_{0.75}As$ (Fig. from Ref. [161], copyright by the American Physical Society).

The geometry and spatial distribution of alloy concentrations obtained from TEM results are summarized in Fig. 7.4, which forms the basis for subsequent electronic state calculations. A choice of suitable methods includes both continuum models [157, 70, 71] and atomistic tight-binding (TB) [117, 158, 159, 160]. One set of investigations in this chapter addresses the influence of the quantum dot geometry and composition on the single-particle energies and on the optical band gap. Here, our goal is to clarify the connection between composition, morphology and emission energy. In the framework of the experimental analysis, geometry of individual QDs was obtained via STEM, while the alloy concentration was determined from EDX-linescans. Therefore, we combine this information with an atomistic TB approach to describe individual QDs by rebuilding them within a supercell on a lattice of atomic sites. Specifically, QD1 and QD2 are modeled in separate calculations by placing individual In, Ga and As atoms on a zinc blende lattice in a way that the experimentally determined geometries and concentration maps in Fig. 7.3 are reproduced.

Due to the different lattice constants of the contributing binary compounds, a finite strain field with respect to the average lattice constant for any distance between two neighboring atoms arises. To determine these local displacements of the individual atoms due to strain effects, we employ a valence force field calculation using the Keating potential [108] implemented in the LAMMPS code [113]. The calculated strain field is displayed in Fig. 7.5. For $\varepsilon_{xx}$ (left), compressive strain arises inside the QD and tensile strain propagates into the barrier, whereas for $\varepsilon_{zz}$ (right), the opposite situation is observed. For the calculation of the strain field in Fig. 7.5, we utilize a supercell of size $120\,\mathrm{nm} \times 120\,\mathrm{nm} \times 90\,\mathrm{nm}$. As before, it is determined in a way that the average strain with respect to the lattice constant of the substrate at the edges is zero. This criterion can, however, only be reached approximately since, in atomistic calculations of InGaAs alloys, different distances between indium/arsenic and gallium/arsenic atoms are realized, whereas in the elastic strain theory averaged distances are considered. Therefore, the distance between two neighboring atoms is always strained with respect to the average value.

The strain-induced equilibrium positions are incorporated into the TB Hamiltonian, following a general Harrison rule as discussed above. Diagonalization of the corresponding matrix for individual QD realizations provides the corresponding eigenenergies of the confined electron and hole states. For the TB calculation, it is possible to reduce the size of the box compared to the strain-field calculation, since we are interested only in confined states inside the quantum dot. To this end, we utilize a supercell of size $90\,\mathrm{nm} \times 90\,\mathrm{nm} \times 45\,\mathrm{nm}$. As before, the size is determined in a way, that the lowest eigenvalue does not change more than 1 meV when increasing the size by 10 nm along all directions or by 20 nm along one direction.

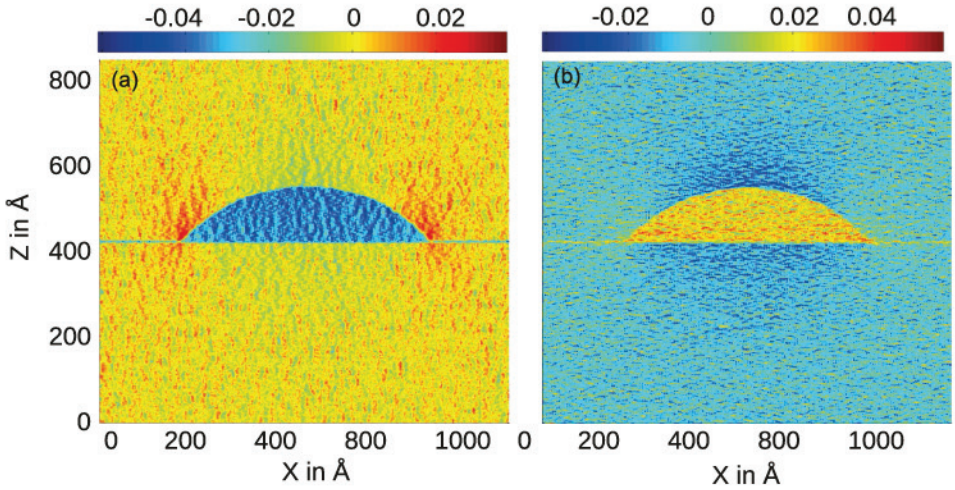


**Figure 7.5. | Strain field**. (a) and (b) Calculated strain components $\varepsilon_{xx}$ (left) and $\varepsilon_{zz}$ (right) along a cross section through the center of QD1 of Fig. 7.4 (Fig. from Ref. [161], copyright by the American Physical Society).

The difference between the lowest electron and highest hole state defines the single-particle (quasiparticle) band gap. This energy is lowered by the exciton binding energy originating from Coulomb interaction between electrons and holes. In the following, our goal is the calculation of the exciton binding energy in QD1. In addition to the knowledge of single-particle states, this requires three additional steps. From the confinement wave functions, Coulomb interaction matrix elements need to be calculated. With the single-particle and Coulomb-Hamilton matrix, configuration interaction calculations need to be performed. Finally, the Coulomb-correlated states and transition energies are obtained. The calculation of Coulomb interaction matrix elements from the single-particle wave functions is extremely demanding for large systems. Moreover, in order to obtain a converged calculation the number of states cannot be truncated in terms of higher shells, since the states differ only by a few milli-electron volts. To reduce the numerical effort, we recalculate the wave functions with a $\mathbf{k} \cdot \mathbf{p}$ model [170]. That computation was performed by Stephan Michael. Since the obtained transition energies (as shown in Fig. 7.6 and Fig. 7.11) deviate by less than 20 meV, we consider this a good approximation, especially since the goals of this investigation are different. The subsequent FCI calculation with 100 electron states and 300 hole states provides an exciton binding energy of $E_X = 10\,\text{meV}$, which is small compared to the overall energy scale of the emission energy. Consequently, the subsequent discussion will be performed with respect to the single-particle band gap $E_G$ as in the previous section.

In the following analysis, we show that the overgrowth of QDs can lead to an accumulation of In resulting in larger dots with higher In concentration, thus resulting in the emission at the C-band. We have identified this effect by comparing experimental data before and after the overgrowth process with theoretical TB calculations. AFM

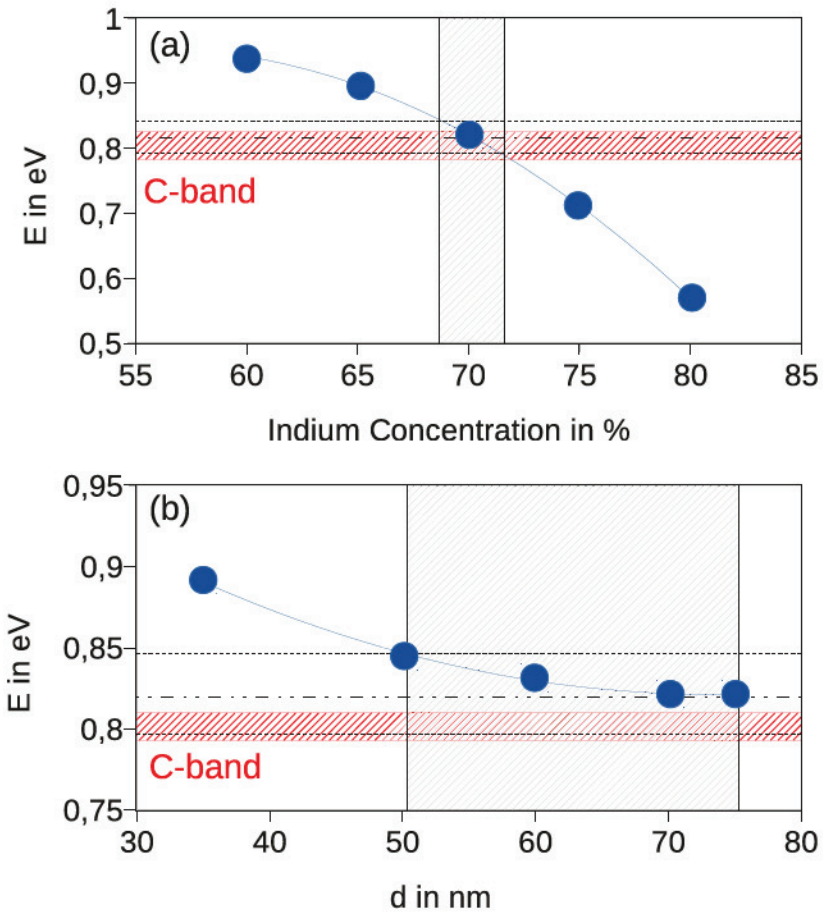


**Figure 7.6. | Change of band gap**. Single-particle emission energies depending on size and concentration fluctuations based on the representative QD1 displayed in Fig. 7.4. (a) Influence of different In-concentrations inside QDs at constant size. (b) Influence of different diameters $d$ of QDs at constant In-concentration and constant ratio of $h/d = 0.2$. The lines between the points are a guide to the eye. The hatched area indicates the concentrations and diameters of interest due to the experimentally observed inhomogeneous broadening. The corresponding energy interval is marked by the dashed horizontal lines. The dashed-dotted horizontal line in between indicates the single-particle emission corresponding to QD1. Note that an energy lowered by the exciton binding energy ($E_X \approx 10\,\text{meV}$) is observed in the experiment, so that the emission of QD1 lies within the range of the C-band (hatched red stripe, Fig. from Ref. [161], copyright by the American Physical Society).

measurements before the overgrowth process reveal similar sizes as obtained from a TEM analysis of QD2 after this process. Consequently, QD2 has not changed noticeably during the overgrowth process. In contrast, the TEM analysis of QD1 reveals a larger size and higher In-concentration. This observation is reflected in TB calculations of QD1 and QD2, from which we obtain single-particle energies of $E_G = 820\,\text{meV}$ and $E_G = 980\,\text{meV}$, respectively. As a result, atomistic TB calculations for the experimentally determined larger size and higher In concentration confirm that these QDs are emitting at the telecom C-band.

In order to describe inhomogeneous broadening effects, we investigate the influences of size and concentration fluctuations on the QD single-particle band gap within the ensemble.

To this end, at each cation lattice site, the atom type In/Ga are placed randomly according to the local target concentrations. Following this procedure, five random realizations with the same local alloy concentration are generated. For each individual realization, we perform the complete calculation consisting of the strain-field simulation and TB diagonalization, leading to a set of single-particle energies. Due to the large In-concentration inside the QD and the large number of atoms, energy fluctuations are rather small and remain within the size of the used data points. The calculated emission energy of QD1 corresponds to the main emission in the PL spectrum (see Fig. 7.1 (d)). Therefore, this geometry is used as a starting point for the investigations of the influences of size and concentration fluctuations. For the analysis of the latter, the structure of QD1 in Fig. 7.4 with fixed size is used. In different calculations of individual QDs, we vary the In-concentration inside the QD between $60 - 80$ %. Here, 60 % of In corresponds to the wetting-layer concentration and is therefore a lower limit, whereas 80 % of In leads to an emission energy which is already 200 meV below the telecom C-band. Fig. 7.6 a) shows that these In concentration fluctuations cover an energy range of about 500 meV. Compared to the quaternary QDs, the impact of the In concentration is even more pronounced. Taking into account the experimentally observed inhomogeneous broadening of about 45 meV at full width at half maximum around the C-band, we conclude that the In concentration should not exhibit fluctuations larger than that of $(70 \pm 2)$ %. A similar analysis is conducted for size fluctuations, in which also the QD structure of Fig. 7.4 a) with fixed concentration and height-to-diameter ratio of $h/d = 0.2$ is used. Regarding the inhomogeneous broadening, we obtain fluctuations of the diameters of about $(63 \pm 12)$ nm (see Fig. 7.6 b)) and respective heights of $(13 \pm 3)$nm as the upper limit necessary to explain the experimentally observed inhomogeneous broadening, provided that only size fluctuations would contribute. The fact that such large size fluctuations are necessary to cover the 45 meV at full width at half maximum is not surprising, given the weak energy dependence on size variations.

## 7.3. Multi-Exciton Spectra

In order to generate a single-photon from a QD, electrons and holes are excited in the barrier material and subsequently captured into the QD states. During this process, not only the exciton but also further charge carrier complexes are formed. For a detailed analysis of the QD emission properties, the multi-exciton emission spectra including charged complexes were investigated theoretically and experimentally. Experiments were performed by F. Olbrich et al. from the group of Prof. Michler in Stuttgart. Figure 7.7a) displays the $\mu$-PL spectrum of a selected QD as well as power- and polarization series (see Fig. 7.7b) and c), respectively) and cross-correlation measurements (see Fig. 7.7e-h)).

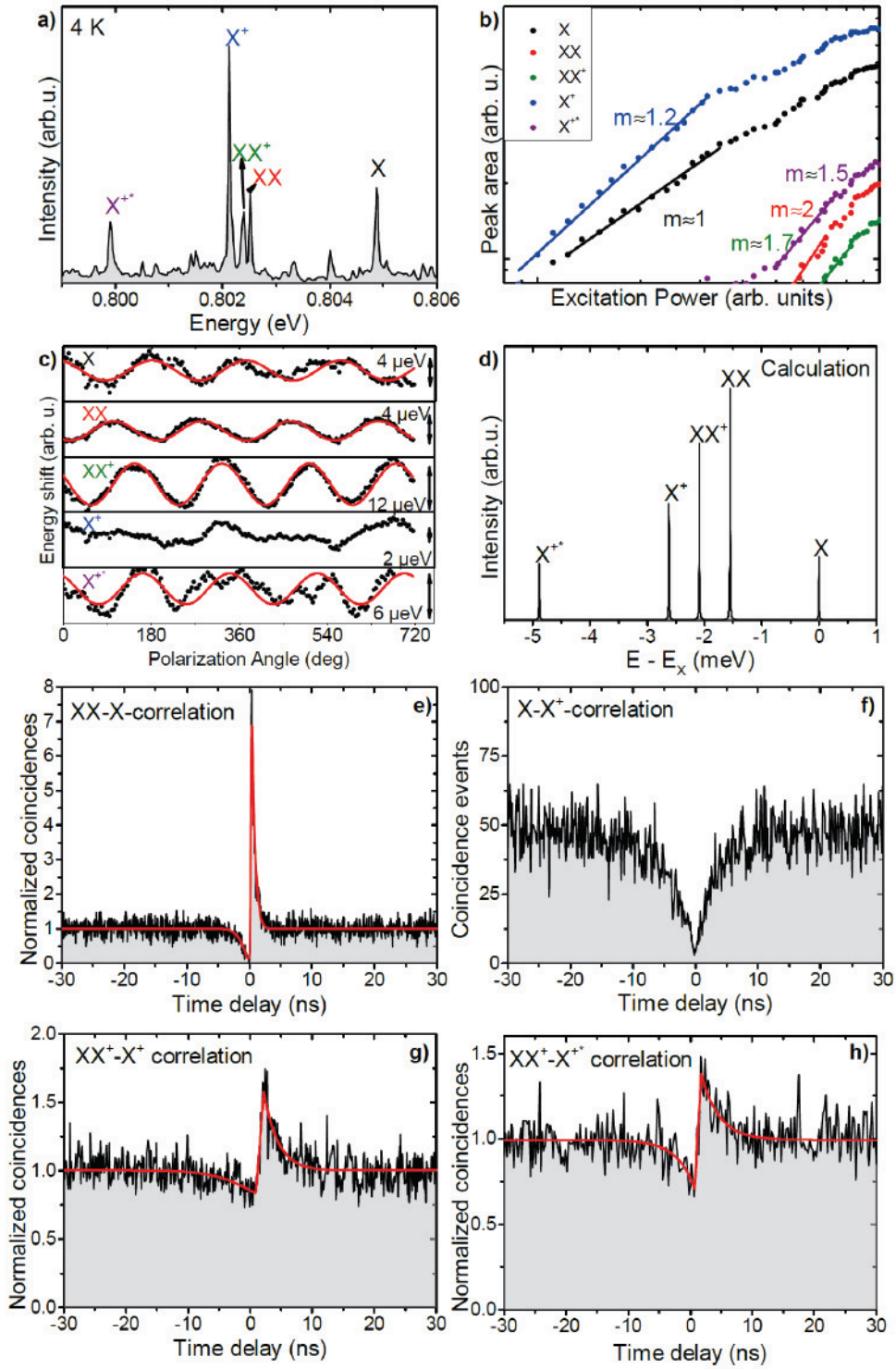


**Figure 7.7.** | **Multi-exciton lines**. a) $\mu$-PL spectrum of the investigated QD with marked, attributed transitions at 4 K. b) Power- and c) polarization series for distinct emission lines. d) Calculated spectrum from the effective mass model. e-h) Cross-correlation measurements between selected transitions (Fig. from F. Olbrich [161], copyright by the American Physical Society).

In a PL measurement, electrons are optically excited from the valence into the conduction band of the surrounding bulk material. From these states, there is a rapid relaxation of the charge carriers into the wetting layer [134] and the energetically lower states of the

quantum dot (see Fig. 7.8). During the subsequent recombination of electron-hole pairs in

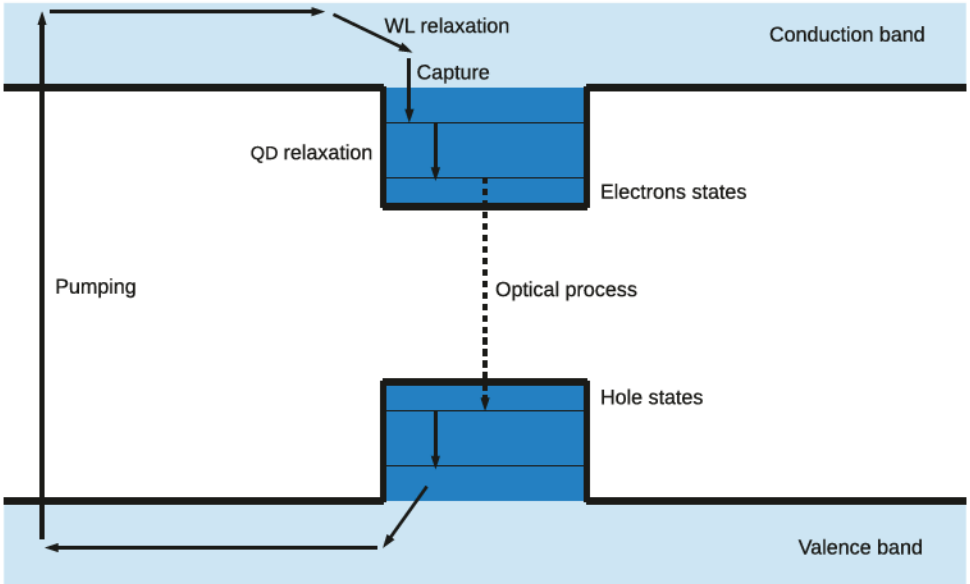


**Figure 7.8. | Non-resonant excitation**. Schematic representation of an excitation process and the subsequent relaxation.

the quantum dot, photons with corresponding energies can be measured.

The power dependency in Fig. 7.7b) serves as an indication for the required number of captured charge carriers for a transition. Following the double logarithmic diagram, the recombination of an exciton (biexciton) should yield a slope of 1 (2), while the recombination of a trion should have a power-dependent slope in between these values. This behavior can be understood qualitatively by the following argument. The intensity of the PL line of an exciton is proportional to the probability of generating an exciton. Assuming that this probability is also proportional to the excitation intensity, a slope of $m = 1$ is to be expected in a double logarithm plot of the PL intensity against the excitation strength. The intensity of the PL line of a biexciton is proportional to the generation of a second exciton, if an exciton is already present. Assuming that the probability of creating the second exciton is independent of the first one, the probability of a biexciton is the joint probability of generating two excitons. Consequently, it is given by the square of the two individual probabilities for excitons and thus a slope of $m = 2$ is to be expected in the double logarithmic plot. Since in the power-dependent spectrum (see Fig. 7.7b)) only slopes between $m = 1$ and $m = 2$ occur, which are characteristic of exciton and biexciton complexes, it is sufficient to consider only such complexes in the analysis. Along these lines, transitions involving a lower number of charge carriers (lower slope) that are saturated at lower excitation powers are associated with excitons ($X$) and trions ($X^+$), while transitions requiring a larger number of carriers (steeper slope), which are saturating at higher excitation powers, are related to biexcitons ($XX$), excited trion ($X^{+*}$) and charged biexciton ($XX^+$).

The polarization dependency in Fig. 7.7c) reveals the existence and magnitude of a fine-structure splitting (FSS) of the involved states via the amplitude of the oscillation. The FSS originates from the deviation of an ideally lens-shaped QD with a continuous cylindrical symmetry $C_{\infty v}$ [171]. This point group includes an $\infty$-fold rotational symmetry and an infinite number of vertical mirror planes. However, this symmetry is reduced due to the underlying structure, since the quantum dot itself consists of individual atoms. Such anisotropies are observed experimentally by measuring the energies of multi-exciton lines at different polarizations. By subtraction of the energies of the same multi-exciton lines at different polarizations the fine structure splitting in Fig. 7.7c) is obtained. For exciton and biexciton transitions, the splitting of the excitonic level is reflected by a polarization-dependent shift of similar amplitude and an out of phase oscillation. Since the trion line is not exhibiting any FSS, only a negligible drift during the measurement is observed. The remaining higher excited, charged states typically undergo larger splittings because of the increased number of involved spins, as visible in Fig. 7.7c).

Additionally, cross-correlation measurements (see Fig. 7.7e-h)) display if a cascaded recombination takes place or if a simultaneous recombination is impossible. To this end, a Hanbury-Brown and Twiss (HBT) setup [2] can be used, as illustrated in Fig. 7.9. In such an experiment, the light to be examined crosses a 50/50 beam splitter. Subsequently,

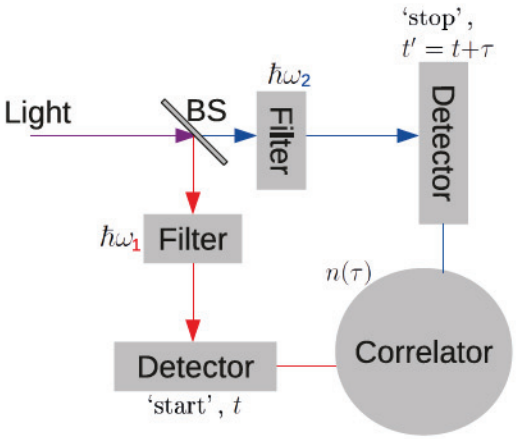


**Figure 7.9. | Cross-correlation measurement**. The incident beam crosses a 50/50 beam splitter (BS). Each of the two split beams passes through a filter and is focused onto a photodetector. The number of detections as a function of the delay time $n(\tau)$ is measured.

each of the two sub-beams passes a filter and is focused on a photodetector. By adjusting the transmission of one filter to the energy of the first line $\hbar\omega_1$ and that of the other filter to $\hbar\omega_2$ it is possible to use photon 1 with energy $\hbar\omega_1$ as a 'start' signal at time $t$ and photon 2 with energy $\hbar\omega_2$ as a 'stop' signal at time $t' = t + \tau$. In this way, the number of detections as functions the delay time $n(\tau)$ between the two signals can be determined. Multiple repetition of the experiment gives the conditional probability that a photon

2 with energy $\hbar\omega_2$ is generated after the first recombination process with emission of a photon 1 with energy $\hbar\omega_1$ has occurred. By inserting a time delay into the beam path of the stop-detector it is possible to measure 'negative time differences'. For instance, if a time delay of 40 ns is chosen and a time difference of 10 ns is measured, one can conclude that the emission of photon 2 occurred 30 ns before the emission of photon 1 occurs, which has triggered the start detector. Such a process is attributed to a time delay of $\tau = -30$ ns. Let us discuss the result of the cross-correlation measurement between the exciton ($X$) and the biexciton ($XX$) in Fig. 7.7e). For large time delays $|\tau|$, photon 1 and photon 2 are uncorrelated. In contrast, the area around $\tau = 0$ is of central importance. For small positive values of $\tau$ an increased number of coincidences is measured, since it is likely to detect a photon with the energy of the biexciton line ($XX$) before one with the energy of the exciton line ($X$). Accordingly, for small positive values of $\tau$ a decreased number of coincidences is measured, as it is unlikely to detect a photon with the energy of the biexciton line ($XX$) after one with the energy of the exciton line ($X$). Such a behavior, where photons with energies of multi-exciton lines are always observed in a given order, as in the case of the biexciton and exciton lines (see Fig. 7.7e)), strongly indicates decay cascades. A similar, but not as prominent development is expected for cascades starting from the charged biexciton (see Fig. 7.7g) and h)), because of the multiple number of decay paths from this configuration. On the other hand, for the excitonic and trionic decay (see Fig. 7.7f)), recombinations of electron-hole pairs in the same level are required and therefore not possible at once.

For an identification of the multi-exciton transition lines and their respective charges in Fig. 7.7a), the experimental results in Fig. 7.7 are combined with our effective mass model calculations for the InGaAs material system as detailed in [172]. The calculated spectrum is displayed in Fig. 7.7d). Of course, our effective mass model renders a more phenomenological approach to the electronic state calculations compared to the level of detail of our $\mathbf{k}\cdot\mathbf{p}$ or TB simulations. However, the calculation of a converged multi-exciton emission spectrum for the present situation of 400 states based on a microscopic theory is numerically not accessible. On the other hand, this is not necessary for our task of identifying the multi-exciton lines and their respective charges. Within our effective mass model, the QD wave functions perpendicular to the growth direction are approximated by those of a two-dimensional harmonic oscillator, and along the growth direction the solutions of a potential well are applied. All single-particle states are spin-degenerate and, assuming rotational symmetry around the QD axis, the p-shells are degenerate as well. The corresponding Coulomb matrix elements for equal envelopes are listed Table A.8 in the appendix. Following this model, the charges of the multi-exciton complexes can be assigned by electrostatic arguments as follows. In case of equal envelopes for electron and hole wave functions, the emission lines of the charged complexes are located in between

the neutral exciton and biexciton line in the spectrum. In this case the electron-hole pair is globally and locally neutral. On the other hand, for non-equal envelopes the exciton is locally charged and therefore more sensitive to the presence of additional charges. The charged complexes are shifted with respect to the neutral ones by means of electrostatic interaction. In InGaAs quantum dots, holes have typically larger spatial extensions than those of the electrons, which leads to a local negative charging of the electron-hole pair and, as a consequence, to a shift of the positively charged complexes to lower energy. Therefore, a positive charge is assigned to the experimentally observed emission lines of the charged complexes, which are energetically below the neutrally charged biexciton.

## 7.4. Temperature-Dependent Analysis

Following the goal of achieving a single-photon source at elevated temperatures, the temperature-dependent QD emission properties were studied in collaboration with experiments, which were performed by F. Olbrich et al. in the group of Prof. Michler in Stuttgart. Figure 7.10a) displays PL spectra of a single QD at different temperatures, whereas in

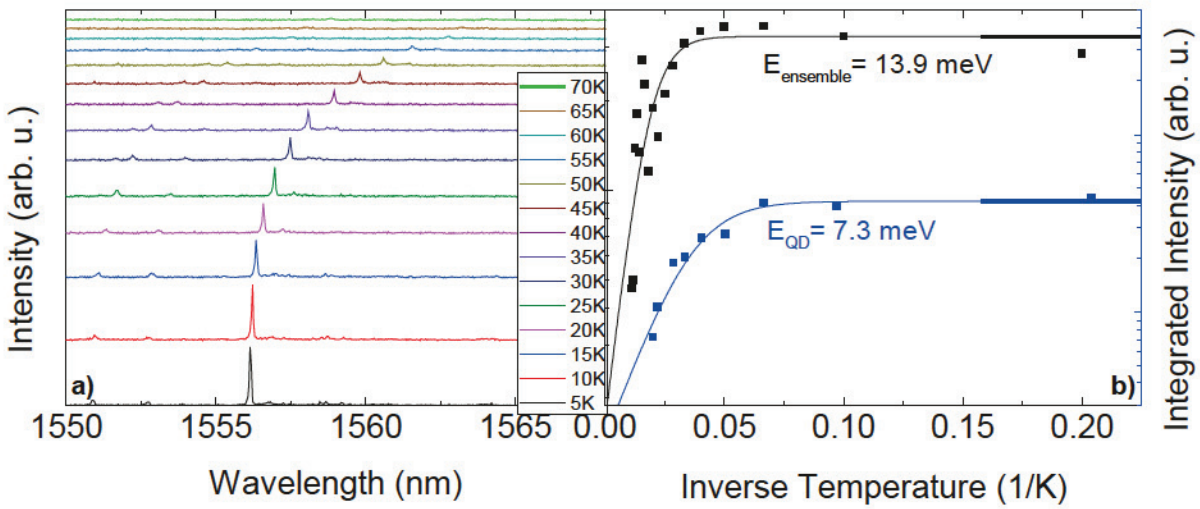


**Figure 7.10. | Temperature-dependent spectra.** Stack plot of a) single QD spectra for increasing temperatures from bottom to top. b) Logarithm of the integrated intensities as a function of the inverse temperature for the results of a) and the ensemble-PL. The underlying spectra were measured well below the ensemble and single dot saturation power. One data set was offset for clarity (Fig. from F. Olbrich [161], copyright by the American Physical Society).

b) the integrated intensities of both this QD and the ensemble are depicted. Note that here the temperature increases from right to left. At lower temperatures the intensity is constant, whereas at higher temperatures the intensity rapidly decreases due to thermal activation of the charge carriers. We analyze this behavior by using the Arrhenius-type

equation [173, 174, 175]

$$I(T) = \frac{I_0}{1 + B \cdot exp\left(\frac{-E_a}{k_B T}\right)}. \tag{7.1}$$

Here, $I_0$ is the integrated PL intensity at low temperatures, $B$ is a constant, $E_a$ is the thermal activation energy, and $k_B$ the Boltzmann constant. We utilize Eq. (7.1) to best reproduce (solid line) the experimental data (dots) in Fig. 7.10b), from which we obtain the thermal activation energies $E_{\text{ensemble}}$ and $E_{\text{QD}}$ for the ensemble and the single QD, respectively.

In Fig. 7.10a) an expected emission redshift and linewidth broadening can be observed [176], accompanied by a constant decrease of the overall intensity. The intensity behaviour can be retraced by keeping track of the intensity curve in Fig. 7.10b), as well. For increasing temperatures (from right to left on the $x$-axis) the integrated intensity stays constant up to a certain temperature and then drops. The Arrhenius-type analysis yields the underlying thermal activation energy of the process causing the decrease of the QD intensity. An explanation of the QD intensity drop is the excitation of charge carriers from the QD confinement potential towards higher energetic states of the wetting-layer. However, the extracted activation energies in Fig. 7.10b) do not directly correspond to the confinement with respect to the wetting-layer. Instead, they are caused by charge carriers, which leave the QD ground state in favor of an excited state. Consequently, these charge carriers do not participate to the ground state emission any longer.

For the theoretical analysis of this effect, we start from the uncorrelated single-particle $k \cdot p$ electron and hole states inside the QD. Due to the Coulomb interaction between these states, new eigenvalues and eigenfunctions of the interacting problem arise. As discussed before, the Coulomb-correlated eigenstates $\{|\phi_i\rangle\}$ can be expressed as an expansion in terms of the uncorrelated single-particle basis states $\{|\varphi_j\rangle\}$ by

$$|\phi_i\rangle = \left(\sum_j |\varphi_j\rangle \langle\varphi_j|\right) |\phi_i\rangle = \sum_j |\varphi_j\rangle \langle\varphi_j|\phi_i\rangle = \sum_j c_{ij} |\varphi_j\rangle , \tag{7.2}$$

where the coefficients $c_{ij}$ are obtained from diagonalization of the CI matrix. The exciton emission spectra between the Coulomb-correlated eigenstates are calculated by using Fermi's golden rule. In Fig. 7.11(a), the transition energies of the ground state exciton $X_0$ at 800 meV and the first excited exciton $X^*$ at 805 meV are displayed. The corresponding energy difference of 5 meV between these two Coulomb-correlated eigenstates is in agreement with the experimentally measured value of 7.3 meV in Fig. 7.10(b), whereas in the uncorrelated single-particle picture an energy difference of only $h_{1,2} - h_{3,4} = 2$ meV is obtained (see Fig. 7.11(b)). In the Coulomb-correlated many-body picture, the ground state exciton $X_0$ is dominantly composed of the single-particle electron and hole ground

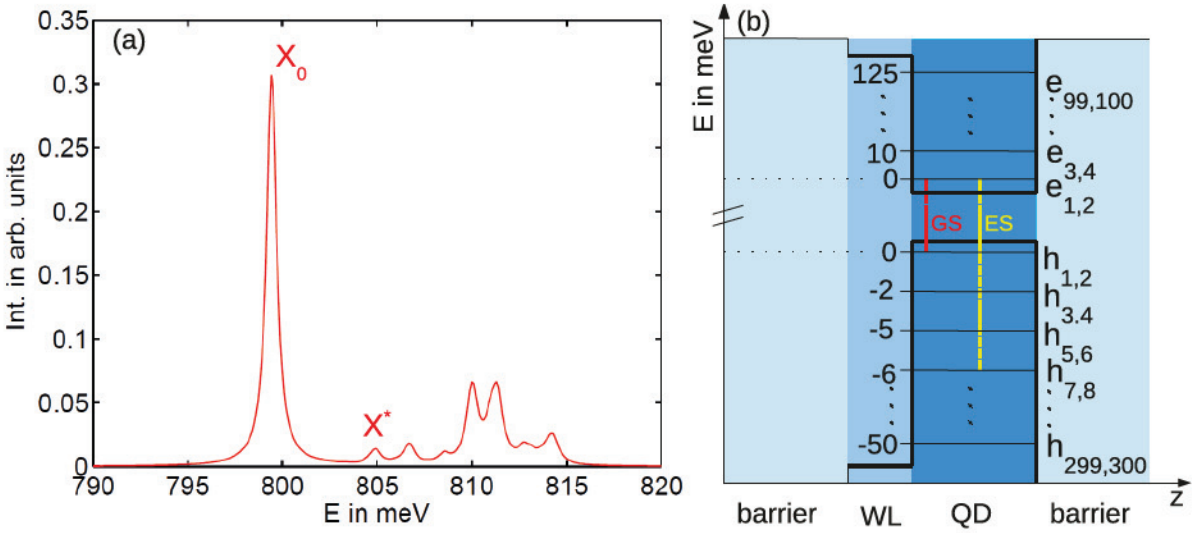


**Figure 7.11.** | **Excitonic energies**. (a) Calculated emission spectrum based on a full configuration interaction calculation and Fermi's golden rule. (b) Energy level scheme along the growth-direction. According to our $k \cdot p$ - calculation, there are 100 bound electron and 300 bound hole states inside the QD. The ground state (GS) transition (dashed red line) as well as one excited state (ES) transition (dashed yellow line) are marked (Fig. from Ref. [161], copyright by the American Physical Society).

state (see $e_{1,2}/h_{1,2}$ in Fig. 7.11(b)), whereas the first excited exciton $X^*$ is composed of the lowest single-particle electron state and an intermixture of single-particle hole states. Consequently, for an increased single-particle level-spacing between these states higher activation energies are expected, which is confirmed in experimental results (see Fig. 7.10).

From these results we conclude that the thermal stability of the present QDs is limited by the inter-shell distance (single-particle level-spacing), which can be modified by variation of the lateral QD size. The charge carriers are thermally activated in multiple steps by subsequently occupying the higher-energetic QD states and finally reaching the wetting layer. A comparison of the activation energy of the ensemble and individual dots shows that the ensemble value is larger. According to the above analysis this implies larger inter-shell distances and consequently larger confinements. As a result, the deviation between the ensemble energy and individual dots can be explained by a carrier redistribution from dots with smaller to larger confinement. For instance, this can happen due to scattering of the charge carriers into the wetting layer and subsequent recapturing into quantum dot states with larger confinement. Consequently, the activation energy of the ensemble is limited by the maximal shell spacings [176]. One necessary condition for single-photon emission at room temperature is the formation of thermally stable excitons, for which the minimum shell spacing can be approximated by the relation $1\,\mathrm{K} \mathrel{\hat{=}} 8.6 \cdot 10^{-5}\,\mathrm{eV}$. For the present system, single-photon emission has been experimentally demonstrated for temperatures up to 77 K [161], which is consistent with activation energies of about 7 meV, as obtained in Fig. 7.10.

# 8. Atomically Thin Semiconductors

As mentioned in the introductory part, atomically thin transition metal dichalcogenides (TMDCs) have emerged as an alternative platform for single-photon emission. Due to the possibility of manufacturing these materials in the form of monolayers, they are referred to as 2D materials. The most prominent 2D material is graphene [42], for whose exfoliation the Nobel Prize in Physics was awarded in 2010. This chapter is organized as follows. We begin with a brief introduction of the TMDC material system and its production techniques. Subsequently, we discuss possibilities of band gap engineering and generating nanostructures in these materials. After this short overview, we present a TB model for a monolayer, which we systematically extend to describe the relevant physics within TMDC nanostructures. As an example of such systems, we present novel results on molybdenum disulfide ($MoS_2$) nanobubbles and discuss them with respect to current developments.

## 8.1. Transition Metal Dichalcogenides

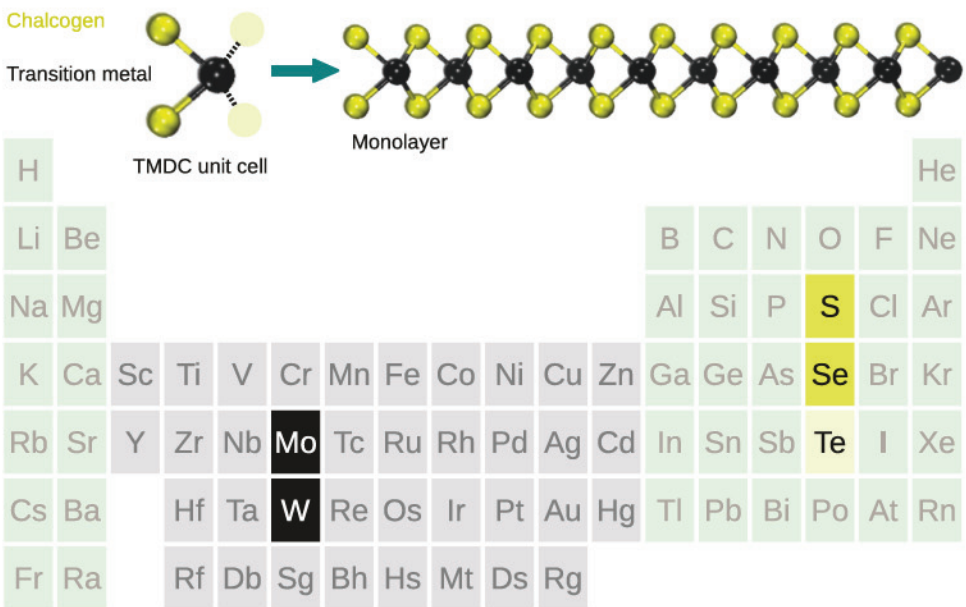


**Figure 8.1. | Transition metal dichalcogenides**. They contain one transition metal (black) for every two chalcogen atoms (yellow). The elements of interest for this work are highlighted.

In this section, we briefly introduce the TMDC material system, which is composed of transition metal atoms that are sandwiched between chalcogen atoms as illustrated in Fig. 8.1. TMDCs are an interesting class of 2D materials for optoelectronic applications due to the direct band gap in the visible frequency range in $MoS_2$, $WS_2$, $MoSe_2$, and $WSe_2$ monolayers [43, 44, 45, 46, 47].

### 8.1.1. Molybdenum Disulfide

As mentioned above, a focus will be placed on $MoS_2$-based systems as a representative semiconductor TMDC material and therefore we briefly summarize basic properties. Molybdenum disulfide or, more generally, TMDCs, can be manufactured in form of bulk crystals, multiple layers (as illustrated in Fig. 8.2), or even atomically thin monolayers. As

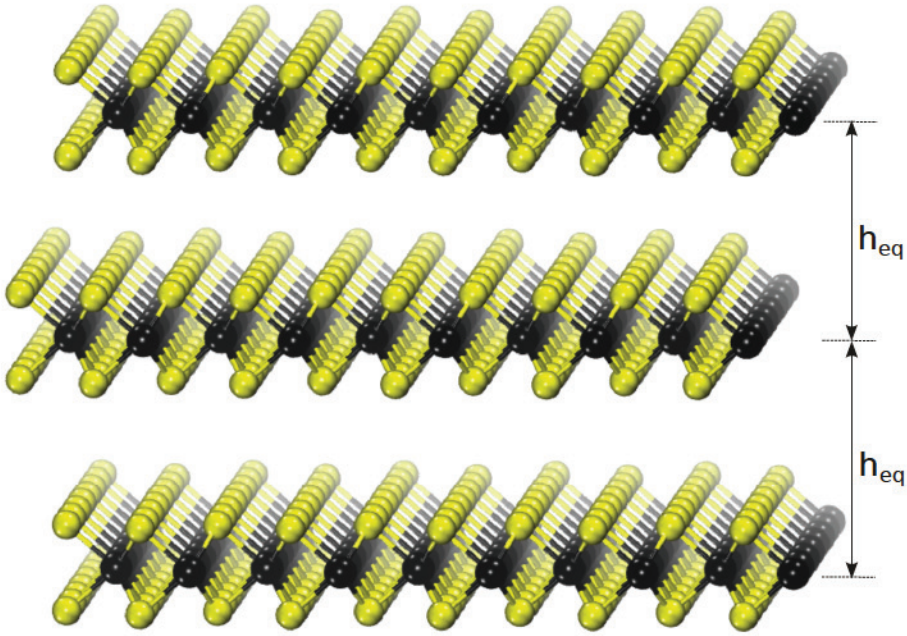


**Figure 8.2. | Molybdenum Disulfide.** Three vertically stacked layers of $MoS_2$, which are separated by an equilibrium height $h_{eq}$.

discussed for III-V semiconductors, the crystal structure and Brillouin zone are important properties, which need to be considered when analyzing the electronic and optical properties. The crystal structure and Brillouin zone of a $MoS_2$ monolayer is illustrated in Fig. 8.3. Furthermore, it depicts the hexagonal lattice and the respective threefold symmetry. Since the $MoS_2$ monolayer is a two-dimensional system, the corresponding Brillouin zone is two-dimensional as well. It includes the $\mathbf{\Gamma}$-point, which is located at (0,0). Additionally, the $\mathbf{\Sigma}$-point is situated half way between $\mathbf{\Gamma}$ and $\mathbf{K}$. The points $\mathbf{K}$ and $\mathbf{K}'$ are mirror-symmetrical to each other. Half way between these points is the $\mathbf{M}$-point. These high-symmetry points are considered in our calculation of the $MoS_2$ monolayer band structure in Fig. 8.9.

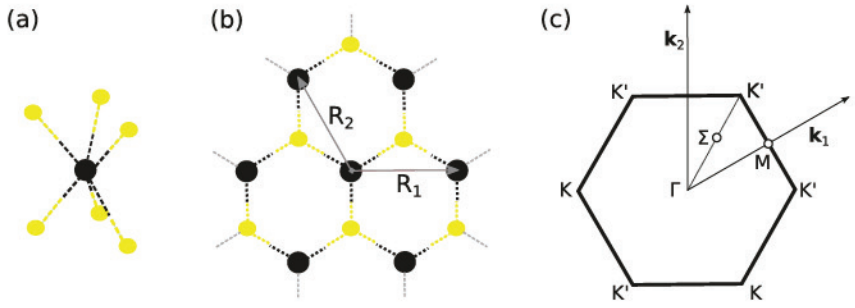


**Figure 8.3. | $MoS_2$ monolayer lattice and Brillouin zone.** (a) Side view: Prismatic arrangement of atoms. Mo and S atoms are marked in black and yellow, respectively. The dashed lines illustrate the bonds. (b) Top view including lattice vectors $\mathbf{R}_1$ and $\mathbf{R}_2$. (c) Brillouin zone including the reciprocal basis vectors $\mathbf{k}_1$ and $\mathbf{k}_2$ as well as important points of high symmetry.

### 8.1.2. Production Techniques

When manufacturing TMDCs, one can choose between so-called top down and bottom up approaches. The most prominent and commonly used top down approach is exfoliation, where TMDC monolayers are produced by micromechanical cleavage, as first demonstrated with graphene [177]. Hereby, adhesive tape is placed on a TMDC bulk material. After its subsequent removal, one obtains tiny TMDC flakes on the tape. These flakes are brought onto a substrate by placing the tape on top of that substrate. Removing the tape from the substrate, TMDC monolayer or multilayer flakes are deposited. By using exfoliation, small samples, typically with diameters ranging from 5 $\mu$m to 10 $\mu$m can be obtained [177]. Larger samples can be produced by using liquid-phase exfoliation by blending TMDC materials with solvents and polymers [178]. A possible bottom up approach is chemical vapor deposition [179]. Hereby, the reactants are delivered on a substrate and the entire system is annealed. An alternative approach is molecular beam epitaxy (MBE), which has been explained in a previous chapter for the III-V semiconductors. Using MBE, $MoSe_2$ samples have recently been grown on graphene [180].

## 8.2. Nanostructured TMDCs

In the rapidly developing field of TMDCs, attention has increasingly shifted towards manufacturing nanostructures for single-photon emission. As for the III-V semiconductors, band gap engineering is possible with TMDCs to modify their optoelectronic properties. To this end, two different effects can be exploited, which are presented in the following. One possibility is strain-engineering, which works particularly well for TMDCs. A linear tuning rate of the optical band gap of about 100 meV per percent strain for a suspended monolayer of $MoS_2$ has been observed by applying large biaxial strains [181]. Additionally, a linear behavior of about 120 meV per percent strain for bilayer $MoS_2$ has been reported [182].

Moreover, an enhancement in photoluminescence intensity by a factor of 35 has been demonstrated for bilayer Tungsten diselenide ($WSe_2$) under uniaxial tensile strain of up to 2 % [183]. Building on these results, a spatial correlation between single-photon emitters and local strain has been observed for instance on a gold substrate [16, 15] and on a substrate with etched holes [14]. This concept has been systematically extended to high areal densities by placing a TMDC layer on top of an array of silicon-based pillars [17, 18], as depicted in Fig. 8.4.

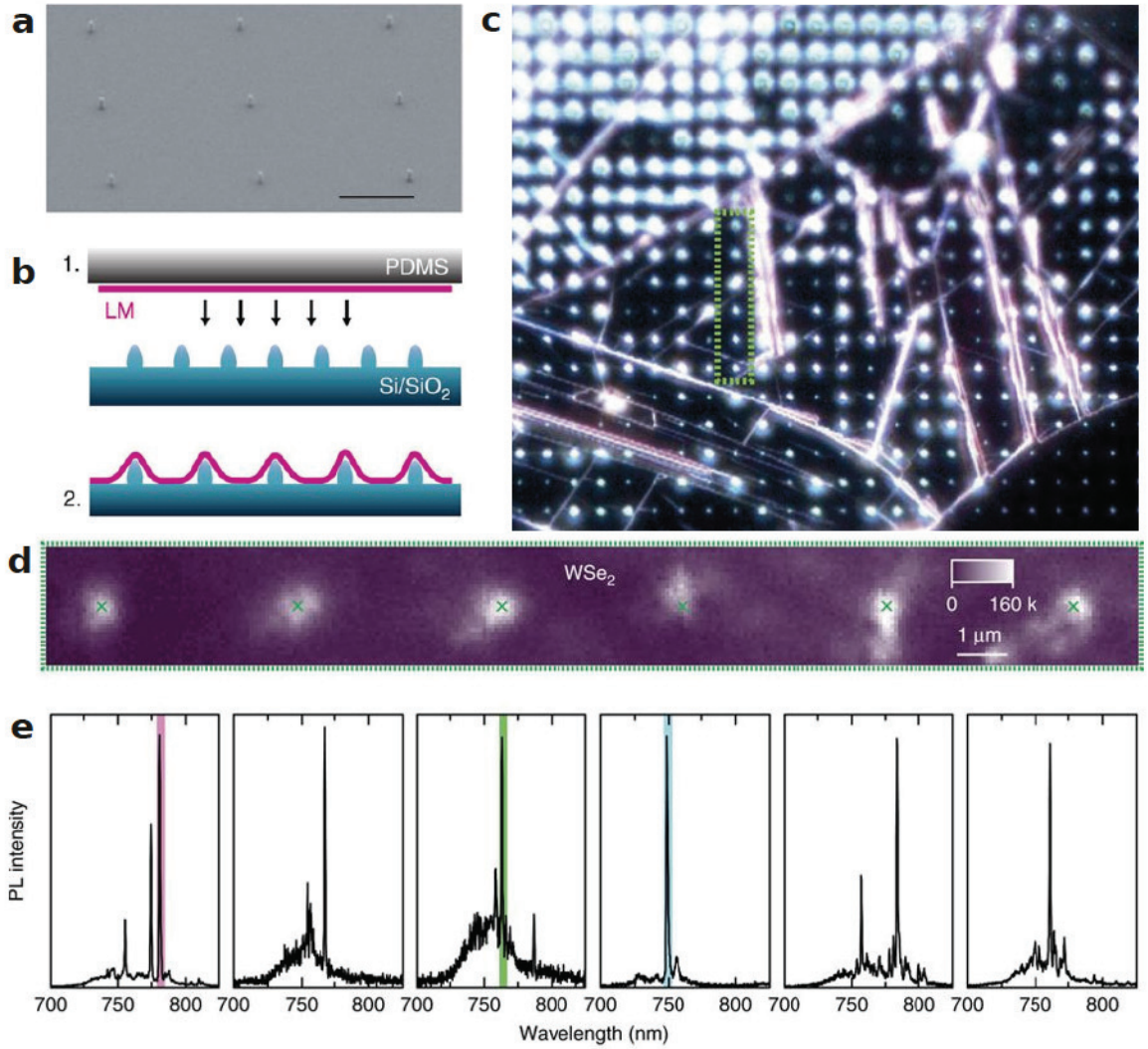


**Figure 8.4. | Nanostructured TMDCs.** Realization of an array of single-photon emitters by C. Palacios-Berraquero, et al. from Ref. [18]. (a) Scanning electron microscope image of the nanopillar substrate, the scale bar covers 2 $\mu$m. (b) Fabrication has been achieved by the deposition of a layered material (LM) on the nanopillar array by using polydimethylsiloxane (PDMS). (c) Optical microscopy image of a $WSe_2$ monolayer on the array. The green box highlights six adjacent nanopillars. (d) Integrated PL intensity measurement of the region enclosed by the green rectangle. Crosses mark the position of the six nanopillars. (e) PL spectra taken at each of the crosses show strong emission and narrow lines. For each of the colored lines, single-photon emission has been demonstrated in Ref. [18] (Figs. (a,b), (d,e), and (c) correspond to Figs. 1(a,b), 2(a,b) and an extraction of Fig. 1d in Ref. [18], `https://www.nature.com/articles/ncomms15093`, Creative Commons Attribution 4.0 International License `https://creativecommons.org/licenses/by/4.0/`).

An alternative route to band-gap-engineering in TMDCs, which is less discussed, is a change of the dielectric environment. Recent work on this topic includes the theoretical prediction of lateral heterojunctions based on non-local manipulations of the Coulomb interaction [48] as well as experiments, demonstrating a change of band gap in the order of 100 meV [49]. Results from these works are displayed in Fig. 8.5.

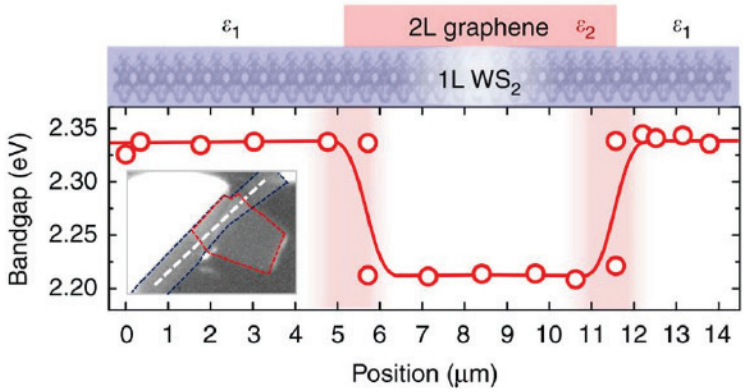


**Figure 8.5. | Dielectric engineering**. Experimental results presented by A. Raja, et al. in Ref. [49] demonstrate a spatially dependent band gap along the profile of a lateral $WS_2$/graphene heterostructure (Fig 4c from Ref. [49], `https://www.nature.com/articles/ncomms15251`, Creative Commons Attribution 4.0 International License `https://creativecommons.org/licenses/by/4.0/`.

An alternative way of changing the band gap is by modifying the interlayer distance of TMDCs. In this case both vertical hybridization of orbitals as well as a change of the dielectric environment due to air between the layers play a role. In case of an increasing air gap between two TMDCs, fewer field lines crossing the layers (see Fig. 8.6) indicate that the Coulomb interaction is screened less efficiently, which results in a larger band gap. A quantitative discussion of the band gap as a function of the interlayer distance is provided for instance by A. Steinhoff et al. in Ref. [184].

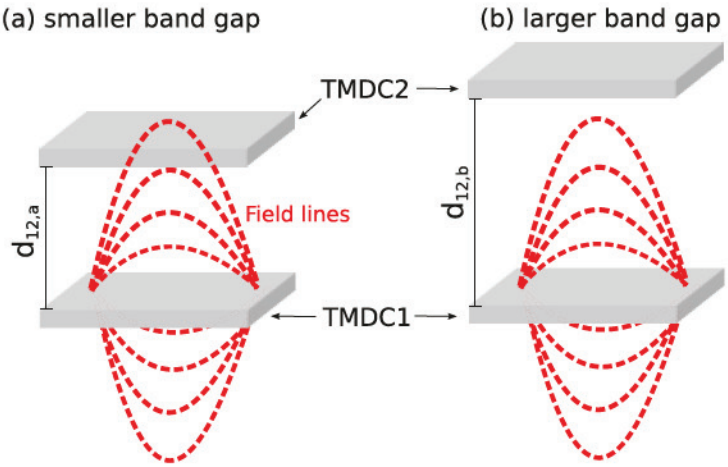


**Figure 8.6. | Dielectric effect**. (a) and (b) Schematic representation of two TMDCs 1/2 with different interlayer distances $d_{12,a/b}$. (b) Additional air between the TMDCs 1/2 changes the dielectric environment, the Coulomb interaction and the electronic band gap.

## 8.3. Monolayer Tight-Binding Model

In the following, we briefly present an effective $MoS_2$ monolayer TB model, for details we refer to the original work by A. Schulz in Ref. [185]. Since we employ this model for the description of $MoS_2$ systems, we shortly summarize its main aspects. The lattice of $MoS_2$ and the twelve vectors to nearest and next-nearest neighbors of a Mo-atom are displayed in Fig. 8.7, respectively.

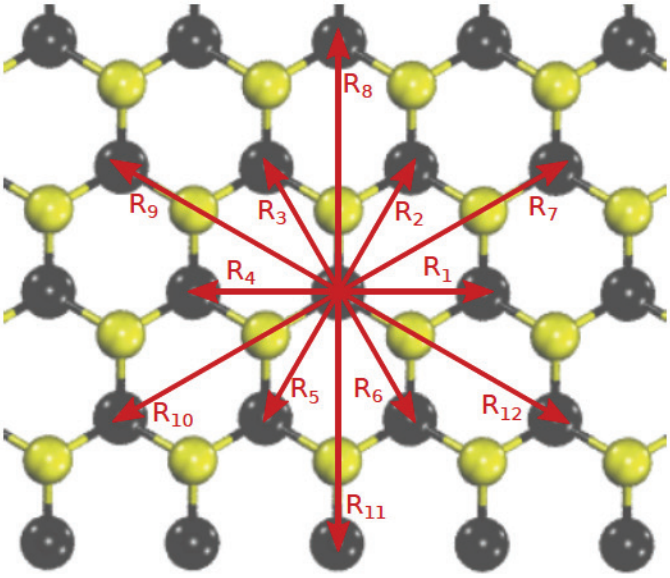


**Figure 8.7. | Monolayer $MoS_2$ lattice.** Nearest neighbor $\{\mathbf{R}_1, ..., \mathbf{R}_6\}$ and next-nearest neighbour vectors $\{\mathbf{R}_7, ..., \mathbf{R}_{12}\}$. S atoms (yellow) are disregarded in the model [185], but the threefold symmetry is preserved artificially as shown in Fig. 8.8.

In our TB model [185], we consider only the Mo-atoms and the corresponding nearest and next-nearest neighbor couplings. As a result, only Mo-Mo couplings along the vectors $\{\mathbf{R}_1, ..., \mathbf{R}_{12}\}$ (see Fig. 8.7) are considered. Furthermore, the finite basis set of our model consists of three d-orbitals $\{|d_\alpha\rangle\}$ with $\alpha \in \{0, \pm 2\}$. These basis states

$$\begin{aligned} d_0 = d_{z^2} &\propto Y_{20} \\ d_{\pm 2} = (d_{x^2} \pm i d_{xy})/\sqrt{2} &\propto Y_{2\pm 2} \end{aligned} \tag{8.1}$$

are essentially complex spherical harmonics $Y_{2\alpha} \propto e^{i\alpha\Phi}$ as introduced in the TB three-band model in Ref. [46]. The basis is constructed out of atomic orbitals $d_{z^2}, d_{x^2}, d_{xy}$ by applying the unitary transformation

$$U = \begin{pmatrix} 1 & 0 & 0 \\ 0 & 1/\sqrt{2} & i/\sqrt{2} \\ 0 & 1/\sqrt{2} & -i/\sqrt{2} \end{pmatrix}, \tag{8.2}$$

so that

$$\begin{pmatrix} d_0 \\ d_{+2} \\ d_{-2} \end{pmatrix} = U \begin{pmatrix} d_{z^2} \\ d_{x^2} \\ d_{xy} \end{pmatrix}. \tag{8.3}$$

Note that the term $d_{x^2}$ is a shorthand notation for $d_{x^2-y^2}$. The Hamilton matrix $H$, which is obtained from this model, is given by

$$H = \begin{pmatrix} H_{d_0d_0} & H_{d_0d_2} & H_{d_0d_{-2}} \\ H^*_{d_0d_2} & H_{d_2d_2} & H_{d_2d_{-2}} \\ H^*_{d_0d_{-2}} & H^*_{d_2d_{-2}} & H_{d_{-2}d_{-2}} \end{pmatrix}, \tag{8.4}$$

with matrix elements

$$H_{\alpha\beta} = \langle \alpha, k|H|\beta, k\rangle = \sum_{\mathbf{R}} e^{i\mathbf{k}\cdot\mathbf{R}} \langle \alpha, 0|H|\beta, \mathbf{R}\rangle, \tag{8.5}$$

where

$$\begin{aligned} \mathbf{R} \in \{&\underbrace{\mathbf{R}_1,\ \mathbf{R}_2,\ \mathbf{R}_3,\ \mathbf{R}_4,\ \mathbf{R}_5,\ \mathbf{R}_6}_{\text{nearest neighbors}}, \\ &\underbrace{\mathbf{R}_7,\ \mathbf{R}_8,\ \mathbf{R}_9,\ \mathbf{R}_{10},\ \mathbf{R}_{11},\ \mathbf{R}_{12}}_{\text{next-nearest neighbors}}\} \end{aligned} \tag{8.6}$$

according to Fig. 8.7. These vectors are given by

$$\begin{aligned} &\mathbf{R}_1 = (1,0), \quad \mathbf{R}_2 = (1,1), \quad \mathbf{R}_3 = (0,1), \\ &\mathbf{R}_4 = (-1,0), \mathbf{R}_5, = (-1,-1) \quad \mathbf{R}_6 = (0,-1), \\ &\mathbf{R}_7 = (2,1), \quad \mathbf{R}_8 = (1,2), \quad \mathbf{R}_9 = (-1,1), \\ &\mathbf{R}_{10} = (-2,-1), \quad \mathbf{R}_{11} = (-1,-2) \quad \mathbf{R}_{12} = (1,-1) \end{aligned} \tag{8.7}$$

in units of the Bravais-lattice vectors

$$\mathbf{a}_1 = a \begin{pmatrix} 1 \\ 0 \end{pmatrix} \qquad \mathbf{a}_2 = a \begin{pmatrix} -1/2 \\ \sqrt{3}/2 \end{pmatrix} \tag{8.8}$$

with the lattice constant $a = 3.18\,\text{Å}$. The matrix elements

$$\langle \alpha, 0|H|\beta, \mathbf{R}\rangle = f_{\alpha,\beta}(\phi) t_{\alpha\beta}(|\mathbf{R}|) \tag{8.9}$$

on the one hand include the TB hopping parameter $t_{\alpha\beta}(|\mathbf{R}|)$ towards nearest and next-nearest neighbors of the Mo-atoms, respectively. On the other hand, the threefold symmetry

of the $MoS_2$ lattice is not preserved when considering the Mo sublattice only. It comes into play artificially by including a phase $\phi$ as shown in Fig. 8.8. This phase towards

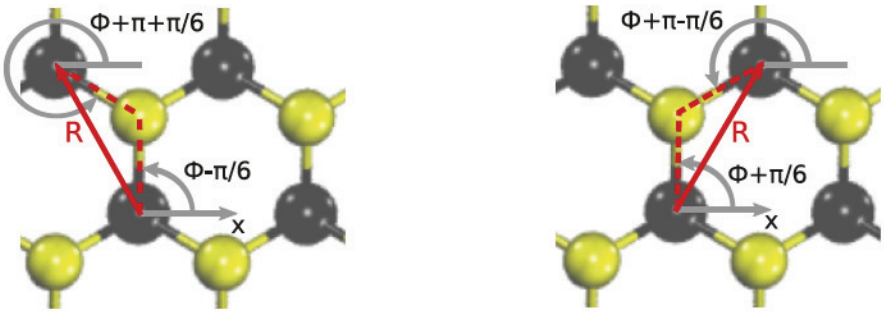


**Figure 8.8. | Illustration of phase factors**. The interaction between neighboring Mo atoms(black) along vector **R** is modified by the presence of the neighboring S atom (yellow). The effective interaction along the dashed line includes two phase factors, which preserve the threefold symmetry in the model [185].

nearest and next-nearest neighbours is included in the function

$$f_{\alpha,\beta}(\phi) = \begin{cases} \text{nearest neighbors} & \\ \exp(-i\alpha(\phi - \pi/6) + i\beta(\pi + \phi + \pi/6)), & \text{if } \phi = 0, 2\pi/3, 4\pi/3 \\ \exp(-i\alpha(\phi + \pi/6) + i\beta(\pi + \phi - \pi/6)), & \text{if } \phi = \pi/3, \pi, 5\pi/3 \\ \text{next-nearest neighbors} & \\ \exp(-i\alpha\phi + i\beta(\pi + \phi)), & \text{if } \phi = \pi/6, 3\pi/2, 5\pi/6 \\ \exp(-i\alpha(\pi + \phi) + i\beta\phi), & \text{if } \phi = \pi/2, 7\pi/6, 11\pi/6, \end{cases} \tag{8.10}$$

where nearest and next-nearest neighbours can be distinguished by different phases. Even though, we employ an effective TB model, in which we consider the Mo atoms only, the band structure of a DFT calculation is well approximated (see Fig. 8.9). The corresponding TB

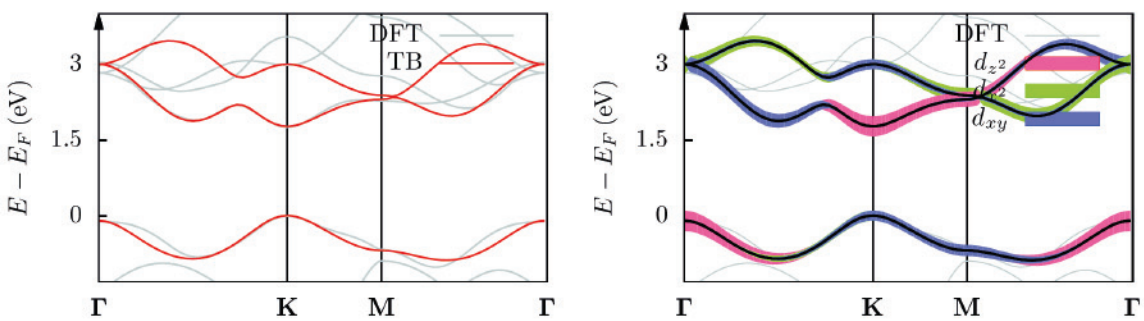


**Figure 8.9. | Tight-binding band structure**. Left: Comparison of the three-band monolayer $MoS_2$ TB band structure (red) with a DFT calculation (gray). Right: Character of the three bands $d_{z^2}$ (red), $d_{x^2}$ (green) and $d_{xy}$ (blue) (Figs. by A. Schulz from Ref. [185]).

parameter for a $MoS_2$ monolayer are displayed in Table. 8.1. Additionally, we include spin-

| | |
|---|---|
| $\varepsilon_0$ | -2.17187 eV |
| $\varepsilon_{\pm 2}$ | -2.07972 eV |
| $t_{00}$ | -0.326583 eV |
| $t_{0\pm 2}$ | 0.561734 eV |
| $t_{\pm 2\pm 2}$ | -0.411327 eV |
| $t_{\pm 2\mp 2}$ | -0.355268 eV |
| $t'_{00}$ | -0.0537226 eV |
| $t'_{0\pm 2}$ | -0.00459159 eV |
| $t'_{\pm 2\pm 2}$ | 0.052774 eV |
| $t'_{\pm 2\mp 2}$ | -0.123627 eV |

Table 8.1.: TB parameters for $MoS_2$ monolayer. The primed terms describe next-nearest neighbor couplings.

orbit coupling in the model. The procedure is similar to the one for III-V semiconductors with the difference that we now consider only d-orbitals. For the implementation, we follow Ref. [46] and obtain

$$H^{SO} = \begin{bmatrix} H + \frac{\lambda}{2} L_z & 0 \\ 0 & H - \frac{\lambda}{2} L_z \end{bmatrix} \tag{8.11}$$

with

$$L_z = \left[\begin{array}{c|cc} 0 & 0 & 0 \\ \hline 0 & 0 & 2i \\ 0 & -2i & 0 \end{array}\right]. \tag{8.12}$$

The Hamiltonian in Eq. (8.11) is block diagonal, which means that the $z$-component of the spin is not mixed by the spin-orbit coupling and therefore is a good quantum number due to the $\sigma_h$ symmetry [46].

### 8.3.1. Hamiltonian at Points of High Symmetry

As discussed above, both strain and the dielectric effect can change the band gap of $MoS_2$. In order to properly describe these changes analytical access to the TB Hamiltonian (see Eq. (8.4)) at points of high symmetry helps identifying which parameters need to be adapted and to what extent. The matrix in Eq. (8.4) at $\mathbf{\Gamma}$ can be diagonalized analytically,

which gives

$$H(\mathbf{\Gamma}) = \begin{pmatrix} \varepsilon_0 + 6t_0 + 6t_0' & 0 & 0 \\ 0 & \varepsilon_2 - 3t_2 + 6t_2' & 0 \\ 0 & 0 & \varepsilon_2 - 3t_2 + 6t_2' \end{pmatrix} \tag{8.13}$$

with the first diagonal element, denoting the eigenvalue of the valence band (VB) and the other two, describing the conduction bands (CBs). At $\mathbf{K}$, one obtains

$$H(\mathbf{K}) = \begin{pmatrix} \varepsilon_0 - 3t_0 + 6t_0' & 0 & 0 \\ 0 & \varepsilon_2 - 3t_2 + 6t_2' & 0 \\ 0 & 0 & \varepsilon_2 + 6t_2 + 6t_2' \end{pmatrix}, \tag{8.14}$$

where the diagonal elements describe the energies of CB1, CB2 and VB in this order.

### 8.3.2. Implementation of Strain

In the case of a $MoS_2$ monolayer, strain leads to an indirect band gap between the $\mathbf{\Gamma}$-point of the VB and the $\mathbf{K}$-point of the CB, as demonstrated for instance in Ref. [186]. The indirect band gap can be addressed by Eqs. (8.13) and (8.14) in our model. We obtain

$$E_{\mathrm{CB}}(\mathbf{K}) - E_{\mathrm{VB}}(\mathbf{\Gamma}) = -9t_0. \tag{8.15}$$

Consequently, the strain-induced change of band gap can be modeled by decreasing the absolute value of the nearest neighbor hopping parameter $t_0$. One option for rescaling $t_0$ is by using the generalized Harrison rule [115]

$$t_0(r) = t_0 / (1+s)^{\eta} \tag{8.16}$$

with $s = (r-a)/a$, where $r$ is the inter-atomic distance and $a$ the lattice constant. The exponent $\eta$ is varied, so that the experimental band gaps in Ref. [182] are reproduced. We obtain a value of $\eta = 11$, see blue curve in Fig. 8.10. This physically motivated scaling behaves approximately linearly in the region between $s = 0$ and $s = 0.04$, as depicted by the red line in Fig. 8.10. The band structure for different strain situations within this approach is depicted in Fig. 8.10.

In order to apply the above change of band gap, the strain-induced equilibrium position and inter-atomic distances need to be calculated. To this end, the valence force field method is employed, which has been introduced for the description of III-V semiconductor quantum dots. Within this approach, the reax potential [187, 188] is a suitable choice since it allows for an accurate description of both bond-stretching as well as in-plane and

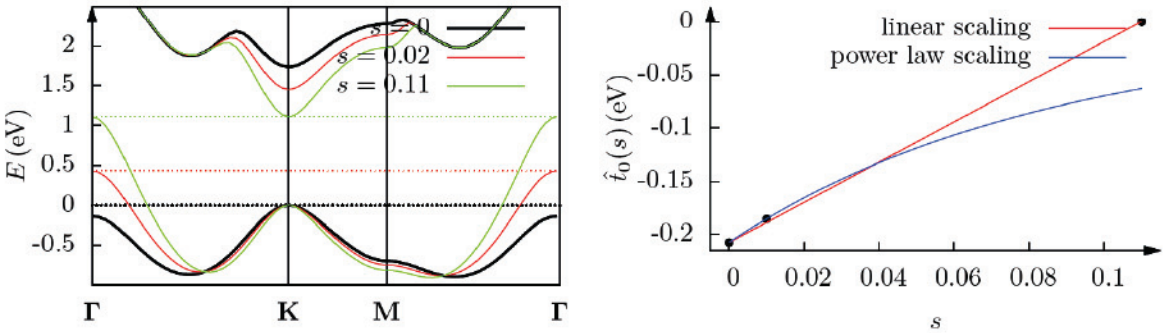


**Figure 8.10.** | **Strain effects**. Left: Band structure of a $MoS_2$ monolayer for different strain situations $s = (r - a)/a$, given through the linear scaling. The dashed lines indicate Fermi levels. Right: Linear scaling (red) and power law scaling (blue) for $t_0$ (Figs. by A. Schulz from Ref. [185]).

out-of-plane bond-bending. This potential includes the energy terms

$$E = E_{\text{bond}} + E_{\text{over}} + E_{\text{under}} + E_{\text{val}} + E_{\text{pen}} + E_{\text{tors}} + E_{\text{conj}} + E_{\text{vdWaals}} + E_{\text{Coulomb}}. \quad (8.17)$$

A detailed explanation of the individual terms is provided in Ref. [187]. Therefore, we only briefly discuss these terms. Aspects of the bond chemistry are included in the term $E_{\text{bond}}$. The summands $E_{\text{over}}$ and $E_{\text{under}}$ account for an over- and undercoordination, respectively. The energy $E_{\text{val}}$ describes deviations from the valence angle. To reproduce the stability of systems an additional energy penalty $E_{\text{pen}}$ can be imposed on atoms that strongly deviate from the equilibrium configuration. The term $E_{\text{tors}}$ describes the torsion angles and $E_{\text{conj}}$ the contribution of conjugation effects on the energy. Conjugation is the overlap of one p- or d-orbital with another across an intervening $\sigma$-bond, thereby bridging the interjacent single bonds. As a result, the $\pi$-electrons are delocalized and do not belong to a single bond or atom, but rather to a group of atoms. Additionally, van der Waals $E_{\text{vdWaals}}$ and Coulomb $E_{\text{Coulomb}}$ interactions, which account for a short-ranged repulsion and a long-ranged attraction, are included for all atom pairs. The reax force field parameters, which are used within this thesis are taken from Ref. [188].

### 8.3.3. Implementation of Dielectric Effect

In addition to strain, the band gap can also be modified by changing the interlayer distance as discussed in the introductory section. When reducing that distance from arbitrarily large values for a monolayer to only a few angstroms, one obtains a bilayer. In that case, not only the band gap changes, but also its character. ARPES[12] measurements by W. Jin et al. in Ref. [189] demonstrate that the $MoS_2$ monolayer band gap is direct, whereas

[12] Angle-resolved photoemission spectroscopy (ARPES), is an experimental technique to determine the electronic distribution in the reciprocal space of solids.

its bilayer band gap is indirect. In the following, we present a way of including both the change of band gap and its character into our TB model.

In order to determine the direct band gap $E_{\mathbf{K}}(z)$ as a function of the interlayer distance $z$, we use data from DFT+GW calculations from Ref. [184, 190]. We assume a bowing-like behavior for the height-dependent change of band gap. Correspondingly, a quadratic interpolation provides

$$E_{\mathbf{K}}(z) = 2.675 \cdot 10^{-5} z^2 + 0.0021 z + 2.3875 \tag{8.18}$$

for the direct band gap at the **K**-point. Additionally, we consider that the character of the band gap is height-dependent. This is reflected in the transition from a $MoS_2$ monolayer to a bilayer, which leads to a change from a direct band gap at the **K**-point to an indirect band gap between the **Γ**- and **K**-point at the VB and the CB, respectively. In the previous subsection, we have demonstrated that such a direct-indirect transition can be controlled by the hopping parameter $t_0$ in our TB model. To include both the height-dependent bowing curve (see Eq. (8.18)) and the height-dependent character of the band gap (see Ref. [189]), we determine the hopping parameter $t_0$ as a function of $E_{\mathbf{K}}(z)$. Consequence, the parameter $t_0$ in our TB model becomes height-dependent $t_0(z)$. As a result, we obtain

$$t_0(z) = -2\left(\frac{E_{\mathbf{K}}(z) - (\varepsilon_0 - \varepsilon_2)}{6} + t_{22} + t'_{22} - t'_{00}\right). \tag{8.19}$$

## 8.4. Modeling $MoS_2$ Nanobubbles

So far we have introduced the TMDC material system, ways of nanostructuring it, as well as a TB model to cover the corresponding physics. Based on this foundation, we investigate TMDC nanobubbles (see Fig. 8.11) that develop when air is enclosed during the stacking of layers. Such nanobubbles have been investigated by E. Khestanova et al. [24] or more recently by G. D. Shepard in Ref. [19]. The situation in these nanobubbles is analogous to the one in semiconductor quantum dots, where localized states can be engineered by variation of strain and band offset with respect to the host material. In the case of TMDC nanostructures, strain and a change of dielectric environment play a role. Within this chapter, we investigate the physics in TMDC nanostructures for the example of $MoS_2$ air nanobubbles, in which single-photon emission has been measured.

To examine the geometric shape of $MoS_2$ nanobubbles, we start from a paraboloid-shaped air bubble between two $MoS_2$ layers as shown in Fig. 8.12. We model this system by placing individual Mo and S atoms on a hexagonal lattice inside a rectangular supercell with periodic boundary conditions. The bottom layer defines the substrate and is therefore

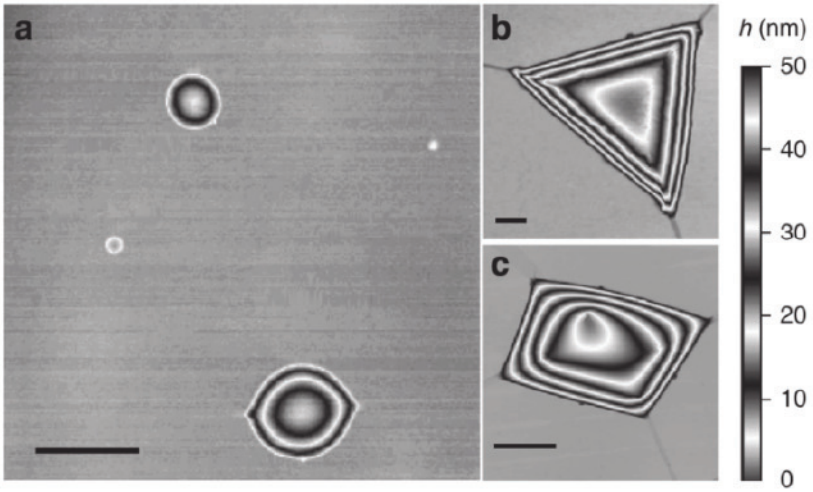


**Figure 8.11.** | **AFM images of bubbles**. Experimental results presented by E. Khestanova, et al. in Ref. [24]. Scale bars cover 500 nm (a), 100 nm (b) and 500 nm (c). The vertical scale for $h$ on the right indicates the height of the bubbles (Fig 1 from Ref. [24], `https://www.nature.com/articles/ncomms12587`, Creative Commons Attribution 4.0 International License `https://creativecommons.org/licenses/by/4.0/`).

kept fixed during the relaxation. On top of the substrate, we place a $MoS_2$ surface layer at an equilibrium distance of 3 Å in accordance with Ref. [188]. That layer is shorter in the lateral direction than the underlying substrate, so that the atoms of the surface layer can slide in the horizontal plane during the subsequent relaxation. The bubble is modeled by increasing the $z$-coordinate of the atoms within a given circle in the horizontal plane, so that these atoms are located on the surface of a paraboloid with height $h$ and radius $r$, leaving the $x$- and $y$-coordinates unchanged.

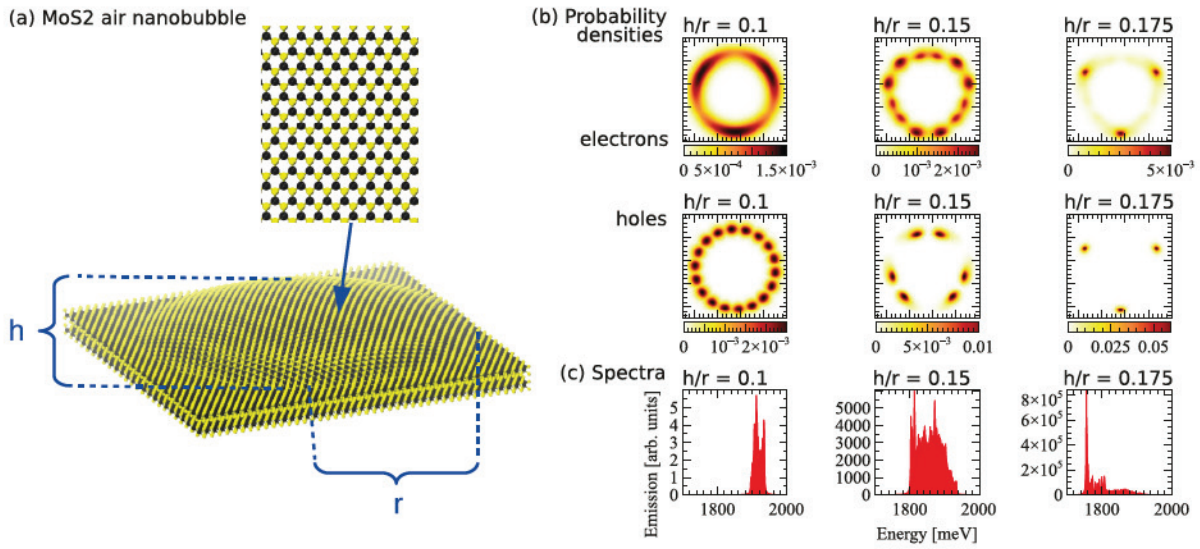


**Figure 8.12.** | **Nanobubble and representative results**. (a) $MoS_2$ bubble with radius $r$ and height $h$ and the corresponding atomic lattice. (b) Top view of the probability densities of electrons and holes states with the largest dipole transition matrix element for three representative aspect ratios $h/r$. (c) Single-particle emission spectra for the aspect ratios in (b).

In order to determine the strain-induced equilibrium atomic positions, we employ a valence force field calculation using the reax potential [187] implemented in the LAMMPS code [113] with a parametrization from Ref. [188]. The reax potential is computationally demanding, but ensures that the out of plane bending of the atoms is modeled in a satisfactory manner. To achieve convergence for the relaxed geometry, we utilize a supercell of dimensions $130\,\mathrm{nm} \times 130\,\mathrm{nm} \times 15\,\mathrm{nm}$, containing about $1.2 \cdot 10^6$ atoms. The relaxation is performed until a force tolerance of $10^{-3}\,\mathrm{eV/Å}$ or a relative energy tolerance of $10^{-16}$ is reached. Furthermore, in each iteration step, the charge equilibration energy is minimized until it reaches a value below $10^{-3}\,\mathrm{eV}$.

The relaxation process includes a set of initial and final atomic coordinates before and after the relaxation, respectively. The initial coordinates carry the full lattice symmetry, whereas the strain-induced equilibrium positions can slightly deviate from that symmetry. In order to preserve the underlying symmetry in any case, the final atomic coordinates are symmetrized after the relaxation. For this purpose, equivalent initial atoms with respect to the center of the bubble are determined as follows. During this procedure, only the Mo-atoms of the surface layer are considered. In a first step, the $x$- and $y$-coordinates of the center of the bubble are determined and the largest possible hexagon around this point is cut out from the supercell. In a second step, sets of three equivalent atoms with respect to the center of the bubble are formed. They are determined by rotating the atomic coordinates by $2\pi/3$ with respect to the center of the bubble. For a given atom, the first two rotations provide coordinates of equivalent atoms, while the third rotation returns the coordinates of that given atom. In the third step, the displacements

$$(\Delta x, \Delta y, \Delta z) = (x_f - x_i, y_f - y_i, z_f - z_i) \tag{8.20}$$

are determined, where the indices $i$ and $f$ denote the initial and final positions, respectively. In the next step, the atomic displacements for each triple of atoms $\{1, 2, 3\}$ are averaged

$$\begin{aligned}&(\Delta x_{1,2,3}, \Delta y_{1,2,3}, \Delta z_{1,2,3})\\ &= [(\Delta x_1, \Delta y_1, \Delta z_1) + (\Delta x_2, \Delta y_2, \Delta z_2) + (\Delta x_3, \Delta y_3, \Delta z_3)]/3.\end{aligned} \tag{8.21}$$

In the last step, the relaxed and symmetrized atomic coordinates are determined, which gives

$$(x_1, y_1, z_1) = (x_1^i, y_1^i, z_1^i) + (\Delta x_{1,2,3}, \Delta y_{1,2,3}, \Delta z_{1,2,3}) \tag{8.22}$$

for the atom 1. The so obtained atomic positions provide access to height profiles of $MoS_2$ bubbles for different aspect ratios $h/r$, which are depicted in Fig. 8.13(a). Due to the underlying lattice, our atomistically calculated height profile is broadened compared to the solid lines that are obtained from continuum elasticity theory (see Ref. [24]). According

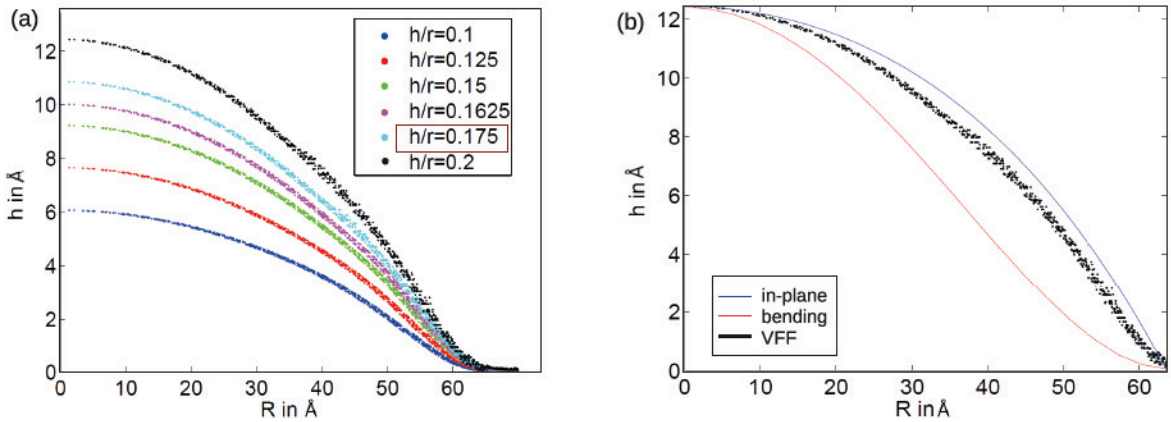


**Figure 8.13.** | **Height profiles of $MoS_2$ bubbles**. (a) Curves for different aspect ratios. The valence force field (VFF) results for the marked ratio of $h/r = 0.175$ are compared to results from E. Khestanova et al. [24] for dominantly in-plane strains (blue line) and bending (red line) in (b).

to Ref. [24] the two cases dominated by in-plane strain and bending can be discussed (see Fig. 8.13(b)). Since our calculated curve for the height profile of the bubble is located in between the ones obtained for in-plane strains and bending, we conclude that both aspects are included in our model.

Having discussed the strain-induced equilibrium positions of individual atoms, the atomic positions of the Mo atoms of the surface layer are incorporated into our TB Hamiltonian. Diagonalization provides access to the single-particle properties, in which strain and dielectric effects are included. As we will see in the following analysis, the height-to-radius ratio $h/r$ of the nanobubble has the dominant influence on the results. In Figs. 8.14 and 8.15, the probability densities for the confined electron and hole states with the largest dipole matrix element are depicted for different sizes and aspect ratios. For the discussion of the overall trends, we consider the situation in Fig. 8.12(b), where the probability densities for three representative aspect ratios of $h/r = 0.1$ (left panel), $h/r = 0.15$ (middle panel) and $h/r = 0.175$ (right panel) for a bubble of radius $r = 18\,\text{nm}$ are depicted. In the case of the smallest aspect ratio $h/r = 0.1$, the charge carrier probability densities follow a ring-like shape along the edge of the nanobubble. The electron distribution exhibits a rather strong radial broadening and three distinct maxima, while the hole distribution shows a multitude of maxima along the circumference of the bubble. For an increased aspect ratio of $h/r = 0.15$ the behavior changes considerably. The probability density of electrons shows a pattern of two subgroups of maxima, each with the $C_{3v}$ symmetry of the underlying crystal lattice and an extension of a few nanometers. For the holes only one set of maxima is found. The trend of stronger localization with increasing aspect ratio is confirmed for $h/r = 0.175$. In this case, the electron and hole wave functions, which are responsible for the strongest optical transition, are localized at only three maxima at the

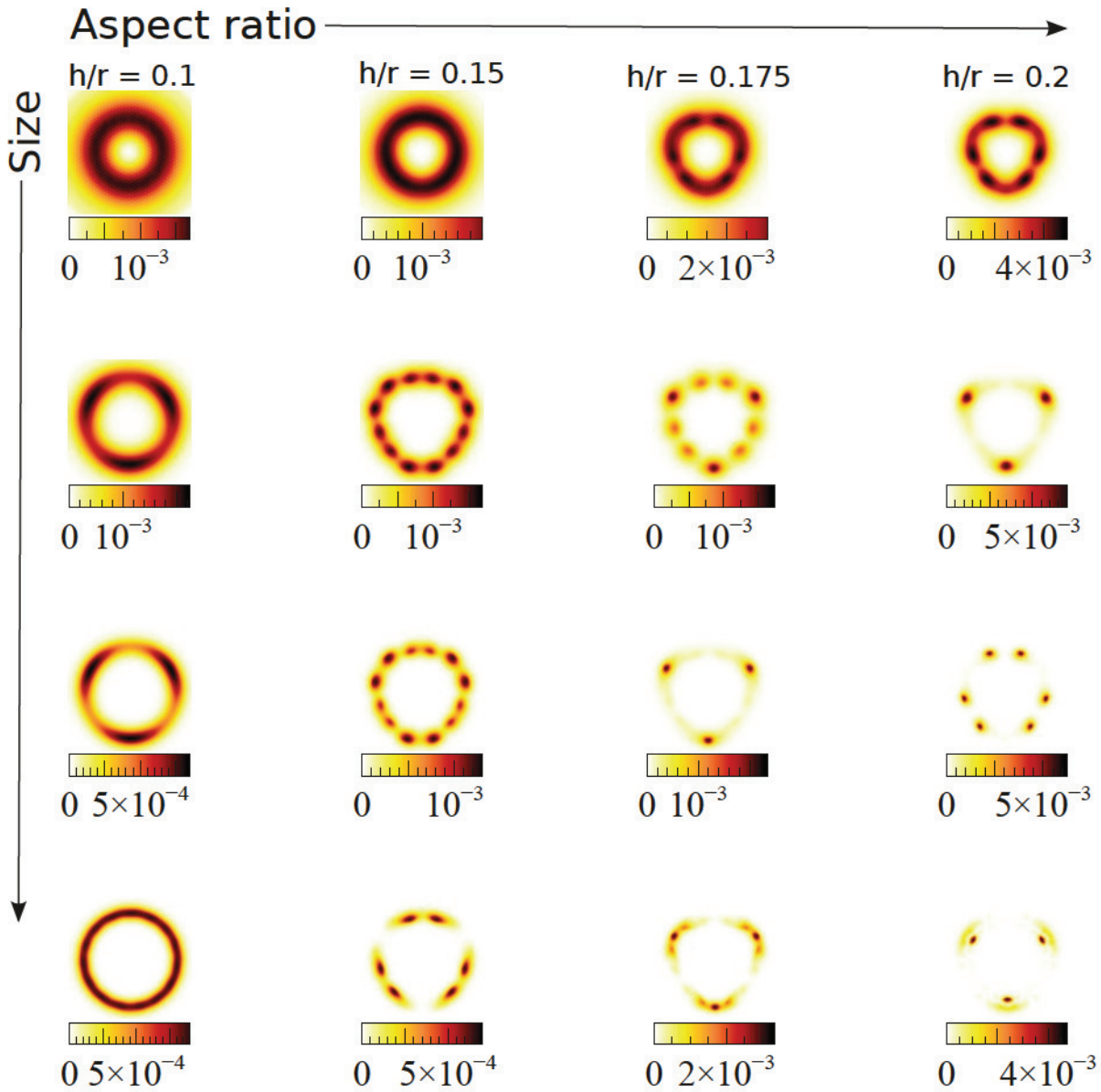


**Figure 8.14. | Probability densities of electrons.** Rowwise: radius $r = [6, 12, 18, 24]$ nm. Columnwise: aspect ratio $h/r$ =[0.1, 0.15, 0.175, 0.2]. The third row for $r = 18$ nm corresponds to the situation in Fig. 8.12(b).

edge of the nanobubble. This localization has consequences for the optical spectra. The single-particle emission spectra, which is obtained from Fermi's golden rule, for different sizes and aspect ratios are displayed in Fig. 8.16. For the discussion we consider the representative situation as depicted in Fig. 8.12(c). In the highly symmetric situation (left panel of Fig. 8.12), the wave functions posses a high degree of degeneracy. In this case, only few very weak emission lines are observed in the optical spectra. One reason for the small dipole interaction matrix element is the much larger radial broadening of the probability density for the electrons than for the holes. As the wave functions start to localize in different parts of the nano-bubble for higher aspect ratios, the degeneracy is lifted and consequently a large number of optical transitions is found. For an aspect ratio of

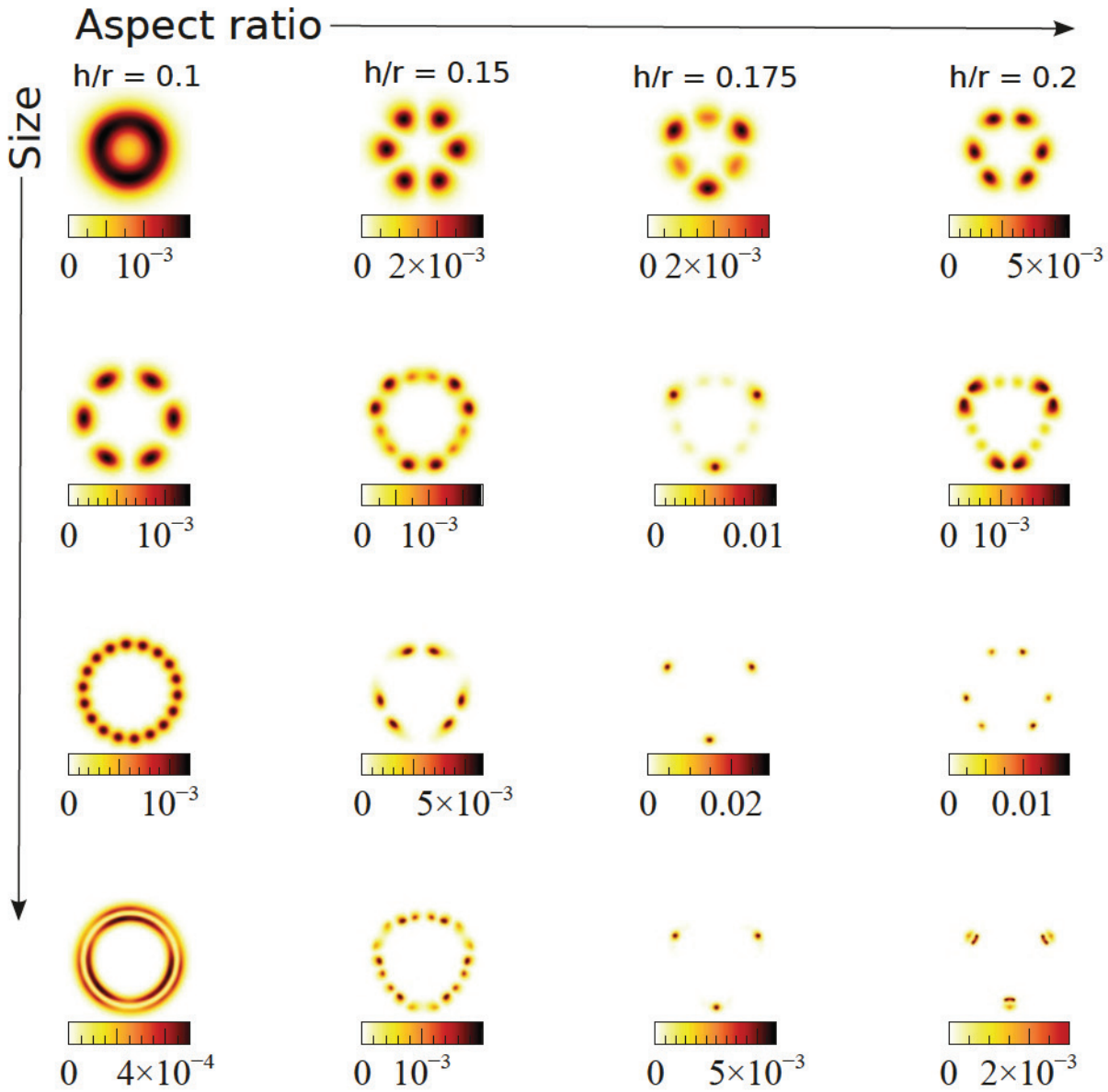


**Figure 8.15. | Probability densities of holes.** Rowwise: radius $r = [6, 12, 18, 24]$ nm. Columnwise: aspect ratio $h/r$ =[0.1, 0.15, 0.175, 0.2]. The third row for $r = 18$ nm corresponds to the situation in Fig. 8.12(b).

$h/r = 0.15$, we observe a broad emission from a multitude of states with moderate emission intensity. The emission spectra for $h/r = 0.175$ show strong emission from the electron and hole states depicted in Fig. 8.12(b) (right panel), as well as a broad background emission from other states. Such spectra are in agreement with the experimental results presented in Ref. [19], where single-photon emission has been demonstrated.

For an analysis of the underlying physics of the results in Fig. 8.12, we discuss the contributions of strain and dielectric environment to the confinement situation. Due to the geometry of the nanobubble, the dielectric situation corresponds to a bilayer outside of the nanobubble. In the center, where the distance between top and bottom layer is large, the situation approaches that of a monolayer (see Fig. 8.17). This effect increases

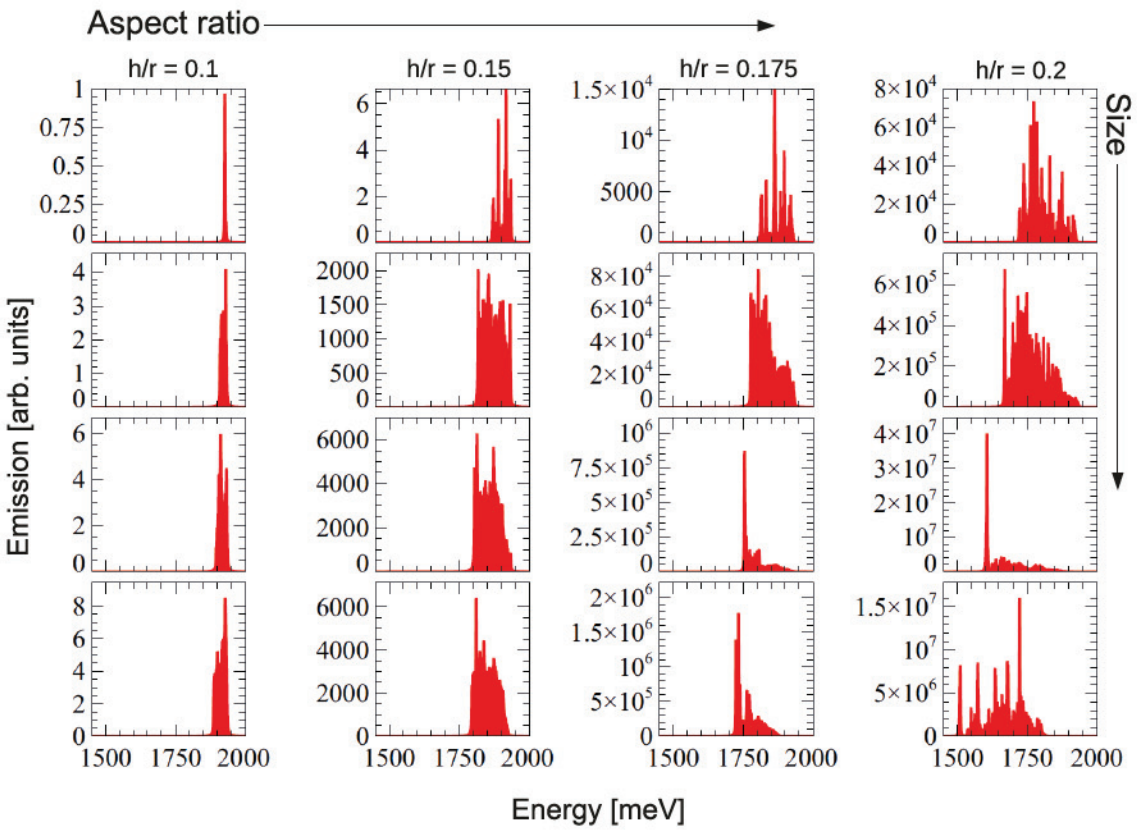


**Figure 8.16.** | **Single-particle emission spectra**. Rowwise: radius $r = [6, 12, 18, 24]$ nm. Columnwise: aspect ratio $h/r = [0.1, 0.15, 0.175, 0.2]$. The third row for $r = 18$ nm corresponds to the situation in Fig. 8.12(b).

with increasing height of the bubble, resulting in a height-dependent change of band gap. The change of band gap inside the nanobubble is shown in Fig. 8.17(c). Due to the (almost) radially symmetric geometry of the bubble, the change of band gap is also radially-symmetric. We find changes of band gap on the order of 100 meV, consistent with recent measurements in Ref. [49]. In our case, the dielectric environment effectively leads to a repulsive potential in the center of the bubble and causes the wave functions to be pushed outwards.

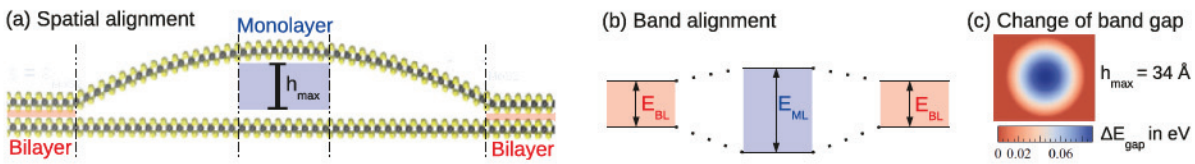


**Figure 8.17.** | **Dielectric effect**. (a) Cross-section through the nanobubble of height $h_{\max}$. (b) Illustration of the band alignment for the situation in (a). (c) Dielectric-induced repulsive potential inside the nanobubble of height $h_{\max} = 34$ Å.

On the other hand, strain leads to a confinement inside the nanobubble due to different inter-atomic distances and a local change of band gap. To provide an overview of both effects, the effective potential, including strain and dielectric shifts, is displayed in Fig. 8.18.

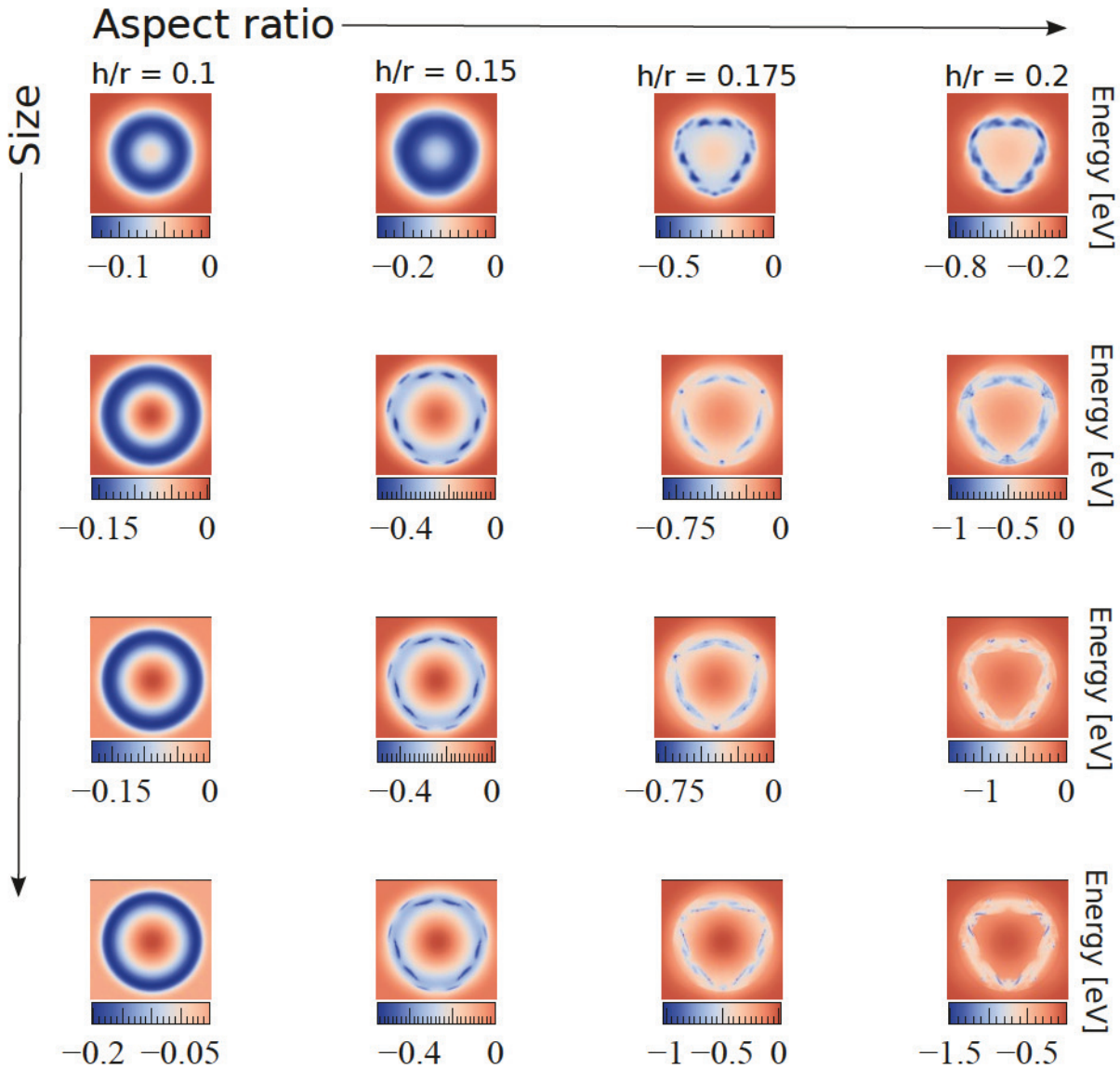


**Figure 8.18. | Effective confinement potential.** Rowwise: radius $r = [6, 12, 18, 24]$ nm. Columnwise: aspect ratio $h/r$ =[0.1, 0.15, 0.175, 0.2]. The third row for $r = 18$ nm corresponds to the situation in Fig. 8.12(b).

From these results we conclude that the repulsive dielectric effect is minor compared to the strain-induced confinement in the nanobubble. Consequently, strain effects are responsible for the increasing localization. A spatial correspondence between strain and localization is in accordance with recent experimental claims, presented in Refs. [14, 15, 16].

For a more detailed analysis of strain effects, we consider the strain-induced shift of band gap for a bubble of radius $r = 18$ nm in Fig. 8.19(a). For both aspect ratios of $h/r = 0.15$ and $h/r = 0.175$, two sets of strain pockets are found (see Fig. 8.19(b)). Each of these sets is located at a different radius and carries the $C_{3v}$ symmetry of the underlying crystal lattice. To illuminate the origin of these strain pockets, the average angle $\alpha$ between normal vectors at neighboring unit cells (as schematically depicted in

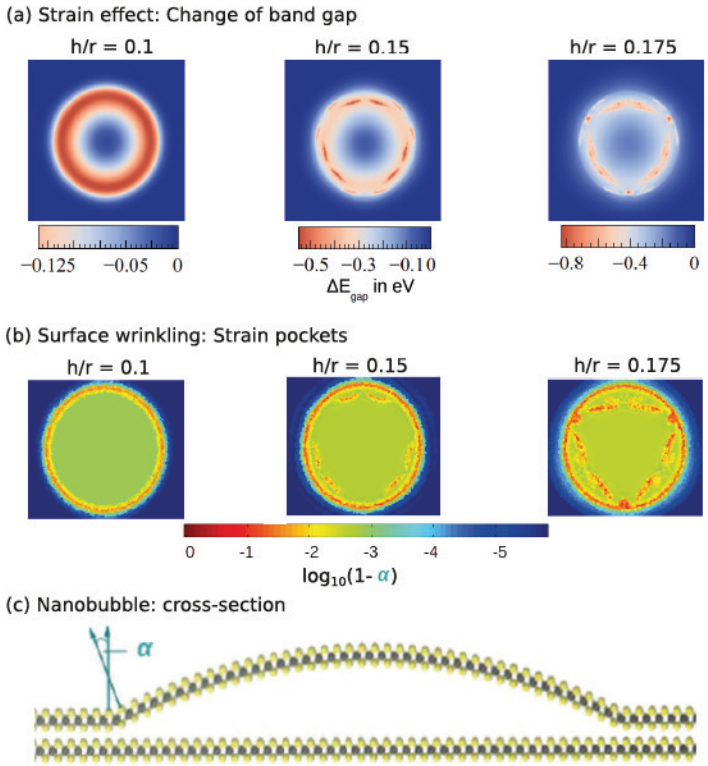


**Figure 8.19.** | **Strain effect**. (a) Strain-induced shift of band gap for different aspect ratios $h/r$. (b) Average angle $\alpha$ (radians) between normal vectors of neighboring unit cells on discretized surface reveals wrinkling that spatially corresponds to the strain pockets. (c) Cross-section through the nanobubble of height $h_{\max}$. The geometric situation implies a change of the dielectric environment for the $MoS_2$ surface layer that is forming the nanobubble. The arrows green arrows illustrate an angle $\alpha$ between normal vectors of neighboring unit cells on the discretized surface as used in (b).

Fig. 8.19(c)) is investigated by means of the normal-normal correlation

$$N_i = \frac{1}{3} \sum_{j,\text{neighbors}} \mathbf{n}_i \cdot \mathbf{n}_j = \frac{1}{3} \sum_{j,\text{neighbors}} \cos\left[\angle(\mathbf{n}_i, \mathbf{n}_j)\right]. \tag{8.23}$$

Due to the symmetry of the system, each cell $i$ has three neighboring cells $j$, which is accounted for by the normalization factor $1/3$. The average angles $\alpha = \arccos(3N_i)$ are displayed in Fig. 8.19(b). They reveal a wrinkling of the surface for aspect ratios of $h/r = 0.15$ and $h/r = 0.175$, as these angles $\alpha$ between the normal vectors of neighboring unit cells vary up to 6°. A comparison between Figs. 8.19(a) and (b) shows that this wrinkle formation spatially corresponds to the areas of maximal strain. The physical reason for this behavior can be traced back to the high Young's modulus of of $MoS_2$ (and other TMDCs). The higher the modulus, the better a material resists against compression/elongation. Consequently, especially for a high modulus, the material tends to minimize its total change of length. In particular, this is possible by introducing a wrinkle as illustrated in Fig. 8.20. On the other hand, this requires a bond-bending for atomically thin layers. Energetically, it is more favorable to strain/bend the material strongly in small areas

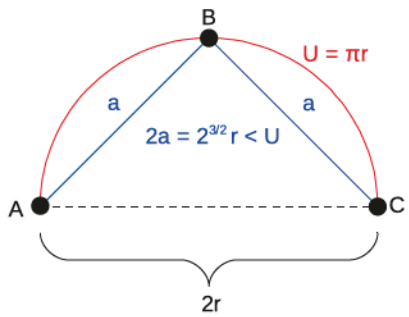


**Figure 8.20.** | **Illustration of wrinkling**. Consider the connection between A, B, and C. Red: The material is bent uniformly, the total distance is $U = \pi r$. Blue: The overall elongation of the material is minimized by forming a wrinkle.

of the nanobubble than in a moderate amount over the whole system. This causes the formation of wrinkles, which are especially pronounced for an aspect ratio of $h/r = 0.175$. In that case, both the normal-normal correlation and the strain-induced shift of band gap reveal deep strain pockets (see Fig. 8.19(a,b)). These pockets cause a localization of the wave function as seen in Fig. 8.12(b).

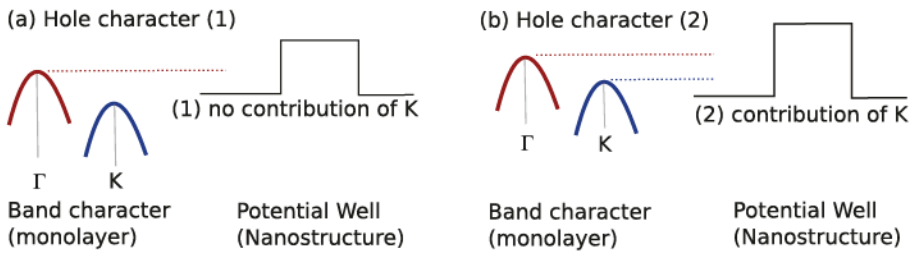


**Figure 8.21.** | **Orbital character of hole states**. (a) and (b) The contribution of **K** depends on the confinement situations (1) and (2).

In the following, we analyze the change of the dipole strength, which increases by several orders of magnitude for increasing aspect ratio, as seen in the spectra in Figs. 8.12(c) and 8.16. The main physical reason for this is illustrated in Fig. 8.21. The localized single-particle states, originating from the CB, inherit the orbital character $d_{z^2}$ of the **K**-point (see Fig. 8.10). Depending on the depth of the confinement potential, the orbital character of the localized hole states is either determined by states originating from the **Γ**-point ($d_{z^2}$), or from both the **Γ**- and the **K**-point ($d_{xy}$). In the former case, the emission is weak, as the orbital character of the electron and hole wave functions is the same ($d_{z^2}$). In the latter case, the hole states partially possess the orbital character $d_{xy}$ and a strong dipole moment with electrons of character $d_{z^2}$ is possible, as known from the 2D monolayer [184].

Summarizing the results for the example of $MoS_2$ nanobubbles as TMDC-based nanostructures, the relative strength of dielectric- and strain-induced potentials is approximately 1 to 3. However, this is strongly dependent on the strain and substrate situation.

In principle, both effects can be used equally to engineer the confinement situation and single-particle properties in TMDC-based nanostructures, with strain leading universally to a confinement, whereas depending on the environment, the dielectric effect can cause both repulsive and confinement potentials. Additionally, our results show that the strain situation in such bended TMDC structures is governed by surface wrinkling, leading to the formation of strain pockets. Such structural changes have an impact on the electronic properties, which change from ring-like states to strongly localized states. These interesting physics provide a basis for investigations of various TMDC nanostructures.

# 9. Summary and Outlook

The present work achieved an understanding of the interplay between morphology, electronic, and optical properties of semiconductor nanostructures for single-photon emission. The latter is important for quantum information applications and in particular quantum key distribution. Essential technical requirements and corresponding physical problems for single-photon sources include an ease of fabrication as well as an on-demand generation of single-photons with high repetition rate and tunable emission energy. In this work, we modeled two distinct material systems, which hold different advantages as possible single-photon sources. On the one hand, we presented results on the relatively established system of III-V semiconductor quantum dots and explained in detail the mechanism behind emission in the technologically important telecom C-band. On the other hand, we investigated single-photon emission in rather new TMDC-based nanostructures. These systems offer a relative ease of fabrication and the potential for large-scale applications. The results provide a deeper understanding of the interplay between strain, dielectric effects, electronic, and optical properties of the investigated systems.

## 9.1. III-V Semiconductors

After an introduction into the fundamental properties of III-V semiconductors and quantum dots, we presented details about the tight-binding theory for the calculation of confined electron and hole bound states and energies. We discussed the differences in modeling semiconductor bulk band structures and bound states in nanostructures, such as quantum dots, for which we include relevant influences like spin-orbit coupling and strain. To determine the strain-induced equilibrium positions, we employed a valence force field calculation that was combined with our tight-binding model. For both methods, we provided numerical details for the implementation. Based on electronic-state calculations, the derivation of Coulomb and dipole matrix elements from the tight-binding coefficients was presented in detail. For the subsequent determination of the many-body Coulomb-correlated eigenstates and optical spectra, we combine the configuration-interaction method with Fermi's golden rule.

Based on this theoretical foundation, we presented results for two different quantum dot systems for single-photon emission in the technologically important telecom C-band. First, we investigated a quaternary InAlGaAs material system in collaboration with the groups of Prof. Reithmaier in Kassel and Prof. Rosenauer in Bremen. For an experimentally characterized QD, we discussed the influence of size and concentration fluctuations on the single-particle emission spectra. Our atomistic TB simulations showed that composition fluctuations within the QD ensemble can modify the emission energy by about 200 meV, whereas size fluctuations have a reduced influence in these rather large QDs. Secondly, we investigated a ternary InGaAs quantum dot material system in collaboration with the groups of Prof. Michler in Stuttgart and Prof. Rosenauer in Bremen. As for the quaternary material system, our atomistic TB calculations for the single-particle states and transitions were based on experimental characterizations. Our calculations showed that the experimentally determined size and alloy concentration leads to an emission in the telecom C-band. Taking into account the inhomogeneous broadening, one finds QDs with In concentrations of $(70 \pm 2)\%$ that contribute to the emission within the experimentally observed energy range. Compared to concentration fluctuations, size fluctuations at a fixed aspect ratio of $h/d = 0.2$ have a reduced influence, which is typical for relatively large QDs. As a consequence of the weak dependence on size fluctuations, QDs with diameters of $(63 \pm 12)$ nm contributed to the emission within the experimentally observed energy range. For a more detailed analysis of the QD emission properties, multi-exciton lines of a single QD were identified by means of experimental measurements and effective mass calculations. For both QD systems, the results provide a deeper understanding of the connection between morphology, composition, electronic and optical properties.

### Outlook

There are several possibilities for further work on III-V semiconductor quantum dots. Regarding the quaternary InAlGaAs quantum dots with rather large concentration fluctuations, a second generation of InAs/InP quantum dots has recently been grown in Kassel in the group of Prof. Reithmaier for the emission in the telecom C-band. For this novel structure, a similar structural, optical, and theoretical characterization compared to the InAlGaAs quantum dots could be interesting.

An alternative system for single-photon emission are AlGaAs quantum dots as presented in Ref. [13]. On the one hand, due to the material composition the emission energy obviously cannot reach the telecom C-band. On the other hand, AlAs and GaAs are lattice-matched, which allows for the production of quantum dots without strain and fixed size and high symmetry by droplet etching and nanohole infilling. These QDs exhibit an averaged fine-structure splitting of $4.8 \pm 2.4\,\mu$eV, short radiative lifetimes of $< 220$ ps, entanglement

fidelities of 0.91, and concurrence rates of 0.90 [13]. In order to combine these findings with theoretical results, we have recently started a collaboration with the group of Prof. Fei Ding in Hannover.

For all considered quantum dot systems the calculation of the fine-structure splitting remains an important property to be studied. Here, not only a comparison of experiment and theory, but also finding a way to systematically reduce the fine-structure splitting would be of interest. A necessary step towards obtaining that quantity is the calculation of the electron-hole exchange Coulomb matrix elements. Due to the large size of the present quantum dots, hundreds of electron and hole states with a small level-spacing of only a few milli-electron volts are confined inside the quantum dot. As a result, many combinations of states for the Coulomb matrix elements have to be taken into account to obtain converged results. This is a challenge that can be tackled in future work.

From a theoretical point of view, one could extend the nearest neighbor $sp^3s^*$ tight-binding model by additionally including next nearest neighbors and/or $d$ orbitals, which would require further computationally cost. Even though band structures and bowing curves are already reproduced with our nearest neighbor $sp^3s^*$ basis set, a comparison with a larger basis set could provide further insight about the accuracy of the presented model. In this work, the individual tight-binding parameters for the different binary compounds (InAs, GaAs, and AlAs) have been averaged in a way that the best agreement with reference data is obtained. An improvement could be to provide a common set of parameters, in which the matrix elements for the arsenic atoms do not deviate between the different compounds. In that case, no averaging procedures would be necessary.

## 9.2. Molybdenum Disulfide Nanobubbles

In the second part of the thesis, we discussed atomically thin TMDCs as an alternative platform for single-photon emission. We presented different possibilities of nanostructuring this material system. As an example, we discussed $MoS_2$ air nanobubbles that develop when air is enclosed during the stacking of layers. After an introduction to the material system and its basic properties, we presented details about a $MoS_2$ monolayer tight-binding model. Subsequently, we extended that tight-binding model to describe $MoS_2$ nanobubbles. To this end, we provided a way to atomistically include strain effects in a proper and robust way in the valence force field method. Additionally, we included a height-dependent change of band gap to account for the change of dielectric environment and screening.

Our novel results showed that the central property in these nanobubbles is the height-to-radius ratio $h/r$. This quantity drives the transition from a ring-like shape of confinement

potential and wave functions towards the localization in strain pockets, which carry the $C_{3v}$-symmetry of the underlying lattice. The formation of these pockets was analyzed by means of the angle between normal vectors of the surface, which is accessible via the normal-normal correlation. This analysis revealed a direct spatial correspondence between wrinkling of the surface and regions of maximum strain. Consequently, we concluded that the origin of the strain pockets can be traced back to the high bending rigidity, which causes an energetically favorable unisotropic strain configuration. Such a behavior is characteristic for TMDCs in general and is not limited to $MoS_2$, which makes it possible to extend this analysis to similar TMDC material systems. On top of that, the physics in $MoS_2$ nanobubbles form the basis for further investigations of various TMDC nanostructures and structural phase transitions in layered materials.

### Outlook

As discussed in this thesis, an atomistic model for $MoS_2$ nanobubbles is provided as an example for similar nanostructures in TMDCs. From a physical point of view, it could be interesting to investigate different geometries, shapes, and materials for TMDC-based nanostructures. Recent experimental situations range from radially symmetric and triangular nanobubbles to TMDCs on top of holes and arrays of pillars. These experiments open a new field of designing TMDC nanostructures for various potential applications. As a material not only $MoS_2$ monolayers, but also $WS_2$, $MoSe_2$, and $WSe_2$ are of interest due to their direct band gap in the visible frequency range. In order to shed light on the physics in various TMDC-based nanostructures, we have recently started a collaboration with the group of Prof. Finley in München.

From a numerical point of view, only a parametrization for $MoS_2$ is currently available in terms of the reax potential that we employ within the valence force field method. For the description of different substrates, an additional parametrization is required, which could be part of future work.

# A. Appendix

## A.1. Tight-Binding Parameters for III-V Semiconductors

The individual parameters for III-V semiconductor bulk materials are listed in Table A.1. The parameters in Ref. [191] have been explicitly designed for the calculation of heterostructures, while the authors of Ref. [192] focused on effective-mass reproducibility. Note that some references provide a value of $3\lambda$, which is the overall value for the spin-orbit

| Parameter | GaAs (Ref. [191]) | InAs (Ref. [191]) | AlAs (Ref. [192]) |
|---|---|---|---|
| $\mathbf{E}_s^a$ | -9.2664 | -9.3562 | -8.381160 |
| $\mathbf{E}_s^c$ | -4.3504 | -3.9611 | -1.744670 |
| $\mathbf{E}_p^a$ | +1.4866 | +1.8201 | +0.229440 |
| $\mathbf{E}_p^c$ | +3.2136 | +3.1842 | +2.832840 |
| $\mathbf{E}_{s^*}^a$ | +8.7826 | +7.0432 | +6.730574 |
| $\mathbf{E}_{s^*}^c$ | +5.8765 | +6.1232 | +5.972840 |
| $\mathbf{V}_{ss}^{ac}$ | -7.9480 | -6.5393 | -6.66420 |
| $\mathbf{V}_{sx}^{ac}$ | +2.7777 | +4.3607 | +5.60000 |
| $\mathbf{V}_{xs}^{ac}$ | +10.005 | +7.0849 | +6.80000 |
| $\mathbf{V}_{s^*x}^{ac}$ | +3.6271 | +3.0007 | +4.22000 |
| $\mathbf{V}_{xs^*}^{ac}$ | +7.0071 | +5.4020 | +7.30000 |
| $\mathbf{V}_{xx}^{ac}$ | +2.3069 | +2.5491 | +1.87800 |
| $\mathbf{V}_{xy}^{ac}$ | +5.0305 | +5.4700 | +3.86000 |
| $\lambda_a$ | +0.140 | +0.140 | +0.14000 |
| $\lambda_c$ | +0.058 | +0.131 | +0.00800 |

Table A.1.: List of TB parameters used in this thesis.

coupling. In Table A.1, we list a value of $\lambda$ since it enters the TB model numerically for each of the three contributions of the $p_x, p_y$ and $p_z$ orbitals. The TB parameters in Table A.1 are used within this work for the description of binary, ternary, and quaternary material compounds as well as quantum dots.

## A.2. Neighbor Numbers

Based on the reverse lexicographic ordering of the atoms in Fig. 4.3, the nearest neighbor numbers can be determined in a numerically advantageous way as demonstrated below. The connecting vectors between a cation and its four nearest neighbors in units of $a/4$

are given by

$$\begin{aligned} v_1 &= (1,1,1), \\ v_2 &= (-1,1,-1), \\ v_3 &= (-1,-1,1), \\ v_4 &= (1,-1,-1). \end{aligned} \tag{A.1}$$

As a result, for an atom, which is located at $(x, y, z)$, we can specify the coordinates $(nx, ny, nz)$ of a nearest neighbor $i \in \{1, 2, 3, 4\}$ via

$$\begin{aligned} nx &= \text{modulo}\left[x + v_i(x) \cdot (-1)^{z+1}, 4 \cdot \text{cellnr}(xy)\right], \\ ny &= \text{modulo}\left[y + v_i(y) \cdot (-1)^{z+1}, 4 \cdot \text{cellnr}(xy)\right], \\ nz &= \text{modulo}\left[z + v_i(z) \cdot (-1)^{z+1}, 4 \cdot \text{cellnr}(z)\right] \end{aligned} \tag{A.2}$$

by taking into account periodic boundary conditions. Here, $\text{cellnr}(xy)$ and $\text{cellnr}(z)$ are the numbers of unit cells in $xy$- and $z$-direction, respectively. Due to the choice of numbering the atoms in reverse lexicographical order, we can determine the atom number corresponding to a given neighbor position $(nx, ny, nz)$ by counting the number of atoms that occur below, in front of, and left to that atom via

$$\begin{aligned} \text{below} &= 2 \cdot \text{cellnr}(xy)^2 \cdot nz, \\ \text{front} &= \text{cellnr}(xy) \cdot \text{floor}(ny/2), \\ \text{left} &= \text{floor}(nx/4). \end{aligned} \tag{A.3}$$

As a result, for an atom located at $(nx, ny, nz)$, we obtain the corresponding atom number by

$$\text{num} = \text{below} + \text{front} + \text{left} + 1. \tag{A.4}$$

The above procedure takes advantage of the choice of numbering and provides atom numbers, atom coordinates, neighbor numbers, and neighbor coordinates simultaneously and scales linearly with the number of atoms, which is particularly important for large systems.

# A.3. Force Field Parameters

## A.3.1. Keating Potential

In the Keating potential, in principle all $4^3 = 64$ combinations of triplets $\{i, j, k\}$, composed of the four elements {In,Ga,Al,As}, need to be considered for the parametrization. However, due to the crystal structure, each anion lattice-site is adjacent to a cation and vice versa. Consequently, only those configurations are relevant, in which one anion and two cations occur or vice versa. They are listed in Table A.2.

| $\{i, j, k\}$ | $r_0$ | $\alpha$ | $\beta$ | $\cos\theta_0$ | $r_{\text{cut}}$ |
|---|---|---|---|---|---|
| **As Ga Ga** | 2.45 | 2.47 | 0.57 | -0.33 | 3.22 |
| As Ga In | 2.54 | 2.27 | 0.47 | -0.33 | 3.34 |
| **As Ga Al** | 2.45 | 2.52 | 0.57 | -0.33 | 3.22 |
| As In Ga | 2.54 | 2.27 | 0.47 | -0.33 | 3.34 |
| **As In In** | 2.62 | 2.08 | 0.36 | -0.33 | 3.45 |
| As In Al | 2.54 | 2.32 | 0.46 | -0.33 | 3.34 |
| **As Al Ga** | 2.45 | 2.52 | 0.57 | -0.33 | 3.22 |
| As Al In | 2.54 | 2.32 | 0.46 | -0.33 | 3.34 |
| **As Al Al** | 2.45 | 2.57 | 0.56 | -0.33 | 3.23 |
| Ga As As | 2.45 | 2.47 | 0.57 | -0.33 | 3.22 |
| **In As As** | 2.62 | 2.08 | 0.36 | -0.33 | 3.45 |
| Al As As | 2.45 | 2.57 | 0.56 | -0.33 | 3.23 |

Table A.2.: Force-field parameters in LAMMPS 'metal' units. Note that these values are rounded. The constants $\alpha$ and $\beta$ are in eV/(Å$^2$), whereas the equilibrium bond length $r_0 = a\sqrt{3}/4$ and the cut-off radius $r_{\text{cut}}$ are in Å. The bond angle $\cos\theta_0$ is unit-less. The cut-off radius $r_{\text{cut}} = (r_{\text{NNN}} - r_{\text{NN}})/2 + r_{\text{NN}}$ is chosen in a way that it includes nearest neighbors (NN), but excludes next-nearest neighbors (NNN) from the interaction.

## A.3.2. Tersoff Potential

In the Tersoff potential, the interaction between atoms is described by triplets $\{i, j, k\}$. Here, element $i$ is the center atom in a 3-body interaction, element $j$ is the atom bonded to the center atom, and element $k$ is an additional atom influencing the $ij$-bond in a bond-order sense. As in the case of the Keating potential, only those configurations of triplets $\{i, j, k\}$ are relevant, in which one anion and two cations occur or vice versa. Since

the parametrizations are only made for two different atom types, the following mixing rules are applied:

$$\begin{aligned}
\lambda_1^{i,j} &= \frac{1}{2}\left(\lambda_1^i + \lambda_1^j\right) \\
\lambda_2^{i,j} &= \frac{1}{2}\left(\lambda_2^i + \lambda_2^j\right) \\
A_{i,j} &= \left(A_i A_j\right)^{1/2} \\
B_{i,j} &= \left(B_i B_j\right)^{1/2} \\
R'_{i,j} &= \left(R'_i R'_j\right)^{1/2} \\
S'_{i,j} &= \left(S'_i S'_j\right)^{1/2} .
\end{aligned} \tag{A.5}$$

Note that when utilizing the LAMMPS code, the parameters $R'$ and $S'$ must be converted to $R$ and $D$ by using the relations $R = (R' + S')/2$ and $D = (S' - R')/2$. The utilized parameters are listed in Table A.3.

| $\{i,j,k\}$ | $m$ | $\gamma$ | $\lambda_3$ | $c$ | $d$ | $\cos\theta_0$ | $n$ | $\beta$ | $\lambda_2$ | $B$ | $R$ | $D$ | $\lambda_1$ | $A$ |
|---|---|---|---|---|---|---|---|---|---|---|---|---|---|---|
| **As Ga Ga** | 3 | 1 | 0.2 | 2.2 | 0.8 | -0.5 | 3.6 | 0.3 | 0.8 | 16.0 | 3.5 | 0.1 | 5.8 | 4.5e5 |
| As Ga In | 3 | 1 | 0.2 | 2.2 | 0.8 | -0.5 | 3.6 | 0.3 | 1.3 | 113.9 | 3.5 | 0.1 | 4.1 | 3.6e4 |
| **As Ga Al** | 3 | 1 | 0.8 | 2.2 | 0.8 | -0.5 | 3.6 | 0.3 | 1.2 | 72.8 | 3.6 | 0.1 | 1.8 | 2.8e4 |
| As In Ga | 3 | 1 | 0.2 | 2.1 | 0.8 | -0.5 | 2.4 | 0.1 | 1.3 | 113.9 | 3.5 | 0.1 | 4.1 | 3.6e4 |
| **As In In** | 3 | 1 | 0.1 | 2.1 | 0.8 | -0.5 | 2.4 | 0.1 | 1.8 | 809.2 | 3.7 | 0.1 | 2.4 | 2.9e3 |
| As In Al | 3 | 1 | 0.8 | 2.1 | 0.8 | -0.5 | 2.4 | 0.1 | 1.7 | 517.5 | 3.6 | 0.1 | 2.5 | 2.3e3 |
| **As Al Ga** | 3 | 1 | 0.8 | 1.0 | 0.9 | -0.5 | 8.4 | 0.4 | 1.2 | 72.8 | 3.6 | 0.1 | 1.8 | 2.8e4 |
| As Al In | 3 | 1 | 0.8 | 1.0 | 0.9 | -0.5 | 8.4 | 0.4 | 1.7 | 517.5 | 3.6 | 0.1 | 2.5 | 2.3e3 |
| **As Al Al** | 3 | 1 | 1.4 | 1.0 | 0.9 | -0.5 | 8.4 | 0.4 | 1.7 | 331.0 | 3.7 | 0.1 | 2.5 | 1.8e3 |
| Ga As As | 3 | 1 | 0.2 | 2.2 | 0.8 | -0.5 | 3.6 | 0.3 | 0.8 | 16.0 | 3.5 | 0.1 | 5.8 | 4.5e5 |
| **In As As** | 3 | 1 | 0.1 | 2.1 | 0.8 | -0.5 | 2.4 | 0.1 | 1.8 | 809.2 | 3.7 | 0.1 | 2.4 | 2.9e3 |
| Al As As | 3 | 1 | 1.4 | 1.0 | 0.9 | -0.5 | 8.4 | 0.4 | 1.7 | 331.0 | 3.7 | 0.1 | 2.5 | 1.8e3 |

Table A.3.: Force-field parameters (from Ref. [112]) for the Tersoff potential in LAMMPS 'metal' units, which are used in this thesis. The parameters $\lambda_i$ are in 1/Å, $A$, and $B$ in eV, and $R, D$ in Å. Other quantities are unit-less. Note that the above parameters are rounded except for $m, \gamma$, and $D$.

### A.3.3. Energy Minimization

An example LAMMPS input file that includes the atomic coordinates corresponding to the example in Fig. 4.3 is presented in Table A.4. It contains the size of the supercell, the number of atoms, the atom types, as well as their corresponding coordinates and masses.

An example of the LAMMPS commands that have been employed to perform an energy relaxation are listed in Table A.5.

Of course some input variables/data/names are examples and can be modified to suit one's needs/preferences. However, it is recommended to employ the conjugate gradient algorithm for energy minimization at all times. While using the conjugate gradient algorithm it is a good choice to set the value 'dmax', which limits the maximal spatial displacement of a single atom in one iteration, to 0.0005 to achieve a converged computation. Furthermore, a force tolerance of $10^{-3}$ eV/Å is reasonable from a physical point of view, since this is typically the tolerance that can be obtained from quantum mechanical state of the art DFT calculations. Therefore, this accuracy physically represents an upper bound for the classical VFF method. When choosing this force tolerance and an arbitrary large number of iteration steps, the energy tolerance typically determines the accuracy of practical calculations. As a result, a sufficiently small energy tolerance provides access to a physically and numerically converged calculation. In that case, the strain-induced equilibrium positions are obtained.

| Example for LAMMPS data file | | | | |
|---|---|---|---|---|
| Lammps data file | | | | |
| 32 atoms | | | | |
| 4 atom types | | | | |
| $x_{min}$ $x_{max}$ xlo xhi | | | | |
| $y_{min}$ $y_{max}$ ylo yhi | | | | |
| $z_{min}$ $z_{max}$ zlo zhi | | | | |
| Masses | | | | |
| 1 74.9216003 | | | | |
| 2 69.7229996 | | | | |
| 3 114.8180008 | | | | |
| 4 26.9815388 | | | | |
| Atoms | | | | |
| 1 | 1 | 0.0000 | 0.0000 | 0.0000 |
| 2 | 1 | 5.6533 | 0.0000 | 0.0000 |
| 3 | 1 | 2.8266 | 2.8266 | 0.0000 |
| 4 | 1 | 8.4799 | 2.8266 | 0.0000 |
| 5 | 1 | 0.0000 | 5.6533 | 0.0000 |
| 6 | 1 | 5.6533 | 5.6533 | 0.0000 |
| 7 | 1 | 2.8266 | 8.4799 | 0.0000 |
| 8 | 1 | 8.4799 | 8.4799 | 0.0000 |
| 9 | 2 | 4.2400 | 1.4133 | 1.4133 |
| 10 | 2 | 9.8933 | 1.4133 | 1.4133 |
| 11 | 2 | 1.4133 | 4.2400 | 1.4133 |
| 12 | 2 | 7.0666 | 4.2400 | 1.4133 |
| 13 | 2 | 4.2400 | 7.0666 | 1.4133 |
| 14 | 2 | 9.8933 | 7.0666 | 1.4133 |
| 15 | 2 | 1.4133 | 9.8933 | 1.4133 |
| 16 | 2 | 7.0666 | 9.8933 | 1.4133 |
| 17 | 1 | 2.8266 | 0.0000 | 2.8266 |
| 18 | 1 | 8.4799 | 0.0000 | 2.8266 |
| 19 | 1 | 0.0000 | 2.8266 | 2.8266 |
| 20 | 1 | 5.6533 | 2.8266 | 2.8266 |
| 21 | 1 | 2.8266 | 5.6533 | 2.8266 |
| 22 | 1 | 8.4799 | 5.6533 | 2.8266 |
| 23 | 1 | 0.0000 | 8.4799 | 2.8266 |
| 24 | 1 | 5.6533 | 8.4799 | 2.8266 |
| 25 | 2 | 1.4133 | 1.4133 | 4.2400 |
| 26 | 2 | 7.0666 | 1.4133 | 4.2400 |
| 27 | 2 | 4.2400 | 4.2400 | 4.2400 |
| 28 | 2 | 9.8933 | 4.2400 | 4.2400 |
| 29 | 2 | 1.4133 | 7.0666 | 4.2400 |
| 30 | 2 | 7.0666 | 7.0666 | 4.2400 |
| 31 | 2 | 4.2400 | 9.8933 | 4.2400 |
| 32 | 2 | 9.8933 | 9.8933 | 4.2400 |

Table A.4.: Example for Lammps input file with lower $(x_{min}, y_{min}, z_{min})$ and upper box boundaries $(x_{max}, y_{max}, z_{max})$, 32 atoms, 4 atom types {As, Ga, In, Al}, and their corresponding masses. The atomic numbers, their coordinates and the colors are provided following the example of the zinc blende structure in Fig. 4.3. The five columns represent the atom number, atom type and coordinates.

| Explanation of individual step | LAMMPS command |
|---|---|
| Select metal units for calculation | units metal |
| Type of calculation | atom_style atomic |
| Periodic boundaries xyz | boundary p p p |
| Read atomic positions from the prepared file 'datafile' | read_data datafile |
| Define usage of 'Keating' potential | pair_style keat |
| Parameters for atom types As, Ga, In, and Al (in this order) are given in file 'potfile' | pair_coeff * * potfile As Ga In Al |
| Write a user-defined output every $10^5$ steps into the file 'dumpfile', the output consists of the atom type, atom number, and $x-, y-, z-$coordinates | dump myforcedump all custom 1e5 dumpfile type id x y z |
| Sort output by atom number | dump_modify myforcedump sort id |
| Define quantities to be printed out every iteration step: Number of iteration, total energy, maximal force component, 2-norm of the force vector (average force) | thermo_style custom step etotal fmax fnorm |
| Choose minimization algorithm to be conjugate gradient | min_style cg |
| Choose maximum allowed distance for moving atoms in one iteration step | min_modify dmax 0.0005 |
| Start minimization algorithm and define criteria for abortion in the following order: relative tolerance of total energy, absolute force tolerance (in metal units eV/Å), maximal iterations of minimizer, maximal number of force/energy evaluations | minimize 1e-12 1e-3 1e5 5e4 |

Table A.5.: Commands, which have been employed to start a relaxation procedure with the LAMMPS code.

## A.4. Strain-Induced Coordinates

In the following, we demonstrate how a smaller box can be cut out of a larger one as displayed in Fig. 4.9. Here, the boxes differ by dcell($xy$) and dcell($z$) numbers of unit cells in the $xy$- and $z$-direction, respectively. Furthermore, we assume that both boxes originate at $(0, 0, 0)$. In the first step, we determine which atom number in the larger box the first atom in the smaller box corresponds to. For this purpose, we shift the coordinates of the smaller box $(x_s, y_s, z_s)$ according to

$$\begin{aligned} x_l &= x_s + \mathrm{dcell}(xy)/2 \cdot 4 \\ y_l &= y_s + \mathrm{dcell}(xy)/2 \cdot 4 \\ z_l &= z_s + \mathrm{dcell}(z)/2 \cdot 4, \end{aligned} \tag{A.6}$$

with $x_l = x_{large}$ and $x_s = x_{small}$ so that the coordinates of the larger box $(x_l, y_l, z_l)$ are obtained. This situation is displayed in Fig. 4.9. For given atomic positions, we can determine the corresponding numbers as before by

$$\begin{aligned} \mathrm{below} &= 2 \cdot \mathrm{cellnr}(xy)^2 \cdot z_l \\ \mathrm{front} &= \mathrm{cellnr}(xy) \cdot \mathrm{floor}(y_l/2) \\ \mathrm{left} &= \mathrm{floor}(x_l/4) \\ \mathrm{num} &= \mathrm{below} + \mathrm{front} + \mathrm{left} + 1. \end{aligned} \tag{A.7}$$

Subsequently, the strain-induced equilibrium positions are assigned to the coordinates within the smaller box by

$$\begin{aligned} x'_s &= x'_l(\mathrm{num}) \\ y'_s &= y'_l(\mathrm{num}) \\ z'_s &= z'_l(\mathrm{num}), \end{aligned} \tag{A.8}$$

where the relaxed coordinates in the small and large box are denoted by $(x'_s, y'_s, z'_s)$ and $(x'_l, y'_l, z'_l)$, respectively.

## A.5. Tight-Binding Diagonalization

The parameters used for the 'Krylov Schur' subspace solver to diagonalze the sparse TB Hamiltonian are listed in Table A.6. Due to the large quantum dot, the eigenvalues are energetically close to each other, which requires a rather large subspace. Depending on the eigenvalue a smaller or even larger number might be best suited. Additionally,

| Krylov Schur parameter | Explanation |
|---|---|
| EPSSetProblemType, EPS_HEP | Define Hermitian eigenvalue problem |
| EPSSetWhichEigenpairs, EPS_TARGET_REAL | Find eigenvalues with real part closest to target |
| EPSSetTarget, target = $\{0.4, 0.7\}$ | Target values {holes, electrons} for the eigenvalue problem solver |
| EPSSetDimensions, nev = 20, ncv = 300 | Define minimum number of nev = 20 eigenvalues that are calculated, Number of ncv = 300 column vectors that are used to deploy a subspace |
| EPSSetTolerances, tol = 1e-16, maxit = 1e7 | Numerical tolerance of the (iterative) eigenvalue solver, maximum number of iterations |

Table A.6.: Numerical parameters used for the 'Krylov Schur' subspace solver within the SLEPC code [122].

the number of eigenvalues 'nev' needs to be chosen carefully. It can be advantageous to choose a larger value than you are actually interested in. For instance, when including spin-orbit coupling, each eigenvalue is two times Kramer's degenerate. If a too small value for 'nev' is chosen, it might happen that larger eigenvalues are obtained before the actual degeneracy is achieved. The numerical tolerance 'tol' is given by 1e-16 in Table A.6, which is a reasonable choice if you are interested in fine-structure splitting, which typically lies within the range of $\mu$eV. If you are not interested in this quantity, it makes sense to choose a larger value for 'tol' to not unnecessarily slow down the calculation. One of the most important parameters is 'epstarget', which determines the starting point of the iterative eigenvalue search. For numerical reasons, it is best to choose a value within the band gap. In our case, the band gap is about 0.8 eV, which corresponds to the C-band, and we use a parametrization, in which zero corresponds to the top of the VB. For this situation, we expect the lowest/highest energy value for the electrons/holes to be around 0.8 eV and 0 eV, respectively. Following the discussion above, for numerical reasons we choose target values for electrons and holes of 0.7 and 0.4, respectively. A suitable selection of these target values is one of the key issues in achieving a fast and convergent eigenvalue calculation.

## A.6. Calculation of Tight-Binding Coulomb Matrix Elements

A flowchart for the numerical evaluation of the Coulomb matrix elements in Eq. (5.8) by using an adaptive multidimensional integration routine [124] is depicted in Fig. A.1. Here, one specific processor (root) provides an adaptive sampling, whereas all other processors hold slices of the parallelized wave function in memory and contribute to the parallel integration by multiplying and adding these slices.

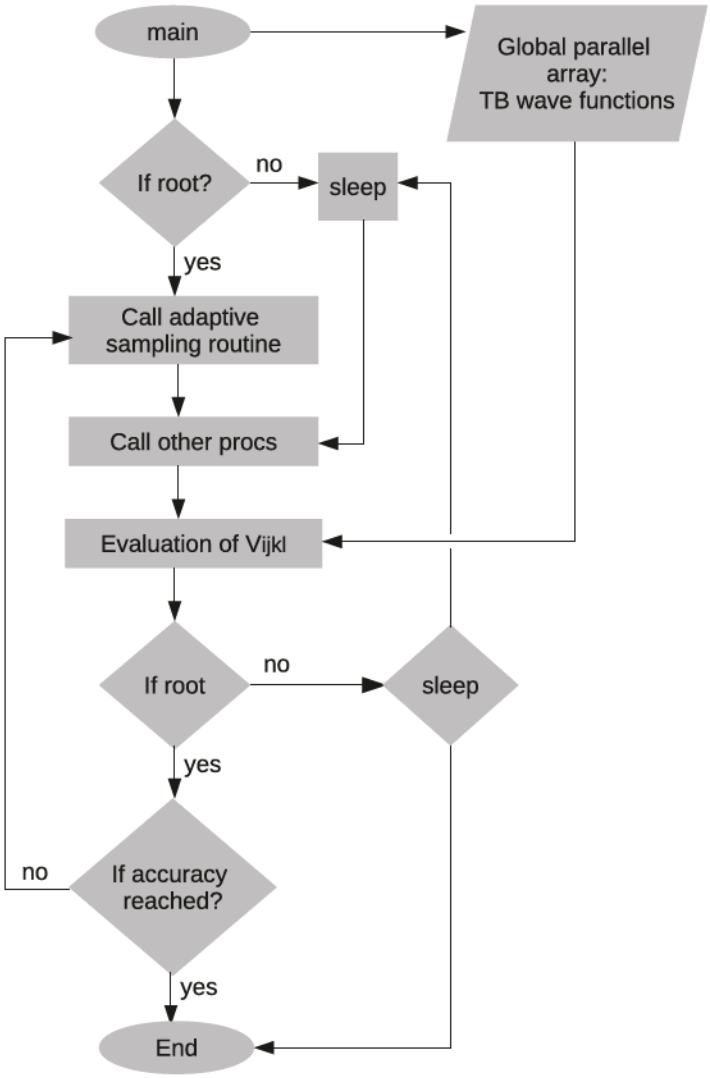


**Figure A.1. | Flow chart**. The Coulomb matrix elements are calculated from the parallelized TB wave functions using an adaptive integration routine.

## A.7. Coulomb Matrix Elements in Envelope-Function Approximation

In this part, the Coulomb matrix elements

$$V_{ij,kl}^{\lambda\lambda'} = \frac{e^2}{2\varepsilon_0\varepsilon_r}\int \frac{d^2q_\parallel F(q_\parallel)}{(2\pi)^2 q_\parallel} \langle\varphi_i^\lambda|e^{-i\vec{q}_\parallel\vec{\rho}}|\varphi_l^\lambda\rangle \langle\varphi_j^{\lambda'}|e^{i\vec{q}_\parallel\vec{\rho}}|\varphi_k^{\lambda'}\rangle\,. \tag{A.9}$$

are calculated, using the envelope approximation [57] and the form factor

$$F(q_\parallel) = \frac{32\pi^4(-1+Lq_\parallel+e^{-Lq_\parallel})+20(Lq_\parallel)^3\pi^2+3(Lq_\parallel)^5}{(Lq_\parallel)^2\left((Lq_\parallel)^2+4\pi^2\right)^2}. \tag{A.10}$$

The overlap matrix elements $\langle\varphi_j|e^{i\vec{q}_\parallel\vec{\rho}}|\varphi_k\rangle$ of the oscillator wave functions are listed in Table A.7. After inserting these matrix elements into Eq. (A.9), a two dimensional integral

| |
|---|
| $\langle\varphi^s_{m=0}\|e^{i\vec{q}_\parallel\vec{\rho}}\|\varphi^s_{m=0}\rangle = e^{-\frac{q^2}{4\beta^2}}$ |
| $\langle\varphi^s_{m=0}\|e^{i\vec{q}_\parallel\vec{\rho}}\|\varphi^p_{m=\pm1}\rangle = \frac{iq}{2\beta}e^{-\frac{q^2}{4\beta^2}}e^{\pm i\Phi}$ |
| $\langle\varphi^p_{m=\pm1}\|e^{i\vec{q}_\parallel\vec{\rho}}\|\varphi^p_{m=\pm1}\rangle = \left(1-\frac{q^2}{4\beta^2}\right)e^{-\frac{q^2}{4\beta^2}}$ |
| $\langle\varphi^p_{m=\pm1}\|e^{i\vec{q}_\parallel\vec{\rho}}\|\varphi^p_{m=\mp1}\rangle = \frac{-q^2}{4\beta^2}e^{-\frac{q^2}{4\beta^2}}e^{\mp 2i\Phi}$ |

Table A.7.: Analytic expressions for the overlap matrix elements of the $s$, $p_+$, and $p_-$ states.

remains to be calculated. In Polar coordinated it is given by

$$V_{ij,kl}^{\lambda\lambda'} = \frac{e^2}{2\varepsilon_0\varepsilon_r}\int_0^{2\pi} d\varphi \int_0^\infty dq_\parallel \frac{F(q_\parallel)}{(2\pi)^2} \langle\varphi_i^\lambda|e^{-i\vec{q}_\parallel\vec{\rho}}|\varphi_l^\lambda\rangle \langle\varphi_j^{\lambda'}|e^{i\vec{q}_\parallel\vec{\rho}}|\varphi_k^{\lambda'}\rangle\,. \tag{A.11}$$

Using Polar coordinated is numerically advantageous since the integrand decreases rapidly for increasing radius. For the numerical evaluation of $\int_a^b f(x)dx \approx \sum_i w_i f(x_i)$, we utilize the grid points $x_i$ and their corresponding weights $w_i$ according to Gauss-Tschebyscheff:

$$\begin{aligned} x_i &= \frac{1}{2\pi}\left[\frac{2\pi}{N+1}i - \sin\left(\frac{2\pi}{N+1}i\right)\right](b-a)+a, \\ w_i &= \frac{1}{2\pi}\left[1-\cos\left(\frac{2\pi}{N+1}i\right)\right]\frac{b-a}{N+1}. \end{aligned} \tag{A.12}$$

Such a choice is numerically advantageous, since the number of grid points can be reduced compared to the equidistant case. The non-vanishing matrix elements for equal oscillator lengths $l_k$ are listed in Table A.7. It can be seen that only 19 of the $3^4 = 81$ matrix elements are non-zero and that only 5 different values are present. This relatively low

| (i,j,k,l) | $V_{ij,kl}/E_c$ |
|---|---|
| (1,1,1,1) | 1.1197 |
| (1,2,2,1), (2,1,1,2) | 0.8690 |
| (1,3,3,1), (3,1,1,3) | 0.8690 |
| (2,2,2,2) | 0.7935 |
| (2,3,3,2), (3,2,2,3) | 0.7935 |
| (3,3,3,3) | 0.7935 |
| (1,1,2,3), (1,1,3,2) ,(2,3,1,1), (3,2,1,1) | 0.2507 |
| (1,2,1,2), (2,1,2,1) | 0.2507 |
| (1,3,1,3), (3,1,3,1) | 0.2507 |
| (2,3,2,3), (3,2,3,2) | 0.1753 |

Table A.8.: All non-zero matrix elements for $l_k^e = l_k^h = 5.4\,\mathrm{nm}$ and $E_c = e^2/4\pi\varepsilon_0\varepsilon_r l_k = 19.478\,\mathrm{meV}$. The index $\kappa \in (i,j,k,l)$ corresponds to the wave function $\varphi_\kappa$, where $\{1,2,3\} \hat{=} \{s, p_+, p_-\}$.

number of 5 is caused by the symmetry of the wave function $\psi_m = \psi_{-m}$ in cylindrically symmetric potentials. Additionally to the s- and p-shells in Table A.7, one can consider the three states of the d-shell ($d_0$, $d_+$ ,$d_-$). The corresponding overlap matrix elements are listed in Table A.9. All additional matrix elements, which are not given in Tables A.7

$$\langle\varphi^s_{m=0}|e^{i\vec{q}_\parallel\vec{\rho}}|\varphi^d_{m=0}\rangle = -\frac{q^2}{4\beta^2}e^{-\frac{q^2}{4\beta^2}}$$
$$\langle\varphi^s_{m=0}|e^{i\vec{q}_\parallel\vec{\rho}}|\varphi^d_{m=\pm2}\rangle = -\frac{q^2}{4\beta^2\sqrt{2}}e^{-\frac{q^2}{4\beta^2}}e^{\pm2i\Phi}$$
$$\langle\varphi^p_{m=\pm1}|e^{i\vec{q}_\parallel\vec{\rho}}|\varphi^d_{m=0}\rangle = \frac{iq}{2\beta}\left(1-\frac{q^2}{4\beta^2}\right)e^{-\frac{q^2}{4\beta^2}}e^{\mp i\Phi}$$
$$\langle\varphi^p_{m=\mp1}|e^{i\vec{q}_\parallel\vec{\rho}}|\varphi^d_{m=\pm2}\rangle = -\frac{iq^3}{8\beta^3\sqrt{2}}e^{-\frac{q^2}{4\beta^2}}e^{\pm3i\Phi}$$
$$\langle\varphi^p_{m=\pm1}|e^{i\vec{q}_\parallel\vec{\rho}}|\varphi^d_{m=\pm2}\rangle = -\frac{iq}{\beta\sqrt{2}}\left(1-\frac{q^2}{8\beta^2}\right)e^{-\frac{q^2}{4\beta^2}}e^{\pm i\Phi}$$
$$\langle\varphi^d_{m=0}|e^{i\vec{q}_\parallel\vec{\rho}}|\varphi^d_{m=0}\rangle = \left(1-\frac{q^2}{4\beta^2}\right)^2e^{-\frac{q^2}{4\beta^2}}$$
$$\langle\varphi^d_{m=\pm2}|e^{i\vec{q}_\parallel\vec{\rho}}|\varphi^d_{m=\mp2}\rangle = \frac{q^4}{32\beta^4}e^{-\frac{q^2}{4\beta^2}}e^{\mp4i\Phi}$$
$$\langle\varphi^d_{m=\pm2}|e^{i\vec{q}_\parallel\vec{\rho}}|\varphi^d_{m=\pm2}\rangle = \left(1-\frac{q^2}{2\beta^2}+\frac{q^4}{32\beta^4}\right)e^{-\frac{q^2}{4\beta^2}}$$
$$\langle\varphi^d_{m=0}|e^{i\vec{q}_\parallel\vec{\rho}}|\varphi^d_{m=\pm2}\rangle = \frac{-q^2}{2\beta\sqrt{2}}\left(1-\frac{q^2}{8\beta^2}\right)e^{-\frac{q^2}{4\beta^2}}e^{\pm2i\Phi}$$

Table A.9.: Analytic expressions of the matrix elements for the states $d_0$, $d_+$, and $d_-$.

and A.9 can be obtained by substituting $q_\parallel \to -q_\parallel$ and complex conjugation via

$$\langle\varphi_m|e^{+i\vec{q}_\parallel\vec{\rho}}|\varphi_{m'}\rangle = \left(\langle\varphi_{m'}|e^{+i(-\vec{q}_\parallel)\vec{\rho}}|\varphi_m\rangle\right)^*. \tag{A.13}$$

Due to the cylindrical symmetry, it additionally yields:

$$\langle\varphi_m|e^{+i\vec{q}_\parallel\vec{\rho}}|\varphi_{m'}\rangle = \langle\varphi_{-m'}|e^{+i\vec{q}_\parallel\vec{\rho}}|\varphi_{-m}\rangle\,. \tag{A.14}$$

# Bibliography

# Bibliography


[1] DOE/Los Alamos National Laboratory. Single-photon emitter has promise for quantum info-processing. `https://www.sciencedaily.com/releases/2017/07/170731164034.htm`, 2017. Accessed: 2018-08-02.

[2] R. Hanbury Brown and R. Q. Twiss. A Test of a New Type of Stellar Interferometer on Sirius. *Nature*, 178, 1956.

[3] L. Gasca. From O to L: The Future of Optical-Wavelength Bands. www.broadbandproperties.com, Juni 2008. Accessed: 2018-08-02.

[4] G. P. Agrawal. *Fiber-optic communication systems, 4th ed.* Wiley, New York, 2010.

[5] X. Z. Liao, J. Zou, X. F. Duan, D. J. H. Cockayne, R. Leon, and C. Lobo. Transmission-electron microscopy study of the shape of buried $In_xGa_{1-x}As/GaAs$ quantum dots. *Phys. Rev. B*, 58:R4235–R4237, Aug 1998.

[6] Jonathan R Orchard, Chris Woodhead, Jiang Wu, Mingchu Tang, Richard Beanland, Yasir Noori, Huiyun Liu, Robert J Young, and David J Mowbray. Silicon-Based Single Quantum Dot Emission in the Telecoms C-Band. *ACS Photonics*, 4(7):1740–1746, 2017.

[7] J. Bahe, Xiaoqing Zhou, T. Kippenberg, A. Stiebeiner, A. Rauschenbeutel, J. Rabeau, and H. Weinfurter. A single photon source based on NV centers in diamond nanocrystals. In *CLEO/Europe - EQEC 2009 - European Conference on Lasers and Electro-Optics and the European Quantum Electronics Conference*, pages 1–1, June 2009.

[8] Anaïs Dréau, Anna Tchebotareva, Aboubakr El Mahdaoui, Cristian Bonato, and Ronald Hanson. Quantum Frequency Conversion of Single Photons from a Nitrogen-Vacancy Center in Diamond to Telecommunication Wavelengths. *Phys. Rev. Applied*, 9:064031, Jun 2018.

[9] Nicolas Maring, Dario Lago-Rivera, Andreas Lenhard, Georg Heinze, and Hugues de Riedmatten. Quantum frequency conversion of memory-compatible single photons from 606  nm to the telecom C-band. *Optica*, 5(5):507–513, May 2018.

[10] T. Wilk, S. C. Webster, H. P. Specht, G. Rempe, and A. Kuhn. Polarization-Controlled Single Photons. *Phys. Rev. Lett.*, 98:063601, Feb 2007.

[11] D B Higginbottom, L Slodička, G Araneda, L Lachman, R Filip, M Hennrich, and R Blatt. Pure single photons from a trapped atom source. *New Journal of Physics*, 18(9):093038, 2016.

[12] Pascale Senellart, Glenn Solomon, and Andrew White. High-performance semiconductor quantum-dot single-photon sources. *Nature Nanotechnology*, 12, Nov 2017.

[13] Robert Keil, Michael Zopf, Yan Chen, Bianca Höfer, Jiaxiang Zhang, Fei Ding, and Oliver G. Schmidt. Solid-state ensemble of highly entangled photon sources at rubidium atomic transitions. *Nature Communications*, 8, 2017.

[14] S. Kumar, A. Kaczmarczyk, and B. D. Gerardot. Strain-Induced Spatial and Spectral Isolation of Quantum Emitters in Mono- and Bilayer $WSe_2$. *Nano Letters*, 15(11):7567–7573, 2015.

[15] Johannes Kern, Iris Niehues, Philipp Tonndorf, Robert Schmidt, Daniel Wigger, Robert Schneider, Torsten Stiehm, Steffen Michaelis de Vasconcellos, Doris E. Reiter, Tilmann Kuhn, and Rudolf Bratschitsch. Nanoscale Positioning of Single-Photon Emitters in Atomically Thin $WSe_2$. *Adv. Mater.*, 28(33):7101–7105, 2017.

[16] Artur Branny, Gang Wang, Santosh Kumar, Cedric Robert, Benjamin Lassagne, Xavier Marie, Brian D. Gerardot, and Bernhard Urbaszek. Discrete quantum dot like emitters in monolayer $MoS_2$: Spatial mapping, magneto-optics, and charge tuning. *Appl. Phys. Lett.*, 108(14):142101, 2016.

[17] Artur Branny, Santosh Kumar, Raphaël Proux, and Brian D. Gerardot. Deterministic strain-induced arrays of quantum emitters in a two-dimensional semiconductor. *Nature Communications*, 8:ncomms15053, 2017.

[18] Carmen Palacios-Berraquero, Dhiren M. Kara, Alejandro R.-P. Montblanch, Matteo Barbone, Pawel Latawiec, Duhee Yoon, Anna K. Ott, Marko Loncar, Andrea C. Ferrari, and Mete Atatüre. Large-scale quantum-emitter arrays in atomically thin semiconductors. *Nature Communications*, 8:ncomms15093, 2017.

[19] Gabriella D. Shepard, Obafunso A. Ajayi, Xiangzhi Li, X.-Y. Zhu, James Hone, and Stefan Strauf. Nanobubble induced formation of quantum emitters in monolayer semiconductors. *2D Mater.*, 4(2):021019, 2017.

[20] Dirk Bouwmeester, Artur Ekert, and Anton Zeilinger. *The physics of quantum information*, volume 3. Springer, Berlin, 2000.

[21] Z. Y. Zhang, A. E. H. Oehler, B. Resan, S. Kurmulis, K. J. Zhou, Q. Wang, M. Mangold, T. Süedmeyer, U. Keller, K. J. Weingarten, and R. A. Hogg. 1.55 $\mu$m InAs/GaAs Quantum Dots and High Repetition Rate Quantum Dot SESAM Mode-locked Laser. *Scientific Reports*, 2, 2012.

[22] D. Bimberg, M. Grundmann, and N. N. Ledenstov, editors. *Quantum Dot Heterostructures.* Wiley, New York, 1999.

[23] Zhiliang Yuan, Beata E. Kardynal, R. Mark Stevenson, Andrew J. Shields, Charlene J. Lobo, Ken Cooper, Neil S. Beattie, David A. Ritchie, and Michael Pepper. Electrically Driven Single-Photon Source. *Science*, 295(5552):102–105, 2002.

[24] E. Khestanova, F. Guinea, L. Fumagalli, A. K. Geim, and I. V. Grigorieva. Universal shape and pressure inside bubbles appearing in van der Waals heterostructures. *Nature Communications*, 7:ncomms12587, 2016.

[25] C. H. Bennett and G. Brassard. Quantum cryptography: Public key distribution and coin tossing. *Proceedings of IEEE International Conference on Computers, Systems and Signal Processing*, 175:8, 1984.

[26] Nick Papanikolaou. An Introduction to Quantum Cryptography. `http://www.nick-p.info/files/qcryp.htm`. Accessed: 2018-08-02.

[27] S. Fafard, Z. R. Wasilewski, C. Ni. Allen, D. Picard, M. Spanner, J. P. McCaffrey, and P. G. Piva. Manipulating the energy levels of semiconductor quantum dots. *Phys. Rev. B*, 59:15368–15373, Jun 1999.

[28] K. Jacobi. Atomic structure of InAs quantum dots on GaAs. *Progress in Surface Science*, 71(5-8):185–215, 2003.

[29] J. Stangl, V. Holy, and G. Bauer. Structural properties of self-organized semiconductor nanostructures. *Reviews of Modern Physics*, 76:725–783, 2004.

[30] Neil S. Beattie, Patrick See, Guillaume Zoppi, Palat M. Ushasree, Martial Duchamp, Ian Farrer, David A. Ritchie, and Stanko Tomić. Quantum Engineering of InAs/GaAs Quantum Dot Based Intermediate Band Solar Cells. *ACS Photonics*, 4(11):2745–2750, 2017.

[31] C. Tessarek, S. Figge, T. Aschenbrenner, S. Bley, A. Rosenauer, M. Seyfried, J. Kalden, K. Sebald, J. Gutowski, and D. Hommel. Strong phase separation of strained $In_xGa_{1-x}N$ layers due to spinodal and binodal decomposition: Formation of stable quantum dots. *Phys. Rev. B*, 83:115316, Mar 2011.

[32] F. Jahnke. *Quantum optics with semiconductor nanostructures.* Woodhead, 2012.

[33] P. Michler. *Single Quantum Dots - Fundamentals, Applications and New Concepts.* Springer, 2003.

[34] P. Michler. *Single Semiconductor Quantum Dots.* Springer, 2009.

[35] Z. M. Wang. *Self-Assembled Quantum Dots. Auflage: 2008.* Springer, 2007.

[36] I-Wen Feng, Sixuan Jin, Jing Li, Jingyu Lin, and Hongxing Jiang. SiO2/TiO2 distributed Bragg reflector near 1.5 $\mu$m fabricated by e-beam evaporation. *Journal of Vacuum Science & Technology A: Vacuum, Surfaces, and Films*, 31(6):061514, 2013.

[37] Kevin Bulls. Quantum Dots Get Commercial Debut in More Colorful Sony TVs. `https://www.technologyreview.com/s/509801/quantum-dots-get-commercial-debut-in-more-colorful-sony-tvs/`, 2013. Accessed: 2018-08-02.

[38] Toshiyuki Miyazawa, Kazuya Takemoto, Yoshiki Sakuma, Shinichi Hirose, Tatsuya Usuki, Naoki Yokoyama, Motomu Takatsu, and Yasuhiko Arakawa. Single-Photon Generation in the 1.55-$\mu$m Optical-Fiber Band from an InAs/InP Quantum Dot. *Japanese Journal of Applied Physics*, 44(5L):L620, 2005.

[39] S. Anantathanasarn, R. Nötzel, P. J. van Veldhoven, T. J. Eijkemans, and J. H. Wolter. Wavelength-tunable InAs quantum dots in InGaAsP/InP (100) grown by metal-organic vapor-phase epitaxy. *Journal of Applied Physics*, 98(1):013503, 2005.

[40] Joanna Skiba-Szymanska, R. Mark Stevenson, Christiana Varnava, Martin Felle, Jan Huwer, Tina Müller, Anthony J. Bennett, James P. Lee, Ian Farrer, Andrey B. Krysa, Peter Spencer, Lucy E. Goff, David A. Ritchie, Jon Heffernan, and Andrew J. Shields. Universal Growth Scheme for Quantum Dots with Low Fine-Structure Splitting at Various Emission Wavelengths. *Phys. Rev. Applied*, 8:014013, Jul 2017.

[41] Matthias Paul, Fabian Olbrich, Jonatan Höschele, Susanne Schreier, Jan Kettler, Simone Luca Portalupi, Michael Jetter, and Peter Michler. Single-photon emission at 1.55 $\mu$m from MOVPE-grown InAs quantum dots on InGaAs/GaAs metamorphic buffers. *Applied Physics Letters*, 111(3):033102, 2017.

[42] K. S. Novoselov, A. K. Geim, S. V. Morozov, D. Jiang, Y. Zhang, S. V. Dubonos, I. V. Grigorieva, and A. A. Firsov. Electric Field Effect in Atomically Thin Carbon Films. *Science*, 306(5696):666–669, 2004.

[43] Andrea Splendiani, Liang Sun, Yuanbo Zhang, Tianshu Li, Jonghwan Kim, Chi-Yung Chim, Giulia Galli, and Feng Wang. Emerging Photoluminescence in Monolayer $MoS_2$. *Nano Letters*, 10(4):1271–1275, 2010. PMID: 20229981.

[44] Kin Fai Mak, Changgu Lee, James Hone, Jie Shan, and Tony F. Heinz. Atomically Thin $MoS_2$: A New Direct-Gap Semiconductor. *Phys. Rev. Lett.*, 105:136805, Sep 2010.

[45] Oriol Lopez-Sanchez, Dominik Lembke, Metin Kayci, Aleksandra Radenovic, and Andras Kis. Ultrasensitive photodetectors based on monolayer $MoS_2$. *Nature Nanotechnology*, 8, Sep 2013.

[46] Gui-Bin Liu, Wen-Yu Shan, Yugui Yao, Wang Yao, and Di Xiao. Three-band tight-binding model for monolayers of group-VIB transition metal dichalcogenides. *Phys. Rev. B*, 88:085433, Aug 2013.

[47] Deji Akinwande, Nicholas Petrone, and James Hone. Two-dimensional flexible nanoelectronics. *Nature Communications*, 5, Dec 2014.

[48] M. Rösner, C. Steinke, M. Lorke, C. Gies, F. Jahnke, and T. O. Wehling. Two-Dimensional Heterojunctions from Nonlocal Manipulations of the Interactions. *Nano Letters*, 16(4):2322–2327, 2016.

[49] Archana Raja, Andrey Chaves, Jaeeun Yu, Ghidewon Arefe, Heather M. Hill, Albert F. Rigosi, Timothy C. Berkelbach, Philipp Nagler, Christian Süller, Tobias Korn, Colin Nuckolls, James Hone, Louis E. Brus, Tony F. Heinz, David R. Reichman, and Alexey Chernikov. Coulomb engineering of the bandgap and excitons in two-dimensional materials. *Nature Communications*, 8:15251, 2017.

[50] N. W. Ashcroft and D. N. Mermin. *Festkörperphysik.* Oldenbourg Wissenschaftsverlag GmbH, München, 2007.

[51] Harald Ibach and Hans Lüth. *Festkörperphysik. Einführung in die Grundlagen.* Springer, 2002.

[52] G. Czycholl. *Theoretische Festkörperphysik: Von den klassischen Modellen zu modernen Forschungsthemen.* Springer, 2007.

[53] Charles Kittel. *Introduction to Solid State Physics.* John Wiley & Sons, Inc., New York, 6th edition, 1986.

[54] S. Schulz. *Electronic and Optical Properties of Quantum Dots: A Tight-Binding Approach.* PhD thesis, Universität Bremen, 2007.

[55] D. Mourad. *Empirische Tight-Binding-Modellierung geordneter und ungeordneter Halbleiterstrukturen.* PhD thesis, Universität Bremen, 2010.

[56] E. Goldmann. *From Structure to Spectra: Tight-Binding Theory of InGaAs Quantum Dots.* PhD thesis, Universität Bremen, 2014.

[57] H. Haug and S.W. Koch. *Quantum Theory of the Optical and Electronic Properties of Semiconductors.* World Scientific Publ., Singapore, 4. edition, 2004.

[58] Felix Bloch. Über die Quantenmechanik der Elektronen in Kristallgittern. *Zeitschrift für Physik*, 52(7):555–600, Jul 1929.

[59] G. Dresselhaus. Spin-Orbit Coupling Effects in Zinc Blende Structures. *Phys. Rev.*, 100:580–586, Oct 1955.

[60] J.E. Prieto and I. Markov. Stranski–Krastanov mechanism of growth and the effect of misfit sign on quantum dots nucleation. *Surface Science*, 664:172 – 184, 2017.

[61] R. F. Schmidt. *Elektrische und optische Untersuchungen an einem einzelnen InAs-Quantenpunkt mit Hilfe ionenstrahlimplantierter Mikro-LEDs.* PhD thesis, Universität Nürnberg, 2006.

[62] P. Schafmeister. *Herstellung und Charakterisierung von InAs-Quantenpunkten auf implantationsdotiertem GaAs (001).* PhD thesis, Ruhr-Universität Bochum, 2002.

[63] F. C. Frank and J. H. van der Merwe. Proceedings of the Royal Society of London, Series A 198, 1946.

[64] I. N. Stranski and L. von Krastanov. Akad. Wiss. Let. Mainz Math. Natur K1 IIb 146, 1939.

[65] D.R. Lide. *CRC Handbook of Chemistry and Physics, 84th Edition.* CRC HANDBOOK OF CHEMISTRY AND PHYSICS. Taylor & Francis, 2003.

[66] E. Schrödinger. Quantisierung als Eigenwertproblem. *Annalen der Physik*, 1926.

[67] W. Kohn. Nobel Lecture: Electronic structure of matter—wave functions and density functionals. *Rev. Mod. Phys.*, 71:1253–1266, Oct 1999.

[68] M. Born and R. Oppenheimer. Zur quantentheorie der molekeln. *Annalen der Physik*, 1927.

[69] O. Stier. *Electronic and optical properties of quantum dots and wires.* PhD thesis, Technische Universität Berlin, 2000.

[70] O. Stier, M. Grundmann, and D. Bimberg. Electronic and optical properties of strained quantum dots modeled by 8-band k·p theory. *Phys. Rev. B*, 59:5688–5701, Feb 1999.

[71] Andrei Schliwa, Momme Winkelnkemper, and Dieter Bimberg. Impact of size, shape, and composition on piezoelectric effects and electronic properties of InGaAs/GaAs quantum dots. *Phys. Rev. B*, 76:205324, Nov 2007.

[72] Gabriel Bester. Electronic excitations in nanostructures: an empirical pseudopotential based approach. *Journal of physics. Condensed matter : an Institute of Physics journal*, 21(2):023202, January 2009.

[73] M.L. Cohen and J.R. Chelikowsky. *Electronic Structure and Optical Properties of Semiconductors*, volume 75. Springer, Berlin, Heidelberg, New York, 1988.

[74] James C. Phillips. Energy-Band Interpolation Scheme Based on a Pseudopotential. *Phys. Rev.*, 112:685–695, Nov 1958.

[75] Marvin L. Cohen and T. K. Bergstresser. Band Structures and Pseudopotential Form Factors for Fourteen Semiconductors of the Diamond and Zinc-blende Structures. *Phys. Rev.*, 141:789–796, Jan 1966.

[76] James R. Chelikowsky and Marvin L. Cohen. Nonlocal pseudopotential calculations for the electronic structure of eleven diamond and zinc-blende semiconductors. *Phys. Rev. B*, 14:556–582, Jul 1976.

[77] Per-Olov Löwdin and Harrison Shull. Natural Orbitals in the Quantum Theory of Two-Electron Systems. *Phys. Rev.*, 101:1730–1739, Mar 1956.

[78] J. C. Slater and G. F. Koster. Simplified LCAO Method for the Periodic Potential Problem. *Phys. Rev.*, 94:1498–1524, Jun 1954.

[79] G. Seifert. Tight-Binding Density Functional Theory: An Approximate Kohn-Sham DFT Scheme. *The Journal of Physical Chemistry A*, 111(26):5609–5613, 2007. PMID: 17439198.

[80] P Vogl, Harold P Hjalmarson, and John D Dow. A Semi-empirical tight-binding theory of the electronic structure of semiconductors. *Journal of Physics and Chemistry of Solids*, 44(5):365–378, 1983.

[81] DJ Chadi. Spin-orbit splitting in crystalline and compositionally disordered semiconductors. *Physical Review B*, 16(2):790, 1977.

[82] F. Schwabl. *Quantenmechanik für Fortgeschrittene.* Springer, 2000.

[83] R.L. Anderson. Experiments on Ge-GaAs heterojunctions. *Solid-State Electronics*, 5(5):341 – 351, 1962.

[84] W. R. L. Lambrecht and B. Segall. Interface-bond-polarity model for semiconductor heterojunction band offsets. *Phys. Rev. B*, 41:2832–2848, Feb 1990.

[85] Daniel Mourad. Tight-binding branch-point energies and band offsets for cubic InN, GaN, AlN, and AlGaN alloys. *Journal of Applied Physics*, 113(12), 2013.

[86] A. Schleife, F. Fuchs, C. Rödl, J. Furthmüller, and F. Bechstedt. Branch-point energies and band discontinuities of III-nitrides and III-/II-oxides from quasiparticle band-structure calculations. *Applied Physics Letters*, 94(1), 2009.

[87] W. Mönch. *Electronic Properties of Semiconductor Interfaces.* Springer-Verlag Berlin Heidelberg, 2004.

[88] A. R. Miedema, P. F. de Châtel, and F. R de Boer. Cohesion in alloys - fundamentals of a semi-empirical model. *Physica B+C*, 100, 1980.

[89] Yoyo Hinuma, Andreas Grüneis, Georg Kresse, and Fumiyasu Oba. Band alignment of semiconductors from density-functional theory and many-body perturbation theory. *Phys. Rev. B*, 90:155405, Oct 2014.

[90] I. Vurgaftman, J.R. Meyer, and L.R. Ram-Mohan. Band parameters for III–V compound semiconductors and their alloys. *Journal of Applied Physics*, **89**:5815–5875, 2001.

[91] G. P. Donati, R. Kaspi, and K. J. Malloy. Interpolating semiconductor alloy parameters: Application to quaternary III–V band gaps. *Journal of Applied Physics*, 94(9):5814–5819, 2003.

[92] M Guden and J Piprek. Material parameters of quaternary III - V semiconductors for multilayer mirrors at 1.55 $\mu$m wavelength. *Modelling and Simulation in Materials Science and Engineering*, 4(4):349, 1996.

[93] C. Carmesin, M. Schowalter, M. Lorke, D. Mourad, T. Grieb, K. Müller-Caspary, M. Yacob, J. P. Reithmaier, M. Benyoucef, A. Rosenauer, and F. Jahnke. Interplay of morphology, composition, and optical properties of InP-based quantum dots emitting at the 1.55 $\mu$m telecom wavelength. *Phys. Rev. B*, 96:235309, Dec 2017.

[94] W. G. Cady. *Piezoelectricity: An Introduction to the Theory and Applications of Electromechanical Phenomena In Crystals.* McGraw-Hill, 1946.

[95] Liberato De Caro and Leander Tapfer. Elastic lattice deformation of semiconductor heterostructures grown on arbitrarily oriented substrate surfaces. *Phys. Rev. B*, 48:2298–2303, Jul 1993.

[96] M. Grundmann, O. Stier, and D. Bimberg. InAs/GaAs pyramidal quantum dots: Strain distribution, optical phonons, and electronic structure. *Phys. Rev. B*, 52:11969–11981, Oct 1995.

[97] D. L. Smith and C. Mailhiot. Theory of semiconductor superlattice electronic structure. *Rev. Mod. Phys.*, 62:173–234, Jan 1990.

[98] M. A. Migliorato, D. Powell, A. G. Cullis, T. Hammerschmidt, and G. P. Srivastava. Composition and strain dependence of the piezoelectric coefficients in $In_xGa_{1-x}As$ alloys. *Phys. Rev. B*, 74:245332, Dec 2006.

[99] Gabriel Bester, Xifan Wu, David Vanderbilt, and Alex Zunger. Importance of Second-Order Piezoelectric Effects in Zinc-Blende Semiconductors. *Phys. Rev. Lett.*, 96:187602, May 2006.

[100] Gabriel Bester, Alex Zunger, Wu Xifan, and David Vanderbilt. Effects of linear and nonlinear piezoelectricity on the electronic properties of InAs/GaAs quantum dots. *Phys. Rev. B*, 74, Aug 2006.

[101] A.D. Andreev and E.P. O'Reilly. Theory of the electronic structure of GaN/AlN hexagonal quantum dots. *Phys. Rev. B*, **62**:15851, 2000.

[102] Magnus Holm, Mats-Erik Pistol, and Craig Pryor. Calculations of the electronic structure of strained InAs quantum dots in InP. *Journal of Applied Physics*, 92(2):932–936, 2002.

[103] Weidong Sheng and Jean-Pierre Leburton. Absence of correlation between built-in electric dipole moment and quantum Stark effect in single InAs/GaAs self-assembled quantum dots. *Phys. Rev. B*, 67:125308, Mar 2003.

[104] V. Ranjan, G. Allan, C. Priester, and C. Delerue. Self-consistent calculations of the optical properties of GaN quantum dots. *Phys. Rev. B*, **68**:115305, 2003.

[105] M. A. Migliorato, D. Powell, S. L. Liew, A. G. Cullis, P. Navaretti, M. J. Steer, M. Hopkinson, M. Fearn, and J. H. Jefferson. Influence of composition on the piezoelectric effect and on the conduction band energy levels of $In_xGa_{1-x}As$/GaAs quantum dots. *Journal of Applied Physics*, 96(9):5169–5172, 2004.

[106] S. A. Saa. *Elasticity: theory and applications.* Pergamon Press, 1974.

[107] C. Pryor, J. Kim, L. W. Wang, A. J. Williamson, and A. Zunger. Comparison of two methods for describing the strain profiles in quantum dots. *Journal of Applied Physics*, 83(5):2548–2554, 1998.

[108] P. N. Keating. Theory of the Third-Order Elastic Constants of Diamond-Like Crystals. *Phys. Rev.*, 149:674–678, Sep 1966.

[109] Sadao Adachi. GaAs, AlAs, and $Al_xGa1 - xAs$: Material parameters for use in research and device applications. *Journal of Applied Physics*, 58(3):R1–R29, 1985.

[110] Yu. A. Burenkov, S. Yu. Davydov, and S. P. Nikanorov. Elastic properties of InAs. *Sov. Phys. Solid State*, 17(7):1446–1447, 1975.

[111] J. Tersoff. Modeling solid-state chemistry: Interatomic potentials for multicomponent systems. *Phys. Rev. B*, 39:5566–5568, Mar 1989.

[112] D. Powell, M. A. Migliorato, and A. G. Cullis. Optimized Tersoff potential parameters for tetrahedrally bonded III-V semiconductors. *Phys. Rev. B*, 75:115202, Mar 2007.

[113] Steve Plimpton. Fast Parallel Algorithms for Short-Range Molecular Dynamics. *Journal of Computational Physics*, 117(1):1–19, 1995.

[114] Sandia National Laboratories. LAMMPS Molecular Dynamics Simulator. `http://lammps.sandia.gov/`, 2018.

[115] Sverre Froyen and Walter A. Harrison. Elementary prediction of linear combination of atomic orbitals matrix elements. *Phys. Rev. B*, 20:2420–2422, Sep 1979.

[116] E. O'Reilly, A. Lindsay, S. Tomic, and M. Kamal-Saadi. Tight-binding and $\mathbf{k} \cdot \mathbf{p}$ models for the electronic structure of Ga(In)NAs and related alloys. *Semiconductor Science and Technology*, 17:870–879, 08 2002.

[117] Jean-Marc Jancu, Reinhard Scholz, Fabio Beltram, and Franco Bassani. Empirical spds* tight-binding calculation for cubic semiconductors: General method and material parameters. *Phys. Rev. B*, 57:6493–6507, Mar 1998.

[118] Timothy B. Boykin, Gerhard Klimeck, R. Chris Bowen, and Fabiano Oyafuso. Diagonal parameter shifts due to nearest-neighbor displacements in empirical tight-binding theory. *Phys. Rev. B*, 66:125207, Sep 2002.

[119] M. Zieliński, M. Korkusiński, and P. Hawrylak. Atomistic tight-binding theory of multiexciton complexes in a self-assembled InAs quantum dot. *Phys. Rev. B*, 81:085301, Feb 2010.

[120] W. Jaskólski, M. Zieliński, Garnett W. Bryant, and J. Aizpurua. Strain effects on the electronic structure of strongly coupled self-assembled InAs/GaAs quantum dots: Tight-binding approach. *Phys. Rev. B*, 74:195339, Nov 2006.

[121] R. B. Capaz, J. P. von der Weid, and Belita Koiller. Physical criteria for the direct-to-indirect gap crossover in $Al_xGa_{1-x}As$ alloys. *Applied Physics Letters*, 60(6):704–706, 1992.

[122] Vicente Hernandez, Jose E. Roman, and Vicente Vidal. SLEPc: A scalable and flexible toolkit for the solution of eigenvalue problems. *ACM Trans. Math. Software*, 31(3):351–362, 2005.

[123] S. Hackenbuchner. *Elektronische Struktur von Halbleiter-Nanobauelementen im thermodynamischen Nichtgleichgewicht.* Selected topics of semiconductor physics and technology. Walter Schottky Inst. der Techn. Univ. München, 2002.

[124] Jarle Berntsen, Terje O. Espelid, and Alan Genz. Algorithm 698: DCUHRE: An Adaptive Multidemensional Integration Routine for a Vector of Integrals. *ACM Trans. Math. Softw.*, 17(4):452–456, December 1991.

[125] Lew D. Landau and Ewgeni M. Lifschitz. *Lehrbuch der theoretischen Physik, 10 Bde., Bd.4, Quantenelektrodynamik.* Harri Deutsch, 1991.

[126] Lew D. Landau and Ewgeni M. Lifschitz. *10 Bde., Bd.3, Quantenmechanik.* Harri Deutsch, 1992.

[127] R.K. Willardson, E.R. Weber, and M. Sugawara. *Self-Assembled InGaAs/GaAs Quantum Dots.* Semiconductors and Semimetals. Elsevier Science, 1999.

[128] S. Schulz, S. Schumacher, and G. Czycholl. Tight-binding model for semiconductor quantum dots with a wurtzite crystal structure: From one-particle properties to Coulomb correlations and optical spectra. *Phys. Rev. B*, **73**:245327, 2006.

[129] Stefan Schulz, Daniel Mourad, and Gerd Czycholl. Multiband description of the optical properties of zincblende nitride quantum dots. *Phys. Rev. B*, 80:165405, Oct 2009.

[130] Schäfer Wilfried and Wegener Martin. *Semiconductor Optics and Transport Phenomena.* Springer, Heidelberg, 1st edition, 2002.

[131] M. Kira and S.W. Koch. *Semiconductor Quantum Optics.* Cambridge University Press, 2011.

[132] Christopher Gies, Jan Wiersig, Michael Lorke, and Frank Jahnke. Semiconductor model for quantum-dot-based microcavity lasers. *Phys. Rev. A*, 75:013803, Jan 2007.

[133] Weng W Chow, Frank Jahnke, and Christopher Gies. Emission properties of nanolasers during the transition to lasing. *Light: Science & Applications*, 3, 2014.

[134] C. Gies. *Theory for Light-Matter Interaction in Semiconductor Quantum Dots.* PhD thesis, Universität Bremen, 2008.

[135] N. Baer. *Optical and electronic properties of InGaAs and nitride quantum dots.* PhD thesis, Universität Bremen, 2006.

[136] J. H. Eberly and K. Wódkiewicz. The time-dependent physical spectrum of light∗. *J. Opt. Soc. Am.*, 67(9):1252–1261, Sep 1977.

[137] M. Kira, F. Jahnke, W. Hoyer, and S. W. Koch. Quantum Theory of Spontaneous Emission and Coherent Effects in Semiconductor Microstructures. *Prog. Quant. Electr.*, **23**:189, 1999.

[138] A. Steinhoff, J.-H. Kim, F. Jahnke, M. Rösner, D.-S. Kim, C. Lee, G. H. Han, M. S. Jeong, T. O. Wehling, and C. Gies. Efficient Excitonic Photoluminescence in Direct and Indirect Band Gap Monolayer $MoS_2$. *Nano Letters*, 15(10):6841–6847, 2015. PMID: 26322814.

[139] N. Baer. Optische Eigenschaften von Halbleiter-Quantenpunkten. Master's thesis, Universität Bremen, 2003.

[140] Hans C. Wolf and Hermann Haken. *Molekülphysik und Quantenchemie: Einführung in die experimentellen und theoretischen Grundlagen.* Springer, Berlin, 2006.

[141] Baer, N., Gartner, P., and Jahnke, F. Coulomb effects in semiconductor quantum dots. *Eur. Phys. J. B*, 42(2):231–237, 2004.

[142] S. Gordon, M. Yacob, J. P. Reithmaier, M. Benyoucef, and A. Zrenner. Coherent photocurrent spectroscopy of single InP-based quantum dots in the telecom band at 1.5 $\mu$m. *Applied Physics B*, 122(2):37, 2016.

[143] Kenichi Nishi, Hideaki Saito, Shigeo Sugou, and Jeong-Sik Lee. A narrow photoluminescence linewidth of 21 meV at 1.35 $\mu$m from strain-reduced InAs quantum dots covered by $In_{0.2}Ga_{0.8}As$ grown on GaAs substrates. *Applied Physics Letters*, 74(8):1111–1113, 1999.

[144] M. B. Ward, T. Farrow, P. See, Z. L. Yuan, O. Z. Karimov, A. J. Bennett, A. J. Shields, P. Atkinson, K. Cooper, and D. A. Ritchie. Electrically driven telecommunication wavelength single-photon source. *Applied Physics Letters*, 90(6):063512, 2007.

[145] Elias Goldmann, Matthias Paul, Florian F. Krause, Knut Müller, Jan Kettler, Thorsten Mehrtens, Andreas Rosenauer, Michael Jetter, Peter Michler, and Frank Jahnke. Structural and emission properties of InGaAs/GaAs quantum dots emitting at 1.3 $\mu$m. *Applied Physics Letters*, 105(15):152102, 2014.

[146] V. M. Ustinov, N. A. Maleev, A. E. Zhukov, A. R. Kovsh, A. Yu. Egorov, A. V. Lunev, B. V. Volovik, I. L. Krestnikov, Yu. G. Musikhin, N. A. Bert, P. S. Kop'ev, Zh. I. Alferov, N. N. Ledentsov, and D. Bimberg. InAs/InGaAs quantum dot structures on GaAs substrates emitting at 1.3 $\mu$m. *Applied Physics Letters*, 74(19):2815–2817, 1999.

[147] H. Y. Liu, M. Hopkinson, C. N. Harrison, M. J. Steer, R. Frith, I. R. Sellers, D. J. Mowbray, and M. S. Skolnick. Optimizing the growth of 1.3 $\mu$m InAs/InGaAs dots-in-a-well structure. *Journal of Applied Physics*, 93(5):2931–2936, 2003.

[148] M. Benyoucef, M. Yacob, J. P. Reithmaier, J. Kettler, and P. Michler. Telecom-wavelength (1.5$\mu$m) single-photon emission from InP-based quantum dots. *Applied Physics Letters*, 103(16):162101, 2013.

[149] M. Yacob, J. P. Reithmaier, and M. Benyoucef. Low-density InP-based quantum dots emitting around the 1.5 $\mu$m telecom wavelength range. *Applied Physics Letters*, 104(2):–, 2014.

[150] Andreas Rosenauer, Katharina Gries, Knut Müller, Angelika Pretorius, Marco Schowalter, Adrian Avramescu, Karl Engl, and Stephan Lutgen. Measurement of specimen thickness and composition in $Al_xGa_{1-x}N/GaN$ using high-angle annular dark field images. *Ultramicroscopy*, 109:1171–1182, 2009. 01.0011.

[151] Andreas Rosenauer, Thorsten Mehrtens, Knut Müller, Katharina Gries, Marco Schowalter, Parlapalli Venkata Satyam, Stephanie Bley, Christian Tessarek, Detlef Hommel, Katrin Sebald, Moritz Seyfried, Jürgen Gutowski, Adrian Avramescu, Karl Engl, and Stephan Lutgen. Composition mapping in InGaN by scanning transmission electron microscopy. *Ultramicroscopy*, 111:1316, 2011.

[152] Florian F. Krause, Marco Schowalter, Tim Grieb, Knut Müller-Caspary, Thorsten Mehrtens, and Andreas Rosenauer. Effects of instrument imperfections on quantitative scanning transmission electron microscopy. *Ultramicroscopy*, 161:146 – 160, 2016.

[153] M. Schowalter, A. Rosenauer, J. T. Titantah, and D. Lamoen. Computation and parametrization of the temperature dependence of Debye–Waller factors for group IV, III–V and II–VI semiconductors. *Acta Crystallographica Section A*, 65(1):5–17, Jan 2009.

[154] Marco Schowalter, Knut Müller, and Andreas Rosenauer. Scattering amplitudes and static atomic correction factors for the composition-sensitive 002 reflection in sphalerite ternary III–V and II–VI semiconductors. *Acta Crystallographica Section A*, 68(1):68–76, Jan 2012.

[155] Knut Müller, Marco Schowalter, Andreas Rosenauer, Dongzhi Hu, Daniel M. Schaadt, Michael Hetterich, Philippe Gilet, Oleg Rubel, Rafael Fritz, and Kerstin Volz. Atomic scale annealing effects on $In_xGa_{1-x}N_yAs_{1-y}$ studied by TEM three-beam imaging. *Phys. Rev. B*, 84:045316, Jul 2011.

[156] Tim Grieb, Knut Müller, Rafael Fritz, Marco Schowalter, Nils Neugebohrn, Nikolai Knaub, Kerstin Volz, and Andreas Rosenauer. Determination of the chemical composition of GaNAs using {STEM} {HAADF} imaging and {STEM} strain state analysis. *Ultramicroscopy*, 117:15 – 23, 2012.

[157] Huaxiang Fu, Lin-Wang Wang, and Alex Zunger. Applicability of the $\mathbf{k} \cdot \mathbf{p}$ method to the electronic structure of quantum dots. *Phys. Rev. B*, 57:9971–9987, Apr 1998.

[158] Ranjani Viswanatha, Sameer Sapra, Tanusri Saha-Dasgupta, and D. D. Sarma. Electronic structure of and quantum size effect in III-V and II-VI semiconducting nanocrystals using a realistic tight binding approach. *Phys. Rev. B*, 72:045333, Jul 2005.

[159] S. Schulz and G. Czycholl. Tight-binding model for semiconductor nanostructures. *Phys. Rev. B*, 72:165317, Oct 2005.

[160] M. Zieliński, M. Korkusiński, and P. Hawrylak. Atomistic tight-binding theory of multiexciton complexes in a self-assembled InAs quantum dot. *Phys. Rev. B*, 81:085301, Feb 2010.

[161] C. Carmesin, F. Olbrich, T. Mehrtens, M. Florian, S. Michael, S. Schreier, C. Nawrath, M. Paul, J. Höschele, B. Gerken, J. Kettler, S. L. Portalupi, M. Jetter, P. Michler, A. Rosenauer, and F. Jahnke. Structural and optical properties of inas/(in)gaas/gaas quantum dots with single-photon emission in the telecom c-band up to 77 k. *Phys. Rev. B*, 98:125407, Sep 2018.

[162] H Jeff Kimble. The quantum internet. *Nature*, 453(7198):1023–1030, 2008.

[163] Je-Hyung Kim, Tao Cai, Christopher J. K. Richardson, Richard P. Leavitt, and Edo Waks. Two-photon interference from a bright single-photon source at telecom wavelengths. *Optica*, 3(6):577–584, Jun 2016.

[164] Xing Ding, Yu He, Z.-C. Duan, Niels Gregersen, M.-C. Chen, S. Unsleber, S. Maier, Christian Schneider, Martin Kamp, Sven Höfling, et al. On-Demand Single Photons with High Extraction Efficiency and Near-Unity Indistinguishability from a Resonantly Driven Quantum Dot in a Micropillar. *Phys. Rev. Lett.*, 116:020401, Jan 2016.

[165] Niccolo Somaschi, Valerian Giesz, Lorenzo De Santis, JC Loredo, Marcelo P Almeida, Gaston Hornecker, Simone Luca Portalupi, Thomas Grange, Carlos Antón, Justin Demory, et al. Near-optimal single-photon sources in the solid state. *Nature Photonics*, 10:340–345, 2016.

[166] Markus Müller, Samir Bounouar, Klaus D Jöns, M Glässl, and P Michler. On-demand generation of indistinguishable polarization-entangled photon pairs. *Nature Photonics*, 8(3):224–228, 2014.

[167] R. Winik, D. Cogan, Y. Don, I. Schwartz, L. Gantz, E. R. Schmidgall, N. Livneh, R. Rapaport, E. Buks, and D. Gershoni. On-demand source of maximally entangled photon pairs using the biexciton-exciton radiative cascade. *Phys. Rev. B*, 95:235435, Jun 2017.

[168] I-Wen Feng, Sixuan Jin, Jing Li, Jingyu Lin, and Hongxing Jiang. $SiO_2/TiO_2$ distributed Bragg reflector near 1.5 $\mu$m fabricated by e-beam evaporation. *Journal of Vacuum Science & Technology A: Vacuum, Surfaces, and Films*, 31(6):061514, 2013.

[169] Thorsten Mehrtens, Stephanie Bley, Parlapalli Venkata Satyam, and Andreas Rosenauer. Optimization of the preparation of GaN-based specimens with low-energy ion milling for (S)TEM. *Micron*, 43(8):902–909, August 2012.

[170] nextnano$^3$ code, TU Munich (WSI), see http://www.nextnano.de/nextnano3/.

[171] Gabriel Bester and Alex Zunger. Cylindrically shaped zinc-blende semiconductor quantum dots do not have cylindrical symmetry: Atomistic symmetry, atomic relaxation, and piezoelectric effects. *Phys. Rev. B*, 71:045318, Jan 2005.

[172] Jan Kettler, Matthias Paul, Fabian Olbrich, Katharina Zeuner, Michael Jetter, Peter Michler, Matthias Florian, Christian Carmesin, and Frank Jahnke. Neutral and charged biexciton-exciton cascade in near-telecom-wavelength quantum dots. *Phys. Rev. B*, 94:045303, Jul 2016.

[173] S. Arrhenius. *J. Phys. Chem.*, 4:226, 1889.

[174] R. Heitz, I. Mukhametzhanov, A. Madhukar, A. Hoffmann, and D. Bimberg. Temperature dependent optical properties of self-organized inas/gaas quantum dots. *Journal of Electronic Materials*, 28(5):520–527, May 1999.

[175] Guillaume Gélinas, Ali Lanacer, Richard Leonelli, Remo A. Masut, and Philip J. Poole. Carrier thermal escape in families of inas/inp self-assembled quantum dots. *Phys. Rev. B*, 81:235426, Jun 2010.

[176] Fabian Olbrich, Jan Kettler, Matthias Bayerbach, Matthias Paul, Jonatan Höschele, Simone Luca Portalupi, Michael Jetter, and Peter Michler. Temperature-dependent properties of single long-wavelength InGaAs quantum dots embedded in a strain reducing layer. *Journal of Applied Physics*, 121(18):184302, 2017.

[177] K. S. Novoselov, D. Jiang, F. Schedin, T. J. Booth, V. V. Khotkevich, S. V. Morozov, and A. K. Geim. Two-dimensional atomic crystals. *Proceedings of the National Academy of Sciences*, 102(30):10451–10453, 2005.

[178] Jonathan N. Coleman, Mustafa Lotya, Arlene O'Neill, Shane D. Bergin, Paul J. King, Umar Khan, Karen Young, Alexandre Gaucher, Sukanta De, Ronan J. Smith, Igor V. Shvets, Sunil K. Arora, George Stanton, Hye-Young Kim, Kangho Lee, Gyu Tae Kim, Georg S. Duesberg, Toby Hallam, John J. Boland, Jing Jing Wang, John F. Donegan, Jaime C. Grunlan, Gregory Moriarty, Aleksey Shmeliov, Rebecca J. Nicholls, James M. Perkins, Eleanor M. Grieveson, Koenraad Theuwissen, David W. McComb, Peter D. Nellist, and Valeria Nicolosi. Two-Dimensional Nanosheets Produced by Liquid Exfoliation of Layered Materials. *Science*, 331(6017):568–571, 2011.

[179] Lee Yi-Hsien, Zhang Xin-Quan, Zhang Wenjing, Chang Mu-Tung, Lin Cheng-Te, Chang Kai-Di, Yu Ya-Chu, Wang Tse-Wei, Chang Chia-Seng, Li Lain-Jong, and Lin Tsung-Wu. Synthesis of Large-Area $MoS_2$ Atomic Layers with Chemical Vapor Deposition. *Advanced Materials*, 24(17):2320–2325, 2012.

[180] Yi Zhang, Tay-Rong Chang, Bo Zhou, Yong-Tao Cui, Hao Yan, Zhongkai Liu, Felix Schmitt, James Lee, Rob Moore, Yulin Chen, Hsin Lin, Horng-Tay Jeng, Sung-Kwan Mo, Zahid Hussain, Arun Bansil, and Zhi-Xun Shen. Direct observation of the transition from indirect to direct bandgap in atomically thin epitaxial $MoSe_2$. *Nature Nanotechnology*, 9, Dec 2013.

[181] David Lloyd, Xinghui Liu, Jason W. Christopher, Lauren Cantley, Anubhav Wadehra, Brian L. Kim, Bennett B. Goldberg, Anna K. Swan, and J. Scott Bunch. Band Gap Engineering with Ultralarge Biaxial Strains in Suspended Monolayer $MoS_2$. *Nano Lett.*, 16(9):5836–5841, 2016.

[182] Hiram J. Conley, Bin Wang, Jed I. Ziegler, Richard F. Haglund, Sokrates T. Pantelides, and Kirill I. Bolotin. Bandgap Engineering of Strained Monolayer and Bilayer $MoS_2$. *Nano Lett.*, 13(8):3626–3630, 2013.

[183] Sujay B. Desai, Gyungseon Seol, Jeong Seuk Kang, Hui Fang, Corsin Battaglia, Rehan Kapadia, Joel W. Ager, Jing Guo, and Ali Javey. Strain-Induced Indirect to Direct Bandgap Transition in Multilayer $WSe_2$. *Nano Lett.*, 14(8):4592–4597, 2014.

[184] A. Steinhoff, M. Rösner, F. Jahnke, T. O. Wehling, and C. Gies. Influence of Excited Carriers on the Optical and Electronic Properties of $MoS_2$. *Nano Letters*, 14(7):3743–3748, 2014. PMID: 24956358.

[185] Alexander Schulz. Tight binding description of monolayer $MoS_2$. Master's thesis, University of Bremen, 2015.

[186] M. Ghorbani-Asl, S. Borini, A. Kuc, and T. Heine. Strain-dependent modulation of conductivity in single-layer transition-metal dichalcogenides. *Phys. Rev. B*, 87:235434, Jun 2013.

[187] Adri C. T. van Duin, Siddharth Dasgupta, Francois Lorant, and William A. Goddard. ReaxFF. A Reactive Force Field for Hydrocarbons. *The Journal of Physical Chemistry A*, 105(41):9396–9409, 2001.

[188] Alireza Ostadhossein, Ali Rahnamoun, Yuanxi Wang, Peng Zhao, Sulin Zhang, Vincent H. Crespi, and Adri C. T. van Duin. ReaxFF Reactive Force-Field Study of Molybdenum Disulfide ($MoS_2$). *J. Phys. Chem. Lett.*, 8(3):631–640, 2017.

[189] Wencan Jin, Po-Chun Yeh, Nader Zaki, Datong Zhang, Jerzy T. Sadowski, Abdullah Al-Mahboob, Arend M. van der Zande, Daniel A. Chenet, Jerry I. Dadap, Irving P. Herman, Peter Sutter, James Hone, and Richard M. Osgood. Direct Measurement of the Thickness-Dependent Electronic Band Structure of $MoS_2$ Using Angle-Resolved Photoemission Spectroscopy. *Phys. Rev. Lett.*, 111:106801, Sep 2013.

[190] Tawinan Cheiwchanchamnangij and Walter R. L. Lambrecht. Quasiparticle band structure calculation of monolayer, bilayer, and bulk $MoS_2$. *Phys. Rev. B*, 85(20):205302, 2012.

[191] Yajun Wei and Manijeh Razeghi. Modeling of type-II InAs/GaSb superlattices using an empirical tight-binding method and interface engineering. *Phys. Rev. B*, 69:085316, Feb 2004.

[192] Timothy B. Boykin, Gerhard Klimeck, R. Chris Bowen, and Roger Lake. Effective-mass reproducibility of the nearest-neighbor $sp^3s^*$ models: Analytic results. *Phys. Rev. B*, 56:4102–4107, Aug 1997.

# Publications and Conference Contributions

## List of Publications

- *Neutral and charged biexciton-exciton cascade in near-telecom-wavelength quantum dots*
  Phys.Rev. B. **94**.045303 (2016)
  J. Kettler, M. Paul, F. Olbrich, K. Zeuner, M. Jetter, P. Michler, Peter, M. Florian, C. Carmesin, and F. Jahnke
- *Interplay of morphology, composition, and optical properties of InP-based quantum dots emitting at the* $1.55\,\mu m$ *telecom wavelength*
  Phys. Rev. B. **96**.235309 (2017)
  C. Carmesin, M. Schowalter, M. Lorke, D. Mourad, T. Grieb, K. Müller-Caspary, M. Yacob, J. P. Reithmaier, M. Benyoucef, A. Rosenauer, and F. Jahnke
- *Structural and optical properties of InAs/(In)GaAs/GaAs quantum dots with single-photon emission in the telecom C-band up to 77 K*
  Phys.Rev. B. **98**.125407 (2018)
  C. Carmesin, F. Olbrich, T. Mehrtens, M. Florian, S. Michael, S. Schreier, C. Nawrath, M. Paul, J. Höschele, B. Gerken, J. Kettler, S. L. Portalupi, M. Jetter, P. Michler, A. Rosenauer, and F. Jahnke
- *Interplay of structural design and interaction processes in tunnel-injection semiconductor lasers*
  arXiv e-print (2018)
  S. Michael, M. Lorke, M. Cepok, C. Carmesin, and F. Jahnke
- *Localized quantum-dot-like states in molybdenum disulfide nanostructures due to the interplay of strain and dielectric confinement: A theoretical study*
  For submission for publication (2018)
  C. Carmesin, M. Lorke, M. Florian, D. Erben, T. O. Wehling, and F. Jahnke

# List of Conference Contributions

- *Tight-Binding Description of InAs/InP-Quantum Dots: From Electronic States to Multi-Exciton Spectra*
  QCOS Project Meeting, Bremen (2016)
  C. Carmesin, and Frank Jahnke
- *Influence of morphology on InAlGaAs quantum dots emitting at telecom wavelength*
  DPG spring meeting condensed matter section, Dresden (2017)
  C. Carmesin, M. Lorke, D. Mourad, and Frank Jahnke
- *Single-photon sources with quantum dots and TMDs*
  Solid State Seminar, Bremen (2017)
  C. Carmesin, M. Lorke, D. Mourad, and Frank Jahnke
- *Microscopic description of localized quantum-dot-like states in $MoS_2$ nanobubbles*
  DPG spring meeting condensed matter section, Berlin (2018)
  C. Carmesin, M. Lorke, M. Florian, D. Erben, and Frank Jahnke
- *Microscopic description of the electronic and optical properties of novel atomically thin semiconductors and quantum dots*
  MAPEX Symposium (2018)
  C. Carmesin, M. Lorke, M. Florian, D. Erben, D. Mourad and Frank Jahnke

# Acknowledgements

First of all, I would like to thank Prof. Dr. Frank Jahnke for the excellent support during my doctoral studies as well as advice regarding publications and this work.

Furthermore, I would like to thank

Prof. Dr. Gerd Czycholl for comments and discussions regarding the tight-binding model and this work as well as being my second advisor and defense examinator;

Prof. Dr. Tim Wehling, and Prof. Dr. Andreas Rosenauer for agreeing to be defense examinators;

Dr. Michael Lorke for the fruitful collaboration on quaternary quantum dots and TMDC nanobubbles as well as proofreading this work;

Dr. Daniel Mourad for the conducive collaboration and discussions on electronic state calculations of semiconductors and quantum dots as well as providing calculations for the valence band offsets;

Dr. Matthias Florian for the gainful collaboration on TMDC nanobubbles, optical spectra of quantum dots, and numerical advice;

Dr. Stephan Michael for the successful collaboration on tunnel-injection lasers as well as providing $k \cdot p$ calculations;

Daniel Erben for the beneficial collaboration on TMDC nanobubbles and proofreading;

Mawussey Segnon for proofreading, Malte Hartmann and Dr. Alexander Steinhoff for proofreading parts of this work, as well as Dr. Christpher Gies for advice regarding the introduction;

Fabian Olbrich, Dr. Marco Schowalter, Dr. Thorsten Mehrtens, and Dr. Mohamed Benyoucef for the fruitful experimental collaboration;

Alexander Schulz for discussions regarding the $MoS_2$ monolayer tight-binding model;

Andreas Beuthner and Klaus Bowe for technical support;

and last but not least my parents and family for always supporting me.